CRISPR ASSAYS AND MICROFLUIDIC DEVICES FOR QUANTITATIVE DIAGNOSTIC METHODS

By
Alexandre S. Avaro and Juan Santiago

Prepared with support from
Robert Bosch LLC

Report No. TF-204

Flow Physics and Computational Engineering Group
Department of Mechanical Engineering
Stanford University
Stanford, CA 94305

August 2025

CRISPR Assays and Microfluidic Devices For Quantitative Diagnostic Methods

By
Alexandre S. Avaro and Juan Santiago

Prepared with support from
Robert Bosch LLC

Report No. TF-204

Flow Physics and Computational Engineering Group
Department of Mechanical Engineering
Stanford University
Stanford, CA 94305

August 2025

Abstract

This thesis explores the chemical kinetics of clustered regularly interspaced short palindromic repeats (CRISPR) enzyme systems and the design and control of microfluidic systems based on isotachophoresis (ITP). CRISPR systems constitute a recent addition to the molecular diagnostic toolbox and have sparked widespread interest over the past decade due to their easy reconfigurability and high specificity. However, the sensitivity of such systems remains limited by low enzymatic kinetic rates and background signal, especially in amplification-free formats. CRISPR kinetic rates have been widely and frequently misreported, and there has been very little quantitative estimation of the background signal. This thesis addresses these limitations through the development of quantitative kinetic models and experimental studies aimed at the rigorous determination of the sensitivity of CRISPR-based assays. ITP is a well-established electrokinetic technique that has been routinely used for sample purification and preconcentration. However, despite its versatility, its broader adoption has been limited by the complexity of assay and buffer design. This dissertation introduces computational tools, methods, and experimental demonstrations to aid the design of ITP experiments and develop complex ITP systems—including ITP-based networks for sample routing, aliquoting, and mixing.

We first focus on the uncertainty associated with the determination of Michaelis-Menten kinetic rates. We derive a closed-form solution for the fluorescence signal in typical CRISPR assays, and leverage this to quantify how experimental errors such as pipetting variability, nonuniform sensor response, and signal miscalibration propagate into the estimates of k_{cat} and K_M. We then investigate the background signal that limits the sensitivity of CRISPR assays and find that the limit of detection is likely set by the degradation of reporter molecules. This degradation occurs independently of enzymatic activity and imposes a fundamental ceiling on assay performance. Further, to improve assay sensitivity, we develop a high-throughput microfluidics pipeline to screen gRNA sequences for *trans*-cleavage activity. The pipeline combines droplet microfluidics, hydrogel beads, and next-generation sequencing to measure activity across a large panel of gRNA candidates.

We subsequently turn to microfluidic ITP as an integrable technique for sample purification, preconcentration, and molecular control. We present two simulation tools: BEAN, a highly parallel buffer design tool, and CAFES, a web-based partial differential equation solver for complex and nonlinear electrophoresis phenomena. The latter enables rapid exploration and tuning of ITP chemistries and device configurations, and

we validate its predictions experimentally. We then introduce a new class of microfluidic networks based on ITP and demonstrate programmable sample manipulation including aliquoting and mixing in branched microchannel fluidic circuits.

Acknowledgments

The authors gratefully acknowledge the support of Robert Bosch LLC with Dr. Christoph Lang as the Director at Research and Technology Center in Sunnyvale.

THIS PAGE DELIBERATELY LEFT BLANK

Contents

List of Tables

List of Figures

Chapter 1

Introduction

Some of the contents of this chapter were published by A. S. Avaro and J. G. Santiago in the journal *Lab on a Chip* [1] and are reproduced here with minor modifications.

1.1 CRISPR-based diagnostics

1.1.1 CRISPR-Cas system for molecular diagnostics

Clustered regularly interspaced short palindromic repeats (CRISPR) enzymes have recently attracted much attention for their gene editing capabilities [5]. A more recent and rapidly developing part of this technology is its application to the field of molecular diagnostics using CRISPR-associated (CRISPR-Cas) systems [6, 7]. Such systems consist of a Cas endonuclease protein (Cas12 or Cas13 for most diagnostic assays) conjugated with a guide RNA (gRNA), which includes a sequence complementary to a sequence in the target nucleic acid [6, 8]. The gRNA is relatively short (typically 40 to 60 nucleotides) and synthetic, so assays are easily reconfigurable [6].

The first demonstrations were based on Cas9 systems and occurred only about 8 years from the time of this thesis [9, 10]. A major development in the field was the application of CRISPR-Cas12 and -Cas13 enzymes which, after recognizing target, exhibit non-specific endonuclease activity [11, 12, 13]. By including specialized synthetic nucleic acids as reporter molecules in the reaction, this non-specific activity can be used as a linear (in time) amplification of a conveniently measurable signal indicating presence of the target sequence.

The recent global pandemic has sparked increased interest for CRISPR-based assays focused on the detection of SARS-CoV-2, the virus that causes COVID-19 [14, 15, 16, 17, 18, 19, 20]. Many of such assays are focused on microfluidic devices in part because of the compatibility of CRISPR-Cas reagents with lyophilization and the easy readout format of lateral flow biosensors (LFB).

We note that CRISPR/Cas systems have recently been the subject of significant private investment,

commercialization efforts, and intellectual property development [21]. Groups seeking to commercialize new assays should consider that many of the proposed CRISPR/Cas assays discussed here may be covered by (issued) patents. For example, the basic target recognition, transduction, and detection mechanisms employed by all of the assays reviewed here may be collectively covered by US patents 10,253,365 [22] and 10,337,051 [23] for DNA and RNA targets, respectively. US patents restrict manufacture and/or sale of products in the US.

1.1.2 Basic steps of CRISPR-based diagnostics assays

We here pose a basic five-step workflow structure for on-chip microfluidic assays based on CRISPR-Cas enzymes. Figure 1.1a shows this five-step workflow structure. All of the assays we mention here used CRISPR as a means of molecular recognition of a nucleic acid sequence to catalyze a reaction which resulted in products which are directly detectable (e.g., via optical or electrochemical sensing). We shall term this key step a chemical transduction (summarized as "transduction"). In the top row of this figure, we show common examples of these assay steps that used traditional equipment, and, in the bottom row, we show microfluidic examples of these steps. We note that not all assays we mention here employed all steps shown here (e.g., some do not use amplification prior to CRISPR), but all published assays did employ at least three of these basic steps. Assays tend to accomplish these steps sequentially, but we note that two or more of these steps may overlap in time or be simultaneous (e.g., Steps 4 and 5 are often simultaneous). The alluvial diagram of Figure 1.1b summarizes characteristics of the workflow structures of all of the studies reviewed by Avaro and Santiago [1]. As with Figure 1.1a, the five sections are arranged horizontally according to the workflow structure we propose here.

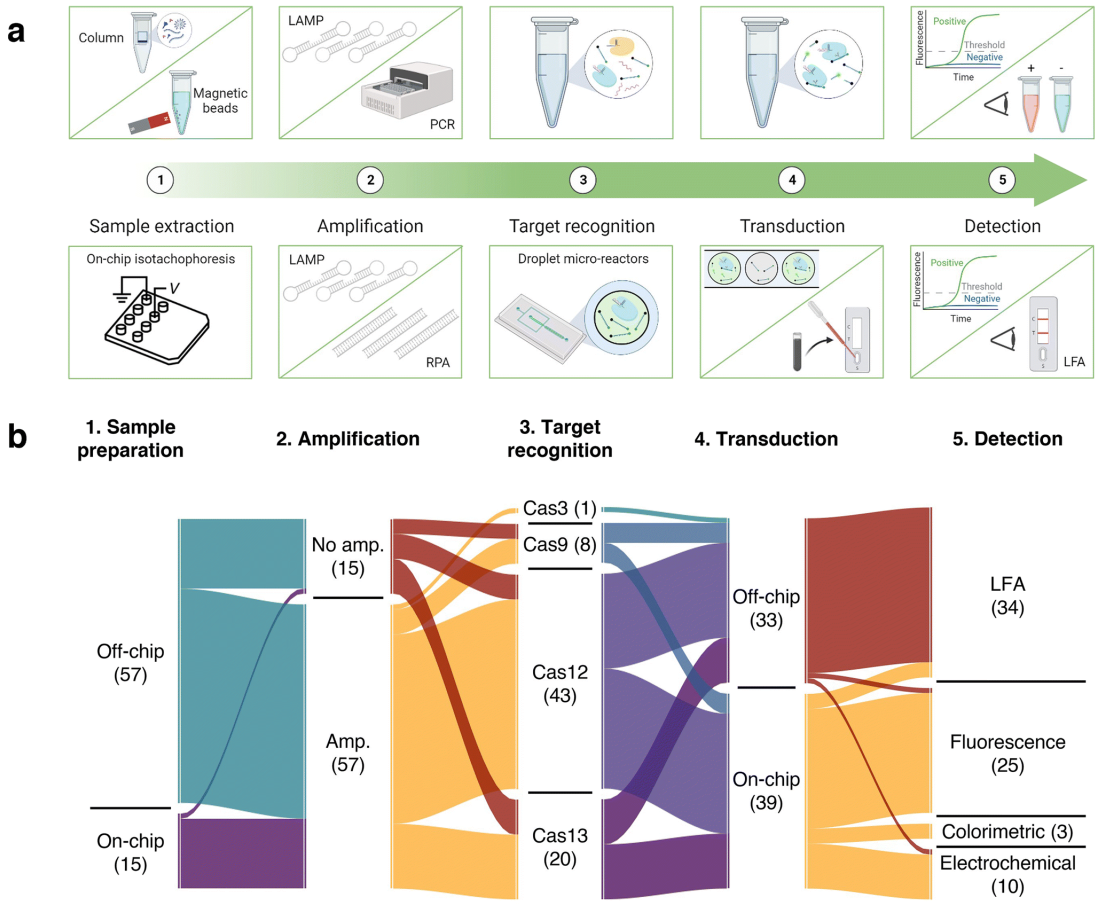

Figure 1.1: a Typical workflow steps for CRISPR-based diagnostics and examples for each step. This structure applies to assays that use traditional equipment (examples in top row), but it is still useful for microfluidics-based assays (bottom row). Here, we classify LFB readout (Step 5) as a microfluidic step. b Alluvial diagram summarizing key aspects of each of the five workflow steps for all of the studies reviewed in Avaro and Santiago [1]. The numbers in parentheses indicate the number of studies corresponding to each classification.

The first step of the proposed framework is sample extraction. PoC applications use a wide variety of starting sample types. These include, among others, nasopharyngeal swab elutes, saliva, blood, and urine. Such samples often contain impurities which may impair each step of the assay. Enzymatic processes in particular are often susceptible to inhibition [24], and blood is often the most challenging starting sample [25]. CRISPR-based assays detect nucleic acid sequences, and so their sample preparation is typically focused on extracting and purifying nucleic acids. Most of the “on-chip” assays do not perform on-chip sample preparation and instead employ commercially available kits (off-chip) prior to introducing the purified sample into a chip. These kits are most often based on spin-columns or magnetic beads. Only a small

fraction of CRISPR assays include on-chip extraction techniques. Another small fraction of assays report extraction-free protocols.

The second step of the framework of Figure 1.1a is nucleic acid amplification (NAA). Most CRISPR-based assays rely on an exponential amplification step prior to (most often) or during detection, using well-known techniques such as polymerase chain reaction (PCR) [26], loop-mediated isothermal amplification (LAMP) [27], or recombinase polymerase amplification (RPA) [28]. Such techniques are either performed using traditional equipment or have been adapted into on-chip protocols.

The next step in a typical CRISPR-based assay is the target recognition by the Cas enzyme. This step is known as *cis*-cleavage and is typically very fast (e.g., completed within a few minutes) [8, 29]. This crucial sequence-recognition step determines the specificity of the CRISPR assay.

Once it recognizes the target (and cleaves it), the Cas enzyme becomes activated. In its activated state, the enzyme thereafter indiscriminately cleaves single-stranded nucleic acids. This is known as *trans*-cleavage and enables transduction, i.e. the generation of a measurable signal. This signal is often fluorescence or electrochemical potential and is further measured to conclude as to the detection of the target nucleic acid.

Note that the vast majority of studies performed at least one essential step off-chip using traditional equipment (as in the top half of Figure 1.1a). This lack of integration, including of the ability to process raw samples, is not specific to CRISPR-based technologies and, unfortunately, common to most "lab-on-a-chip" systems. This trend reflects the importance and difficulty of research into new and improved on-chip sample preparation methods. More than 75% of the studies leverage some sort of pre-amplification in order to improve sensitivity. We attribute this to the inherent current limitation of CRISPR kinetic rates [8, 2]. Lastly, a significant number of studies perform the detection step using LFBs. Most of these use it as the only chip-related technology. On one hand, LFB-based assays offer convenient (often colorimetric) readout in a miniaturized fluidic device compatible with lyophilized reagents. On the other hand, LFB is merely a readout of post-transduction products produced using traditional methods and the equipment of a centralized laboratory.

1.1.3 Brief review of CRISPR *trans*-cleavage kinetics

We focus here on assays using CRISPR-Cas12 and -Cas13, by far the most common CRISPR types used in molecular diagnostics assays. Before any assay, the CRISPR-Cas enzyme is functionalized using a guide RNA (gRNA). The gRNA is a single, synthetic molecule with typically 40 to 60 bases, and which contains two important regions. A first region is a sequence designed to bind to the CRISPR enzyme to form a ribonucleoprotein (RNP) complex. A second region of the gRNA is a reconfigurable sequence that is complementary to the target molecule of interest. Cas12 targets DNA, while Cas13 targets RNA. It is the RNP complex which is used as a starting reagent in nearly all CRISPR assays and in CRISPR microfluidic assays.

A typical CRISPR-based assay then involves two sequential cleavage reactions. First, the CRISPR-Cas/gRNA complex (the RNP) recognizes the target that is complementary to the reconfigurable portion

of its gRNA. The target is cleaved in this so-called "*cis*-cleavage" reaction. This also results in the so-called "activation" of the enzyme. *Cis*-cleavage determines molecular specificity to the nucleic acid sequence of the target. Once it is activated, the CRISPR-Cas enzyme complex repeatedly cleaves nucleic acids irrespective of sequence in a catalytic step known as *trans*-cleavage. *Trans*-cleavage defines the transduction step (c.f. Figure 1.1) wherein a molecular recognition creates a measurable result. For this reason, synthetic nucleic acid strands are included in the reaction as reporter molecules. See Li et al. [30] and Swarts et al. [31] for more detailed descriptions of the *cis*- and *trans*-cleavage reactions of CRISPR assays.

The detectable signal in CRISPR-based assays is created by the reaction rate of the *trans*-cleavage portion of the reaction. We therefore here analyze in detail the *trans*-cleavage kinetic rates since they represent a fundamental limitation to signal-to-noise (and signal-to-background) ratios affecting all CRISPR-based detection assays [2]. We note that there may exist other limitations associated with integrating the enzymatic assay into a microfluidic system. These may include non-specific binding of reagents (e.g., Cas enzyme) to the high-surface-to-volume-ratio structures of a microfluidic chip. A second example may be the common situation where the microfluidic device processes smaller reagent volumes and so there exists a lower volume-integrated number of molecules that can be detected.

The characteristic time scale for the *cis*-cleavage reaction is typically short [32] and scales inversely with the concentration of the enzyme [8]. This is true even for trace concentrations of target [31, 32, 33, 34]. Therefore, it is widely accepted that the *cis*-cleavage step is not rate-limiting and that the time scales of typical CRISPR reactions are limited by the *trans*-cleavage step [29]. For this reason, we here focus on a model of the *trans*-cleavage kinetics of CRISPR-Cas enzymes. The *trans*-cleavage reaction can be summarized as follows [35]:

$$E + S \underset{k_r}{\overset{k_f}{\rightleftharpoons}} C \xrightarrow{k_{cat}} P \tag{1.1}$$

where E is the target-activated Cas enzyme after *cis*-cleavage, S is the uncleaved reporter, C is an intermediate complex and P is the cleaved reporter. k_f and k_r are respectively the forward and reverse rate constants for the formation of the complex, and k_{cat} is the turnover rate of the enzyme. Reporters molecules are typically short, functionalized, synthetic single-stranded nucleic acids. Cas12 uses ssDNA reporters while Cas13 uses ssRNA reporters. The functional groups of the reporter molecules depend on the detection method. The most commonly employed reporters use fluorescent-quencher pair reporters for fluorescence detection (see, for example, Ramachandran et al. [36] or Shinoda et al. [37]). A second common functionalization is FAM-biotin pair reporters useful in, for example, subsequent LFB-based assays (see, for example, Barnes et al. [38] or Azhar et al. [39]). Other examples of reporter functionalization include those for electrochemical potential [40, 41, 42] or current-based [43, 44, 45, 46] detection techniques.

The *trans*-cleavage reaction above is modeled using the well-known Michaelis-Menten kinetics model. This model comprises the following set of rate equations [35]:

$$\frac{d[E]}{dt} = -k_f[E][S] + k_r[C] + k_{cat}[C], \tag{1.2}$$

$$\frac{d[S]}{dt} = -k_f[E][S] + k_r[C], \tag{1.3}$$

$$\frac{d[C]}{dt} = k_f[E][S] - k_r[C] - k_{cat}[C], \tag{1.4}$$

$$\frac{d[P]}{dt} = k_{cat}[C]. \tag{1.5}$$

In addition to equations 1.2 to 1.5, the conservation of species for both enzyme and reporters adds the following constraints, combined with initial conditions:

$$[E]_0 = [E] + [C], \tag{1.6}$$

$$[S]_0 = [S] + [P] + [C], \tag{1.7}$$

$$[P]_0 = [C]_0 = 0. \tag{1.8}$$

The "0" subscripts indicate the initial concentration of the species. Under the reactant-stationary assumption [47] and the quasi-steady state assumption [48], these equations combine to yield the Michaelis-Menten equation:

$$\frac{d[S]}{dt} = -\frac{d[P]}{dt} = -\frac{k_{cat}[E]_0[S]}{K_M + [S]}, \tag{1.9}$$

where $K_M = \frac{k_{cat}+k_r}{k_f}$ is the Michaelis-Menten constant. The vast majority of CRISPR-based assays satisfy both simplifying assumptions, hence k_{cat} and the ratio k_{cat}/K_M fully describe the temporal response of the system. We here note that these kinetic rate parameters require controlled experiments at varying substrate (i.e., reporter molecule) concentrations for quantification. We further note that both experimental uncertainties and bias in experimental design can lead to significant errors in the quantification of k_{cat} and K_M [49].

The assay limit of detection (LoD) is typically not limited by the detector's ability to detect a signal (sensitivity of detector), but rather by its ability to discriminate (specific) signal from background. One common source of background signal in the case of fluorescent reporters is the significant signal associated with imperfect quenching of fluorescence reporters. That is, uncleaved, quenched reporters also contribute to the fluorescence signal. In fact, the cleaved-to-uncleaved signal ratio is typically only order 10-fold [29, 2].

Despite their importance, CRISPR kinetic parameters have been vastly misreported in the CRISPR diagnostics literature. Reports of k_{cat} and K_M have exhibited grossly inconsistent data which violate basic laws of mass conservation and chemical kinetics [8, 29]. Ramachandran and Santiago proposed three back-of-the-envelope calculations which can be used to check enzyme kinetics data for self-consistency [8, 29]. They

also identified published reports, including some that employed microfluidics techniques [19, 50], which included kinetics data that was demonstrably and highly inconsistent. Following the publication of an initial preprint of these results [51], two seminal papers in CRISPR-based diagnostics (Chen et al. [12] and Slaymaker et al. [13]) issued errata lowering their reporter kinetic rates by more than two orders of magnitude. Further, Santiago [8] pointed out that reported LoDs in some papers are difficult to reconcile given the kinetic rates of CRISPR and its background activity. For example, some assays reported sensitivities which approached that of PCR [19, 52, 53].

Another important factor governing CRISPR activity is the temperature at which the enzyme is stored and used. This limits the compatibility of CRISPR assays with amplification methods that require high temperatures, at which the enzyme degrades [18]. However, the advent of thermostable CRISPR orthologs [54] will likely benefit the development of one-pot or quasi-one-pot assays, e.g. where the amplification step and CRISPR-based detection are performed simultaneously.

Lastly, we end this section with a positive aspect of CRISPR. CRISPR diagnostics methods are highly reconfigurable. The CRISPR-Cas enzyme can be functionalized to recognize virtually any desired nucleic acid target by adjusting the portion of the gRNA complementary to said target. Broughton et al. [55] reported that CRISPR-based technologies can be reconfigured for various target sequences within days, since the only modification to a given assay is gRNA customization. Kaminski et al. [6] discussed design considerations for gRNAs. gRNAs are typically 40 to 60 nucleotides long, and their length depend on the chosen Cas system [6]. For example, Cas12 enzymes target both dsDNA and ssDNA using a 40 nucleotide-long gRNA, but require a proto-spacer adjacent motif (PAM) sequence for efficient targeting of dsDNA [56]. The high reconfigurability of CRISPR assays highlights an important potential of this technology for multiplexed assays. One salient example is the system of Ackerman et al. [57], who performed 169 detection reactions in parallel (each reaction using a different gRNA) using droplet generation and merging techniques.

1.2 Microfluidic isotachophoresis (ITP)

1.2.1 ITP basics

Isotachophoresis (ITP) is a well-established electrophoretic technique that has been applied for a wide variety of applications [58], including separation [59, 60], purification [61, 62], analyte preconcentration [63], sample preparation upstream of bioassays [17], or accelerating biochemical reactions [64]. The latter include both homogeneous reactions [17, 65] (i.e., where all reagents are in solution) and heterogeneous reactions [66] (i.e., wherein at least one reagent is immobilized on a surface).

The theoretical description of ITP, along with a description of its existing applications, has been recently extensively reviewed by Ramachandran and Santiago [58]. ITP can be applied to either anionic or cationic sample ions. It uses a heterogenous buffer system that consists of a leading electrolyte (LE) and a trailing electrolyte (TE). Both the LE and the TE contain at least one co-ion, i.e. one ion whose valence has the same

sign as that of the sample ion(s) that is focused. The LE co-ion and TE co-ion are typically selected so that they have respectively higher and lower electrophoretic mobility than the sample ions. When an electric field is applied, all co-ions migrate in the same direction, at a velocity proportional to their electrophoretic mobility and the local electric field. Species whose effective electrophoretic mobility is bracketed by the one of the LE and the TE ions are focused in a sharp concentration peak at the interface. The width of this interface can be derived from a balance between electromigration and molecular diffusion [67]. LE and TE chemistries can be optimized to enable selective focusing and preconcentration of specific samples based on their electrophoretic mobility [68].

1.2.2 Simulation tools for ITP

Despite its high potential for many applications, the adoption of ITP in routine microfluidic processes remains relatively rare. We attribute this to the steep learning curve required to design and perform ITP experiments. Indeed, ITP experiments sometimes involve more than ten different chemical species, whose concentrations and mobilities vary in space and time. These quantities must be properly tracked to accurately predict the behavior of ITP systems (e.g., whether a sample will focus at an ITP interface or not) [58].

Simulation tools offer an effective response to this challenge. Accessible numerical tools enable users to easily understand, model, and design complex ITP processes. Several ITP simulation tools have been developed and are currently available. We distinguish ITP zone chemistry calculators, which are based on algebraic forms of species conservation equations [59, 69], from PDE solvers that enable the determination of the "where and when" of the various species. The latter require to solve the differential form of the electromigration-diffusion-reaction conservation equations. One of the first freely accessible nonlinear electrophoresis simulators is SIMUL [70, 71]. SPRESSO is a MATLAB-based tool first developed [72] in 2009 (and later updated [73, 74]) that enables the user to resolve sharp gradients (which routinely occur in ITP processes) and to include ionic strength effects.

1.3 Scope of the dissertation

The objective of this thesis is to develop methods and devices for quantitative molecular diagnostics. The dissertation is composed of five main chapters. Chapters 2 to 4 focus on fundamental kinetics of CRISPR-Cas assays. Chapters 5 and 6 focus on ITP experimental design tools and networks.

In Chapter 2, we present a quantification of the uncertainty inherent to the experimental determination of kinetic rate parameters for enzymatic reactions. We study the influence of several sources of uncertainty and bias, including the inner filter effect, pipetting errors, number of points in the Michaelis–Menten curve, and flat-field correction. Using Monte Carlo simulations and analyses of experimental data, we compute typical uncertainties of k_{cat}, K_M, and catalytic efficiency k_{cat}/K_M. As a salient example, we analyze the extraction of such parameters for CRISPR-Cas systems.

In Chapter 3, we demonstrate that the background signal and limits of detection of most CRISPR assays are very likely limited by the degradation of reporter molecules. This degradation is dynamic and is not associated with enzymatic activity. We present theory and experiments to design and calibrate CRISPR assays. We introduce a new kinetic framework to account for the degradation of reporter molecules and derive a fundamental limit of detection for CRISPR-based assays.

In Chapter 4, we introduce a screening method for gRNA to identify sequences that result in high *trans*-cleavage enzymatic activity. We first screen 364 sequences. We then introduce a microfluidics pipeline based on droplet microfluidics, hydrogel beads, and next-generation sequencing to screen gRNA with a much higher throughput.

In Chapter 5, we present a rapid, highly parallelized steady-state solver for the design of buffer electrolytes in ITP experiments. This solver is designed to facilitate the evaluation and identification of functional buffer chemistries for ITP. We also introduce a client-side web-based simulator for complex electrophoresis phenomena, including isotachophoresis, along with experimental validation.

In Chapter 6, we introduce a new class of microfluidic networks based on ITP. We present a theoretical framework to describe these networks. We leverage this framework to create numerical simulations of branched ITP circuits. We then build, control, and experimentally study a variety of ITP networks

Finally, in Chapter 7, we summarize the main contributions of this work, and suggest directions for future research.

Chapter 2

Uncertainty quantification of Michaelis–Menten kinetic rates and its application to the analysis of CRISPR-based diagnostics

The contents of this chapter were previously published by A. S. Avaro and J. G. Santiago [49] in the journal *Angewandte Chemie* and are reproduced here with minor modifications. Supplementary information associated with this chapter is presented in Appendix A.

2.1 Introduction

The Michaelis-Menten set of reaction rate equations is the most used model to describe enzyme kinetics. Since its original formulation in 1913 [35], there has been considerable work to refine the quantification of the kinetics of enzymatic reactions. A seminal variation of Michaelis and Menten's work was derived by Briggs and Haldane [48], who formulated the quasi-steady state assumption. In this framework, enzyme kinetics are fully described by two constants: a turnover rate (k_{cat}) and the Michaelis-Menten constant (K_M). Protocols to measure these parameters have been studied extensively in the past century. Some proposed methods proport to require a single experiment to measure k_{cat} and K_M [75, 76, 77]. However, most studies recommend variation of the initial substrate concentration and measure the corresponding initial reaction velocities. These velocities are plotted versus substrate concentration to create a so-called "Michaelis-Menten curve" and the data is fitted to extract k_{cat} and K_M [75, 78, 79, 80, 81]. Small errors in the initial velocities can lead to significant discrepancies in the estimation of the kinetic parameters [79]. To

date, we know of only one study that has considered the propagation of uncertainty in the Michaelis-Menten model for the specific case of microbial pollutant degradation [82]. The latter work quantified uncertainty due to the effect of fitting a finite number of data points but took into account neither sources of experimental uncertainty nor their propagation. A few such experimental uncertainties have been studied separately, including the influence of the inner filter effect on experimental Michaelis-Menten curves [83] and the number of points in the Michaelis-Menten curve (corresponding to the number of dilutions performed) required for the determination of K_M [84]. However, we know of no work that systematically quantifies the major sources of experimental uncertainty typical of Michaelis-Menten kinetics analyses (including for clustered regularly interspaced short palindromic repeats (CRISPR) systems). We also know of no study that performs propagation of error analyses to estimate the combined influence of such uncertainties on the uncertainty in k_{cat} and K_M.

A recent and important example of Michaelis-Menten rate parameter evaluation is the quantification of CRISPR-associated (Cas) enzyme kinetics. CRISPR-Cas systems are used to detect nucleic acid sequences with high specificity [6, 85, 57, 86, 11], and the limit of detection of such assays is directly governed by the kinetic rates of the enzyme [29, 2, 8]. The accurate quantification of the kinetic parameters is therefore paramount to evaluate the reliability and regime of applicability of CRISPR-based diagnostics assays. Despite its importance, the vast majority of CRISPR-Cas enzyme kinetics reports have exhibited grossly inconsistent data that clearly and demonstrably violate basic laws of mass conservation and chemical kinetics. Ramachandran and Santiago [29] and Santiago [8] collectively discuss over 10 examples of publications which exhibit gross errors in kinetic rate data and/or report limits of detection which are difficult to reconcile given current capabilities of CRISPR-Cas systems. At the same time, k_{cat} and K_M values are often reported to three significant figures. As just one example, Santiago [8] points out that the two highest values of k_{cat} ever reported (about 4,850 s^{-1}) agree with each other to three significant figures, despite corresponding to two different CRISPR-Cas orthologs.

In this work, we characterize and quantify important sources of experimental uncertainty typical of enzymatic kinetics analyses in the Michaelis-Menten framework. As a case study, we analyze kinetic rate studies typical of CRISPR-Cas enzymes. To this end, we first derive a closed-form solution for the fluorescent signal intensity, the measured quantity in CRISPR-based assays. Next, we characterize each source of input uncertainty in the processes of solution dilution, signal calibration, and other experimental methods and variables. This includes an estimate formulation of the input probability density distributions of each experimental variable. We then simulate experimental realizations of the kinetic rate analyses using Monte Carlo simulations which leverage the Michaelis-Menten model with triplicate averaging. In this way, we propagate the experimental variable uncertainty to estimate the uncertainties on the kinetic parameters k_{cat}, K_M, and $\eta = k_{cat}/K_M$. The analyses highlight key sources of uncertainty and strongly suggest that the experimental measure of the catalytic efficiency η exhibits higher precision than the individual estimation of k_{cat} and K_M.

2.2 Results and discussion

We here describe the governing equations for the time evolution of signal of a wide range of assays based on Michaelis-Menten processes. In interpreting assay signal and its associated background and uncertainties, we consider the specific application of CRISPR-based diagnostics assays. In particular, we focus on CRISPR assays which quantify fluorescence signal resulting from cleaving of reporter molecules. First, we derive a closed-form solution for the concentration of cleaved reporters. Next, we consider calibration between concentration and fluorescence signal and quantification of background signal from uncleaved reporters and the inner filter effect. Lastly, we present a model for the uncertainty associated with pipetting and typical serial dilution processes. The goal of these formulations is to provide a closed-form expression for the fluorescence signal and a model for experimental uncertainties and bias. These uncertainties and bias errors are then combined with Monte Carlo simulations of many Michaelis-Menten kinetics analyses to compute corresponding distributions of k_{cat} and K_M.

2.2.1 Closed-form solution of the cleaved substrate concentration

We here summarize some key aspects of Michaelis-Menten kinetics, particularly in the context of CRISPR-diagnostics assays. CRISPR assays involve two reactions: a specific *cis*-cleavage step during which the enzyme is activated and a *trans*-cleavage step where the activated enzyme indiscriminately cleaves single-stranded nucleic acids [11, 12, 87]. The *cis*-cleavage step is analogous to a second-order reaction, where the low-abundance target is consumed. As we discuss in Section A.7, for typical detection assays, the time-scale for completion of the *cis*-cleavage portion of CRISPR assays is typically significantly lower than that of the *trans*-cleavage [8]. Hence, the *trans*-cleavage step has been identified as the rate-limiting reaction in diagnostics assays [29], and this is true even for trace amounts of target. The *trans*-cleavage step is here modeled by Michaelis-Menten kinetics and is the main focus of the present work.

The *trans*-cleavage CRISPR enzymatic reaction can be described using the following equation:

$$E + S \underset{k_r}{\overset{k_f}{\rightleftharpoons}} C \xrightarrow{k_{cat}} P + E \tag{2.1}$$

where E denotes the target-activated Cas enzyme, S the uncleaved reporter, C an intermediate complex and P the cleaved reporter. k_f and k_r are respectively the forward and reverse rate constants for the formation of the complex, and k_{cat} is the turnover rate of the enzyme. Typically, CRISPR assays use fluorophore-quencher reporters whose quantum yield significantly increases when cleaved. The rise in fluorescence signal implies the presence of activated enzyme and enables detection of the target nucleic acid. Although an important source of background, for simplicity, we here do not consider the background non-specific cleavage activity of the non-activated enzymes [2].

The kinetic equations that describe *trans*-cleavage are known as the Michaelis-Menten system and are detailed in Section A.1. Under both the reactant-stationary assumption [47] and the quasi-steady state assumption [48], the reaction velocity is governed by the Michaelis-Menten equation:

$$\frac{d[P]}{dt}(t=0) = v_0([S]_0) = k_{cat}[E]_0 \frac{[S]_0}{K_M + [S]_0}. \tag{2.2}$$

where $K_M = \frac{k_{cat}+k_r}{k_f}$ is the Michaelis-Menten constant. In practice [2], the kinetic rate parameters k_{cat} and K_M are determined by fitting the Michaelis-Menten curve, i.e. the variations of the initial reaction velocity v_0 as a function of the initial substrate concentration $[S]_0$. Multiple experiments are performed with varying $[S]_0$ and measured values v_0 are used to build the Michaelis-Menten curve. The best fit of Equation 2.2 then yields values of k_{cat} and K_M. Note that reliable Michaelis-Menten curves should include values of $[S]_0$ which encompass K_M [88], even though this value is initially unknown. The relatively high value of K_M of Cas enzymes [29] ($K_M \sim O(100\text{ nM to }1\ \mu\text{M})$) compel the research to use proportionally high initial concentrations of reporters. This contributes to increase the absorbance of the solution in which the *trans*-cleavage reaction takes place and the so-called inner filter effect, which is discussed in a subsequent section. In order to derive a closed-formed solution for all time instants, the Michaelis-Menten system can be integrated to derive a well-known solution [89]:

$$[S](t) = K_M W\left(\frac{[S]_0}{K_M} e^{\frac{[S]_0}{K_M} - \frac{k_{cat}[E]_0}{K_M} t}\right) \equiv K_M \mathcal{A}\left(t; [S]_0, [E]_0, k_{cat}, K_M\right). \tag{2.3}$$

where W is the Lambert-W function that satisfies:

$$xe^x = y \Leftrightarrow x = W(y). \tag{2.4}$$

We here defined $\mathcal{A}\left(t; [S]_0, [E]_0, k_{cat}, K_M\right)$ for simplicity. We show details of the latter derivation Section A.1.

Despite the utility of the latter solution, our current analysis requires a solution to the kinetics of the cleaved substrate concentration. The latter is required as a model of the measured fluorescence signal in CRISPR assays. We here therefore here derive a closed-form solution for the so-called "progress curve," i.e. the time evolution of the concentration of cleaved reporters. To this end, we again apply the quasi-steady state assumption and the rate of formation of product to formulate the concentration of intermediate complex:

$$[C](t) \approx \frac{[E](t)[S](t)}{K_M} = \frac{[E]_0 [S](t)}{K_M + [S](t)}. \tag{2.5}$$

We provided details of the derivation of Equation 2.5 in Section A.1. In the latter discussion, we also compared Equation 2.5 to a numerical solution of the full Michaelis-Menten system. We then apply the conservation of reporters and formulate the progress curve as follows:

$$[P](t) = [S]_0 - K_M \mathcal{A}(t) - [E]_0 \frac{\mathcal{A}(t)}{1 + \mathcal{A}(t)}. \tag{2.6}$$

In the next section, we quantify the fluorescence signal from uncleaved (Equation 2.3) and cleaved (Equation 2.6) reporters.

2.2.2 Error due to neglecting signal from uncleaved reporters

We now present the calibration of the progress curve, i.e. the conversion from the fluorescence signal to the corresponding value of cleaved reporter concentration. Unfortunately, the vast majority of measurements of CRISPR enzyme kinetics studies [6, 11, 19, 13] do not report calibration data relating signal to product concentration. Of those that report such data, only a few [85, 29, 2, 17] report separate calibrations for uncleaved versus cleaved reporters–even though typical cleaved-to-uncleaved signal ratios [29] are only on the order of 10. Assuming negligible inner filter effect (which will be discussed in the next section), the actual fluorescence signal measured during a CRISPR *trans*-cleavage assay is well described by the following calibration curve [17]:

$$I(t) = F_{Ucl}\,[S](t) + F_{Cl}\,[P](t)\,. \tag{2.7}$$

Here, F_{Ucl} andF_{Cl} are calibration parameters accounting for the signal respectively produced by uncleaved and cleaved reporters and $I(t)$ is the measured fluorescence signal. Note that the reporters complexed with the enzyme (noted C) are ignored in this calibration because their concentration is typically much lower than both $[S]$ and $[P]$.

We can therefore quantify the error incurred on the concentration of cleaved reporters if the fluorescence signal due to uncleaved reporters is ignored (as is apparently commonly done in the field). From Equation 2.7, this error can be quantified as:

$$[\widetilde{P}] - [P] = \alpha([S]_0 - [P]). \tag{2.8}$$

Here, $[\widetilde{P}]$ is the overprediction of the concentration $[P]$. As expected, the error scales with the dynamic range (i.e., the cleaved-to-uncleaved signal ratio) of the reporters $\alpha = \frac{F_{Ucl}}{F_{Cl}}$. A derivation of Equation 2.8 along with the study of influence of α on the determination of k_{cat} and K_M is detailed in Section A.2. Briefly, not accounting for the signal of uncleaved reporters tends to result in an underprediction of k_{cat}, but has negligible effect on K_M.

2.2.3 Error associated with the inner filter effect and calibration between fluorescence signal and concentration

In practice, CRISPR assays are performed in solutions that have nonzero absorbance. This leads to the so-called inner filter effect, which originates from the self-absorption of both excitation and emission photons [90]. This results in a non-linear calibration curve. Huyke et al. [2] suggest the following correction to account for this effect:

$$I(t) = \frac{F'_{Ucl}[S](t) + F'_{Cl}[P](t)}{10^{[S]_0/c_0}}. \tag{2.9}$$

This calibration curve depends on three calibration factors. First, c_0 has the dimension of a concentration and is inversely proportional to the product of the molar extinction coefficient and the optical path length, as per the Beer-Lambert law [91]. F'_{Ucl} and F'_{Cl} are the parameters obtained from fitting the calibration data.

We can then infer from Equations 2.3, 2.6 and 2.9 the closed-form solution of the fluorescence signal for a typical CRISPR assay:

$$I(t) = \frac{F'_{Ucl}K_M\mathcal{A}(t) + F'_{Cl}\left([S]_0 - K_M\mathcal{A}(t) - [E]_0\frac{\mathcal{A}(t)}{1+\mathcal{A}(t)}\right)}{10^{[S]_0/c_0}}. \tag{2.10}$$

The solution therefore depends on the kinetic parameters of the enzyme (k_{cat}, K_M), initial concentrations ($[S]_0$,$[E]_0$) and the calibration parameters (F'_{Cl}, F'_{Ucl},c_0).

2.2.4 Model for the uncertainty associated with pipetting and serial dilutions

We now model the uncertainty associated with pipetting steps and the associated error propagation during the serial dilution process typical of CRISPR assays. The construction of a Michaelis-Menten curve requires the iterative preparation of N several solutions of varying uncleaved reporter concentration noted $[S]_{0,n}$ ($0 \leq n \leq N$) [36]. We derive the concentration distribution for each dilution.

We define s_n and x_n as the random variables associated with the error in the concentration at the n^{th} dilution (dilution factor f) and the pipetting error associated with the n^{th} dilution step, respectively. Similarly to previous studies [92], we model x_n (for a single dispensation step) as normally distributed, such that $x_n \hookrightarrow \mathcal{N}(0, \sigma_n)$. We here propose that the dilution protocol imposes the following recurrence relation:

$$s_{n+1} = \frac{s_n}{f} + x_{n+1}. \tag{2.11}$$

We can iterate for all $n \geq 1$:

$$s_n = \frac{s_0}{f^n} + \sum_{j=1}^{n} \frac{x_j}{f^{n-j}}. \tag{2.12}$$

s_n has therefore the following distribution:

$$s_n \hookrightarrow \mathcal{N}\left(\frac{s_0}{f^n}, \left(\sum_{j=1}^{n}\left(\frac{\sigma_j}{f^{n-j}}\right)^2\right)^{1/2}\right). \tag{2.13}$$

We then add an additional pipetting step to account for the dilution of the stock solution to the tube in which the *trans*-cleavage reaction is performed. We can therefore conclude for $0 \leq n \leq N$:

$$[S]_{0,n} \hookrightarrow \mathcal{N}\left(\frac{s_0}{f^{n+1}}, \left(\sigma_{n+1}^2 + \sum_{j=1}^{n}\left(\frac{\sigma_j}{f^{n-j}}\right)^2\right)^{1/2}\right). \tag{2.14}$$

Note that this result is irrespective of the assumed distribution of x_n (as long as $\sigma_n \neq 0$) due to the Central Limit Theorem. We demonstrate the accuracy of our pipetting model Equation 2.14 by benchmarking it with a Monte-Carlo model accounting for a large number of realizations of serial pipetting in Section A.3.

The input parameters for this model are here taken from the tabulated uncertainty values for micropipettes [93] and the typical choice of substrate concentrations [29]. Consistent with the experimental data we will present, we take the following values:

$$\sigma_j \simeq 0.04\frac{s_0}{f^j},\ f = 2. \tag{2.15}$$

2.2.5 Estimates of uncertainty distributions of k_{cat} and K_M based on Monte Carlo simulations

We first present purely computational estimates based on the previously described uncertainty and bias errors and the closed-form solution for the fluorescence signal (Equation 2.10). To this end, we performed Monte Carlo simulations to estimate the distribution of the kinetic parameters k_{cat} and K_M due to various errors for known constant values of these parameters k_{cat}^* and K_M^*. We first study the separate influence of the phenomena described in the previous sections on the estimation of k_{cat} and K_M and we will later examine the propagation of error if such phenomena are superposed. Here, we generated distributions of input parameters corresponding to experimental uncertainties. For now, we consider three sources of uncertainty, each characterized by an input parameter: the inner filter effect (c_0, see Equation 2.9), pipetting errors ($[S]_{0,n}$ and $[E]_0$, see Equation 2.14) and the number of points in the Michaelis-Menten curve (N). Each value of the input parameter is then used to derive a unique set of progress curves, with varying initial substrate concentrations. Each set of progress curves is repeated three times, to simulate triplicates (experiments repeated three times). The effect of replicates of the experiment is discussed in more detail in Section A.4. We then plotted the corresponding Michaelis-Menten curve and extracted the values of the kinetic parameters corresponding to the input parameter. This enabled us to construct distributions of k_{cat} and K_M given distributions of the input parameter. All simulations and fits were performed using Python 3.7.11 [94] and SciPy 1.7.3 [95].

Figures 2.1a-b show the bias error influence of the inner filter effect calibration on the estimation of the kinetic parameters. Figure 2.1a shows a plot of Michaelis-Menten curves for six values of the absorption parameter c_0. The apparent initial reaction velocity gradually decreases with increasing values of the absorbance (i.e., decreasing values of c_0). Figure 2.1b shows the apparent values of k_{cat} and K_M for 97 values of c_0 ranging from 3 to 100 μM. True values of the kinetic parameters k_{cat}^* and K_M^* are shown with a cross.

The inset shows the corresponding relative error on k_{cat} and K_M defined as $u_\kappa = \frac{|\kappa^* - \kappa|}{\kappa^*}$ ($\kappa = k_{cat}, K_M$). Neglecting the inner filter effect (Equation 2.9) in calibration for c_0 and $[S]_0$ values observed experimentally [85] results in relative errors of more than 50% on each kinetic constant. This observation is important as at least some papers in the field exhibit data with strong inner filter effect but do not account for this in calibration (see Li et al. [96] for an extreme case). Importantly, the distribution data in Figure 2.1b also suggests that all estimates of k_{cat} and K_M yield roughly approximately equal, and fairly accurate, values of the ratio of these parameters which is, of course, the Michaelis-Menten kinetic efficiency $\eta = \frac{k_{cat}}{K_M}$. From this observation we conclude that η is insensitive to c_0 and the inner filter effect bias error.

Figure 2.1c shows Michaelis-Menten curve data for 10,000 simulated realizations of the pipetting process. Each cluster shows a distribution induced by the distributions of $[S]_{0,n}$ (Equation 2.14) and $[E]_0$ (normal distribution). In inset are plotted progress curves for each repeat. Figure 2.1d shows the corresponding distributions of k_{cat} and K_M. Relative errors solely due to pipetting errors are as high as 10% and 20% for k_{cat} and K_M, respectively. Note that the distributions shown in this figure include the effect of averaging over triplicates. As shown and discussed in Section A.4, the distribution of individual realizations of K_M is markedly skewed toward larger values.

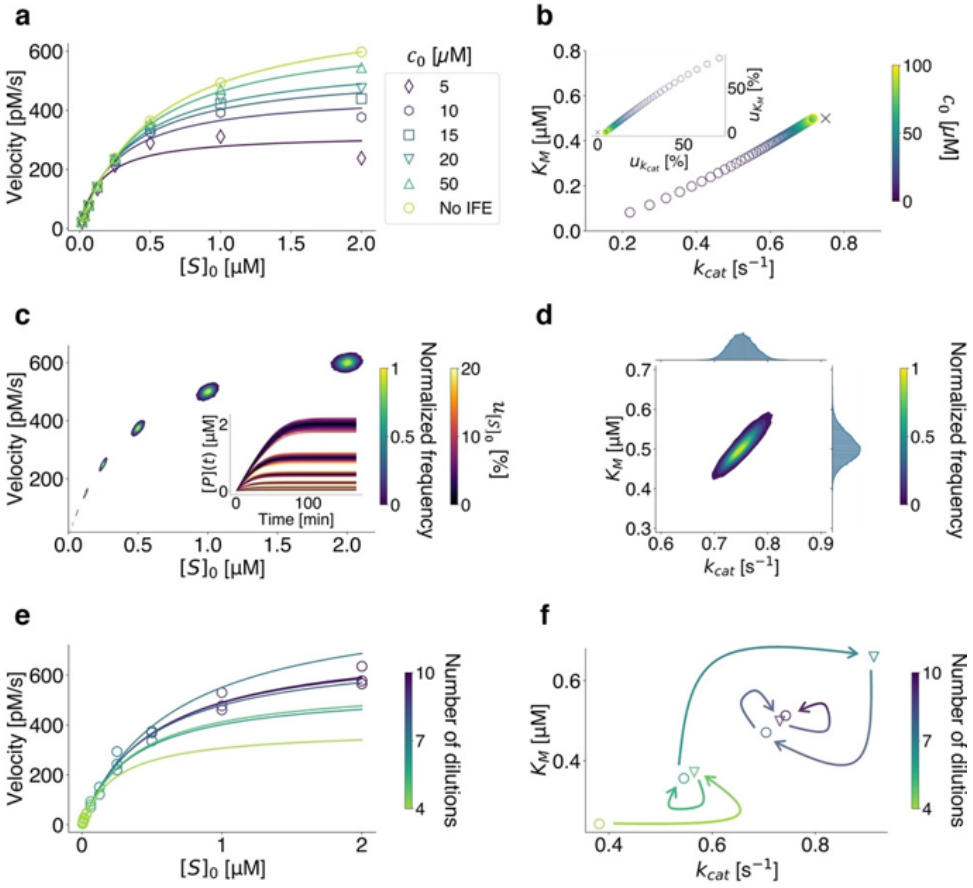

Figure 2.1: Estimates of kinetic constants given uncertainty on experimental parameters using simulated progress curves. All simulation results are shown for fixed kinetic parameters of $k^*_{cat} = 0.75$ s^{-1} and $K^*_M = 0.5$ μM. a and b quantify the inner filter effect (IFE). a Initial reaction velocities vs varying concentration of reporters $[S]_0$ (symbols) and Michaelis-Menten curves (solid lines) for six values of c_0 (Equation 2.9). No IFE corresponds to $c_0 = +\infty$. b Distribution of k_{cat} and K_M for 97 values of c_0 (circles). k^*_{cat} and K^*_M are marked with a cross. Inset shows relative error of each parameter. c and d quantify pipetting errors. c Michaelis-Menten curves for 10,000 repeats of the pipetting process (Equation 2.14). Inset shows the corresponding progress curves. The relative error in substrate concentration for each repeat is defined as $u_{[S]_0} = \frac{|[S]_{0,th} - [S]_{0,exp}|}{[S]_{0,th}}$, where $[S]_{0,th}$ is target concentration and $[S]_{0,exp}$ is pipetted concentration of the individual repeat. d shows corresponding distributions of k_{cat} and K_M. The marginal distribution of k_{cat} (resp. K_M) is plotted on the top (resp. right) axis. e and f quantify the effect of varying the number of $[S]_0$ values used to generate the Michaelis-Menten curves. e Initial reaction velocities vs $[S]_0$ (symbols) and Michaelis-Menten fits (solid line) considering four to ten points of the Michaelis-Menten curve. f Corresponding values of k_{cat} and K_M (circles for even number of dilutions, triangles for odd). Curved arrows indicate the progression of values extracted with increasing number of $[S]_0$ values.

Figure 2.1e shows Michaelis-Menten fits for seven choices for the number of dilutions of reporter (i.e., numbers of values of $[S]_0$ used to generate the curve). The cardinality of the subsets of dilutions ranges from four to ten. This simulation also includes the effect of simulated pipetting errors as described by Equation 2.14. Figure 2.1f shows the corresponding values of k_{cat} and K_M. Values of k_{cat} and K_M corresponding to even (odd) number of points in the Michaelis-Menten curve are shown with a circle (triangle). Curved arrows track the progression of the estimation of the kinetic parameters with increasing numbers of $[S]_0$ values used for the Michaelis-Menten curve. Here, the kinetic parameter estimates converge as the number of dilutions increases. Conversely, Michaelis-Menten curves constituted of four or five points, as sometimes reported in CRISPR studies [96], yield estimates of k_{cat} and K_M off by a factor 2 compared to the theoretical values k^*_{cat} and K^*_M. We therefore recommend eight points on the Michaelis-Menten curve for reliable estimates of k_{cat} and K_M. This is consistent with the recommendation for the estimation of K_M only by Ritchie and Prvan [84].

2.2.6 Uncertainty propagation in the estimation of the kinetic parameters

We now present the results of Monte Carlo simulations to estimate the values of k_{cat} and K_M considering both individual sources of uncertainty and considering combinations of such sources. Similarly to what we presented in the previous section, we generated modified progress curves using Equation 2.10 and extracted initial velocities to build Michaelis-Menten curves. We then fit these curves yields values of the kinetic constants k_{cat} and K_M. Figure 2.2 shows the relative error on k_{cat} (resp. K_M), denoted $u_{k_{cat}}$ (resp. u_{K_M}), on the lower (resp. upper) diagonal half using two color scales and for test cases of propagated uncertainty. These cases involve both individual sources of uncertainty ((a)-(d)) or combinations thereof. For random sources of uncertainty ((a) and (b)), the value shown in Figure 2.2 was calculated as the averaged relative error across 1,000 realizations of the random process. Similarly to the previous section, each set of progress curves is replicated thrice to simulate triplicates. Note that the cumulative effect of two sources of uncertainty is reported at the intersection of the corresponding row and column. As expected, adding more sources of uncertainty increases the error on the estimation of the kinetic parameters. Inclusion of three or more sources of uncertainty results in relative errors which easily exceed 70% for each kinetic parameter. Uncertainties in K_M are particularly amplified given errors which we believe are typical of Michaelis-Menten experiments. A good rule of thumb may be that estimates in K_M and k_{cat} values are, at best, good to within a factor of 2 for carefully executed experiments with three replicates of each progress curve.

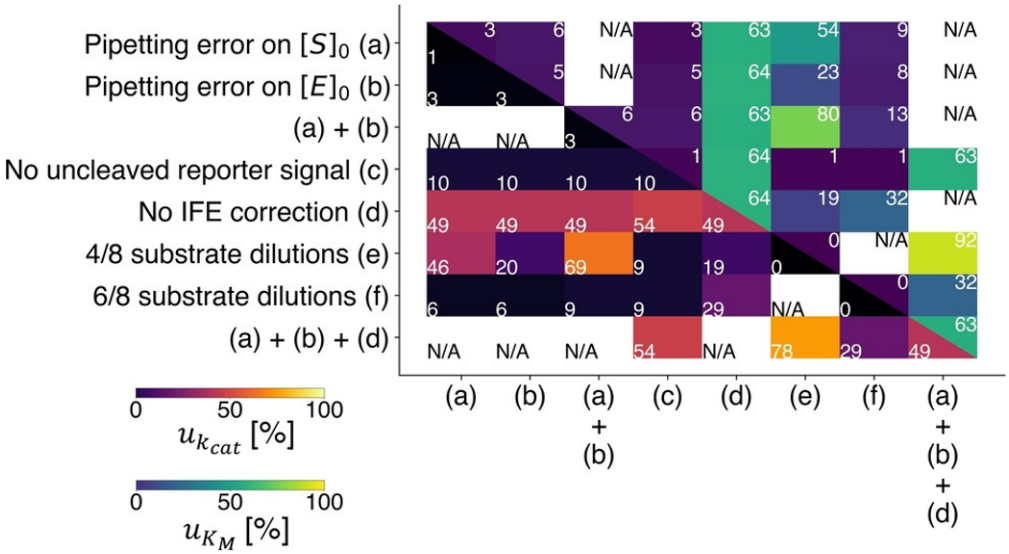

Figure 2.2: Relative error in the determination of k_{cat} and K_M for case estimates of uncertainty. These cases were chosen as either individual effects or the combinations of the effects of five distinct sources of uncertainty (a-d) as shown. Reported are values of relative error in k_{cat} (resp. K_M) on the lower-left (resp. upper-right) portion. Relative error is defined as $u_\kappa = \frac{|\kappa^* - \kappa|}{\kappa^*}$ ($\kappa = k_{cat},\ K_M$) where κ^* is the true value and κ the measured value. The values of k_{cat} and K_M obtained considering two sources of uncertainty are shown at the intersection of the corresponding row and column. Mutually exclusive cases are noted "N/A." Unless specified otherwise, we used eight points of the Michaelis-Menten curve. The following values were used: $k^*_{cat} = 0.5\ \mathrm{s}^{-1}$, $K^*_M = 0.5\ \mu\mathrm{M}$, $[E]_0 = 1\ \mathrm{nM}$, $s_0 = 2\ \mu\mathrm{M}$, $c_0 = 7\ \mu\mathrm{M}$, $\alpha = 0.1$.

2.2.7 Uncertainty quantification for kinetic parameters extracted from experimental data

This section presents analyses of bias errors in Michaelis-Menten curves with a typical experimental setup. As a case study, we present analyses of the raw experimental calibration, progress curves, and Michaelis-Menten curve data for CRISPR AsCas12a and AapCas12b of Huyke et al. [2] These analyses serve to demonstrate how three biases influence the measured value of kinetic constants.

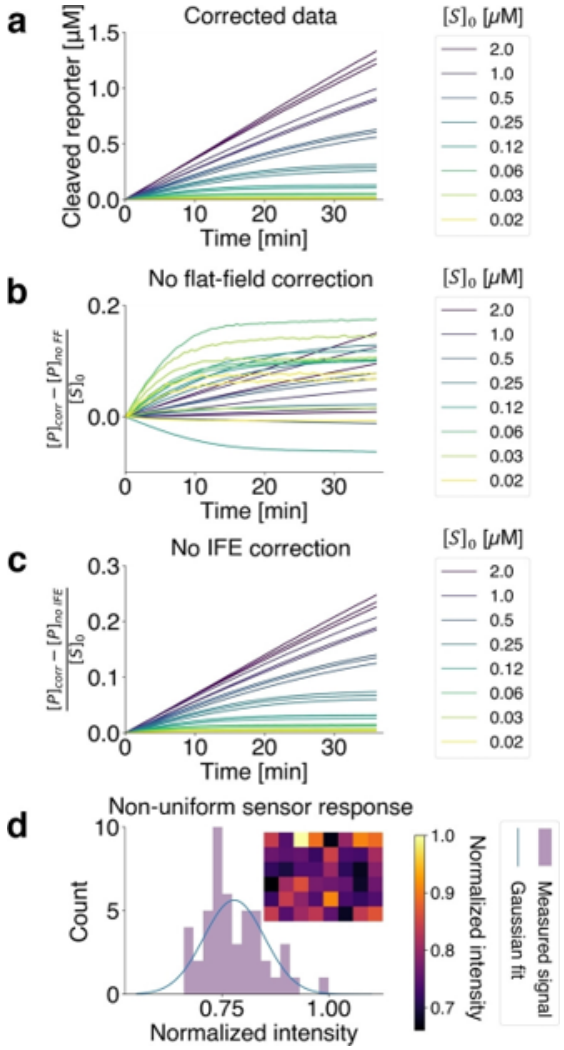

Figure 2.3: Influence of non-uniform sensor response (FF) and inner filter effect (IFE) on experimental progress curves. a Cleaved reporter concentration vs time for eight different initial reporter concentrations. Triplicates are shown with the same color. Data was corrected for both non-uniform sensor response and inner filter effect. b Scaled concentration deficit vs time due to the omission of the flat-field correction. c Scaled concentration deficit vs time due to omission of only the inner filter effect correction. d shows the non-uniform sensor response of a recently serviced thermocycler. Shown is a histogram of normalized intensity measured across 48 wells of the plate reader (bars) and a corresponding Gaussian fit (solid line). The inset shows the spatial distribution of the flat-field signal over the 48-well plate.

Figure 2.3a shows experimental progress curves for eight initial substrate concentrations using the

CRISPR ortholog AapCas12b. The enzyme was pipetted at concentration $[E]_0 = 1$ nM in presence of reporters functionalized with a fluorophore-quencher pair at initial concentration $[S]_0$. The fluorescence signal was measured using a MiniOpticon thermal cycler (Bio-Rad Laboratories, CA, USA) and corrected for optical effects as we shall discuss next. The sensitivity of microwell-type array fluorescence detectors is not uniform. A single value of fluorophore concentration and a very uniform dispensing of sample volumes results in a non-uniform measured signal. We hypothesize that this may be due to well-to-well differences in illumination and in the light-capture optics. A significant component of this non-uniformity in response is repeatable across experiments over periods of one week or two. Hence, this non-uniformity may be corrected by accounting for the non-uniform response. We here term this correction "flat-field" in analogy to the correction used to correct for non-uniform system response in fluorescence microscopy (which is typically mostly due to non-uniform illumination) [97]. For micro-well arrays of thermocyclers, we recommend the following correction to the raw data:

$$I_{corr} = \frac{I - I_{BG}}{I_{FF} - I_{BG}}. \tag{2.16}$$

where I, I_{BG}, I_{FF} and I_{corr} are respectively the raw signal from the thermal cycler, the background, flat-field, and corrected signals. The quantity I here refers to a matrix quantity whose elements each correspond to the well-specific signal. The flat-field signal of the aforementioned thermocycler was obtained by filling each well of the thermal cycler with the same volume of the same solution of cleaved reporters (concentration 2.5 μM). This I_{FF} is shown as an inset in Figure 2.3d for the recently serviced (by manufacturer) thermocycler array system. Figure 2.3d shows a histogram distribution of the intensity of the flat-field signal in the 48 wells of the thermal cycler and the corresponding raw signal for each well (inset).

The flat-field-corrected progress curve data can be compared to the uncorrected version to analyze the well-specific bias errors incurred from uncorrected data. For the current data, this is shown in Figure 2.3b which plots a scaled concentration deficit $\frac{[P]_{corr} - [P]_{no\ FF}}{[S]_0}$ versus time. Here, $[P]_{corr}$ is the product concentration calculated using the (fluorescence signal to concentration) calibration (i.e., inverting Equation 2.9). Accordingly, $[P]_{corr}$ is the concentration obtained after flat-field correction and inner filter effect correction and $[P]_{no\ FF}$ is the concentration obtained after inner filter correction only.

Note that flat-field correction and calibration (including IFE) are coupled in any analysis. To isolate the effect of the IFE, Figure 2.3c shows the scaled concentration deficit $\frac{[P]_{corr} - [P]_{no\ IFE}}{[S]_0}$ versus time observed if the inner filter correction is not applied on the experimental signal. Here, $[P]_{corr}$ is the concentration obtained after flat-field correction and inner filter effect correction and $[P]_{no\ IFE}$ is the concentration obtained after flat-field correction only. In this case, the scaled concentration deficit can exceed 20% and, as predicted by Beer-Lambert law, it is always positive and strictly increases with concentration.

The errors in concentration shown in Figure 2.3 propagate to the Michaelis-Menten curves and therefore impair accurate determination of the kinetic parameters. As a demonstration of the combined effect of various uncertainties, Figure 2.4 shows the influence of the nonuniform sensor response, inner filter effect, and the number of points chosen to build the Michaelis-Menten curve on the experimental estimation of

k_{cat} and K_M. Data is shown for the two orthologs AsCas12a and AapCas12b. We present in Section A.4 distributions of k_{cat} and K_M accounting for all effects presented in this chapter on simulated data.

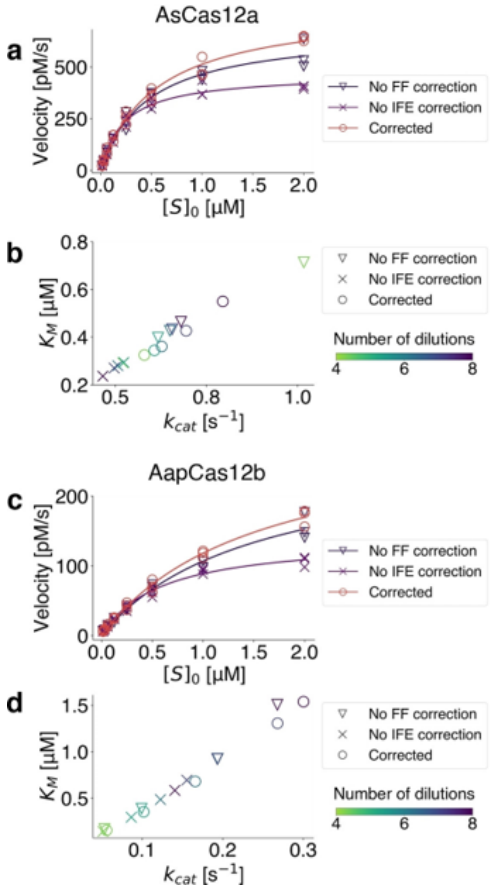

Figure 2.4: Influence of non-uniform sensor response (FF), inner filter effect (IFE) and number of points in the Michaelis-Menten curve on kinetic constants determination. a shows measured reaction velocity vs initial substrate concentration for AsCas12a omitting flat-field correction (triangles), inner filter effect correction (crosses) and correcting for both effects (circles). Shown are measured velocities (symbols) and corresponding Michaelis-Menten fits (solid lines). b shows corresponding values of k_{cat} and K_M. Shown are measured values of the kinetic parameters without flat-field correction (triangles), without inner filter effect correction (crosses) and with both corrections (circles), for four to eight points in the Michaelis-Menten curve. c-d Analogous plots for the CRISPR ortholog AapCas12b.

Figure 2.4a shows Michaelis-Menten curves for AsCas12a without flat-field correction, without inner filter correction and with both corrections. Figure 2.4b shows the corresponding measured values of k_{cat} and K_M using four to eight points of each Michaelis-Menten curve. Figures 2.4c and 2.4d show analogous data than respectively Figures 2.4a and 2.4b for AapCas12b. Relative variations of k_{cat} and K_M exceed 60%

for AsCas12a and 80% for AapCas12b. This compares well with the uncertainty estimation obtained in the Monte Carlo simulations. The number and range (relative to K_M) of $[S]_0$ values used to construct the Michaelis-Menten curve is critically important given that reported data is often limited to just a few values. As just two examples, Shinoda et al. [37] and Li et al. [96] present data for k_{cat} and K_M using three and five $[S]_0$ values, respectively.

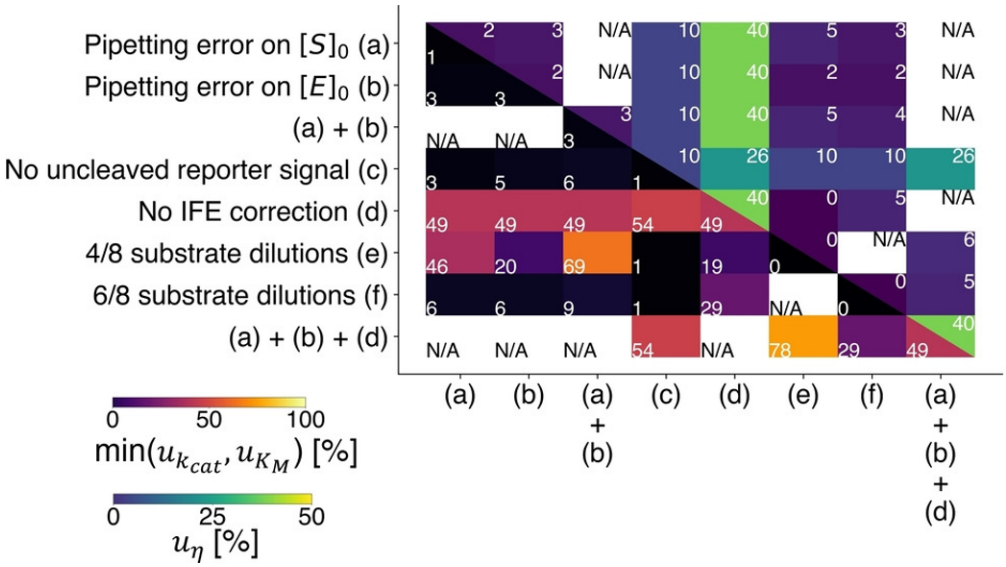

Figure 2.5: Relative error in the determination of the kinetic parameters separately and for the kinetic efficiency η. The various cases analyzed (e.g., row and column labels and interpretation of intersections) are the same as those of Figure 2.2. The lower-left portion shows reported values of the minimum of the relative errors of k_{cat} and K_M. Relative errors in η are listed in the upper-right portion. Relative error is defined as $u_\kappa = \frac{|\kappa^* - \kappa|}{\kappa^*}$ ($\kappa = k_{cat}, K_M, \eta$) where κ^* is the true value and κ the measured value. The following values were used: $k^*_{cat} = 0.5\ s^{-1}$, $K^*_M = 0.5\ \mu M$, $[E]_0 = 1\ nM$, $s_0 = 2\ \mu M$, $c_0 = 7\ \mu M$, $\alpha = 0.1$.

Figures 2.1 and 2.4 highlight an important trend in much of current analyses of bias and random errors associated with Michaelis-Menten-type analyses. Namely, individually or collectively, the various sources of uncertainty very strongly affect determination of k_{cat} and K_M. However, these errors have a significantly weaker influence on the estimation of the catalytical efficiency parameter $\eta = k_{cat}/K_M$. This precision in the quantification of catalytic conversion is manifested in the approximate groupings of measured values of k_{cat} and K_M along diagonals in Figures 2.4b, 2.4d and 2.4f. To further illustrate this observation, Figure 2.5 shows the relative error on η and the minimal relative error made on either k_{cat} or K_M for the same test cases (i.e., column and row labels) of Figure 2.2. In most cases, the estimation of the kinetic efficiency of the enzyme yields relative errors lower than or on the order of the minimum of the two uncertainties on k_{cat} and K_M separately.

We attribute this to several aspects of the extraction of k_{cat}, K_M and η. For example, the inner filter

effect more strongly attenuates measured signals for higher values of $[S]_0$. This modifies the shape of the Michaelis-Menten curve and results in lower apparent values of both k_{cat} and K_M. Further, we note that bias error resulting from a lack of flat-field correction tends to affect k_{cat} and K_M in approximately the same way. Hence, both constants are either over-predicted or under-predicted so that η is less affected. Similarly, we note that pipetting errors also tend to affect the estimation of k_{cat} and K_M in the same way, such that the estimation of η is, relatively speaking, more precise.

Lastly, we note that the precision of the measurement of η relative to determination of k_{cat} or K_M individually is convenient as η is likely much more important to the design and implementation of CRISPR-based assays. We hypothesize that most assays based on the cleavage of fluorophore-quencher pair reporters will employ relatively low values of $[S]_0$ (compared to K_M) to avoid the significant background due to uncleaved reporters [2]. In the latter regime, the reaction velocity is more sensitive to η (as $v_0 \underset{[S]_0 \to 0}{\approx} \frac{k_{cat}[E]_0[S]_0}{K_M} \propto \eta$), in contrast to the high substrate regime where $\lim_{[S]_0/K_M \to +\infty} v_0 = k_{cat}[E]_0$.

2.3 Conclusion

We used analytical derivations, Monte Carlo simulations, example analyses of models and experimental calibrations, and experimental data to estimate typical uncertainties associated with the determination of kinetic constants of enzymatic reactions following the Michaelis-Menten model. We focused this presentation by exploring the case of measurements of the Michaelis-Menten kinetics parameters of CRISPR-Cas enzymes which use reporter molecules consisting of synthetic nucleic acids functionalized with fluorophore-quencher pairs. We considered the independent and combined influences of neglecting background of uncleaved fluorescence reporters, inner filter effect, pipetting errors (including typical serial dilutions), the number of points in the Michaelis-Menten curve, and flat-field correction on the estimation of k_{cat} and K_M. We constructed multi-dimensional probability distributions of these errors using our models and Monte Carlo simulations. This included estimations of the influence of the combined effects of various independent (and small groupings of the) sources of uncertainty. We also considered the effect of triplicate repetitions. As an example case study, we applied our uncertainty models to the experimental uncertainty associated with the estimation of k_{cat} and K_M for two CRISPR-Cas orthologs, AsCas12a and AapCas12b. We characterized each source of uncertainty with an input parameter.

Typical experimental distributions of input parameters led to substantial relative error for both k_{cat} and K_M. From the results of the Monte Carlo simulations, we conclude that both these constants are typically measured within a factor 2 and that uncertainties for reported experimental conditions prevent precise estimations of k_{cat} and K_M. However, the measure of the kinetic efficiency k_{cat}/K_M leads to significantly more precise estimations than the estimation for either k_{cat} or K_M independently, given the same input uncertainty. This suggests using k_{cat}/K_M rather than k_{cat} and K_M as an index of enzymatic performance–especially, as we have shown, for CRISPR-Cas systems.

Chapter 3

Degradation of reporter molecules imposes a fundamental limit of detection on CRISPR diagnostics

The contents of this chapter were previously published by A. S. Avaro, A. D. Griffiths, and J. G. Santiago [98] in the journal *Analytical Chemistry* and are reproduced here with minor modifications. Supplementary information associated with this chapter is presented in Appendix B.

3.1 Introduction

Clustered regularly interspaced short palindromic repeats associated enzymes (CRISPR-Cas) have raised significant attention in the field of molecular diagnostics in the past few years [6, 7, 99, 1]. CRISPR-Cas systems typically consist of a Cas endonuclease (e.g., Cas12 [100, 12] or Cas13 [11]) conjugated to a synthetic guide RNA (gRNA), which includes a sequence complementary to the target nucleic acid. The enzyme first recognizes and cleaves target in a specific *cis*-cleavage step which activates the enzyme. The activated enzyme subsequently exhibits a non-specific collateral *trans*-cleavage of single-stranded nucleic acid (e.g., DNA for Cas12 and RNA for Cas13) [6, 99, 30]. A great variety of strategies have been developed to leverage this mechanism for diagnostic purposes. The majority of these assays use synthetic single-stranded nucleic acid reporters labeled with a fluorophore on one end and a quencher on the other [12, 101, 102]. In such assays, a rise in fluorescence signal is used to detect enzymatic *trans*-activity and this signal informs on the presence of target, the target's initial concentration, and/or the reaction kinetics of the enzyme. CRISPR-based detection methods are often presented as an alternative to exponential molecular amplification methods such as quantitative polymerase chain reaction (qPCR) and loop-mediated isothermal amplification (LAMP) [103, 104, 105]. The latter methods are robust, but can be prone to false positives and

often require bulky and expensive equipment for target quantitation. By comparison, CRISPR-based methods are highly specific, easily reconfigurable, and do not require thermal cycling, and this makes them an increasingly popular addition to the molecular diagnostics toolbox [1, 102, 106].

An important disadvantage of CRISPR-based assays over molecular amplification techniques is their limited sensitivity [1, 107], which is limited by both their kinetic rates and observed non-specific background activity. Early reports [12, 13] claimed CRISPR catalytic rates exceeded 1,000 turnovers per second, but these and other similar reports are now known to be gross errors [2, 29, 8]. Catalytic rates are typically on the order of 1 turnover per second [2]. Further, CRISPR-Cas systems that leverage the cleavage of fluorophore-quencher reporters exhibit finite background activity [2, 8, 108, 109]: a measured fluorescence signal increases with time even in the absence of target molecules. These limitations constitute a major obstacle to the detection of trace concentrations of nucleic acids [8]. Despite the fundamental importance of the background activity on the limit of detection of CRISPR assays, there has been, to our knowledge, no kinetics description nor model that accounts for this phenomenon.

In this work, we report on and present experimental evidence of the essential role played by the non-enzymatic degradation of fluorescent reporters. We show that this degradation happens independently of CRISPR activity. Yet, because it becomes the dominant reaction mechanism at low target concentrations, it has immense consequences on CRISPR assay sensitivity. Further, the kinetics of this reporter degradation imply that the traditional Michaelis-Menten kinetic system does not capture empirical observations. We use our model to derive an analytical expression for a fundamental limit of detection imposed by reporter degradation on CRISPR assays. We provide a novel approach to calibrate CRISPR assay signals which incorporates a modified kinetic framework (different from Michaelis-Menten). We also present a controlled experimental study demonstrating this degradation, and experimental validation of our model and how this degradation directly limits the sensitivity of a Cas12 assay.

3.2 Methods

3.2.1 Reagents

LbCas12a (a Cas12 ortholog from *Lachnospiraceae bacterium ND2006*) at a concentration of 100 μM and NEBuffer r2.1 were purchased from New England Biolabs (MA, USA). NEBuffer r2.1 is composed of 50 mM NaCl, 10 mM Tris-HCl, 10 mM MgCl2, and 100 μg/ml recombinant albumin (pH 7.9 at 25°C). Reporter molecules were purchased from Eurofins Genomics (France) and resuspended at 100 μM. All other oligonucleotides reported in Table B.1 (Section B.7) were obtained from Integrated DNA Technologies (IDT) and resuspended at 100 μM. All fluorescence measurements were performed using a CFX384 Touch Real-Time PCR Detection System (Bio-Rad Laboratories). In all experiments, fluorescence measurements were taken at 37°C and every 30 s.

3.2.2 *Trans*-cleavage kinetics experiments

We first prepared a solution of 1 μM ribonucleoprotein (RNP) by incubating 1 μM synthetic gRNA and Cas12a at 37°C for 30 min. RNP were first diluted to 80 nM in NEBuffer r2.1 before activation with 20 nM synthetic dsDNA target at 37°C for 30 min. The kinetics of *cis*-cleavage have been extensively discussed elsewhere [49, 34, 110, 31, 33], and we here consider the reaction complete after incubation. We then performed *trans*-cleavage kinetics assays using 1 nM activated RNP and varying synthetic reporter concentrations (ranging from 14 to 900 nM in 2-fold dilutions). The reactions were buffered in 1X NEBuffer r2.1. All mixing steps prior to data acquisition were performed on ice. Three replicates were taken for each reporter concentration. Fluorescence values were converted to concentrations using the models described in this chapter and the calibration curves reported in Section B.8. The initial reaction velocities were computed using a linear fit to the first ~3 min of the reaction progress curves. Kinetic rates k_{cat} and K_M were computed using a nonlinear Michaelis-Menten fit using GraphPad Prism 10 (Graph-Pad Software, CA, USA). Note the Michaelis-Menten model here is sufficient as target concentrations are sufficiently high.

3.2.3 Reporter degradation experiments

We conducted similar experiments to what was performed in the *trans*-cleavage kinetic experiments omitting one or several critical component(s) of the CRISPR reaction. For the no target experiment (Figure 3.3b), we prepared a solution of 80 nM RNP following the same protocol as described above. We then diluted the RNPs to 5 nM (final concentration) and mixed them with solutions containing varying synthetic reporter concentrations (ranging from 14 to 900 nM in 2-fold dilutions). For the no gRNA experiment (Figure 3.3c), we mixed 50 nM Cas12a with 1 nM dsDNA target and the same varying concentrations of ssDNA reporters. For the no Cas experiment (Figure 3.3d), we mixed 10 nM gRNA with 1 nM target, and varying concentrations of reporters. Finally, for the reporter-only experiment (Figure 3.3e), we diluted the ssDNA reporter stock to varying concentrations ranging from 14 nM to 900 nM in two-fold serial dilutions. Three replicates were taken for each reporter concentration for all cases.

In all cases, we then proceeded to fluorescence measurements. Reactions were performed in 1X NEBuffer r2.1. Initial reaction velocities were computed using a linear fit to the first ~15 min of the reaction progress curves. The value of k_{rep} was computed using a linear fit using GraphPad Prism 10.

3.2.4 Limit of detection experiments

We first prepared a solution of 1 μM ribonucleoprotein (RNP) by incubating 1 μM synthetic gRNA and Cas12a at 37°C for 30 min. RNP were first diluted to 80 nM in NEBuffer r2.1 before incubation with 110 nM reporters and concentrations of synthetic target dsDNA ranging from 1 fM to 10 nM in 10-fold dilutions. Reactions were performed in 1X NEBuffer r2.1. Fluorescence values were converted to concentrations using the calibration process described in chapter 3. The initial reaction velocities were computed using a linear fit to the first ~500 s of the reaction progress curves.

3.3 Results and discussion

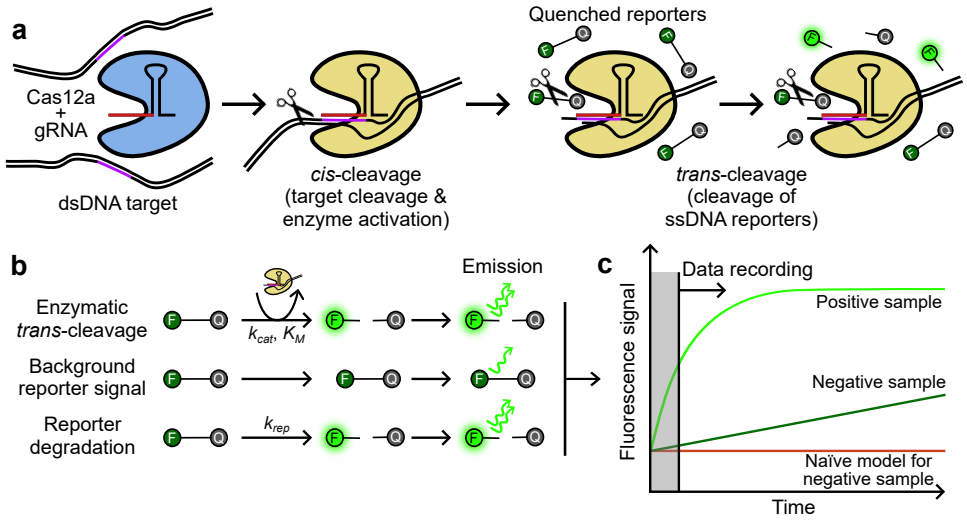

Figure 3.1: CRISPR diagnostic fluorescent signals. a Schematic for DNA detection using CRISPR-Cas12. The Cas12/gRNA complex (ribonucleoprotein, RNP) first recognizes a specific ~20-nucleotide DNA sequence complementary to the gRNA. This activates the enzyme (shown in yellow color), triggering non-specific cleavage of ssDNA fluorophore-quencher reporters. b Schematic of three sources of fluorescent signal. In addition to background signal (e.g., from plastic thermocycler tubes, not shown), photons are emitted by reporters cleaved by the Cas12 enzyme upon activation; uncleaved reporters that are imperfectly quenched; or reporters that are degraded non-enzymatically. c Schematic of fluorescence signals versus time from a positive sample (with target), a negative sample (no target), and the prediction by a (commonly used) naïve model for a negative sample.

3.3.1 Signal kinetics in the low target concentration limit

Figure 3.1a summarizes a typical CRISPR-Cas12 diagnostic assay. The assay involves two sequential reactions [12, 30]. First is a relatively rapid [49, 34, 110, 31] reaction called *cis*-cleavage during which the enzyme is activated by recognizing and cleaving a specific target DNA sequence complementary to the gRNA. Second is the rate-limiting step called *trans*-cleavage where the enzyme indiscriminately cleaves single-stranded nucleic acid reporter molecules. The vast majority of the published Cas12 assays use short, dually-labeled ssDNA fluorophore-quencher reporters whose quantum yield significantly increases when cleaved [6, 12, 111]. An increase in fluorescence signal is used to detect enzyme activation, and the presence of target nucleic acid is deduced from this signal.

The most successful model to describe the *trans*-cleavage kinetics of the Cas enzyme is the Michaelis-Menten model [29, 112]. In this framework, the rate of production of cleaved reporter is proportional to the

activated enzyme concentration, and this can allow the quantification of initial DNA target concentration. For such questions, we often want relations between measured signals and kinetic rates of the reaction. However, as reported by Santiago [8], a large fraction of all CRISPR diagnostics studies [12, 13, 109, 111, 113, 114] report absolutely no calibration method nor calibration data. This deficit in reporting can make it impossible to verify and even reproduce studies. It can also lead to gross errors in kinetic rates [115, 116]. We summarize in Section B.1 a brief history of kinetics model formulations and calibration methods (including successive improvements) for CRISPR-based diagnostics methods. To our knowledge, the most comprehensive calibration has been reported by Blanluet et al. [85] Here, we derive a closed-form expression for the fluorescence signal in the limit of low initial target concentration, as predicted by the Michaelis-Menten framework.

Under the quasi-steady state and the reactant-stationary assumptions [47], we first adapt the calibration equation (10) from Avaro and Santiago [49] (equation 2.10 from the current thesis) and include the extension proposed by Blanluet et al. [85] We present a detailed derivation of this approach in Section B.1. This calibration yields the following relation:

$$I^{corr}_{naïve}(t;[E]_0) = 10^{-\frac{[S]_0}{c_0}}\left(F'_{Ucl}K_M\mathcal{A}(t) + F'_{Cl}\left([S]_0 - K_M\mathcal{A}(t) - [E]_0\,\frac{\mathcal{A}(t)}{1+\mathcal{A}(t)}\right)\right), \tag{3.1}$$

where:

$$\mathcal{A}(t) = W\left(\frac{[S]_0}{K_M}\exp\left(\frac{[S]_0}{K_M} - \frac{k_{cat}}{K_M}\,[E]_0\,t\right)\right). \tag{3.2}$$

Here, $I^{corr}_{naïve}(t;[E]_0)$ denotes the so-called "flatfield-corrected" [49, 85] fluorescence intensity at time t as predicted by the Michaelis-Menten model. F'_{Cl}, F'_{Ucl}, and c_0 are calibration constants, k_{cat} and K_M are the kinetic rates of the enzyme, $[E]_0 = [E]\ (t=0)$ is the initial activated enzyme concentration, $[S]_0 = [S]\ (t=0)$ represents the total concentration of reporters in the reaction, and W is the Lambert-W function [89]. We note that the model represented by equation 3.1 accounts for the signal originating from uncleaved reporters, the so-called "inner-filter effect", and the well-to-well (i.e., position-to-position) variation in fluorescence detector response [85]. In the limit where the target concentration $[E]_0$ is low, this closed-form solution is well approximated at the first order by:

$$I^{corr}_{naïve}(t;[E]_0) \approx 10^{-\frac{[S]_0}{c_0}}\,[S]_0\left(F'_{Cl}\left(1 - \frac{[E]_0}{K_M+[S]_0}\right) - \left(F'_{Cl}-F'_{Ucl}\right)\left(1-\frac{k_{cat}\,[E]_0\,t}{K_M+[S]_0}\right)\right). \tag{3.3}$$

The derivation of equation 3.3 involves a Taylor series expansion of the Lambert-W function and we discuss these details in Section B.2.

Next, we discuss the rates of increase of signal of these systems. We often want a signal which is a weak function of initial signal value and initial background value. As such, we consider the first derivative with respect to time of equation 3.3:

$$\frac{dI^{corr}_{naïve}}{dt}([E]_0) \approx 10^{-\frac{[S]_0}{c_0}} \left(F'_{Cl} - F'_{Ucl}\right) k_{cat}\, [E]_0\, \frac{[S]_0}{K_M + [S]_0}. \tag{3.4}$$

As expected, this model of signal rate is proportional to the initial velocity predicted by the Michaelis-Menten model:

$$\frac{d[P]_{naïve}}{dt} = k_{cat}\, [E]_0\, \frac{[S]_0}{K_M + [S]_0}. \tag{3.5}$$

We here refer to equations 3.3 to 3.5 as the "naïve" model for CRISPR kinetics which we seek to criticize and expand upon in this chapter. This naïve model is consistent with the prevalent theory of CRISPR reactions which assumes that the target concentration limits the maximum value of $[E]_0$; and, if $[E]_0 = 0$, the signal is not expected to increase in time.

As we shall discuss and demonstrate with quantitative experiments, the prediction and interpretation that signals will not increase for negative samples (i.e., lack of target molecules) is incorrect. There is in fact published experimental data showing that reaction velocities (as interpreted from fluorescence signals and calibration) plateau to a constant, nonzero value as target concentrations approach zero [2, 29, 108, 109, 117]. The mechanism behind this non-specific signal rise has not been explained, but the evidence implies that there exists another source of fluorescent signal that is unaccounted for by the aforementioned models or calibrations and not predicted by the Michaelis-Menten framework.

Figure 3.1b summarizes the three different sources of fluorescence signal of a CRISPR reaction. The first source consists of reporters cleaved by the enzymatic *trans*-cleavage. The second source involves the imperfectly quenched, yet uncleaved reporters ($I_{naïve}(t; 0)$), which was introduced and accounted for in equation 3.1 above and which we detail in Section B.8. The third source of signal is the effect upon which is the focus of this work: The degradation of reporters independent of the CRISPR enzyme. The latter two sources of signal are not directly related to the activated enzyme concentration, and are therefore usually considered as background signal for any diagnostic assay or enzyme kinetics measurement. However, we know of no published work that accounts for the observed degradation rate of reporters. Figure 3.1c shows schematic progress curves (i.e., evolution of fluorescence signal versus time) that result from the summation of the three sources of signal listed in Figure 3.1b. Shown here are progress curves in the presence of target (light green) and absence of target (negative, dark green). We also show the prediction by the naïve model (equation 3.1) for the negative case. As mentioned earlier, the naïve model predicts zero signal increase in absence of target molecules.

3.3.2 Proposed modifications to Michaelis-Menten kinetics to include first order reporter degradation

We now introduce an important factor in the interpretation of CRISPR kinetics which we recently discovered and quantified as part of the current study. The discrepancy between the experimental observations and the naïve Michaelis-Menten predictions implies the existence of an underlying complexity in the kinetics description of any CRISPR system that involves the fluorescently-labeled reporters. Namely, a critical

source of background signal originates from reporters which can degrade in the absence of target and/or the CRISPR-Cas enzyme.

To account for this observation, we here introduce a so-called "augmented" (as opposed to "naïve") kinetics framework to describe enzymatic assays with first order reporter molecule degradation. We select a first-order model to keep the model as simple as possible while capturing essential experimental observations. We describe this reaction system using the following equations:

$$E + S \underset{k_r}{\overset{k_f}{\rightleftharpoons}} C \xrightarrow{k_{cat}} P + E \tag{3.6}$$

$$S \xrightarrow{k_{rep}} P \tag{3.7}$$

Here, equation 3.7 corresponds to the observed degradation of reporters that is not mediated by the Cas enzyme. The corresponding system of rate equations is then more fully described as:

$$\frac{d[S]}{dt} = -k_f[E][S] + k_r[C] \mathbf{- k_{rep}[S]}, \tag{3.8}$$

$$\frac{d[E]}{dt} = -k_f[E][S] + (k_r + k_{cat})[C], \tag{3.9}$$

$$\frac{d[C]}{dt} = k_f[E][S] - (k_r + k_{cat})[C], \tag{3.10}$$

$$\frac{d[P]}{dt} = k_{cat}[C] \mathbf{+ k_{rep}[S]}, \tag{3.11}$$

With the following initial conditions:

$$[S](t=0) = [S]_0 \tag{3.12}$$

$$[E](t=0) = [E]_0 \tag{3.13}$$

$$[C](t=0) = 0 \tag{3.14}$$

$$[P](t=0) = 0 \tag{3.15}$$

Similar to the Michaelis-Menten system, we define $K_M = \frac{k_{cat}+k_r}{k_f}$. Closed-form solutions [118] for similar systems of rate equations have been derived, but they rely on transcendental functions that are specially defined for these systems and that are not available in most scientific computing packages. Under the reactant-stationary assumption and the quasi-steady state assumption [89], we can derive an analytical expression for the initial reaction velocity analogous to the naïve Michaelis-Menten case (equation 3.5):

$$\frac{d\,[P]}{dt}\,(t=0) = k_{cat}\,[E]_0\,\frac{[S]_0}{K_M + [S]_0} + k_{rep}\,[S]_0\,. \tag{3.16}$$

In the special case where $[E]_0 = 0$ (no target), equations 3.8 to 3.11 collapse to:

$$\frac{d\,[S]_{BG}}{dt} = -\frac{d\,[P]_{BG}}{dt} = -k_{rep}\,[S]_{BG}\,. \tag{3.17}$$

Equation 3.17 then yields an analytical solution for the fluorescence intensity in the no-target case:

$$I^{corr}_{meas,BG}\,(t) = \frac{I\,(t) - I_{BG}\,(t)}{I_{FF}\,(t) - I_{BG}\,(t)} = 10^{-\frac{[S]_0}{c_0}}\,[S]_0\left(F'_{Cl} - \left(F'_{Cl} - F'_{Ucl}\right)e^{-k_{rep}t}\right). \tag{3.18}$$

In equation 3.18, I_{FF} and I_{BG} are respectively the flatfield and background signal arrays (associated with the array of reaction-tube-specific detectors). Unlike equation (1) in Blanluet et al. [85], the quantities I_{BG} and I_{FF} are here time-dependent arrays and not averages in time. The time rate of change of the signal is then:

$$\frac{dI^{corr}_{meas,BG}}{dt}\,(t) = 10^{-\frac{[S]_0}{c_0}}\,\left(F'_{Cl} - F'_{Ucl}\right)k_{rep}\,[S]_0\,e^{-k_{rep}t}, \tag{3.19}$$

where $I^{corr}_{meas,BG}$ is the flatfield-corrected fluorescence intensity in the no target limit. This corresponds to the following characteristic time scale τ_d:

$$\tau_d = \frac{1}{k_{rep}}. \tag{3.20}$$

Here, the subscript "d" denotes "degradation". For characteristic observed rates, as we will show below, this characteristic time is much longer than typical experiments (e.g., $\tau_d > 8$ days for $k_{rep} = 1.4 \times 10^{-6}$ s^{-1}). We indicate with τ_e the characteristic duration of the experiment (5 min $< \tau_e <$ 2 h for typical *trans*-cleavage experiments). Assuming $\tau_e \ll \tau_d$, then the rate of increase of the background signal, as derived in equation 3.19, is approximately constant throughout the measurement:

$$\frac{dI^{corr}_{meas,BG}}{dt} \approx 10^{-\frac{[S]_0}{c_0}}\,\left(F'_{Cl} - F'_{Ucl}\right)k_{rep}\,[S]_0\,. \tag{3.21}$$

We will later in this chapter refer to this estimate of the initial rate of signal growth.

Before validating our model with experimental data, we present simple visualizations of the theory. Specifically, Figure 3.2a shows plots of the predicted, initial (linear) portions of the progress curves. Shown are product concentration profiles ($[P](t)$) for seven concentrations of the target (i.e., $[E]_0$). We show two sets of predictions. First, the solid lines are predictions by the naïve Michaelis-Menten model. Second, the data symbols show results from our augmented model (equations 3.8 to 3.15). Note the data symbols are color coded to the corresponding curves of the naïve model. Figure 3.2b shows a subset of five of these curves in the low product concentration region ($[P](t) < 1$ nM) for clarity of presentation. As derived in equation 3.5, the initial reaction velocity predicted by the naïve model is proportional to the target concentration, and therefore approaches zero as $[E]_0$ approaches zero. However, unlike the naïve model, the augmented model curves converge towards a nonzero, linear increase in product concentration as target concentration approaches zero (shown using cross data symbols). This corresponds to the zero-target limit derived in

equations 3.17 to 3.19, where the degradation of reporters dominates the production of cleaved reporters over the enzymatic *trans*-cleavage reaction. We indicate with shading in Figures 3.2a and 3.2b the region where detection is extremely difficult for the specified values of k_{rep} and $[S]_0$. In this low-target regime, accurate detection would require precise knowledge of the degradation of reporters and would require that this degradation be extremely repeatable from experiment to experiment. Note the degradation of CRISPR reporters has analogies to qPCR TaqMan probes which we discuss briefly in Section B.7.

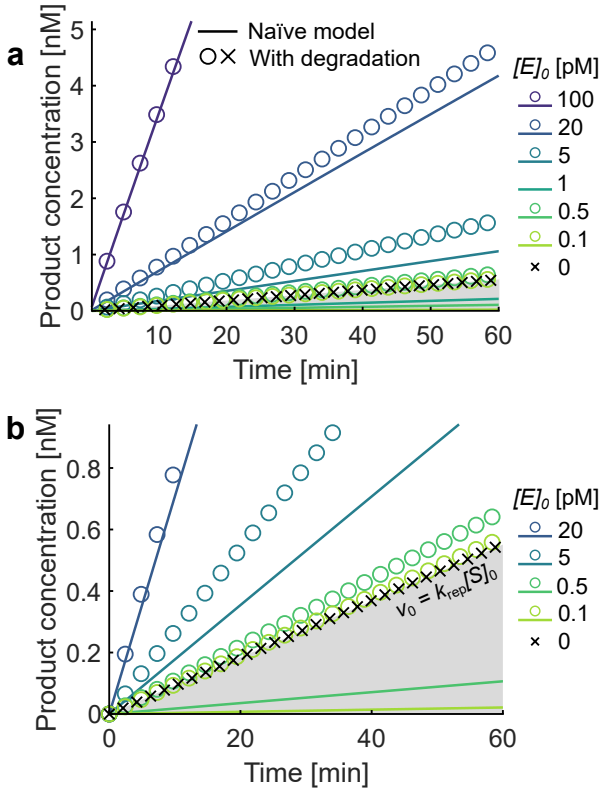

Figure 3.2: Comparison of naïve versus augmented models. a Example cleaved reporter concentrations versus time for a fixed initial reporter concentration ($[S]_0 = 110$ nM) and seven values of target concentration $[E]_0$. Shown are numerical solutions to the full Michaelis-Menten system (equations 3.8 to 3.15), with (symbols) or without (naïve model, lines) reporter degradation. b Selected curves from a, in the zone of low product concentrations. As target concentration ($[E]_0$) approaches zero, the curves converge to a minimum signal rise determined by reporter degradation (and not by *trans*-cleavage by CRISPR). The shaded region highlights the region that is practically inaccessible in the augmented kinetic framework. We used the following values for this example: $k_f = 10^{10}$ $M^{-1}s^{-1}$, $k_{cat} = 2.0$ s^{-1}, $K_M = 3.6$ μM, and $k_{rep} = 1.4 \times 10^{-6}$ s^{-1}.

3.3.3 A fundamental limit of detection for CRISPR fluorescence-based assays

We here derive a simple algebraic expression describing a fundamental limit of detection for any enzymatic assay given first order reporter degradation. As an important reference value, we define $[E]_{0,\,LoD}$ as the theoretical initial target concentration for which *trans*-cleavage with no reporter degradation exactly matches an observed signal increase due solely to reporter degradation (*sans* target). $[E]_{0,\,LoD}$ can therefore be interpreted as an apparent target concentration that would, in the framework of the naïve model, explain a signal that is actually due solely to reporter degradation. To this end, we set equal the right-hand sides (RHSs) of equations 3.4 and 3.21, and derive the following:

$$[E]_{0,\,LoD} = (K_M + [S]_0)\,\frac{k_{rep}}{k_{cat}}. \tag{3.22}$$

The latter also corresponds to the situation where each of the two terms in the RHS of equation 3.16 have an equal contribution to the cleaved reporter production. We will term this condition as a signal-to-background ratio of unity. $[E]_{0,\,LoD}$ is an extremely useful estimate for the design of all CRISPR kinetics and CRISPR diagnostic assays which rely on reporter molecules. First, this concentration is directly proportional to reporter degradation rate k_{rep}–highlighting the great importance of this reporter degradation effect. Second, this concentration is a linear function of reporter concentration. Depending on the magnitude of K_M, increasing reporter concentration $[S]_0$ can have a strongly deleterious effect on sensitivity.

3.3.4 Late readout effect on the reaction velocity

In this section, we introduce a scaling argument to evaluate the reliability of experimentally measured reaction velocities as approximation of initial reaction velocities. The characteristic timescale of completion the Michaelis-Menten reaction τ_{MM} is determined by the kinetic rates of the enzyme [29, 8]:

$$\tau_{MM} = \frac{K_M}{k_{cat}\,[E]_0}. \tag{3.23}$$

However, the *trans*-cleavage reaction is initiated upon mixing reagents and there is a time delay before signal acquisition begins. This delay corresponds to the time necessary to mix reagents into a reaction vessel, load the vessel (tube or well-plate) into a detection instrument, heat the vessel to incubation temperature, and initiate data collection. We denote this time delay τ_{pre} (where the subscript denotes "preparation time" or "pre-data-collection"). In our experience, τ_{pre} is typically on the order of a few minutes ($\tau_{pre} \approx 5$ min). For high values of $[E]_0$, the characteristic time of completion of the reaction τ_{MM} can be on the same order of magnitude than τ_{pre}. For instance, for $[E]_0 = 10$ nM and typical measured values for the kinetic rates for LbCas12a ($k_{cat} = 2.0\ \mathrm{s}^{-1}$, $K_M = 3.6$ µM), $\tau_{MM} \approx 3$ min. In this case, the measured reaction velocity (after a delay τ_{pre}) substantially underpredicts the real initial reaction velocity (as depicted in Figure 3.1c). We will here term this underprediction of the reaction velocity the "late readout effect". As an illustration, we provide in Section B.5 example estimates of the apparent reaction velocity for varying target concentrations

for five values of the time delay τ_{pre} ranging from 0 to 7 min.

Of course, at low target concentrations, τ_{MM} is much larger than τ_{pre}, and the late readout effect is negligible. For instance, for $[E]_0 = 1$ pM, $\tau_{MM} > 20$ days. In such cases, the measured reaction velocity over the first minutes (even hours) of reaction is a very good approximation of the initial reaction velocity.

We can also define a characteristic target concentration $[E]_{0,\,late}$ for which the finite reaction time τ_{pre} prior to signal recording affects estimates of reaction kinetics:

$$[E]_{0,\,late} \approx \frac{K_M}{k_{cat}\tau_{pre}}. \tag{3.24}$$

We approximate the value of K_M/k_{cat} as the value ultimately estimated from the kinetics experiments (e.g., at the final incubation temperature of interest). This limit makes exploring high target concentrations difficult. Equation 3.24 should be interpreted as an order of magnitude estimate that is nevertheless helpful in designing CRISPR experimental protocols.

3.3.5 Experimental validation of the kinetic model

We now present an experimental validation of the model presented in equations 3.6 to 3.19. Figure 3.3 shows progress curves, i.e., the typical measurement of cleaved reporter concentration as deduced using the calibration equation B.5. Figure 3.3a shows the progress curves for *trans*-cleavage experiments in presence of 1 nM target. As expected, the concentration of cleaved reporter increases with time and this increase varies with initial substrate concentration. In parallel to *trans*-cleavage experiments, we measured the increase in fluorescence of solutions containing the same concentrations of reporters as those reported in Figure 3.3a, but omitting one (or several) critical component(s) of the CRISPR reaction. Figures 3.3b, 3.3c, and 3.3d respectively show progress curves in absence of either dsDNA target, gRNA, or LbCas12a enzyme. Figure 3.3e shows progress curves corresponding to reporters incubated in buffer at 37°C in absence of Cas enzyme, DNA target, and gRNA (i.e., only in reaction buffer). Strikingly, all cases resulted in a slow, yet measurable increase in cleaved reporter concentration with time and, as expected for a first-order reaction, the rate of increase depends on the initial reporter concentration $[S]_0$. Further, this increase is similar in magnitude regardless of the presence of Cas enzyme, dsDNA target, or gRNA. This suggests that the observed rise in fluorescence is mainly due to the non-enzymatic reporter degradation. We also note that the deviation from linearity in Figures 3.3b-e may originate from photobleaching after prolonged exposition, which is not captured by our simple model. Importantly, all cases shown in Figures 3.3b to e correspond to the case $[E]_0 = 0$, resulting in no predicted fluorescence signal increase in the naïve Michaelis-Menten framework. Note signal versus time curves of CRISPR reporters in absence of CRISPR enzymes are extremely rare and to our knowledge have never been discussed (see Section B.8).

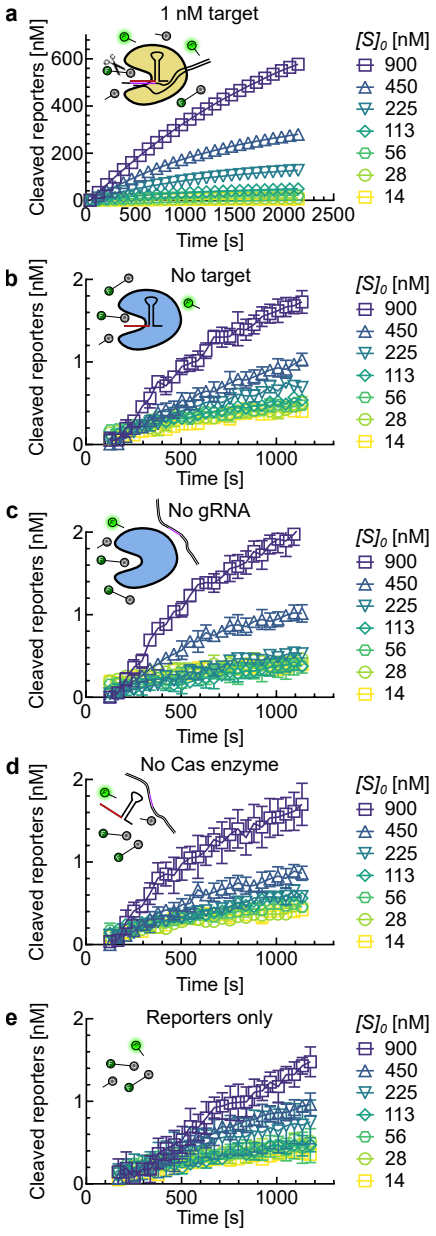

Figure 3.3: Measurements of fluorescence signal from CRISPR assay reporters. a Progress curves with a target concentration of 1 nM (i.e., maximum value of $[E]_0$ = 1 nM) and eight representative values of the initial reporter concentration $[S]_0$. b Progress curves for the same chemistries as in a, but in the absence of target DNA. c Progress curves for the same chemistries as in a, but in the absence of gRNA. d Progress curves for the same chemistries as in a, but in absence of Cas enzyme. e Progress curves for the same eight reporter concentrations as in a in buffer only. The fluorescent signal is governed by reporter degradation at 37°C. These experimental data were used to quantify reporter degradation rate constant k_{rep}.

Figures 3.4a and 3.4b show initial reaction velocities corresponding to the progress curves shown in Figures 3.3a to e, as function of initial reporter (a.k.a. substrate) concentrations. Figure 3.4a shows data in a linear-linear plot, while Figure 3.4b shows the same data in a log-log plot for clarity. Initial reaction velocities in presence of 1 nM target dsDNA (red circles) were further fitted using the Michaelis-Menten model (equation 3.5) to extract values of k_{cat} and K_M for this specific gRNA sequence. The best fit for this data yields $k_{cat} = 2.0\ \mathrm{s}^{-1}$ and $K_M = 3.6\ \mu\mathrm{M}$. These values are consistent with previously reported values for LbCas12a [2, 29]. Also plotted in Figures 3.4a and 3.4b are initial reaction velocities measured in the different cases reported in Figures 3.3b to e. Each data set was fit using a linear regression (see equation 3.17). Regardless of the presence of Cas enzyme, dsDNA target, or gRNA, the reaction velocity is well approximated by a single linear function of the initial reporter concentration. The collapse of the bottom four curves in Figure 3.4 constitutes further evidence that the background reaction velocity originates from a degradation of reporter molecules which is not mediated by the Cas enzyme. A linear regression of the reaction velocities shown for reporters only (green squares) yields $k_{rep} = 1.4 \times 10^{-6}\ \mathrm{s}^{-1}$. To our knowledge, this measurement is the first quantification of the degradation rate of reporters in absence of CRISPR enzyme. We also investigated the influence of temperature and fluorescence acquisition settings on this kinetic rate (see Sections B.9 and B.10), and found that the reporter degradation rate increases both with incubation temperature and frequency of fluorescence readouts.

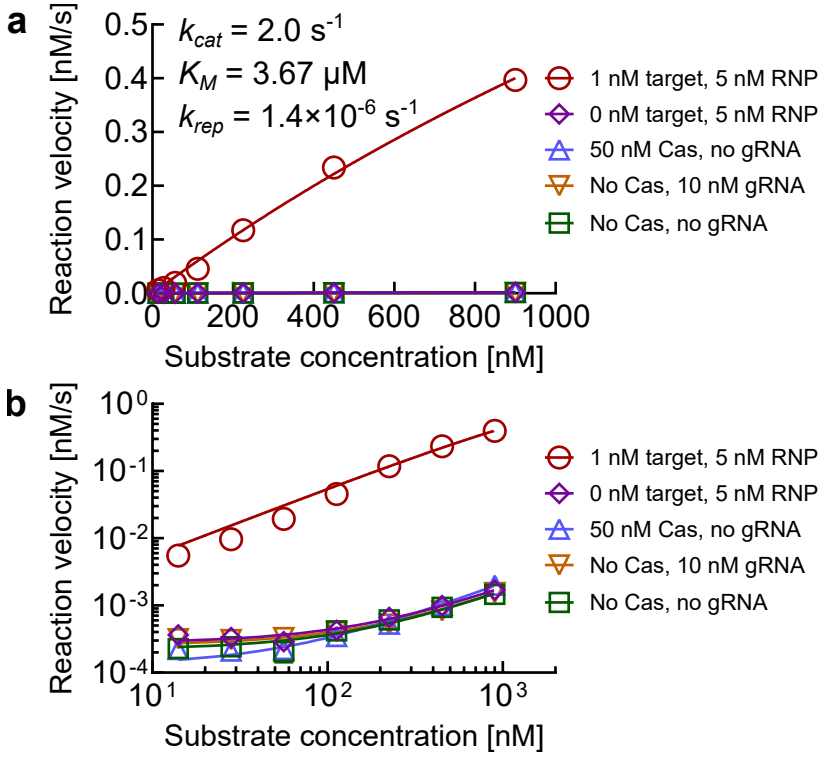

Figure 3.4: Comparison of naïve versus augmented models. a Example cleaved reporter concentrations versus time for a fixed initial reporter concentration ($[S]_0$ = 110 nM) and seven values of target concentration $[E]_0$. Shown are numerical solutions to the full Michaelis-Menten system (equations 3.8 to 3.15), with (symbols) or without (naïve model, lines) reporter degradation. b Selected curves from a, in the zone of low product concentrations. As target concentration ($[E]_0$) approaches zero, the curves converge to a minimum signal rise determined by reporter degradation (and not by *trans*-cleavage by CRISPR). The shaded region highlights the region that is practically inaccessible in the augmented kinetic framework. We used the following values for this example: $k_f = 10^{10}$ M^{-1}s^{-1}, k_{cat} = 2.0 s^{-1}, K_M = 3.6 µM, and $k_{rep} = 1.4 \times 10^{-6}$ s^{-1}.

3.3.6 Experimental validation of the limit of detection of CRISPR-based assays

Next, we experimentally investigate the effect of the reporter degradation on the limit of detection of CRISPR-based assays. Figure 3.5 shows the measured reaction velocities for target concentrations ranging from 1 fM to 10 nM in our limit of detection experiments. To highlight the limiting effect of reporter degradation, reaction velocities were normalized using the product $k_{rep}\,[S]_0$, where $k_{rep} = 1.4 \times 10^{-6}$ s^{-1} (as measured earlier) and target concentrations were normalized using $[E]_{0,LoD}$, as estimated from equation 3.22 and the enzymatic rates measured above (k_{cat} = 2.0 s^{-1}, K_M = 3.6 µM). We also show in Figure 3.5 the corresponding predictions using three kinetic models: the naïve Michaelis-Menten model (green dashed line, equation 3.5), a simple version of our augmented model (orange dashed line, equation 3.16), and our

augmented model further corrected for a late readout of the reaction velocity (black solid line). The latter model is computed using a numerical solution to the full augmented ODE system (equations 3.8 to 3.15) wherein the reaction velocity is evaluated 5 min after the reaction has started (i.e., $\tau_{pre} = 5$ min). The latter is estimate is consistent with our experimental protocol.

Importantly, the reaction velocity measurements shown in Figure 3.5 exhibit the expected leveling off of signal as target concentration decreases; a feature typical of sensitivity curves of many assays. As highlighted in the figure, the curve exhibits three regimes associated with low, intermediate, and high initial target concentrations. As a reference, we include in Figure 3.5 two vertical dashed lines to delineate these three regimes of the sensitivity curve.

The left-most vertical dashed line of Figure 3.5 highlights the value of $[E]_{0,LoD}$ as computed using the kinetic rates determined in the previous section. For target concentrations lower than $[E]_{0,LoD}$, the contribution of the reporter degradation to the signal is larger than that due to enzymatic *trans*-cleavage. In this regime, the reaction velocity becomes independent of the initial target concentration, effectively rendering detection of target impractical. In this regime, the measured saturation velocity is well approximated by the predicted noise floor reporter cleaving rate of $k_{rep}\,[S]_0$ (again, using the measured value of $k_{rep} = 1.4\times10^{-6}$ s^{-1}). This behavior is well captured by both our augmented kinetics model (equation 3.16) and the numerical solution to the full ODE system including late readout. This experimental saturation is, of course, not captured by the naïve Michaelis-Menten model, which predicts a proportional relationship between target concentration and reaction velocity (see equation 3.5).

The second vertical line of Figure 3.5 highlights the value of $[E]_{0,late}$, as computed using the kinetic rates and $\tau_{pre} = 5$ min. For target concentrations between $[E]_{0,LoD}$ and $[E]_{0,late}$, the *trans*-cleavage enzymatic activity dominates over reporter degradation and target concentration is low enough that the late readout effect is negligible. In this intermediate regime, all three models and the experimental measurements agree.

For target concentrations larger than $[E]_{0,\,late}$, the late readout effect becomes significant on the measurement of the reaction velocity. As detailed earlier, this typically results in an underprediction of the measured reaction velocity compared to the expected initial reaction velocity. As expected, only the augmented model corrected for late-readout effect correctly captures the observed inflection in reaction velocity.

Finally, as additional experimental validation of our model, we compared our model to the experimental data published by Huyke et al. [2] The latter work reported sensitivity curves for three different Cas12 orthologs and eleven different gRNA sequences, and two different Cas13 orthologs. They performed Michaelis-Menten-type kinetics measurements for each one of the 11 RNP with both dsDNA and ssDNA targets for Cas12, and for four different Cas13 RNP. Critical to the current comparison, their sensitivity measurements used a single fluorophore-quencher reporter type and a single reporter concentration ($[S]_0 = 200$ nM across all Cas12 sensitivity measurements, $[S]_0 = 1$ μM for Cas13 measurements). We provide in Section B.11 the superposition of all sensitivity curves for Cas12 and Cas13. The fact that Huyke's sensitivity curves asymptote to approximately the same signal plateau at low target concentrations and across all Cas12

orthologs and 11 gRNA sequences, and across all Cas13 orthologs, is further strong evidence that the measured limits of detection are determined by reporter degradation and not by the kinetic rates of the various CRISPR enzymes.

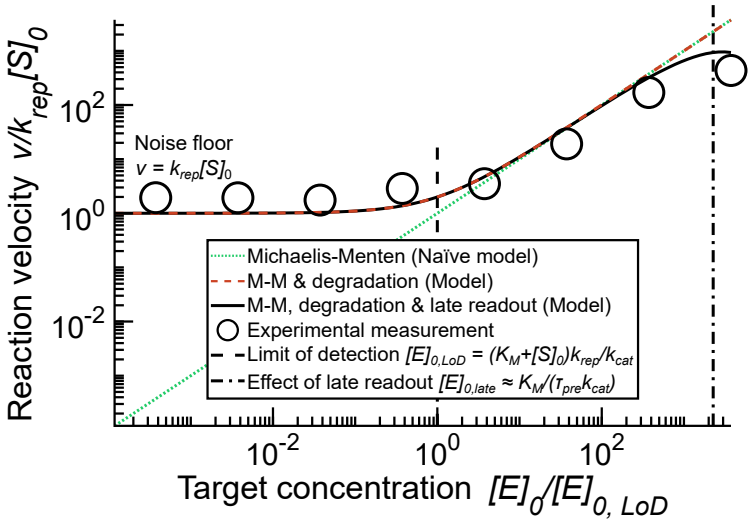

Figure 3.5: Measurements of maximum velocity of progress curves for LbCas12a activated by varied dsDNA target concentrations. The latter experimental measurements (circles) are compared to a prediction using the naïve Michaelis-Menten model (green dotted line, equation 3.5), the Michaelis-Menten model augmented with reporter degradation (orange dashed line, equation 3.16), and the augmented model with the effect of a "late readout", i.e. the effect of starting data acquisition delayed after the reaction starts (black solid line). At low target concentration, the apparent reaction velocity is governed by the reporter degradation rate $k_{rep}\ [S]_0$. Hence, reporter degradation imposes a limit of detection on the CRISPR assays.

Last, we note that DNA is usually very stable and typically not subject to cleaving in sterile solutions. However, there is strong evidence that dark quenchers are highly prone to degradation [119, 120, 121]. For example, Black Hole quenchers (BHQ) and Iowa Black FQ quenchers contain azo functional groups, which may undergo reduction [122], oxidation [123], or photodegradation [124, 125]. Hence, such degradation may result in the dynamic degradation of the reporter molecules which we observe.

3.4 Conclusion

We presented a new kinetics model for CRISPR *trans*-cleavage assays which use reporter molecules as a readout. The model captures the rise in fluorescence signal measured even in absence of target molecules (and in the absence of CRISPR enzyme). We attributed this persistent rise in background signal to the kinetics of the degradation of the reporter molecules at 37°C. Despite its immense importance and consequence in limiting the sensitivity of CRISPR assays, we know of no quantitative efforts to incorporate this effect

into the interpretation of CRISPR assays. First, we modeled this degradation as a measurable, first-order decay. We also developed a novel kinetics model to account for the coupling between this degradation reporters and the kinetics of *trans*-cleavage. The coupling of these reactions directly implies that the kinetics of cleaved reporters does not follow Michaelis-Menten kinetics. Second, we used our model to derive an analytical expression for a fundamental limit of detection of CRISPR assays which use fluorophore-quencher probes. Third, we validated our new model using experimental measurements of reporter cleaving rates. We also showed comparison of our model with existing published data (in Section B.11). The model shows excellent agreement with experimental data and shows that CRISPR assay limits of detection can be limited directly by reporter degradation.

The measurable rate of degradation of reporter molecules presents a fundamental limit to the sensitivity of any CRISPR-based assay which uses such probes. This has important consequences as the vast majority of published studies use fluorophore-quencher type probes as the primary signal readout for CRISPR activity, including bulk assays, but also droplet and microwells assays. It is likely that the reporter degradation rate depends on a variety of factors including sequence, length, fluorophore type, and quencher type. Future work could also investigate degradation mechanisms of the reporter probes, including using specialized analysis techniques such as mass spectrometry. Moreover, assays that rely on the collateral activity of CRISPR-Cas enzyme but use different reporter compositions may also be subject to similar background noise floor. This may include, for instance, lateral-flow assays that use biotin-labeled probes to distinguish positive from negative samples. The current results imply that the development of probes with repeatable and low degradation kinetic rates should be a major topic of research for studies aimed at increasing the sensitivity of CRISPR assays. Other possibilities for improvements include increasing the cleaved-to-uncleaved fluorescence ratio and increasing the catalytic efficiency of *trans*-cleavage.

Chapter 4

Preliminary screening of gRNA for CRISPR-based diagnostics

The research presented in this chapter was carried out in collaboration with J. Källberg, P. Ibáñez, J. Baudry, and A. D. Griffiths. Supplementary information associated with this chapter is presented in Appendix C.

4.1 Introduction

Clustered regularly interspaced short palindromic repeats associated enzymes (CRISPR-Cas) have sparked significant interest in the past several years [6, 7, 99, 1]. In particular, CRISPR-based methods have emerged as new approaches for specific and sensitive detection of nucleic acids, and aim to complement [11, 17] or replace [103, 104, 105] traditional nucleic acid amplification-based (NAA) techniques. Such methods typically leverage subtypes of the Cas12 [100, 12], Cas13 [13], or Cas14 [126] enzymes to design programmable detection systems. However, in the absence of pre-amplification (e.g., using PCR or LAMP), CRISPR-based tools often fall short of the detection levels required for diagnostically relevant target concentrations [2, 29, 8]. Strategies to improve the sensitivity of the CRISPR assay component include microfluidic techniques [1, 106, 127, 128], protein engineering [129, 130], and guide RNA (gRNA) modifications [131, 132]. Another approach is to target multiple loci of the activator oligonucleotide simultaneously using several gRNAs [19]. However, variations in gRNA sequence result in variations in enzymatic activity for both Cas12 and Cas13 [2, 19]. The relationship between gRNA sequence and *trans*-cleavage kinetic rates, which set the limit of detection of CRISPR-based assays [2], remains an open question.

In this chapter, we present two preliminary studies around methods to screen a large number of gRNA sequences based on the resulting *trans*-cleavage activity for Cas12a. We first introduce a simple pipeline to produce and screen 364 gRNAs using an automated liquid handling platform and identify high-performing gRNAs (i.e., associated with rapid *trans*-cleavage). We then design a microfluidic pipeline to increase the

throughput of our gRNA screening. The objective of this second pipeline is to test enough gRNAs to identify trends between gRNA sequences and *trans*-cleavage activity. Preliminary experimental results are presented for both methods.

4.2 Materials and methods

4.2.1 Screening of 364 gRNA sequences using robotic liquid handling

4.2.1.1 Reagents

LbCas12a (a Cas12 ortholog from *Lachnospiraceae bacterium ND2006*) at a concentration of 100 µM, NEBuffer r2.1, and the HiScribe T7 High Yield RNA Synthesis Kit were purchased from New England Biolabs (MA, USA). Reporter molecules were purchased from Eurofins Genomics (Germany) and resuspended to 100 µM. All other oligonucleotides listed in Section C.1 were obtained from Integrated DNA Technologies (IDT).

Three 384-well plates containing the target sequences ("TS"), the corresponding reverse-complementary sequences (hereafter referred to as the non-target sequence, "NTS"), and ssDNA precursors (see Figure 4.1), were purchased from IDT. All sequences corresponding to the same target sequence were assigned to the same well position across well-plates. The T7 promoter sequence was purchased in tube format. All purchased oligonucleotides were normalized to 10 µM and aliquoted prior to use.

All pipetting steps described in this section and shown in Figure 4.1A were carried out using the Freedom EVO liquid handling unit (Tecan), except for RNA purification.

4.2.1.2 Annealing of TS, NTS, and DNA precursor

TS and NTS were mixed in equal volumes, heated to 95°C, and slowly cooled to 20°C (at the rate of 0.1°C/s) to promote annealing. This yielded 5 µM target dsDNA for each of the 364 sequences (shown as "Target dsDNA" in Figure 4.1A). The ssDNA precursor was similarly annealed with the T7 promoter to form a double-stranded promoter region in the precursor prior to the in-vitro transcription (IVT) reaction. The resulting product is shown as "DNA precursor" in Figure 4.1A.

4.2.1.3 In-vitro transcription

IVT kit components were first combined into a master mix according to the manufacturer's instructions. 8 µl of the 5 µM DNA precursor was mixed with 22 µl of the IVT master mix. The reaction was incubated at 37°C overnight. The resulting RNA was purified using RNAClean XP beads (Beckman Coulter, CA, USA) according to the manufacturer's standard protocol. RNA products were resuspended in 30 µl nuclease-free water, and aliquoted into two 384-well plates.

4.2.1.4 CRISPR-Cas12 assay

An aliquot of the RNA products was mixed with the Cas12a enzyme and incubated for 30 min at 37°C to form ribonucleoproteins (RNPs) at a final concentration of 100 nM. The RNPs were incubated with the annealed dsDNA target at 37°C for 30 min (activated RNP concentration: 50 nM). Finally, dually labeled fluorophore-quencher ssDNA reporters were added to two aliquots of the activated RNP. The final activated RNP concentration was 3.3 nM and the final reporter concentration was 1 µM. Fluorescence measurements for both replicates were then performed every 30 s at 37°C for 210 min using a CFX384 Real-Time PCR Detection System (Bio-Rad Laboratories). Initial reaction velocities were estimated using a linear fit up to ~100 min.

4.2.2 Bulk verification of the molecular biology pipeline

4.2.2.1 Reagents

Reporter molecules were purchased from Eurofins Genomics (Germany) and resuspended to 100 µM. All other oligonucleotides listed in Section C.1 were obtained from IDT. Q5 High-Fidelity DNA Polymerase, Nt.BspQI, Q5 Reaction Buffer, NEBuffer r3.1, and deoxynucleotide solution mix were purchased from New England Biolabs. The PowerTrack SYBR Green Master Mix qPCR kit was purchased from Thermo Fisher Scientific (MA, USA).

4.2.2.2 PCR and nicking bulk reactions

Bulk polymerase chain reaction (PCR) with the Q5 polymerase were performed using 0.5 µM forward and reverse primers and 1.25 ng DNA template. The forward primer ("Bead primer", see Table C.1) includes a spacer region and binding site A (forward annealing site for the PCR). The template contains binding site A, the T7 promoter sequence, the crRNA sequence, a 20-nt variable region, and binding site B. The reverse primer consists of the reverse complement of binding site B, a unique molecular identifier (UMI) sequence, binding site C, a spacer region containing two repeats of the recognition sequence for the nicking enzyme Nt.BspQI, and binding site D. Primer and template sequences are reported in Table C.1, and PCR thermocycling conditions are detailed in Section C.2. PCR product size was estimated on a 3% agarose gel (Figure 4.3A). PCR products were purified using the NucleoSpin Gel and PCR Clean-up kit (Macherey-Nagel, Germany) according to the manufacturer's protocol. PCR product concentration and purity after clean-up were estimated using spectrophotometry (NanoDrop, ThermoFisher). The sequences of the PCR products were further validated with Sanger sequencing (Eurofins GATC, Germany).

PCR products were then diluted to 20 ng/µl and nicked using 5 U of Nt.BspQI, in either 1X NEBuffer r3.1 (recommended buffer for Nt.BspQI) or 1X T7 reaction buffer (from the HiScribe T7 High Yield RNA Synthesis Kit). The nicking reaction was performed at 50°C for 1h, followed by heat inactivation at 80°C for 20 min.

4.2.2.3 IVT-CRISPR reaction with fluorophore-quencher reporters

The nicked products were then used as a template for the one-pot IVT-CRISPR reaction. IVT reaction components were used at the recommended concentrations per the manufacturer's instructions. The final concentrations were 10 nM for LbCas12a and 1 µM for the fluorophore-quencher reporters. The reaction was incubated at 37°C and fluorescence measurements were taken every 30 s for 100 min.

4.2.2.4 IVT-CRISPR reaction with qPCR readout

For the quantitative PCR (qPCR) experiments, the IVT-CRISPR reaction was performed using 2 nM LbCas12a without fluorophore-quencher reporters at 37°C for 90 min. Serial dilutions of the products were used as a template for qPCR. qPCR was performed according to the manufacturer's protocol, using binding site A as the forward primer, and either binding site C or D as the reverse primer. qPCR thermocycling conditions are detailed in Section C.2.

4.2.3 Hydrogel bead fabrication

Polyacrylamide hydrogel microbeads were fabricated using a process similar to that described by Zilionis et al. [133] Microfluidic polydimethylsiloxane (PDMS) devices were fabricated and silanized using standard soft lithography methods. We produced a water-in-oil emulsion composed of monodisperse 10 pl droplets. The oil phase was composed of 2% Krytox and 0.4% *N,N,N',N'*-Tetramethylethylenediamine (TEMED) in HFE-7500 (Novec). The composition of the aqueous phase ("Bead production mix") and various buffers is detailed below. Acrydited primers were purchased from IDT (see Table C.1). All other reagents were purchased from Sigma-Aldrich.

	Initial concentration	**Volume**	**Final concentration**
Tris-HCl pH 8.0	1 M	100 µl	10 mM
NaCl	5 M	274 µl	10 mM
KCl	1 M	27 µl	10 mM
EDTA	500 mM	200 µl	10 mM
Triton X-100	100%	100 µl	10 mM
NFW		9.3 ml	10 mM
TBSET		10 ml	

	Initial concentration	Volume	Final concentration
Acrylamide	40% (wt/wt)	382 µl	10.32%
Acrylamide/Bis-acrylamide	40% (wt/wt), molar ratio 19:1	258 µl	14.4%
NFW		360 µl	
AA/BA solution		1 ml	

	Initial concentration	Volume	Final concentration
NFW		68.75 µl	
TBSET	1X	31.25 µl	0.75X
4X AA/BA	4X	78.1 µl	1X
Acrydited primer	1 mM	125 µl	400 µM
Ammonium persulfate (APS)	10%	9.4 µl	0.3%
Bead production mix		312.5 µl	

All aqueous solutions were filtered through a 0.2 µm membrane and stored at 4°C prior to use.

The emulsion was collected in a tube containing 1 ml mineral oil. Once the emulsion was produced, we incubated the tube at 65°C in a dry bath overnight. The next day, the emulsion was briefly centrifuged at 5,000 *g*. The fluorinated oil (bottom phase) and mineral oil (top phase) were removed using syringes. Equal volumes of TBSET and 10% (vol/vol) 1H,1H,2H,2H-perfluorooctanol in HFE-7500 were added to the beads (1 volume of TBSET per volume of emulsion) and vortexed for 30 s between each addition. Tubes were then centrifuged at 5,000 *g* for 30 s. The PFO phase was then removed and replaced by an equal volume of fresh PFO. This step was repeated until the milky bead phase turned into a solid, translucent mass. 1 ml of 1% (vol/vol) Span 80 (Sigma-Aldrich) in hexane was then added. The tubes were then vortexed for 30 s and centrifuged at 5,000 *g* for 30 s. The supernatant was carefully aspirated, and the hexane wash was repeated once. Subsequently, 4 ml TBSET was added. The beads were vortexed for 30 s and centrifuged at 3,000 *g* for 3 min. The supernatant hexane phase was aspirated. TBSET washes were repeated until the top hexane phase was no longer visible. Finally, the bead solution was passed through a 40 µm cell strainer using ice-cold TBSET to facilitate the passage of the beads.

4.2.4 PCR on hydrogel beads

The acrylamide/bis-acrylamide beads were used as forward primers in PCR. We adapted the protocol from Diehl et al. [134] for PCR on microparticles. As a preliminary test, we performed PCR in bulk rather than in water-in-oil emulsions. We used the following PCR mix:

	Initial concentration	Volume	Final concentration
NFW		15.54 µl	
Q5 buffer	5X	10 µl	1X
dNTP	10 mM each	1 µl	200 µM
Beads	300/µl	16.6 µl	5,000 beads/reaction
Template DNA	33 nM	1 µl	660 pM
Fluorescent reverse primer	5 µM	5 µl	0.5 µM
Forward primer (non-acrydited)	5 µM	0.5 µl	0.05 µM
Q5 High-Fidelity enzyme	2 U/µl	0.36 µl	0.014 U/µl
Total pre-mix		50 µl	

PCR thermocycling conditions are described in Section C.2. After the reaction, 10 µl of the product solution was dispensed into a cell-counting slide (Kova) and imaged with an epifluorescence microscope (Nikon Eclipse Ti2-E) equipped with a 10× magnification objective (Plan Apo λ, NA: 0.45) and a CMOS camera (Hamamatsu Orca-Flash 4.0).

4.3 Results and discussion

4.3.1 Screening of 364 gRNA using automated liquid handling

Figure 4.1A shows the pipeline to screen 364 distinct gRNA sequences. As an internal control, we included repeats of 20 sequences, bringing the total to 384 parallel reactions. We first designed ssDNA precursors consisting of three DNA regions. The first sequence is the T7 RNA polymerase promoter [135] (orange), followed by the DNA sequence encoding the gRNA. The latter comprises the Cas-specific gRNA sequence (hereafter referred to as crRNA, shown in green in Figure 4.1A) and a variable region of 19 to 23 base pairs (shown in blue in Figure 4.1A). We designed 364 ssDNA precursors, each corresponding to a different target region. In parallel, we designed the corresponding target DNA library, containing the corresponding 364 target DNA sequences flanked by constant regions (shown in black in Figure 4.1A).

We first annealed TS to NTS to form the double-stranded target DNA for the *cis*-cleavage step. Similarly, the T7 promoter reverse complement was annealed to the ssDNA precursor to form a double-stranded promoter region required to initiate IVT. The resulting product, which we refer to as "DNA precursor", is then used as template for IVT. We then purified the produced gRNA using standard solid-phase reversible immobilization (SPRI) magnetic beads. Finally, we combined the Cas12a enzyme, gRNA, and target to produce activated RNPs. The Cas enzyme concentration was set as limiting to ensure that the final RNP concentration was uniform across all sequences, independent of IVT and purification efficiency.

Figure 4.2A shows the 384 resulting progress curves, i.e. cleaved reporter concentration evolution over time. We converted raw fluorescence signals to cleaved reporter concentrations with a calibration that

corrects for non-uniform illumination, inner-filter effect, and background signal from uncleaved reporters (see Chapter 3). We show in red the progress curve corresponding to the sequence with the largest kinetic efficiency reported in the study by Huyke et al. [2], LbCas12a-1, which we use as a reference gRNA sequence. Figure 4.2B shows the distribution of the measured initial reaction velocity. Once again, we show in red the value of the reaction velocity measured for Huyke's LbCas12a-1 sequence. As expected, and as reported previously [2], there are substantial variations in the *trans*-cleavage activity of the Cas enzyme depending on the gRNA sequence. We observe that a large fraction of the gRNAs yields low to no activity. Conversely, 78 sequences yielded higher *trans*-cleavage activity than Huyke's LbCas12a-1 sequence. These sequences represent strong candidates for further diagnostic applications.

Figure 4.2C shows the relative contribution of each nucleotide, per position, to the gRNA activity. For a given nucleotide and position, the letter size in Figure 4.2C corresponds to the difference between the average reaction velocity of gRNAs that contain this nucleotide at this position and the mean reaction velocity across all screened gRNAs. Figure 4.2D shows the t-statistic from a two-sided Student's t-test that evaluates whether there is a statistically significant difference in reaction velocities between gRNAs that contain this nucleotide at this position and those that do not. Figure 4.2E shows the corresponding log-transformed p-value. We observe that gRNAs rich in A and U tend to result in stronger *trans*-cleavage activity than those rich in G and C. However, as shown in Figure 4.2E, there is low statistical significance for most of the nucleotide-position pairs. We attribute this to the small number of sampled sequences (order 10^2) per nucleotide-position pair, compared to the number of possible gRNA sequences (order $4^{20} \sim 10^{12}$). Therefore, even though this method allowed us to identify sequences with high kinetic efficiency, its throughput remains far too low to support generalizable design guidelines for high-performing gRNAs. In the next section, we introduce a high-throughput microfluidic pipeline to screen a much larger number of sequences.

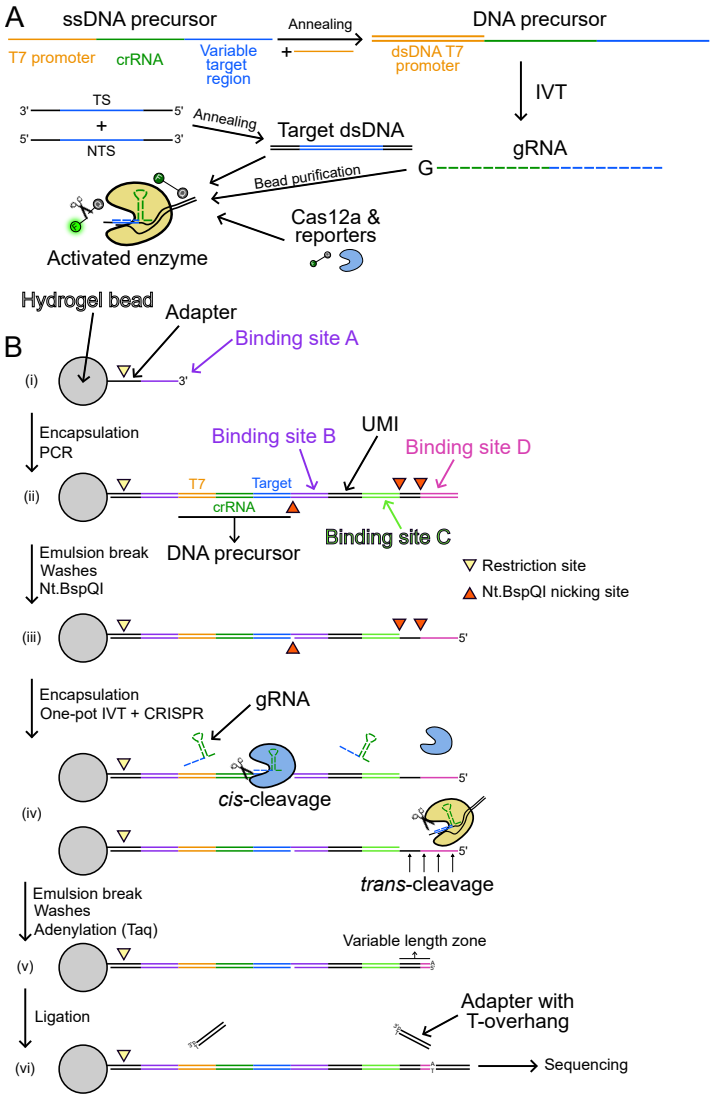

Figure 4.1: A Overview of the molecular biology pipeline for the screening of 364 gRNA using automated liquid handling. The pipeline includes annealing, IVT, and the CRISPR-Cas assay. B Overview of the microfluidic pipeline for the high-throughput screening of gRNA. This pipeline uses polyacrylamide beads to perform the IVT-CRISPR reaction in droplets.

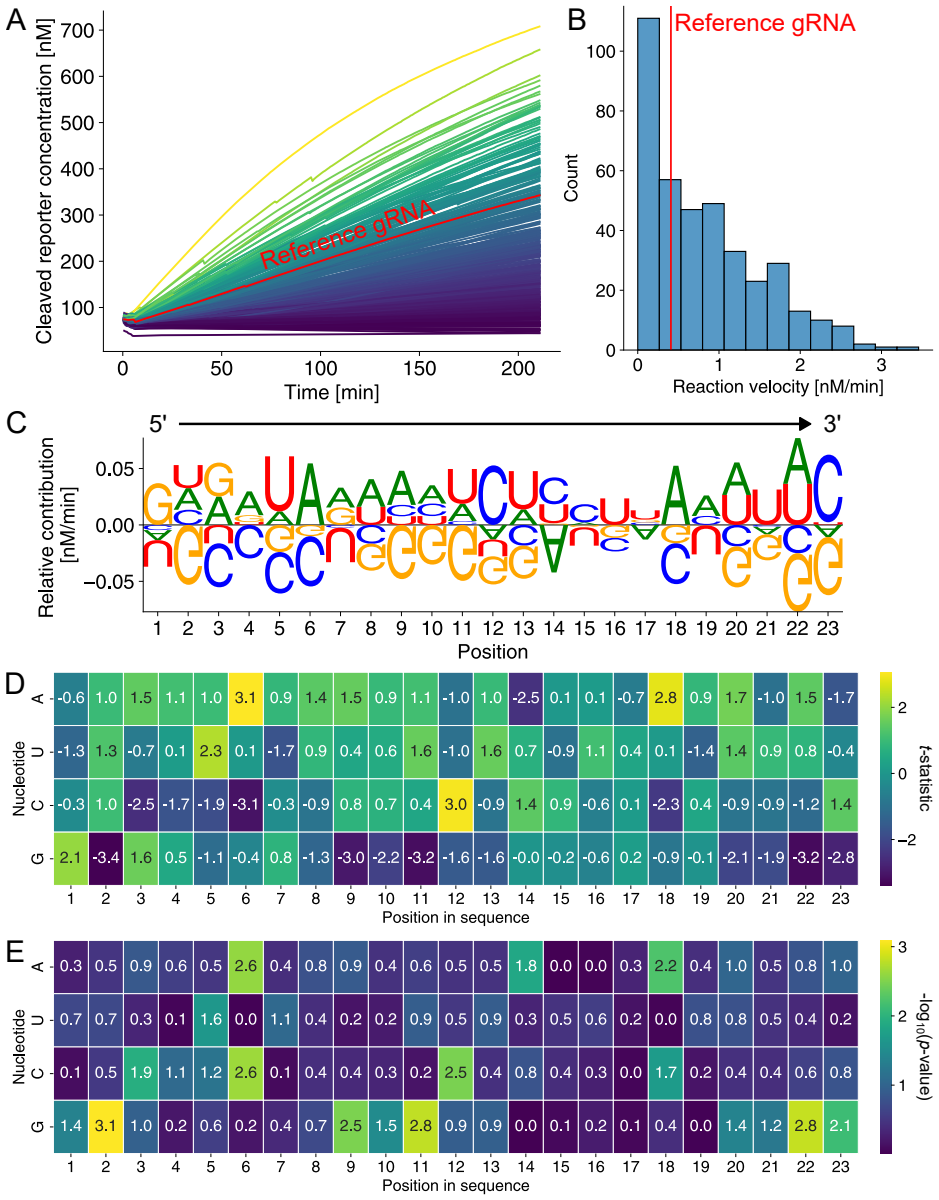

Figure 4.2: A Progress curves for 384 parallel CRISPR reactions. Shown in red is the progress curve corresponding to the gRNA sequence associated with the highest kinetic efficiency reported in Huyke et al. [2] B Distribution of initial reaction velocities corresponding to the progress curves shown in A. C gRNA sequence logo showing position-specific deviations in average reaction velocity relative to the global mean across all gRNAs. D t-statistic from a two-sided Student's t-test comparing reaction between gRNAs with or without a given nucleotide at each position. E Corresponding log-transformed p-values.

4.3.2 Hydrogel bead-based screening of gRNA

In this section, we describe a microfluidic pipeline to scale up the number of gRNAs that can be screened per experiment. Here, we run the IVT and CRISPR reactions in nanoliter-size water-in-oil droplets, so that up to millions of reactions can be performed in parallel. To screen gRNAs, we must ensure that each droplet contains at most one DNA precursor sequence. However, a single DNA precursor molecule will only activate a single RNP per droplet, which does not yield sufficient signal to be detected. To overcome this issue, we first produce hydrogel beads that carry a high number ($\sim 10^9$) of DNA precursors using droplet-based PCR. We also design the amplicon so that part of it may be cleaved by the activated Cas enzyme. The DNA carried by the bead therefore serves three purposes: template for IVT, target for *cis*-cleavage, and substrate for *trans*-cleavage. IVT and CRISPR reactions are then performed in droplets containing at most one bead. Once the reactions are performed, the sequence of the molecules on the bead informs both on the screened gRNA sequence and the corresponding activity.

Figure 4.1B shows the working principle of the microfluidic pipeline. First, we fabricate 10 pl hydrogel beads functionalized with an acrydited oligonucleotide primer (step (i)). This primer consists of an adapter sequence, a restriction site, and a PCR binding site denoted "A". The beads are then encapsulated in water-in-oil droplets along with a single DNA template molecule and the necessary reagents for droplet PCR. The template molecules contain an adapter sequence, binding site A, the DNA precursor (similar to the previous pipeline i.e., T7 polymerase promoter sequence, crRNA sequence, and a 20-bp variable sequence), and reverse binding site "B". The reverse primer consists of the binding site B, a 15-base UMI (i.e., a stretch of random bases), and binding sites "C" and "D" separated by a spacer region. The latter region includes two repeats of the recognition site of the nicking enzyme Nt.BspQI.

After the PCR, the hydrogel beads are coated with double-stranded amplicons (step (ii)). The emulsion is broken, and the beads are pooled into a common aqueous phase. They are then subjected to nicking with Nt.BspQI. The reaction results in three nicks on the amplicons. The first nick is shown in Figure 4.1B on the bottom strand (i.e., the template strand for the T7 polymerase) and terminates transcription after the variable section. This prevents the rest of the amplicon from being transcribed during IVT and appended to the gRNA. The remaining two nicking sites generate short DNA fragments with low melting temperatures (50-53°C). After stringent washes, these fragments are cleaned off the hydrogel beads. The latter are then coated with partially single-stranded templates (step (iii)).

The beads are then re-encapsulated in aqueous droplets, together with T7 and LbCas12a enzymes and the necessary reagents for both reactions. As shown in panel (iv), the gRNA is produced by the IVT reaction, complexes with the Cas12a enzyme, and the single-stranded region of the bead DNA template serves as the substrate for the Cas *trans*-cleavage reaction. The *trans*-cleavage occurs at an *a priori* unknown and variable locus.

After the CRISPR reaction, the emulsion is broken. The beads are washed and undergo filling of ss-DNA and adenylation using Taq polymerase. This results in dsDNA molecules bound to the beads with A-overhangs (step (v)). An adapter with a complementary T-overhang is then added and ligated. Step

(vi) shows the final product, which is flanked by two sequencing adapters and sequenced. For each DNA molecule bound to the beads (identified by its UMI), we can infer from the sequence whether it has undergone *trans*-cleavage and, if so, at which position. These molecules can then be pooled by gRNA sequence. For each gRNA, the ratio of cleaved molecules to total sequenced molecules serves as a proxy for *trans*-cleavage activity. Alternatively, sequencing using D and C binding sites for adapter addition and amplification allows the estimation of the ratio of intact over degraded reporters on bead targets.

4.3.3 Preliminary results for the high-throughput screening of the gRNA

In this section, we show preliminary results from the development of this pipeline. First, Figure 4.3 shows the results of preliminary testing of the molecular biology steps. Here, we ran all chemical reactions up to the CRISPR reaction using two gRNA sequences ("E" and "7") of known activity: the "E" sequence exhibits stronger *trans*-cleavage activity than the "7" sequence [2]. Figure 4.3A shows gel electrophoresis of two amplicons from the PCR step ((i) to (ii) in Figure 4.1), and for seven serial dilutions of the target from 33 nM to 33 fM. An important difference between these results and the final pipeline is that the forward primer here is in solution and not bound to a hydrogel bead. Gel electrophoresis confirms that the PCR produces the amplicon at the right size. Sanger sequencing of the amplicon confirmed that the PCR yielded the expected products.

We further cleaned the amplicons using standard post-PCR clean-up protocols and used them a template for nicking, IVT, and CRISPR reactions. As a preliminary experiment, we verified that the Cas enzyme was properly activated by introducing fluorophore-quencher reporters. We performed the nicking reaction in either NEBuffer r2.1 (recommended buffer for the Cas enzyme), NEBuffer r3.1 (recommended buffer for Nt.BspQI), or the IVT buffer (recommended buffer for the T7 polymerase). We then ran the IVT and CRISPR reactions simultaneously, either in NEBuffer r2.1 (following nicking in NEBuffer r3.1 or r2.1), or in IVT buffer (following nicking in NEBuffer r3.1 or IVT buffer). We show the corresponding fluorescence measurements in Figures 4.3B and 4.3C. Briefly, we observed no difference between the no-template control (NTC) and all other conditions when the IVT-CRISPR reaction was run in NEBuffer r2.1. Conversely, we observed a significant increase in fluorescence signal over time when the IVT-CRISPR reaction was performed in IVT buffer. The rise in signal was greater when the nicking reaction was run in IVT buffer than in NEBuffer r3.1. Further, consistently across both nicking buffer conditions, the "E"-target sequence resulted in faster *trans*-cleavage activity than the "7" target sequence. This is consistent with the expected order of kinetic efficiency reported by Huyke et al [2].

Finally, we used qPCR to assess whether the CRISPR enzyme cleaves the single-stranded region (step (iv)). We detail the process in Figure 4.1D. Briefly, we ran the nicking reaction, followed by the IVT-CRISPR reaction in the absence of fluorophore-quencher reporters. We then performed two sets of qPCR reactions using two different reverse primers: one corresponding to binding site "C" (shown in green) and the other to binding site "D". Binding site "C" remains intact after both reactions, whereas binding site "D" lies in the single-stranded region that may be cleaved during *trans*-cleavage. If an activated Cas enzyme cleaves

binding site “D”, the annealing of the reverse primer (and therefore amplification) is disrupted. Figure 4.3E shows the corresponding ΔC_q for three dilutions of the IVT-CRISPR product, defined as the difference in C_q between the qPCR reactions that used “C” or “D” primers. Lower C_q values indicate earlier amplification and therefore higher initial template concentrations. ΔC_q values were consistently higher for the “E” target than for the “7” target across all template dilutions. This suggests that there was a greater concentration difference in available “C” versus “D” sites for the “E” target than for the “7” target, and that more sites were cleaved in the “E” sample than the “7” sample. This is consistent with the previous reports suggesting that the “E” sequence yields stronger *trans*-cleavage activity than the “7” sequence.

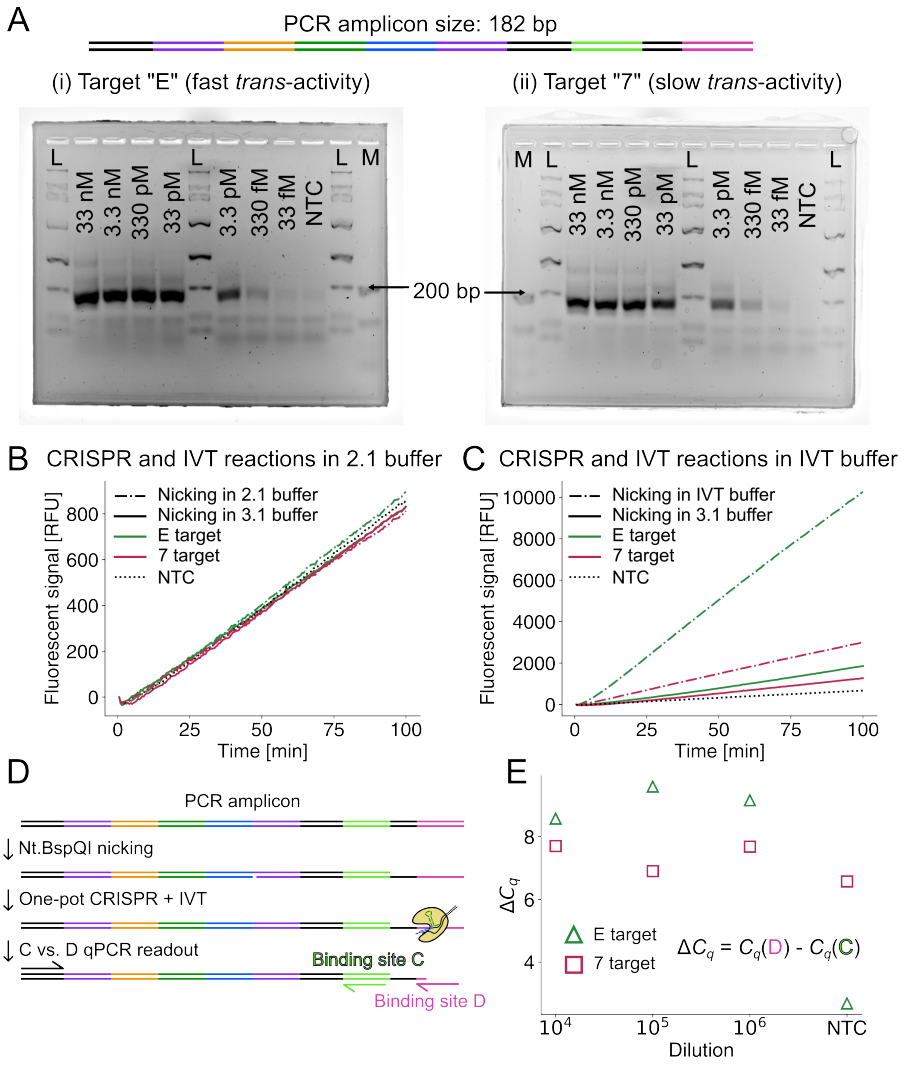

Figure 4.3: Preliminary results from the molecular biology pipeline. A Gel electrophoresis of PCR products. In this experiment, the PCR template was in solution (i.e., not attached to a hydrogel bead). B-C Measured fluorescence signal resulting from CRISPR-Cas12a activation using PCR amplicons as IVT templates. Fluorophore-quencher molecules were introduced to assess the activation of the Cas enzyme with the gRNA produced during IVT and the PCR amplicon. D Schematic of the qPCR verification experiment. After PCR, the amplicon is nicked and serves both as template for the IVT and target for *cis*-cleavage. qPCR is then performed using either binding site C or D as the reverse primer. E Results of the qPCR verification experiment. Shown are ΔC_q values for several dilutions of the IVT-CRISPR products, where $\Delta C_q = C_q(D) - C_q(C)$ is the difference in cycle number between the two qPCR experiments using either binding site C or D as the reverse primer.

4.3.4 PCR with hydrogel beads

In this section, we show preliminary results on the fabrication of polyacrylamide beads and PCR using these beads as a template. We used a protocol similar to that of Zilionis et al. [133] for the bead production, and of Diehl et al. [134] for the PCR on microparticles. We show here preliminary results from the first PCR step on the bead ((i) to (ii) in Figure 4.1). Here, the forward primer was covalently bound to the hydrogel bead during the bead production, and the reverse primer was labeled with a 5'-end fluorescein amidite (FAM) modification. Note that, in these preliminary results, PCR was performed in bulk unlike the process described in Figure 4.1. Figure 4.4 shows fluorescence (A-C) and brightfield (B-D) images of the hydrogel beads after PCR. Panels 4.4A and 4.4B show products in the presence of 33 nM of PCR template, and panels 4.4C and 4.4D show beads in the absence of the DNA template. The comparison of Figures 4.4A and 4.4C indicates that fluorescent primers are preferentially localize on hydrogel beads only if the PCR template is present. This strongly suggests that PCR amplicons are formed on the beads during the reaction. However, we note that there is significant bead-to-bead variation in the fluorescence signal. We hypothesize that this is due to the settling of the beads during the PCR. As the beads settle, the available surface for PCR differs from one bead to another. If this is indeed the case, the bead-to-bead variation should significantly decline when the PCR is performed using single beads encapsulated in droplets.

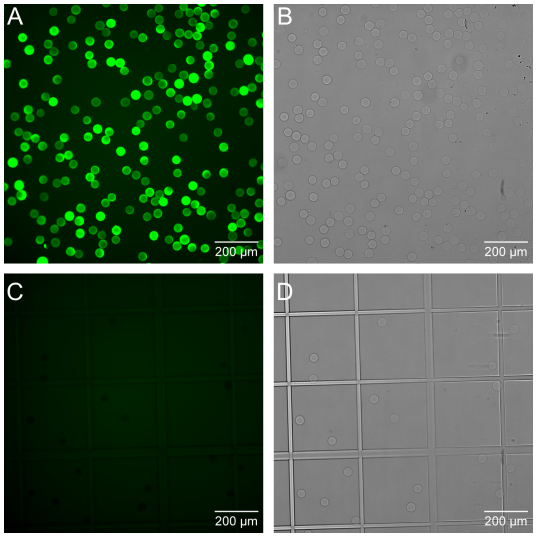

Figure 4.4: Epifluorescence images (A-C) and corresponding brightfield images (B-D) of the hydrogel beads after PCR. The forward primer is covalently bound to the hydrogel bead, and the reverse primer is labeled with a fluorophore. Shown are images of the beads if the reaction is performed in the presence of 33 nM template DNA (A-B), or in the absence of template DNA (C-D).

4.4 Conclusion

In this chapter, we presented preliminary work toward the development of two pipelines to screen gRNA sequences for CRISPR-Cas12a *trans*-cleavage activity. First, we screened 364 gRNAs using an automated liquid handling platform. This preliminary screen enabled the identification of 78 sequences that result in higher *trans*-cleavage activity compared to a reference gRNA. To address the limited throughput of this approach, we introduced a second screening pipeline using hydrogel beads to perform parallel CRISPR assays in droplets and relying on next-generation sequencing to identify high-performing gRNAs. Preliminary results show that the IVT and CRISPR reactions can be run simultaneously, that we can infer the relative gRNA performance from such experiments, and that PCR can be performed on hydrogel beads.

Several challenges remain to ensure that the microfluidic pipeline we introduced in this chapter becomes fully functional. First, the PCR and the IVT-CRISPR reactions must be optimized to function effectively in droplets. These steps work well in bulk, but their performance in emulsions may be compromised. Further optimization will likely be needed. Moreover, the adenylation and sequencing steps have yet to be performed. Finally, a bioinformatics pipeline still needs to be developed to analyze and interpret the sequencing data.

CRediT statement

Alexandre S. Avaro: Conceptualization, Methodology, Investigation, Data Curation, Writing - Original Draft, Writing - Review & Editing, Formal analysis. **Julia Källberg**: Conceptualization, Methodology, Investigation, Data Curation, Writing - Review & Editing, Project administration. **Pablo Ibáñez**: Conceptualization, Methodology, Writing - Review & Editing. **Jean Baudry**: Conceptualization, Writing - Review & Editing, Supervision, Funding acquisition. **Andrew D. Griffiths**: Conceptualization, Writing - Review & Editing, Supervision, Funding acquisition.

Chapter 5

Simulation tools for isotachophoresis

5.1 ITP buffer design using BEAN-ITP

The contents of this section were previously published by A. S. Avaro, A. Schwarzbach, A. Jangra, S. S. Bahga, and J. G. Santiago [136] in the journal *Analytica Chimica Acta* and are reproduced here with minor modifications. Supplementary information associated with this section is presented in Appendix D.

5.1.1 Introduction

Isotachophoresis (ITP) is a well-established electrophoretic focusing technique applicable to a wide range of processes for the separation, purification, and/or preconcentration of analytes [58, 61]. ITP focuses analytes at a self-sharpening interface between a leading electrolyte (LE) and a trailing electrolyte (TE) to create an electric field gradient that focuses target analyte ions (A). ITP also offers a method for mixing species [137] and accelerating biochemical reactions [66, 138, 65], including enzymatic reactions [17]. ITP is particularly compatible with microfluidic devices [58], including portable microfluidic systems [139].

ITP has been applied to a wide range of applications, including environmental monitoring, pharmaceuticals, food analysis, forensics, and chemical and biological detection [58, 140]. The analyte focusing in ITP is governed by the relative electrophoretic mobilities of analyte, and the co-ions of leading and trailing electrolytes. Most applications and implementations of ITP involve LE and TE buffers which comprise weak electrolytes, and often involve weak electrolyte analytes, whose mobilities depend strongly on the local pH. However, the non-linear dynamics of ITP result in spatiotemporal variations in local ion concentrations and pH, which can affect the relative order of effective mobilities of various ionic species. Hence, the design of LE and TE mixtures to focus a certain analyte can require detailed computations of the pH of multi-species mixtures, including ionic strength effects on mobility and pK_a [61, 138, 64].

To address the complexity of ITP design, there has been significant work to develop simulation tools to help design, understand, and troubleshoot ITP processes. Simulators for electrokinetic phenomena have

been reviewed elsewhere [58, 141]. We here briefly distinguish between two categories of ITP simulation tools. The first consists of simple zone chemistry solvers which rely on algebraic integral form of species conservation equations coupled with chemical equilibrium relations [58, 59, 69]. Such tools have been used to, for example, generate so-called ITP existence diagrams. These diagrams describe the number and types of zones formed with distinct chemical makeup, and can be used to determine whether given analytes focus or not [142]. However, we know of no publicly available algebraic tool which allows for the easy or rapid design of an ITP system. The second category of solvers consists of dynamic solvers of the spatiotemporal solutions of the differential form of electromigration-diffusion-reaction conservation equations [58]. Complex partial differential equations solvers are now commonly used to precisely predict ITP concentration, pH, and electric field profiles. Popular tools include SIMUL [71], GENTRANS [143], SPRESSO [72], and more recently SPYCE [144] and CAFES [145]. These approaches offer more temporal and spatial information of ITP dynamics but can require significant time to produce an answer. This is because they are required to solve a stiff set of partial differential equations which is expensive in terms of computing power and difficult to parallelize. This limits the number of parameters and conditions which can be tested. Another limitation of current ITP simulation tools of both categories is that they are mostly limited to testing one or a small number of ITP chemistries, and this impedes assay design and optimization [58].

We here present a new platform for the design of ITP chemistries and processes. We named this tool Browser-based Electrolyte Analyses for ITP (BEAN). BEAN enables fast and parallelized computation of chemical species concentrations values in plateau-mode ITP [58]. Importantly, BEAN computes electrophoretic mobilities and dissociation constants of weak electrolytes, including ionic strength and ion valence effects. BEAN includes features to quickly explore a variety of buffer compositions for ITP, and to choose effective chemistries for a given application. The tool enables rapid estimation of whether a sample will focus within a given set of LE and TE buffer chemistries chosen by the user. BEAN also allows the evaluation of the effects of a broad range of different titrations of the LE. This includes demonstrating whether the analyte is focused, the degree to which it is preconcentrated, and the associated pH values in the sample region. We emphasize that the ITP process equations described in Section 5.1.3 are not new. Indeed, the associated theory is well established and validated [58, 67, 74]. The novelty of BEAN lies in the integration of these equations with a searchable database of weak electrolyte properties [146], a massively parallel computation framework, and a web-based interface, to rapidly evaluate many quantities of interest for ITP. This results in an open-source tool that enables users to test for a wide range of ITP conditions at once, and presents relevant outputs in the form of heatmaps and automated plots of given physicochemical properties.

5.1.2 Qualitative description of ITP zones and dynamics

We here present a brief qualitative summary of the various mixtures, zones, and dynamics of ITP, while a detailed description (including detailed diagrams) is given by Ramachandran and Santiago [58]. ITP focuses analyte ions (A) of a specific range of mobilities at the interface between two electrolyte mixtures. The LE

contains a leading ion (LI) which has the same sign of charge as the target analyte's (a co-ion) and a mobility magnitude higher than of A. The TE contains a co-ionic trailing ion (TI) with a lower mobility magnitude. In this chapter, we consider ITP systems wherein LE and TE share the same counter-ion (CI) with a charge opposite to that of LI, TI, and A. Upon application of an electric field, LI, A, and TI migrate in the same direction. This migration forms a new zone adjoining the TE which we term the adjusted TE (ATE). This zone forms in the region formerly occupied by LI but newly occupied by TI. See Figure D.1 in Section D.1 (Appendix D) for a schematic of these dynamics.

At the interface between the LE zone (containing LI and CI) and the ATE zone (containing TI and CI), there forms a strong electric field gradient at the diffuse interface between the LI and TI. For short times, and for analytes with initially very low concentrations, the analyte focuses in so-called "peak mode", a small peak whose axial width is determined largely by the properties of the TE and LE and the applied current [58, 147]. For sufficient accumulation times and sufficiently high initial analyte concentrations, the analyte focuses into a so-called "plateau mode" where the analyte is purified (relative to TI and LI) and governs the local electrical conductivity. We here term this region of purified analyte the sample zone (S). For most applications, LE, TE, and ATE are pH buffers, necessarily including one or more weak electrolytes, and many analytes are themselves weak electrolytes. All weak electrolytes have observable ion mobilities which depend strongly on local pH and the ionic strength of the electrolyte. For this reason, calculations of pH and ionic strength in all zones must be performed in order to predict whether an analyte will indeed be focused by a specific LE and TE combination. Also, if it does focus, we wish to compute the concentrations and pH of the S and ATE zones. We created BEAN in order to facilitate and speed up such calculations, including computation of many variations of buffer titration. BEAN is an open-source solver built as an easy-to-use web-based tool and can be found at the following address: microfluidics.stanford.edu/bean. We also provide the source code for BEAN at the following address: github.com/adarschwarzbach/BEAN-ITP.

5.1.3 Model description

5.1.3.1 Physico-chemical calculations

Conservation laws and governing equations to describe ITP phenomena have been extensively reviewed and applied [58, 71, 72]. These weak-electrolyte formulations were strongly influenced by the work of Saville and Palusinski [67]. We here summarize these equations in the case of plateau-mode ITP with four zones: TE, ATE, S, and LE. Quantities of interest for ITP experimental design are molar concentrations, pH, and effective mobilities in each zone. In turn, these quantities are a function of thermophysical parameters like fully ionized mobilities, acid dissociation constants, and relevant ion valences. We will first review the expressions for zone concentration and mobilities in the infinite dilution limit, and then review models to account for ionic strength effects.

We use the notation conventions and nomenclature of Ramachandran and Santiago [58] for ITP. In particular, μ is the electrophoretic mobility (a signed quantity; with units of $m^2/(V{\cdot}s)$), and c is the molar concentration (molar unit; e.g., M). Subscripts indicate the identity of chemical species LI, CI, A, or TI.

Superscripts are used to indicate the zone of interest, among TE, ATE, S, and LE. For example, μ_A^{ATE} and c_{LI}^{LE} respectively refer to the effective mobility of the analyte ion in the ATE region, and the concentration of the leading ion within the leading electrolyte zone.

The total (analytical) concentration of a general ampholyte family X (i.e., multiple proton dissociation states of a chemical group) is given by:

$$c_X = \sum_{z=n_X}^{p_X} c_{X,z}, \tag{5.1}$$

where $c_{X,z}$ is the concentration of the ionic state of valence z belonging to the family X. c_X is generally a known quantity (an initial condition) within the LE and the TE. For example, LE and TE are often buffers mixed in preparation for the experiment and then introduced into a channel using pressure driven flow. n_X and p_X are respectively the minimum and maximum valence states of species X. We define the acid dissociation constant $K_{X,z}$ between valences z and $z+1$ as:

$$K_{X,z} = \frac{c_{X,z} c_H}{c_{X,z+1}}. \tag{5.2}$$

Here, c_H denotes the local concentration of hydronium ions H+, such that $\text{pH} = -\log_{10}(\frac{c_H}{1\text{M}})$. As shown by Bercovici et al. [72], the electroneutrality assumption leads to the following formulation:

$$\sum_{X=1}^{N} c_X \sum_{z=n_X}^{p_X} \frac{z L_{X,z} c_H^z}{\sum_{z'=n_X}^{p_X} L_{X,z'} c_H^{z'}} + c_H - \frac{K_w}{c_H} = 0, \tag{5.3}$$

where:

$$L_{X,z} = \begin{cases} \prod_{z'=z}^{-1} K_{X,z'} & \text{if} z < 0, \\ 1 & \text{if} z = 0, \\ \prod_{z'=0}^{z-1} K_{X,z'}^{-1} & \text{if} z > 0, \end{cases} \tag{5.4}$$

and K_w is the water dissociation constant. Equation 5.3 is used to calculate the pH of an electrolyte solution based on its chemical composition.

We define the effective mobility of species X, μ_X, and the local electric conductivity, σ, such that:

$$\mu_X = \sum_{z=n_X}^{p_X} \mu_{X,z}^o \frac{L_{X,z} c_H^z}{\sum_{z'=n_X}^{p_X} L_{X,z'} c_H^{z'}}, \tag{5.5}$$

$$\sigma = \sum_{X=1}^{N} c_X \sum_{z=n_X}^{p_X} \mathcal{F} z \mu_{X,z}^o \frac{L_{X,z} c_H^z}{\sum_{z'=n_X}^{p_X} L_{X,z'} c_H^{z'}}. \tag{5.6}$$

Here, $\mu_{X,z}^o$ is the fully-dissociated ionic mobility at valence z, and $\mathcal{F}$ is the Faraday number.

Plateau zone concentrations in ITP are governed by the species transport equation, which includes

electromigration and diffusive fluxes. In this analysis, we ignore diffusion because it is negligible away from the sharp ITP interfaces and does not affect the ITP plateau concentrations significantly. The integral form of mass conservation for species X across an ITP zone boundary moving at constant speed V_{ITP} yields [58]:

$$V_{ITP}\left(c_X^{\alpha} - c_X^{\beta}\right) = j\left(\frac{\mu_X^{\alpha} c_X^{\alpha}}{\sigma^{\alpha}} - \frac{\mu_X^{\beta} c_X^{\beta}}{\sigma^{\beta}}\right), \tag{5.7}$$

Here, j denotes the current density (charge per time per area). The superscripts α and β indicate any two zones separated by an ITP zone boundary. We assume that, at steady state, the S zone does not contain LI nor TI. Similarly, we assume negligible A in the LE zone. Applying equation 5.7 for LI and A at the boundary between LE and S, we obtain the familiar ITP condition [58]:

$$V_{ITP} = j\frac{\mu_{LI}^{LE}}{\sigma^{LE}} = j\frac{\mu_A^S}{\sigma^S}. \tag{5.8}$$

Similarly, we apply equation 5.7 to the CI:

$$V_{ITP}\left(c_{CI}^{LE} - c_{CI}^{S}\right) = j\left(\frac{\mu_{CI}^{LE} c_{CI}^{LE}}{\sigma^{LE}} - \frac{\mu_{CI}^{S} c_{CI}^{S}}{\sigma^{S}}\right). \tag{5.9}$$

From equations 5.8 and 5.9, we deduce the CI concentration in S:

$$c_{CI}^{S} = c_{CI}^{LE}\frac{\frac{\mu_{CI}^{LE}}{\mu_{LI}^{LE}} - 1}{\frac{\mu_{CI}^{S}}{\mu_A^S} - 1}. \tag{5.10}$$

The value of c_A^S are then deduced from the values of c_{CI}^S and σ^S. We perform the same process for the ATE, which yields:

$$c_{CI}^{ATE} = c_{CI}^{LE}\frac{\frac{\mu_{CI}^{LE}}{\mu_{LI}^{LE}} - 1}{\frac{\mu_{CI}^{ATE}}{\mu_{TI}^{ATE}} - 1}. \tag{5.11}$$

Equations 5.3, 5.5, 5.10, and 5.11 fully describe the ITP quantities of interest in the limit of infinite dilution. Note that, unlike Jovin and Alberty conservation laws [58], this analysis is valid for arbitrary ion valences. However, these equations form a system of nonlinear implicit equations, because effective mobilities and zone conductivities depend on local concentrations. Therefore, we employ an iterative method to solve these equations. At each iteration, we use guessed values of c_A^S and c_{CI}^S to compute the local pH and effective mobilities in the S zone. This allows to update the value of c_{CI}^S using equation 5.10, and σ^S using equation 5.8. This allows to update the value of c_A^S. This process is iterated until the values of c_{CI}^S and c_A^S converge. In practice, under-relaxation at the end of each iteration improves the stability of this iterative scheme. A similar iterative scheme is used to compute species concentrations in the ATE zone.

We now describe model corrections to account for ionic strength and finite ionic radius effects. There have been extensive demonstrations of the effects of finite ionic strength on the electrophoretic mobility and the acid dissociation constants [74]. The Pitts equation is a popular correction to electrophoretic mobility in binary electrolytes. In water at 25°C, it states the following [148]:

$$\mu^o_{X,z} = \mu^\infty_{X,z} - \left(3.1 \times 10^{-4} z + 0.39\,|z|\,|z_{CI}|\,\frac{2q}{1+\sqrt{q}}\mu^\infty_{X,z}\right)\frac{\sqrt{I}}{1+0.33a\sqrt{I}}\,. \tag{5.12}$$

Here, $\mu^\infty_{X,Z}$ denotes the ion mobility at infinite dilution (expressed in $\mathrm{cm}^2/(\mathrm{V}\cdot\mathrm{s})$), a is the effective atomic radius given in A, and z and z_{CI} are respectively the ion and the counter-ion valences. The ionic strength I and q are defined as:

$$I = \frac{1}{2}\sum_{X,\,z} z^2 c_{X,z}, \tag{5.13}$$

$$q = \frac{|z z_{CI}|}{|z| + |z_{CI}|}\,\frac{\mu^\infty_{X,z} + \mu^\infty_{CI,z}}{|z|\,\mu^\infty_{X,z} + |z_{CI}|\,\mu^\infty_{CI,z}}. \tag{5.14}$$

The Pitts formula is often regarded as a useful trade-off between accuracy and simplicity [148]. For increased accuracy, the Onsager and Fuoss model offers a more general correction for the electrophoretic mobility which is valid for an arbitrary mixture of ions. The latter can be summarized as follows [149]:

$$\mu^o_{X,z} = \mu^\infty_{X,z} - \left(A_{X,z}\mu^\infty_{X,z} + B_z\right)\frac{\sqrt{2I}}{1+aD\sqrt{I}}\,, \tag{5.15}$$

$$D = \sqrt{\frac{2e^2 N_A}{\varepsilon k_B T}}, \tag{5.16}$$

$$A_{X,z} = z\frac{e^3}{12\pi}\sqrt{\frac{N_A}{(\varepsilon k_B T)^3}}\sum_{n=0}^{+\infty} C_n R^n_{X,z}\,, \tag{5.17}$$

$$B_z = |z|\,\frac{e^2}{6\pi\eta}\sqrt{\frac{N_A}{\varepsilon k_B T}}\,. \tag{5.18}$$

Here, e is the elementary charge, N_A the Avogadro number, ε is the permittivity of the solution, k_B is Boltzmann's constant, T is the temperature of the solution, and η is the viscosity of the solution. A fixed value $\frac{aD}{\sqrt{2}}$ of 1.5 $\mathrm{mol}^{-1/2}\mathrm{mol}^{-3/2}$ yields a good approximation for a wide range of buffers [74]. The values of C_n and $R^n_{X,z}$ are given by Onsager and Fuoss [149], and we provide in Section D.2 of Appendix D the details of this calculation applied to the mobility.

The Debye-Hückel theory yields a correction for dissociation constants of weak acids and bases. For the dissociation of an acid HA^z with valence z [74, 150]:

$$\mathrm{p}K_\mathrm{a}\,(I) = \mathrm{p}K_\mathrm{a}^{\infty} - \log_{10}\left(\frac{\gamma_{X,z+1}}{\gamma_{X,z}\gamma_H}\right), \tag{5.19}$$

where:

$$\log_{10}\gamma_{X,z} = -z^2\frac{A_{DH}\sqrt{I}}{1 + aD\sqrt{I}} + 0.1z^2 I. \tag{5.20}$$

Here, $\mathrm{p}K_\mathrm{a}\,(I)$ is the $\mathrm{p}K_\mathrm{a}$ at the ionic strength of interest, $\mathrm{p}K_\mathrm{a}^{\infty}$ is the $\mathrm{p}K_\mathrm{a}$ at infinite dilution (i.e., at $I = 0$), and $A_{DH} = 0.5102\ \mathrm{dm}^{1/2}\mathrm{mol}^{-1/2}$ at room temperature. $\gamma_{X,z}$ is the molar scale activity coefficient, which quantifies the departure of the activity from the ideal behavior for the species X in valence state z.

5.1.3.2 Input parameters and thermophysical properties

The basic inputs for BEAN computations are the species which make up LE and TE. Figure 5.1 depicts the input panel of BEAN. First, the user selects a chemical species for each of the relevant ions (LI, CI, A, and TI). The user may search and select a species from among those stored in the fast-search database we include in BEAN. BEAN's database includes 521 common chemical species, including 303 weak acids, 161 weak bases, and 57 ampholytes [145, 3, 151, 152, 153, 154]. In addition, the user can create custom species by specifying mobilities and one (or more) $\mathrm{p}K_\mathrm{a}$ values along with the relevant valence state(s). As shown in Figure 5.1, each of the selected ions has a dedicated panel on the input interface. In this example, chloride ion (listed as HCl) is the LI, creatinine (a lactam commonly used as counterion for ITP [58, 3, 60], soluble up to roughly 0.7 M [155]) is the CI, glyceric acid (a sugar acid) is the A, and acetic acid (a common weak acid buffer ion) is the TI. These LI, TI, and A have previously been used in isotachophoresis assays [156].

For each ion, at least four physicochemical quantities must be specified by the user. These are valence, fully ionized mobility (at infinite dilution), $\mathrm{p}K_\mathrm{a}$, and analytical concentration (again, the sum of concentrations for the species family across all its valence states). Mobilities are specified as 10^{-8} $\mathrm{m}^2/(\mathrm{V{\cdot}s})$ and concentrations in mM. SI units are displayed with a mouseover operation. If the user selects a species from our database, the input fields corresponding to valence, mobility, and $\mathrm{p}K_\mathrm{a}$ are automatically populated with the corresponding values. If there exist multiple relevant valences for a given species, values of the physicochemical quantities for each of the valence states should be entered in the same field separated with commas. The user chooses whether ionic strength effects should be included (or not) in the calculations using the toggle button on the top left of the input interface. The "Run" button initiates the calculations.

The simplest output is a table listing the zone chemistries computed for the case specified in the input panel. Table 5.2 shows example output zone concentrations for the inputs of Figure 5.1. These data are provided by the BEAN website and reformatted here for clarity of presentation. The "Run" button initiates computation of a series of "ITP checks" for whether an analyte is successfully focused given the TE and LE. These checks consist of the following inequalities:

$$|\mu|_{LI}^{LE} > \max\left(|\mu|_{A}^{LE}, |\mu|_{TI}^{LE}\right), \tag{5.21}$$

$$|\mu|^S_{LI} > |\mu|^S_A > |\mu|^S_{TI}\,, \tag{5.22}$$

$$|\mu|^{ATE}_{TI} < \min\left(|\mu|^{ATE}_A, |\mu|^{ATE}_{LI}\right). \tag{5.23}$$

These three inequalities are sufficient and necessary conditions for a "stable" ITP system. We here refer to "stable ITP" if a finite injection of the analyte results in a steady analyte concentration within a zone between the TE and LE zones [69]. The results of these three checks are displayed below the zone concentration table on the BEAN website.

The next output produced by BEAN is a computation of the effective mobility of all selected ions as a function of pH. Figure 5.2 shows the computed effective mobilities versus pH for the inputs shown in Figure 5.1. This plot of mobility dependence on pH for all species are designed to help the user evaluate various titrations (pH and ionic strength variations) of the LE and TE ions which may yield workable pH values of the LE.

Importantly, the tool further enables evaluation of a large number of buffer variations for each combination of chemical species. The "Create Heatmaps" button initiates 972 parallel independent simulations, whose results are displayed in the form of three heatmaps. Table 5.1 summarizes the various parameters that are varied in these parallel calculations, and the displayed quantity of interest, for each heatmap. Figures 5.3D-F show example output heatmaps for the inputs shown in Figure 5.1. We note that even though LI and CI concentrations are varied from 1 mM to 1 M, some relevant species may not be soluble over this range. The variations of mobility values associated with the first two heatmaps is designed to help the user estimate alternate chemical species and LE zone titrations which are variations of the nominal (input) chemistry. For example, a workable range of TI mobilities can be compared to select values from the species database. For simplicity, the computations assume the mobility ranges for candidate alternate species apply to A and TI species with at most one pK_a. If relevant, this pK_a applies to an ionization state transition between -1 and 0 (weak acid) or between 0 and $+1$ (weak base). The third heatmap assumes only the species mobilities and pK_a of the input case, and consider wide variations in titration of the LE buffer. ITP chemistries obtained using these heatmaps should therefore be considered estimates which are subsequently validated and computed more precisely using the explicit computations associated with the Zone Concentrations table.

Table 5.1: Overview table of the parameters and quantities of interest of the heatmaps for BEAN.

	Heatmap 1	**Heatmap 2**	**Heatmap 3**
Quantity of interest	pH in the sample region pH^S	A-to-TI mobility ratio in the ATE $\frac{\mu_A^{ATE}}{\mu_{TI}^{ATE}}$	
Abscissa parameter	CI concentration in the LE c_{CI}^{LE}	TI absolute mobility μ_{TI}^o	A absolute mobility μ_A^o
Abscissa range	1 mM to 1 M	Anionic ITP: -5×10^{-8} to -1×10^{-8} $\mathrm{m}^2/(\mathrm{V{\cdot}s})$ Cationic ITP: $1{\times}10^{-8}$ to $5{\times}10^{-8}$ $\mathrm{m}^2/(\mathrm{V{\cdot}s})$	
Ordinate parameter	LI concentration in the LE c_{LI}^{LE}		
Ordinate range	1 mM to 1 M		

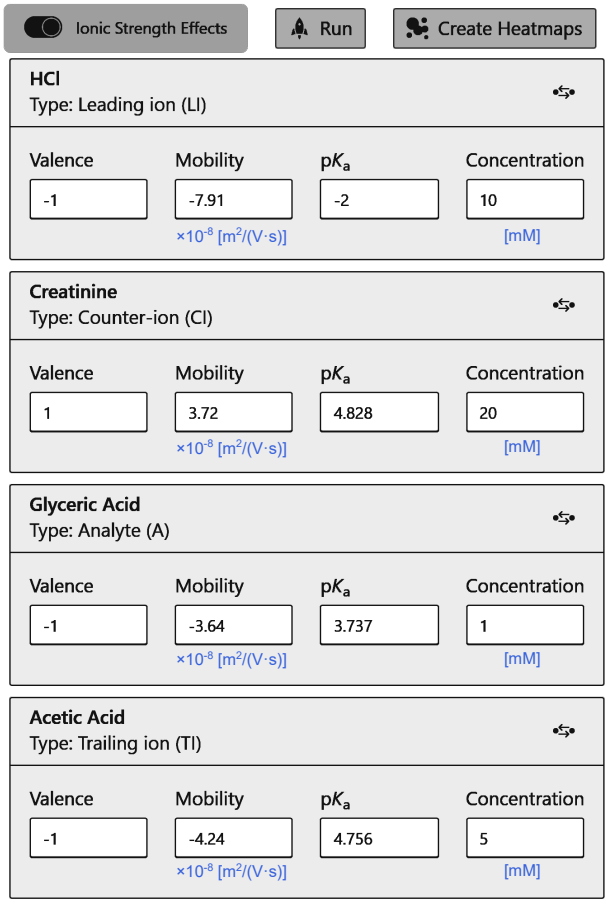

Figure 5.1: Input data panel for BEAN with an example ITP chemistry. The user inputs physicochemical properties of the four ionic species (LI, CI, A, and TI). Clicking on the two-dot, opposing-arrows icon in the top right of each entry opens a window to our (optional) searchable database of 521 electrolyte species, including most buffer ions. In this example, HCl acts as the LI, creatinine as the CI, glyceric acid as the analyte ion, and acetic acid as the TI. The panel is shown here with inverted greyscale for clarity. SI units of mobility and concentration were added here in square brackets in blue text, whereas units are displayed as a tooltip (visible upon mouseover) on the website. Fully-ionized, infinite dilution mobility and pK_a values are taken from [3].

5.1.3.3 AWS implementation

The 972 parallel runs of the calculation are implemented using AWS cloud computing services. We here provide a brief summary and plan to report a more detailed description of the computational architecture in the future. Briefly, the tool uses AWS services, including Lambda, Lambda Layers and API Gateway, coupled with Python libraries (NumPy), to run the parallel runs of the ITP simulation and create three heatmaps.

We estimate with PyPAPI [157] that each "Create Heatmaps" execution in BEAN requires roughly 5.0×10^9 floating point operations if ionic strength effects are included in the calculation, and 9.1×10^8 if they are not. With the current implementation, this requires less than 30 s from the time the user requests the heatmap generation to the time the heatmaps are displayed on the website. We estimate that the same calculation would take over 1,700 s (~ 60 times longer) to run using the best personal computers currently available for the general public.

5.1.4 Results

5.1.4.1 Rapid plateau concentration calculation & ITP checks

As mentioned, the simulation tool website provides a table of the molar concentration for each species and in each zone. Table 5.2 shows an example output using the inputs of Figure 5.1. The LE (respectively TE) is composed of LI (respectively TI) and CI. Concentrations in the ATE and S regions are computed using the aforementioned conservation laws and chemical equilibria relations (eqs. 5.10 and 5.11). As part of this, fully ionized mobilities and pK_a values are corrected for ionic strength effects using respectively the Onsager-Fuoss correction (eqs. 5.15 to 5.18) and the Debye-Hückel formula (eqs. 5.19 and 5.20). pH values for each of the zones are also reported in the last row of Table 5.2.

Table 5.2: Example computed plateau concentrations and pH table for inputs of Figure 5.1 including ionic strength effects. Concentrations are specified in mM for each of the zones (columns: TE, ATE, S, and LE) and for each ion (LI: HCl, CI: creatinine, A: glyceric acid, TI: acetic acid). pH values for each zone are reported in the last row.

	TE	ATE	Sample	LE
HCl	0	0	0	10
Creatinine	20	17.8	17.2	20
Glyceric Acid	0	0	7.15	0
Acetic Acid	5	7.75	0	0
pH	5.44	5.18	5.05	4.87

5.1.4.2 Effective mobility plot calculation

The tool then provides a plot of the effective mobilities of the relevant species as a function of pH, using equation 5.5, with varying c_H. Figure 5.2 shows plots of example mobility computations using the inputs from Figure 5.1. The website has a similar plot, and the data is plotted here in a more compact form for clarity. Anion mobilities (TI, A, and LI) are plotted on the right ordinate, and cation (CI) mobility is shown on the left ordinate. Solid curves indicate mobilities in the infinite dilution limit, and dashed curves indicate mobilities corrected for ionic strength effects; here, for simplicity, using the Pitts formula (equation 5.12) and the Debye-Hückel correction (equations 5.19 and 5.20). The values required for these calculations include

ionic strength, ion valence, counter-ion valence, and infinite dilution pK_a values. As nominal, relevant values, the plots correspond to local mobilities within the specified ATE for the TI, A, and CI ions, and within the LE for the LI. Note that similar plots have been reported for the design of ITP experiments with specific analytes [152, 153, 154], but the latter references did not consider ionic strength corrections. BEAN provides a general tool to generate this plot for all analytes and includes corrections for ionic strength and species valence.

In the example of Figure 5.2, the LI is chloride (a strong electrolyte) whose effective mobility is insensitive to pH. Conversely, TI, CI, and A are weak electrolytes with valence and mobility which are strong functions of pH. Specifically, TI, A, and CI have two possibly relevant valence states ($(0, 1)$ for CI, and $(-1, 0)$ for TI and A). Plateaus in these mobility curves typically correspond to pH regions where one valence state is dominant over the other valence states. Transitions between plateaus typically occur near pH = pK_a. Stable ITP occur in pH ranges where the magnitude of the effective mobility of A is bracketed by those of LI and TI. In the example shown in Figure 5.2, this condition is only met for pH < 5.5 in the infinite dilution case. At higher pH, no stable ITP is predicted. Note that the cutoff pH value(s) depends on the ionic strength of the ATE.

For a fixed pH, the effective mobility magnitude of species decreases when ionic strength effects are considered. As described by Bahga et al. [74], this reduction is due to two effects related to the counter-ionic atmosphere surrounding each ion. The first is associated with the polarization between the ion and its counter-ions (lowering local electric field); and the second is the additional drag experienced by the ion due to the opposing electromigration of its counterions.

Good estimates of effective mobilities are important for ITP experimental design. Indeed, ITP can only occur if, and only if, all of the mobility checks (equations 5.21 to 5.23) are satisfied. These constraints have a major influence on the experimental design of ITP experiments. For instance, finding a pH range that is workable (i.e., wherein all mobility checks are satisfied) for a given analyte has a direct impact on the choice of the pK_a of the buffering counterion. Further, mobility values strongly influence other quantities relevant to ITP, including rates of ion accumulation, plateau concentrations, and plateau lengths.

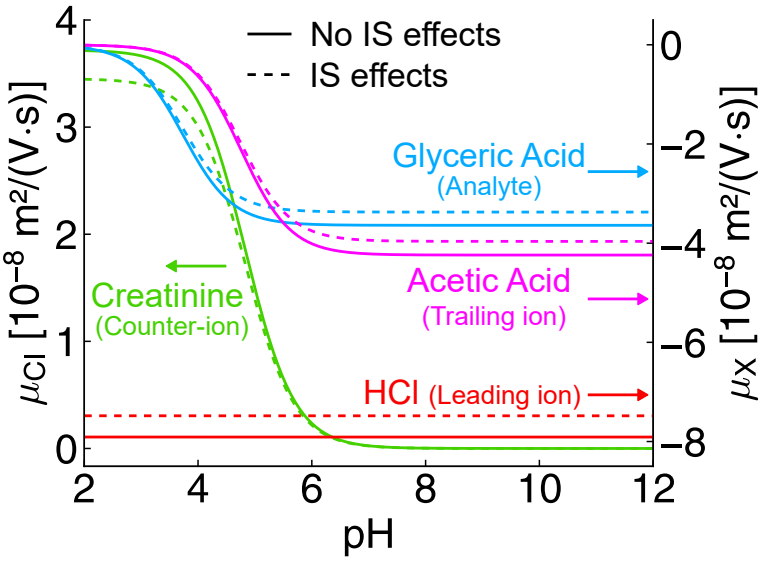

Figure 5.2: Mobility of user-selected ions as a function of pH without (solid curves) and with (dashed curves) ionic strength corrections. TI, A, and LI mobilities are on the right ordinate, whereas CI mobility is on the left ordinate. Ionic strength effects are specific to buffer ion species and ionic strength. As a nominal reference, we plot corrections for the ionic strength of the ATE computed by the solver (here I_{ATE} = 5.54 mM) for A, TI, and CI, and for the ionic strength of the LE (I_{LE} = 9.74 mM) for the LI. Similar curves are provided by BEAN as line plots where a mouseover operation shows precise values of ordinate and abscissa for each point.

5.1.4.3 Heatmaps

BEAN enables the user to evaluate a large number of variations of the specified buffer ions using three heatmaps. Figure 5.3 shows two example sets of output heatmaps demonstrating possible variations of the ITP chemistry inputs shown in Figure 5.1. The top row, Figures 5.3A, 5.3B, and 5.3C, show computed variations without ionic strength correction. The bottom row, Figures 5.3D, 5.3E, and 5.3F, show corresponding results including ionic strength correction. For each set of three heatmaps, each of the 972 pixels corresponds to one run of the simulation (as opposed to the single simulation initiated with the "Run" button). For each heatmap, two of the input parameters are varied over 18 values, resulting in 324 combinations of input parameters. The latter variations make up the abscissa and the ordinate of the heatmap, and the map intensities are outputs. Within each heatmap, all other input parameters remain fixed and equal to the value specified by the user in the input panel. White pixels indicate cases where at least one of the ITP checks (equations 5.21 to 5.23) is not satisfied. Grey pixels indicate instances where the run timed out (> 22 s). We set this timeout limit to comply with the timeout limit of the AWS API gateway of 29 s. We also specify with a white dot the cases where the root finding routine for the chemical equilibrium computation did not converge within 2,000 iterations, and this is strong evidence of poor buffering conditions.

We first note that the operational envelopes found by the solver are relatively narrow, and this is reflected in the relatively small regions of valid ITP cases across all heatmaps. These envelopes are shown in Figure 5.3 with colored pixels (i.e., neither white nor grey pixels). We here purposely chose an ITP chemistry which has a relatively narrow operational range. The LI is a strong titrant to the weak base CI. As is typical for such an arrangement, the pH in the S (and ATE) zones is then close to the pK_a of the CI provided the LI-to-CI analyte concentration ratio is within an order of magnitude of 0.5. For LI-to-CI analytical concentrations further from 0.5, the pH can vary quickly and we lose the ability to buffer [150]. More importantly, we chose here an analyte which has a relevant pK_a near that of the pK_a of the CI. Hence, significant variations of the LE zone pH quickly result in failure of ITP to focus and/or the solver to converge–resulting in the narrow operational envelopes.

We next discuss details of the heatmaps for each of the three columns of Figure 5.3. Heatmaps 5.3A and 5.3D, in the first column, show the pH in the S region as a function of c_{CI}^{LE} and c_{LI}^{LE} in the abscissa and ordinate, respectively. These heatmaps clearly show the narrow operational range of c_{LI}^{LE} for this ITP chemistry. Note the workable cases found by the solver occupy the approximately well-buffered region where the LI-to-CI concentration ratio is close to 0.5. The latter region occurs approximately within the antidiagonal region of the heatmap. Cases in the upper left corner of the heatmap correspond to cases where the LI concentration is significantly larger than the CI concentration, which are poorly buffered cases in which the CI is nearly fully ionized by the strong acid LI. Cases in the lower right corner of the heatmap correspond to cases where the sample pH is larger than about 5.5. In this regime, consistent to the results of Figure 5.2, the effective mobility magnitude of A is lower than that of TI and condition 5.22 is not satisfied. Finally, pH not only strongly affects mobility (c.f. Figure 5.2), but it is itself a crucial quantity in the design of biochemical separation, preconcentration, and reaction applications. For instance, protein activity and solubility are strong functions of local pH [158].

Heatmaps 5.3B and 5.3E, in the second column, show A-to-TI mobility ratio in the ATE zone, as a function of infinite-dilution, fully dissociated TI mobility (abscissa) and c_{LI}^{LE} (ordinate). The populated intensity region shows a range of candidate TI mobilities for which the ITP conditions are met and which are tractable for the solver. As expected, for fixed c_{LI}^{LE}, the mobility ratio decreases with increasing TI mobility. TI mobilities larger than a cutoff mobility value result in unstable ITP, wherein at least one of the conditions of equations 5.21 to 5.23 is violated. Similarly, c_{LI}^{LE} larger than a cutoff concentration value for a given TI mobility results in unstable ITP. As expected for this chemistry, c_{LI}^{LE} strongly influences ATE chemistry and pH, and therefore strongly influences the effective mobilities of A and TI in the ATE. As discussed previously, glyceric acid only focuses if pH $<$ 5.5. Values of c_{LI}^{LE} larger than about 20 mM (given the other concentrations given in Figure 5.1) result in a poorly buffered system. Increasing the value of the buffering counterion (here, creatinine) results in a larger critical value for c_{LI}^{LE}. Interestingly, low $\left|\mu_{TI}^{o}\right|$ and c_{LI}^{LE} also result in poorly buffered systems. We attribute this to the fact that low values of $\left|\mu_{TI}^{o}\right|$ and c_{LI}^{LE} yield large $c_{CI}^{ATE}/c_{TI}^{ATE}$, disrupting the balance of buffering in the ATE. Lowering CI concentration in the LE zone mitigates the latter issue. Heatmaps 5.3B and 5.3E facilitate the identification of TI candidates that can focus the specified analyte among a wide

range of LI titrations.

Heatmaps 5.3C and 5.3F, in the rightmost column of Figure 5.3, show the A-to-TI mobility ratio in the ATE zone as a function of the mobility of fully dissociated, infinite-dilution mobilities for A (abscissa) and c_{LI}^{LE} (ordinate). Values of this ratio greater than unity satisfy equation 5.23. For a fixed c_{LI}^{LE}, the mobility ratio increases monotonically with candidate analyte mobility, as expected. For the cases computed here (but not always), the mobility ratio increases with LI concentration. For this configuration, we note that analytes with mobility magnitudes between about 2.5×10^{-8} m^2/(V·s) and 4×10^{-8} m^2/(V·s) focus only if c_{LI}^{LE} is within a narrow operating range. For example, overly high values of c_{LI}^{LE} result in a loss of buffering and unstable ITP, as discussed above. On the other hand, overly low c_{LI}^{LE} results in pH > 5.5 in either S or ATE, which leads to a violation of conditions 5.22 or 5.23. Heatmaps 5.3C and 5.3F help users identify analytes that can be focused using the nominal ITP chemistry specified by the user, and across a significant range of LI titrations.

As mentioned in Section 5.1.3, the calculations of the heatmaps 5.3B, 5.3C, 5.3E, and 5.3F assume at most univalent species. This has two important implications. First, the heatmap computations are most useful and most general for the common case of buffering species with a single relevant (or most important) pK_a for a given application. Second, for buffer systems with two or more pK_a values in the useful pH ranges, the user should select the nominal input case carefully to explore the pH range(s) of most interest. The choice of a pH range may be straightforward in some applications as pH is often dictated by the analyte of interest. Again, we recommend using the heatmaps as a first rough estimation to determine working ranges of LI concentration and mobilities for the chemistry of interest. More precise and ad hoc estimations should then be computed using the more general single-point "Run" calculations of BEAN.

Finally, it should be noted the heatmaps also serve as an instructional tool for users who are novice in the use and design of ITP systems. By leveraging the parallel computation of AWS, a large number of ITP configurations may be visualized simultaneously. This provides insights about the relationships among species concentrations, pH, mobility, and sample plateau concentration.

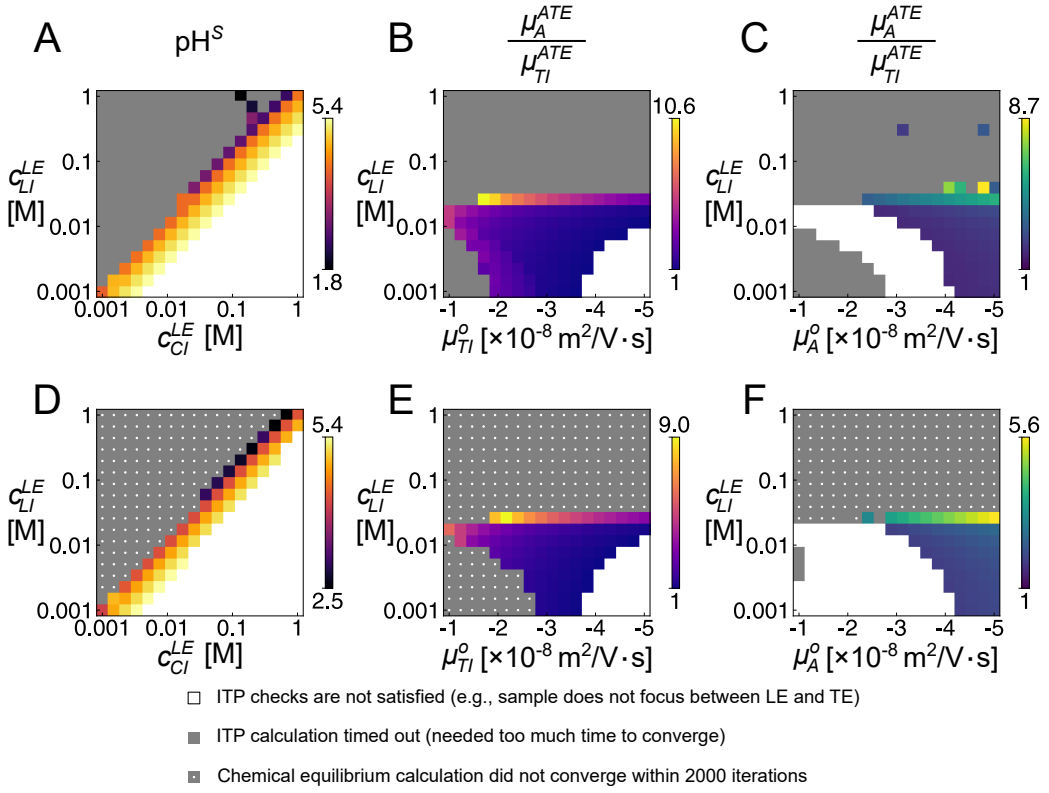

Figure 5.3: Heatmaps provided by the BEAN website. The heatmaps show results of 972 parallel runs of BEAN to estimate workable variations (including candidate A and/or TI species) of the input ITP chemistry. A to C show results at infinite dilution, and D to F show results with ionic strength corrections. The heatmaps display pH in the sample region (A, D), and A-to-TI mobility ratio in the ATE (B, C, E, F). As indicated, the parameters varied are LI concentration in the LE (all heatmaps); CI concentration in the LE (A, D); fully ionized, infinite-dilution TI mobility (B, E); fully ionized, infinite-dilution A mobility (C, F).

5.1.5 Conclusion

We developed and implemented a new web-based simulation tool for the design of ITP buffer chemistries. BEAN first facilitates the rapid evaluation of an ITP chemistry system for a given application. The tool determines whether a given analyte focuses given the LE and TE chemistries provide by the user. If the analyte successfully focuses, it quickly provides estimates of the plateau concentration and pH values of each ITP zone. BEAN also offers an evaluation of 972 variations of the specified ITP system (including buffer titrations). BEAN is integrated with a searchable database of 521 weak electrolyte chemistries, including common buffer ions. We showed example results of BEAN with glyceric acid as a model analyte ion. BEAN computations can consider the effects of ionic strength and arbitrary mixture valences. An important limitation of the tool is that it only provides plateau concentration values, and no information on

the spatial distribution of the species (e.g., estimates of plateau zone lengths). We therefore recommend BEAN as an initial, rapid evaluation of feasible ITP chemistries for an application. Once a small number of chemistries is chosen, then the user should turn to a more comprehensive partial differential equation solvers such as SIMUL, SPRESSO, SPYCE or CAFES (another free, browser-based tool) for more complete spatiotemporal information, including plateau widths, ion (including analyte) accumulation rates, and the unsteady formation of zones.

5.2 ITP experimental design with CAFES

The contents of this section were previously published by A. S. Avaro, Y. Sun, K. Jiang, S. S. Bahga, and J. G. Santiago [145] in the journal *Analytical Chemistry* and are reproduced here with minor modifications. Supplementary information associated with this section is presented in Appendix E.

5.2.1 Introduction

Isotachophoresis (ITP) is a well-established electrophoresis technique for preconcentration, separation and purification of ionic sample species depending on their effective electrophoretic mobility. ITP uses a leading electrolyte (LE) buffer and trailing electrolyte (TE) buffer. Sample ions focus if their mobility magnitude is larger than the TE's co-ion and smaller than the LE's co-ion. Trace ions focused for a short time will focus at the LE-to-TE interface in relatively narrow, strongly overlapping peaks [159, 160]. A higher concentration sample ion focused for longer times can eventually develop its own purified zone called a plateau. These plateaus have a maximum concentration determined by their absolute mobility, acid dissociation constant, and the properties of the LE buffer. Multiple sample ions can be focused and separated into a train of adjoining plateaus between the LE and TE [160, 161]. Interest in ITP is growing due to its versatility, robustness, and ease of integration into microfluidic assay systems. For example, ITP can purify nucleic acids from complex samples [61], be integrated with capillary electrophoresis to achieve both high sensitivity and resolution [162] and can be used to control and accelerate biochemical reactions [163]. ITP can be integrated into one or more steps of complex assays such as immunoassays [138] or CRISPR-based enzyme detection [17].

Easily accessible simulation tools offer an excellent way to understand the basics of ITP, design, and model ITP processes, and to help troubleshoot and understand complex ITP phenomena. One example design challenge is the selection and specification of buffer ions, in particular the initial concentrations and mobilities of LE co-ion, TE co-ion, and the LE counter-ion. Also interesting is the evaluation of various sample injection and other spatial configuration strategies. Several ITP simulation packages, namely numerical solvers for coupled, unsteady, multi-species electromigration and diffusion, are currently available. Among these, the most useful and robust for quick evaluation of buffer chemistries, injection schemes and ITP dynamics are tools which consider the highly simplified case of unsteady but one-dimensional transport, including multi-species electromigration and diffusion of weak electrolytes. The original version of SIMUL [70], whose latest version was published in 2021 [71], was likely the earliest of such freely available, nonlinear electrophoresis tool. The current version of SIMUL can, among other features, be used to optimize separation conditions, analyze focusing and preconcentration of several analytes, and capture electromigration dispersion. SPRESSO [72] is an open-source and free tool first developed in 2009 which includes a sixth order compact finite difference scheme, an adaptive grid refinement to resolve high gradients, moving frames of reference for faster simulations, and detailed model for dependance of mobility and dissociation constants. Bahga et al. [74] added the ability to account for ionic strength effects on both pK_a of ions and ion

mobilities. More recently, Dagan [73] published a package based on SPRESSO that included a new module for handling finite kinetic rate reactions among sample ions. All these tools require some preparation by the user prior to execution, including download, file extraction, and operating-system dependent installation. The improved accuracy and complexity of these codes also mean that their execution is resource-intensive in terms of computational time and computer hardware requirements. Consequently, these simulators do not offer a short turnaround time for setting up and performing ITP simulations. Moreover, none of these simulators can be used on low-power devices such as tablets and smartphones, which have found increasing utility in laboratory and classroom settings.

Most ITP process designs require only one-dimensional models as these require the least computational expertise on the part of the user and provide the fastest simulations. Short simulation times enable rapid evaluation of candidate buffer ions and injection strategies. The main quantities of interest in such designs are the general "where and when" of the various species and the spatiotemporal development of pH. The latter is important as it governs weak electrolyte mobility as well as, for example, the stability, activity, and solubility of biochemical species. The "where and when" includes the time for plateaus and/or peaks to develop, the rate of accumulation of species and the net amount of substance(s) accumulated in these zones, the velocities of interfaces and peaks, the spatial order of plateaus, and estimates of the concentration of peaks and plateaus at the place and time of detection or elution. With the exception of peak-mode concentration, all of the latter quantities are weak functions of the spatial extent of the thin high-gradient regions between plateaus. These regions are, ideally, governed by the competing effects of non-uniform electromigration and diffusion. In practice, the spatial extent of such interfaces also depends on the dispersive effects associated with two- and three-dimensional geometries, externally applied pressure gradients, and internally generated pressure-driven flows (e.g., from residual electroosmotic flow or Joule heating) [147]. The latter effects are difficult to capture and validate experimentally and so it is fortunate that the precise prediction of the spatial profile of such interfaces is not a requirement for most ITP assays [72, 147]. Even the advanced electrophoresis simulators such as SIMUL and SPRESSO do not model these practically observed dispersive effects, reducing the need for resolving steep concentration gradients using computationally expensive simulations.

In view of these considerations, we here present a simple-to-use ITP simulation tool we have called Client-based Application for Fast Electrophoresis Simulation (CAFES). CAFES is a free and open-source simulation of ITP which benefits from the client-side features and wide cross-browser compatibility of JavaScript. CAFES can be used for simulating ITP processes through various web-browsers on devices running any operating system, including mobile devices. The code enables accurate and fast evaluation of pH and the "when and where" of species in ITP with the relatively minor trade-off of offering only approximate evaluation of the spatial extent of the highest gradients in an ITP process (e.g., the width of a highly focused peak or the details of the interface between adjoining plateaus). CAFES offers an intuitive interface enabling specification of a wide range of buffer species and sample injection configurations and mixtures. It includes a database [72, 151] of 521 selectable species in addition to custom user-defined species.

We also present experimental validation of CAFES using data from well-controlled peak- and plateau-mode ITP processes.

5.2.2 Physical process and model description

5.2.2.1 Advection diffusion equations and boundary conditions

Assuming no bulk flow (e.g., pressure-driven or electroosmotic flows) and electromigration within a long straight channel with a uniform cross-section, the mass conservation of weak electrolyte species is described by the following set of advection-diffusion equations:

$$\frac{\partial c_i}{\partial t} = \frac{\partial}{\partial x}\left[\frac{\partial (D_i c_i)}{\partial x} - \mu_i E c_i\right],\ i = 1, 2, \ldots N. \tag{5.24}$$

Here c_i represents the analytical concentration of the i-th species family in a mixture of N species [72] and E is the local electric field. The first term on the right-hand side represents molecular diffusion while the second corresponds to the electromigration of ionic species. The derivation leading to this equation includes writing the conservation equations (including diffusion, electromigration, and reaction) for an arbitrary species and then summing these over each species "family", defined as all the ionization states of each molecule group. Hence, the source (creation and destruction) terms associated with acid-base dissociation reactions do not appear explicitly since the "species concentration" c_i represents the sum concentration across all ionization states [72]. The species family effective mobility and diffusivity are then respectively denoted μ_i and D_i. As described by Bercovici [72], a good estimate of the latter quantities (particularly mobility) is obtained by solving the chemical equilibrium of the total ion mixture at each point in space and time (see equations (19) in Bercovici et al. [72]). The set of all advection-diffusion equations for each species family is coupled through the local electric field E, which depends on the local conductivity field and thus all ionic species. For a constant applied current density, j, as simulated in CAFES, the local electric field is governed by the following equation (see equation (18) in in Bercovici et al. [72]):

$$E = \frac{1}{\sigma}\left(j + \frac{\partial S}{\partial x}\right). \tag{5.25}$$

Here, σ is the local ionic conductivity (itself a function of local species concentrations and ionization states). The gradient involving S is associated with the ionic current carried by diffusion, and the variable S results from the proper summations over ionization states and families [72].

5.2.2.2 Spatial discretization

The governing equations are discretized in space using a finite volume method based on the symmetric limited positive (SLIP) scheme of Jameson [164]. The formulation of this scheme for simulating electrophoretic transport phenomena is described in detail by Bahga et al. [165] For simplicity, speed of computation, and to manage memory in the JavaScript implementation, we discretized the spatial domain $[0, L]$ with

a uniform and stationary grid. (Note this is unlike SPRESSO which uses an adaptive grid to resolve the high-gradient interfaces of such multispecies electrokinetic dynamics much more precisely.) The current finite-volume-based SLIP scheme yields second-order spatial accuracy in the regions with smooth solution and automatically switches to first-order accuracy in the regions with oscillations or local extrema. The SLIP method's unconditional numerical stability allows for fast and stable simulations performed with a minimal number of grid points immediately prior to performing more accurate (but longer) simulation. It also explicitly conserves the mass of ionic species.

It is often unnecessary to simulate the entire length of the microchannel and we can instead simulate ITP in a small, relevant portion. It is thus necessary to impose non-reflecting boundary conditions to prevent spurious reflections of concentration gradients propagating out of the computational domain [72]. These conditions are enforced by extending the computational domain on both ends using ghost cells in which the species concentrations are equal to the species concentrations at the corresponding boundary at every time step [72, 166].

5.2.2.3 Time discretization

We adopted the fifth order Runge-Kutta Dormand-Prince (DorPri45) method for time integration. (This is the method used by, for example, the `ode45` function in MATLAB, although we here use JavaScript.) It adjusts the time step at each timestep. The DorPri45 scheme not only offers higher accuracy, but also broader stability compared to lower-order Runge-Kutta methods. This enables our solver to use comparatively larger time steps and a lower number of timesteps. CAFES performs chemical equilibrium calculations at the end of each timesteps and not for each sub-step of the Runge-Kutta scheme, therefore using DorPri45 results in lower computational overhead compared to methods that require more timesteps. The process of each time timestep is saved as a TensorFlow graph which can be called upon by the JavaScript interface. The simulation sequence can be described as follows:

1. User inputs the settings of the simulation and initiates the simulation.
2. The domain is discretized in regular and constant spatial intervals.
3. The TensorFlow graph object for the timesteps is generated based on the user-defined inputs and serialized.
4. The governing equations for the species profiles are integrated using DorPri45 integration. At each timestep, the model generated in Step 3 is re-loaded and infers the solution using the current adapted time step.
5. Step 4 (and therefore Step 3) is repeated until the total time specified by the user is reached, or if the user stops the simulation.

All computations are performed on the client's side, i.e. within the user's browser software. This means there is no need to download the results file through the Internet. The computed solution can, in all cases, be observed and interacted with using the Plotly [167] user interface.

5.2.2.4 User input and output

CAFES takes as input the parameters summarized in the Inputs section of Table 5.3. An example image of the input General User Interface (GUI) panel is shown as Figure E.1 in Section E.1.

The user defines the channel cross-section area and total length of the channel of interest. The initial configuration of buffers and sample ions is then established as follows. First, the user selects each chemical species, either choosing from the database or by defining a custom species. Next, the user determines the initial distribution of the species and its physicochemical properties.

The chemical properties of interest are the valence(s), the fully ionized (i.e., absolute) mobility(ies), and the pK_a('s) of each species. The code includes a database [72, 151] of 521 common chemical species, whose makeup is summarized in Table 5.3. The user can search through this database using the provided string-based search tool and automatically add the desired species with a click of an add "+" button. The user can also enter custom species and families of custom species (e.g., protonated and deprotonated forms of a weak acid), which can be specified using commas in the same input row. Lastly, the user sets the electric current to drive ITP. We assume only constant current mode for simplicity.

Each species can be introduced into the problem with one of four different initial spatial profiles. The "Left Plateau" and "Right Plateau" profiles are useful in the simulation of species which begin at respective left and right end of the domain, extend into the domain, and terminate somewhere within it. These distributions are prescribed by the initial species concentration (c_0), the injection location (x_{inj}) (i.e., the location where the species is terminated), and interface width (σ) associated with the interface as follows:

$$c(x) = \frac{c_0}{2}\left(1 \pm \operatorname{erf}\left(\frac{x - x_{\text{inj}}}{\frac{\sigma}{2}}\right)\right). \tag{5.26}$$

Next, the "Peak" distribution can be used to model a species injected into some finite space within the channel. This distribution is parametrized by the total injection amount (N) in moles, an injection location (x_{inj}), an injection width (w), interface width (σ), domain length (L), and cross section area (A) following the equation:

$$c(x) = \frac{N \cdot g\,(x)}{\int_0^L g\,(s) \cdot A \cdot ds}. \tag{5.27}$$

Here $g\,(x)$ is defined as:

$$g(x) = \operatorname{erf}\left(\frac{2}{\sigma}\left(x - x_{\text{inj}} + w\right)\right) - \operatorname{erf}\left(\frac{2}{\sigma}\left(x - x_{\text{inj}} - w\right)\right). \tag{5.28}$$

The characteristic injection width w can approach (and even be smaller than) the characteristic interface

width. For $w < \sigma$ (which is a valid input to the simulation), the spatial profile approaches a Gaussian-like top hat distribution. Lastly, the "Uniform" distribution can be used to simulate some background species injected with uniform fixed concentration throughout the whole domain length (and presumably outside of it so that the species can enter and leave the domain). This distribution is thus specified by only one parameter: the uniform initial concentration (c_0).

In the Simulation and Numerics section of the input panel, the user sets the number of grid points, the total simulation time, and the absolute ordinary differential equation integration tolerance (ODEIT). Lower ODEIT implies that the simulation is more accurate, and we recommend a value of less than about 10^{-2} for rough estimates and less than 10^{-4} for more accurate results (see E for additional details on ODEIT). The whole input configuration can be saved and exported for future use as a JavaScript Object Notation (JSON) file.

The Start button initiates the simulation. The Plotly interface provides direct visualizations of all species concentrations and the pH at the latest timestep. This interface allows the user to interact with the plot in real time using the tools provided by Plotly. The user can manually (Zoom, Zoom in/out and Pan buttons) or automatically (Autoscale button) adjust the zoom on a portion of the abscissa and/or ordinance of the simulation, toggle spike lines to easily read numerical values, isolate the plot of a single species (double click on the legend of the corresponding species), and reset the original view (via the Reset Axes button). At any time, the user is free to pause (or stop) the simulation and export the results as a .zip folder containing multiple JSON files. These files contain the input, the time steps, and the electrolyte concentration profiles (H^+ having a separated JSON file). This export is not directly readable, but we have provided Python tools to decode it and describe these in Section E.3. The concentration and pH profiles can be obtained for each time.

5.2.3 Experimental methods

We validated the computations of CAFES by comparing its predictions to experimental data for both peak and plateau mode ITP. We compared the output of the simulation to two sets of experimental data. First is a set of data obtained as part of the current study (specifically to evaluate peak-mode dynamics). The second is a set of plateau-mode ITP data originally published by Chambers et al. [4] We describe these below.

We performed peak-mode focusing of AlexaFluor (AF) 488 in a single, off-the-shelf borosilicate microfluidic chip (model NS12AZ, Caliper Life Sciences, subsidiary of PerkinElmer, Inc.). Figure E.3 in Section E.4 shows a schematic of the chip. It consists of two channels wetetched to a 20 μm depth with a 50 μm mask width. This results in an approximately 1,630 μm^2 D-shaped cross-section. A constant but adjustable current (from 1 μA to 5 μA) was imposed between positive and negative electrodes separated by a total distance of 72 mm. The LE buffer consisted of 100 mM Tris and 50 mM HCl, and TE consisted of 100 mM Tris, 50 mM HEPES and 0.2 μM AF488. The initial buffer loading is detailed in Figure E.3 in Section E.4. We monitored the progression of the peak using an inverted epifluorescence microscope with an objective with 4X magnification and NA of 0.2 (Nikon Plan Apochromat CFI60). We recorded all the movies using a CMOS camera

Table 5.3: Overview table of the parameters, features, inputs, outputs, and limitations of CAFES.

Model descriptor	Description	Units	Comment or reference
Physical equations	Multispecies 1D unsteady electromigration and diffusion		Bercovici [72]
Spatial discretization	Symmetric limited positive (SLIP) scheme		Jameson [164], Bahga [165]
Time-stepping	Runge Kutta Dormand Prince (DorPri45, 5th order)		Bercovici [72]
Model restrictions	ODE tolerance (see below) minimum of 10^{-2} (see Section E)		
	Initial interface widths σ assumed to be 1 mm	mm	Read-only value
	Suggested pH range of 3 to 11		
Maximum grid points	No limit due to the numerical implementation		Maximum set by results export
Boundary and initial conditions	User-specified initial loading (see species parameters)		Bercovici [168]
	Non-reflective boundary conditions		Leveque [166] and Bercovici [168]
	Current density evolution equations		Equations 35-44 of Bercovici [168]
Implementation languages	Simulation: JavaScript (TensorFlow) - Python		
	UI: JavaScript - HTML - CSS		
	Post-processing using Python		
Input parameters	Simulation time (physical duration to be simulated)	s	
	Steps per plot update	steps	Increase to plot less often
	ODE error tolerance		
	Domain length	mm	
	Applied current	μA	Signed float
	Channel cross-sectional area	μm^2	
	Species parameters (see below)		
Species parameters	Species name		Character string
	Type: Right/Left plateau, Peak/Plateau or Uniform distribution		Type describes spatial distribution
	Total species concentration, c_0 (for Right/Left plateaus and Uniform)	mM	Nonnegative float

Species parameters	Total moles of species (only for Peak/Plateau distribution)	pmole	Nonnegative float
	Injection location (required for Peak/Plateau and Right/Left Plateau) x_{inj}	mm	Nonnegative float
	Injection width (required only for Peak/Plateau zone)	mm	Nonnegative float
	Species valence(s)		Signed integer
	Species mobility(ies) of respective valence(s) $\lvert\mu\rvert$	10^{-9} $m^2/(V{\cdot}s)$	Nonnegative float
	pK_a(s) associated with valence transition	pH units	Signed float
Common species database	Contains a total of 521 species: 303 weak acids, 161 weak bases, 57 ampholytes. 179 species have multiple relevant valences.		Hirokawa [151]
	String search		
	Direct integration of the database in the input (Add button)		
Alternate input	Configuration file (contains all input parameters and species data, Load Config button)		JSON file
Output	Configuration file (Save Config button)		JSON file
	Save Results folder contains non-readable spatial-temporal cube and inputs		ZIP file
	Analyze tool replays concentration plot dynamics directly in the UI (no post-process)		Plotly [167]
Real-time line plot features (Analyze tool)	Plotted are color-coded total (analytical) concentrations and pH vs. distance	mM and pH units vs. mm	Plotly [167]
	Species name in legend corresponds to input name		
	Reset scale by clicking the home button		
	Zoom in/out, pan and autoscale features		
	Isolate one profile by double-clicking on its legend	mM vs. mm	
	Plot shows simulated time	s	

(Hamamatsu ORCA-Flash 4.0) at 20 fps (frames per second) and used a flat field correction to account for inhomogeneous illumination. The imaging results in a spatial, line-of-sight averaging of intensity along the depth of the channel. In post-process, we then averaged the fluorescence signal along the spanwise width of the channel to isolate streamwise variations of dye concentration using a custom MATLAB code. Each averaged frame then constituted a single point-value versus time from which we constructed the spatial-temporal plot in Figure 5.5A. For simplicity of presentation, the intensities of Figure 5.5A were normalized by the highest measured intensity across all experiments. This intensity maximum occurred near the end of the highest current condition, as expected.

The experimental setup for the plateau mode data is detailed in Chambers et al. [4], and only summarized here. Chambers used a similar, off-the-shelf glass microchip. Their LE buffer consisted of 100 mM MES, 200 mM Bis-Tris, 2 mM $Ba(OH)_2$, 0.4% PVP and their TE buffer consisted of 100 mM tricine, 20 mM $Ba(OH)_2$ and 0.4% PVP. Variable concentrations of analytes (HEPES and MOPS) were added to the TE buffer in three different cases to observe different plateau lengths. AF488 was used as a non-focusing tracer [4] in the plateau mode ITP experiments.

5.2.4 Results

5.2.4.1 ITP simulations using CAFES

The simulation tool outputs the concentration profiles of all species at each time instant. The different injection types ("Left plateau", "Right plateau" and "Peak/Analyte") can be combined to construct a wide variety of complex initial concentration profiles.

To show the versatility of the tool, we simulated a simultaneous a fairly complex anionic ITP process and show four selected time instants of the simulation in Figure 5.4. In this example, the initial concentrations of three analytes results in two plateau-mode analytes (weak acids MES and MOPS) and one peak-mode analyte (fluorescent dye AF488). The initial LE mixture included a rapid reduction in concentration at $x = 60$ mm. This LE distribution is simulating so-called cascade ITP [169] wherein an initial high LE concentration is used to improve the sample ion capacity of the system and then transition to a higher electric field region which provides better plateau resolution. The dynamics show the development and motion of various ion interfaces and pH throughout the computational domain of interest. Note the two stationary "top hat" features in the HEPES distribution (centered near $x = 20$ and 40 mm) are stationary, expected, and due to the Jovin and Alberty regulating functions established by the initial distribution of ions [58]. We present additional examples of CAFES simulations for cationic and for bidirectional ITP in Section E.6 (and provide example input files for these computations). In the next two sections, we will show experimental validation for the tool by comparing predictions to peak- and plateau-mode anionic ITP experimental data.

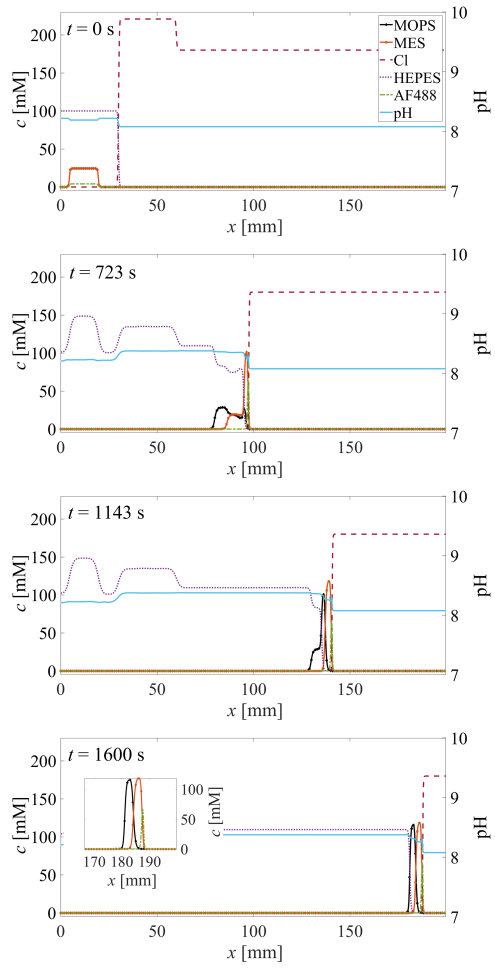

Figure 5.4: Simulation of anionic ITP process using CAFES. Plotted are concentration profiles of ions (left ordinate) and pH (right ordinate) at four time instants. Species are an LE anion (HCl), TE anion (HEPES), and three simulated analytes (MOPS, MES, and AlexaFluor 488). TE buffer is 200 mM Tris and 100 mM HEPES (computed pH = 8.2). LE buffer is 440 mM Tris and 220 mM HCl for $x_i \in [30\,\text{mm}, 60\,\text{mm}]$ (at $t = 0$ s) and 360 mM Tris and 180 mM HCl for $x_i \in [60\,\text{mm}, 200\,\text{mm}]$. Initial amounts of MOPS, MES, and AlexaFluor 488 are respectively 600 pmol, 600 pmol, and 100 pmol. The inset plot at $t = 1600$ s shows the detailed concentration profile of the three analytes. Two of these focus in plateau mode and a third in peak mode. This simulation was performed using 1,000 grid points.

5.2.4.2 Peak-mode simulations and comparison to experiments

For peak-mode simulations, we followed the input protocol described above to match the conditions of the experiment. To this end, we simulated a total length of 32 mm segmented into 3,000 uniform intervals. Theoretical diffusivities and absolute mobilities values of AF488 were reported in Milanova et al. [170]

Taking advantage of the expected (and observed) proportionality between ITP velocity and current, we ran each simulation for a total time inversely proportional to the imposed current to match the final spatial position of the ITP peak in every simulation. We then post-processed the JSON output file to plot the concentration profile of AF488 at each time step and obtain spatial-temporal plots comparable to the ones resulting from the experimental data. Each spatial-temporal plot in Figure 5.5B was normalized by the corresponding integrated fluorescent signal in the experimental plot (Figure 5.5A).

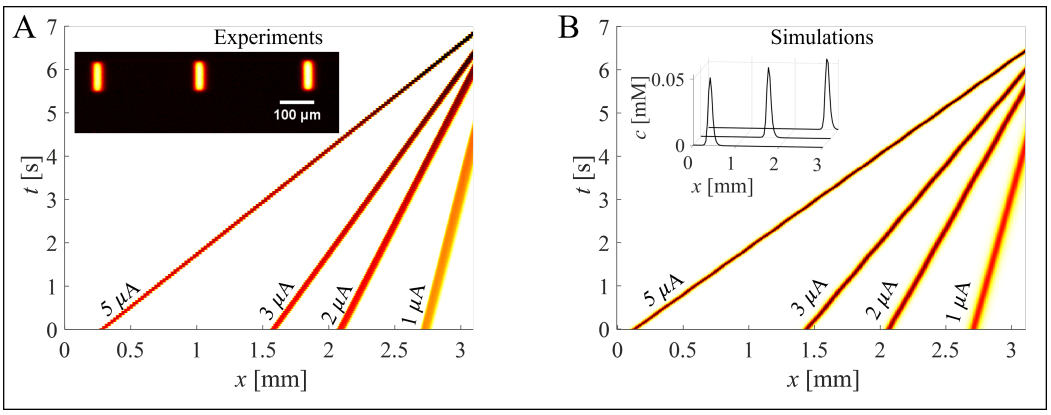

Figure 5.5: Comparison between experimental quantitative visualizations of a focused dye (A) and corresponding simulations (B) for peak-mode ITP. (A) Spatio-temporal plots of width-averaged fluorescent signal on chip. Four spatio-temporal data traces are superposed in the main plot. The inset shows three experimental images of the same ITP peak at three different times for an applied current of $I = 5$ µA. (B) Spatio-temporal plot of the focused species concentration as predicted by CAFES. Four simulated traces are superposed in the same figure. The inset shows the predicted concentration profiles at three different times for an applied current of $I = 5$ µA. The simulations well capture propagation speed, accumulation rate, and the trends in peak width, with higher currents resulting in proportionally narrower widths.

As shown by Figure 5.5, the predicted peak-mode dynamics compare well to the experimental data. The predicted velocities (corresponding to slope values in the figure) for 1, 2, 3 and 5 µA respectively match within 7, 10, 11, and 5% of the measured values. In all cases, the observed velocity was slightly higher than the prediction and this may be due to a bias error in the estimate of the channels' cross-sectional area. Further, the simulations well capture the trend in peak width, with the highest current resulting in the thinnest peak as expected. The simulations also capture the finite rate of accumulation of analyte observed in the semi-infinite ITP injection. This is most apparent in the plot for the data at 5 µA where we observe a 1.25 concentration fold-increase within the observation frame in the simulation, compared to 1.22 in the corresponding experiment. Lastly, note that the experimentally observed straight and perpendicular (to channel axis) shape of the ITP zone (see inset images in the inset of Figure 5.5A) is consistent with an experiment with very low dispersive effects (e.g., from residual electroosmotic flow or mismatched reservoir

liquid heights).

5.2.4.3 Plateau-mode simulations and comparison to experiments

We set up the plateau-mode simulations to match the experimental conditions of Figure 4 of Chambers et al. [4] The simulation domain was 50 mm long and divided into 1,500 intervals. Our simulations included all of the chemistry specifications of the Chambers experiments including AF488 dye (modeled [170] using a fully ionized mobility of 36×10^{-9} $m^2/(V{\cdot}s)$ and pK_a of -2). After performing the simulations, we used the Python post-processing tools to plot the concentration profile of AF488 using an intensity color scale similar to that of the experimental data.

Simulations and experiments are both shown and compared in Figure 5.6. The AF488 dye fluorescence intensity distribution is expected to be proportional to local electric field and consistent with simulations. In particular, the fluorescence intensity varies rapidly within each plateau-to-plateau interface, and so this intensity distribution is useful in quantifying plateau width and location. From left to right, the observable plateaus are the TE, HEPES, MOPS, and the LE. We note that the CAFES predictions of plateau widths and locations match very well with the experimental data. The relative intensities among plateaus also compare well between simulations and experiments. Note the simulation captures the observed variations in plateau width associated with the variations in initial focused amount of each species in these finite-injection ITP experiments. The differences between model predictions and the quantitative measurements of ion concentration of the various plateau regions differ by less than about 6%. We attribute this to various experimental uncertainties, including minor irreproducibility in background signals and the dependence of the dye quantum yield on ionic strength and pH. Note also that the current simulations do not include ionic strength effects. Bahga et al. [74] describe quantitative experiments and comparison with ITP models that include the effect of ionic strength on ion mobilities and on weak electrolyte (acid) dissociation constants (i.e., pK_a values). The largest discrepancy between simulations and experimental visualizations is around the significant overshoot of fluorescence intensity observed by Chambers et al. [4] near the left-edge of the LE. In the experiment, the fluorescence intensity rises sharply as you travel from left to right through the MOPS-to-LE interface (as expected) but then overshoots the expected intensity within the LE before settling down to the expected locally uniform value for the LE. This type of overshoot is commonly observed in such NFT experiments (e.g., Bahga et al. [171]). Interestingly, the physical reason for this overshoot is not well understood and currently not captured by ITP simulations. We hypothesize this overshoot may be due to trace fluorescent impurities in the system (e.g., perhaps degraded or complexed forms of the dye itself) that focus in peak-mode at the left-edge of the LE zone.

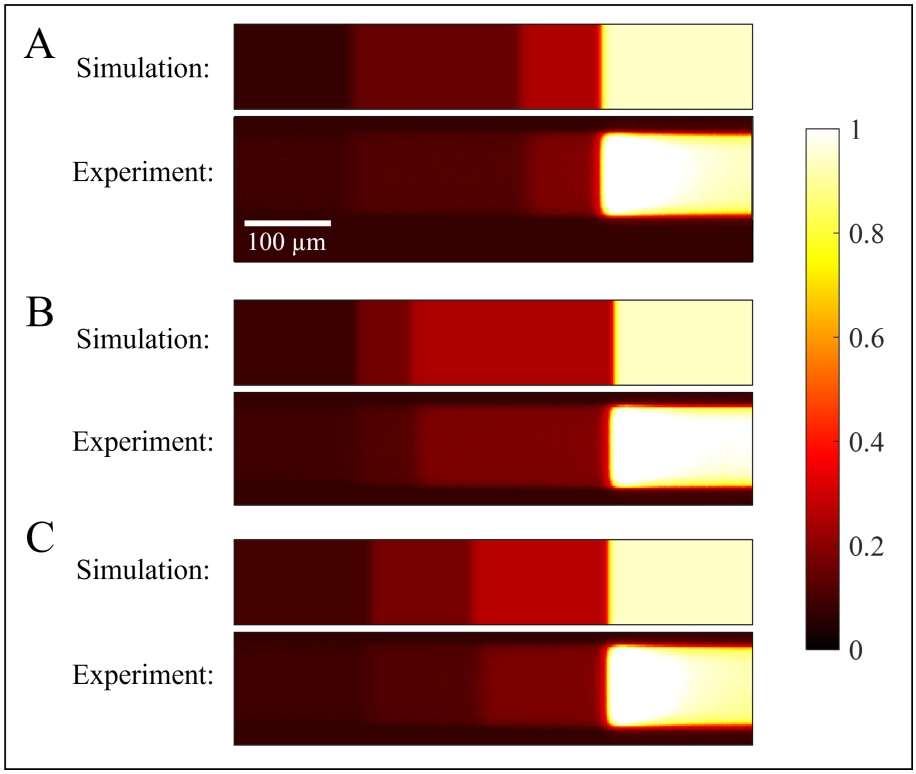

Figure 5.6: Detection of analyte plateaus with a fluorescent nonfocusing tracer (NFT) (second, fourth, and sixth images, starting from the top) and corresponding simulations (first, third, and fifth images). For each experimental condition, the top panel shows fluorescent on-chip experimental [4] signal. The plateaus correspond to, from left to right, TE, HEPES, MOPS and LE. Concentration of the HEPES and MOPS (injected as a finite sample zone) were respectively 9 and 3 mM (A), 3 and 9 mM (B), or 6 mM each (C). The bottom panels show the corresponding predictions from CAFES: the NFT concentration profile is plotted using a color scale similar to that of the experimental figure. All three simulations show good estimates of plateau lengths and relative intensities.

5.2.5 Conclusion

We demonstrated implementation and experimental validation of CAFES, a web-based simulator for nonlinear and complex electrophoresis problems, including ITP. This highly interactive tool provides quick estimations of ITP dynamics of weak electrolytes using the SLIP scheme and Dormand-Prince 45 integration and benefits from the broad compatibility of JavaScript and its operation on client-side browser software. CAFES provides a platform that can be used to design and evaluate ITP experiments including parameters such as spatio-temporal concentration fields of all species and of pH, interface velocities, and plateau

lengths. For simplicity, and to decrease the computational time, the code uses a uniform grid which captures these parameters accurately but then only very approximately captures the spatial extent of the sharp gradients associated with plateau-to-plateau interfaces. We validated the simulations using experimental data from both peak and plateau mode experiments. CAFES was able to well capture propagation velocities, accumulation rates, plateau order, plateau widths, and plateau intensities. It is currently available for free at microfluidics.stanford.edu/cafes and requires no license nor compilation.

Chapter 6

Microfluidic networks using isotachophoresis

Some of the contents of this chapter have been submitted for a journal publication by A. S. Avaro, S. Mirjalili, A. D. Griffiths, and J. G. Santiago and are reproduced here with minor modifications. Supplementary information associated with this chapter is presented in Appendix F.

6.1 Introduction

The creation and application of microfluidic networks is a storied and active field [172, 173]. As early as the 1950s, small-scale fluidic devices integrated into a planar network were proposed to mimic analog and digital circuits, including logic gates [174, 175]. This work has waned and resurged over the decades [176, 177, 178]. Aside from potential uses for computing and logic functions, fluidic networks have been developed to achieve a variety of chemical and biological analysis functions [179, 180, 181]. For example, the use of a top-layer pneumatic channel network to apply pressure to and deform a silicone (i.e., polydimethylsiloxane, PDMS) membrane and so effect valving in a lower-layer liquid network dates to work by Pharmacia in the 1980s [182]. Since the late 1990s, microfabrication techniques have been employed to create new network systems, which have employed a great variety of structures, transport phenomena, and control methods. These include the microfabrication of two-layer (pneumatic and liquid) microchannels for what is now termed Quake valves [183]; the use of laminar mixing junctions and diffusion to generate prescribed concentration gradients [184] and serial/parallel dilutions [185]; particle/structure steric interactions for routing and separation of particles (e.g., cells) into arrays of traps and/or reaction chambers [186, 187]; and, perhaps most successfully, the generation, control, splitting, merging, and routing of droplets to achieve many parallel reactions [188, 189].

In this work, we pursue and demonstrate the feasibility of a new type of electrically controlled fluidic

network based on an electrokinetic phenomenon known as isotachophoresis (ITP). ITP is a well-established electrophoretic technique which is routinely used for preconcentration, purification, separation, mixing, and reaction of ionic species in microchannels [58, 137]. ITP has been used extensively to perform automated sample preparation from complex samples like blood, urine, and lysate [17]; achieve highly selective oligonucleotide purification [61]; and accelerate both homogeneous [65] and heterogeneous [66] biochemical reactions. ITP has traditionally been applied such that each ITP zone is created and contained within a single channel (which may be in parallel with others). To our knowledge, the only two precursor demonstrations of ITP networks are the work of Persat and Santiago [190] and the work of Goet et al. [191]. Persat and Santiago [190] studied a single ITP peak being "split" at a single, one-inlet, two-outlet Y-junction. Importantly, this work derived and demonstrated a simple scaling law for the behavior of ITP peaks at such intersections: The relative amounts of sample in each of the two outlet ITP peaks are controlled by the current ratio of the two outlet peaks. They also identified the effect of electrohydrodynamic instabilities on the loss of symmetry and repeatability in the splitting. Subsequently, Goet et al. [191] introduced a method to bring two different samples into contact at the intersection of two microfluidic channels using isotachophoresis. The latter study reported an example case in which two ITP peaks arrive at different times at a single channel junction and eventually merge downstream.

We present a new type of microfluidic network using the ITP process. This includes a new, simple theoretical framework to design and analyze these networks; a network model for numerical simulations of their spatiotemporal development; and experimental observations (and model validation) of example arbitrary ITP networks. As two case examples, we demonstrate the controlled aliquoting of the contents of one ITP peak into 32 peaks in a network of (two-way) bifurcations, and the merging of 32 peaks through a network of two-way junctions into a single peak. We show that ITP networks can be well described by a spatiotemporal graph whose nodes are the junctions of the microfluidic network, reservoirs, and the ITP peaks, and whose edges are the microfluidic channel sections located between these nodes. We use fluorescently labeled DNA as a sample for our experiments, although the work is applicable to many ionic samples. We also present an example system where we control four variations of a biochemical reaction in parallel using an ITP network. ITP networks may constitute a new tool for the molecular control of samples (in this study, DNA) in microfluidic chips. The ITP network chips we demonstrate here are easy to fabricate, require no moving parts, and can be easily integrated into miniature devices.

6.2 Results

6.2.1 General ITP network theory

The inset of Figure 6.1A shows a schematic plot of conductivity (σ), concentration (c), and electric field (E) distributions in ITP. ITP uses two buffers: a high-mobility leading electrolyte (LE) buffer and a low-mobility trailing electrolyte (TE) buffer. Upon the application of an electric field, sample ions whose electrophoretic mobility is bracketed by the co-ions (i.e., ions of the same sign of charge as sample ions) of the TE and

LE selectively migrate into and concentrate at the TE-to-LE interface [58]. For trace analytes, sample ions focus into a sharp peak in so-called "peak-mode" ITP. The degree of preconcentration within this peak is determined by a balance between gradients in electrophoretic drift velocities and dispersion forces [147]. To first order, the dispersion is ruled by the molecular diffusion of the ions. The electric field drives migration of the TE-to-LE interface, hereafter called the ITP zone, in the TE-to-LE direction. Hence, the channel region(s) initially occupied by the LE co-ion are replaced by the TE co-ion. The ionic concentrations in this newly formed zone are governed by concentrations and mobilities of the LE buffer, and are independent of the initial concentrations of the TE. Hence, we term this newly formed zone the adjusted TE (ATE) zone [58].

ITP systems in general–and ITP networks especially–constitute complex, three-dimensional, and unsteady electrohydrodynamic problems [58]. We first describe a simplified network model useful in designing and analyzing channel systems used to split and mix multiple ITP peaks in arbitrary networks composed of channel sections, reservoirs, and channel junctions. The model assumes simple, one-dimensional ITP physics within each (single) channel section but considers the coupling of all ionic currents, potentials, and ITP peak dynamics. The model captures ITP peak locations and velocities, ionic currents, and node potentials, and is useful for the design of multifurcation and recombination of ITP peaks.

6.2.1.1 ITP network structure

We first describe notations, conventions, and equations for ITP networks and their evolution. We show in Figure 6.1A a typical ITP experimental setup, and Figures 6.1B and 6.1C show two example ITP networks. At all times, we describe the ITP network as a two-dimensional graph whose nodes correspond either to ITP peaks (purple vertical dashes in Figures 6.1B-C, indexed with $p \in \{1, \ldots, P\}$), geometrical vertices, or end-channel reservoirs. The geometrical vertices are K microfluidic channel junctions (open circles, indexed with k) and Γ chip reservoirs (filled circles, indexed with γ). We index the Q channel length segments bounded by these nodes ("ITP segments") by q. As shown in Figure 6.1, each segment q is bounded by a reservoir, a channel intersection, or an ITP peak. In the specific case where all channel junctions are three-way junctions (one inlet and two outlets or two inlets and one outlet) and reservoirs are connected to only one edge, the characteristics of the network satisfy $2P+3K+\Gamma = 2Q$. We provide a derivation of this equation in Section F.1. For instance, in the network shown in Figure 6.1C, $2P+3K+\Gamma = 2\cdot3+3\cdot3+3 = 18 = 2\cdot9 = 2Q$.

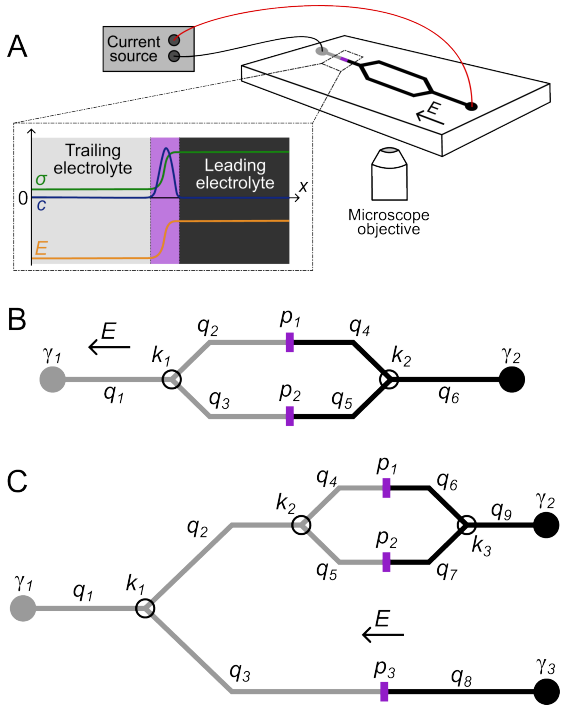

Figure 6.1: ITP networks structure and model. A ITP experimental setup schematic including microfluidic chip. Shown in inset is a schematic of the electric field E (orange), conductivity σ (green), and analyte (in this work, DNA) concentration c (blue) along the streamwise coordinate of the channel. The conductivity gradient at the interface between LE and ATE results in a self-sharpening analyte concentration peak. B-C Schematic of two ITP networks with different structures. Vertices of the network consist of reservoirs (filled circles, indexed with γ), channel intersections (open circles, indexed with k), or ITP peaks (vertical purple dashes, indexed with p). ITP segments (indexed with q) are delimited by two vertices and filled with ATE (grey), LE (black), or a mixture of both (not shown). Quantities of interest in the description of ITP networks include voltage at the nodes (V_n), local ionic current (I_q) and local conductivity in (σ_q) the ITP segments, and peak positions (x_p).

6.2.1.2 Governing equations for ITP networks

The complete description of the ITP network evolution requires the determination of the voltage V_n at each node n ($1 \leq n \leq K+\Gamma$), the current I_q through each channel segment q ($1 \leq q \leq Q$), and the position x_p and the amount of focused analyte N_p for each ITP peak p ($1 \leq p \leq P$). This amounts to $K+\Gamma+Q+2P$ unknown variables at a given ITP state. These quantities are only known at the initial state. We next describe the equations we iteratively solve to evolve the network through subsequent time steps.

For a given node n, we define Q_n as the subset of ITP segments where $q \in Q_n$ if n is a vertex of q. Then for all nodes k, Kirchhoff's current relation yields:

$$\sum_{q \in Q_k} I_q = 0. \tag{6.1}$$

Here, I_q is the algebraic current in segment q, where I_q is positive (respectively negative) if the current goes towards (respectively away from) k. Equation 6.1 constitutes K independent equations. Similarly, for a given set of ITP segments $\mathcal{L}$ that forms a closed loop in the circuit, we denote $Q_{\mathcal{L}}$ the set of ITP segments that constitute this loop. We define ΔV_q as the voltage drop in the ITP segment q. Kirchhoff's voltage relation states:

$$\sum_{q \in Q_{\mathcal{L}}} \Delta V_q = 0. \tag{6.2}$$

We assume that every ITP segment has, by construction, a constant conductivity. We denote $R_q = \frac{L_q}{\sigma_q A_q}$ the electrical resistance of segment q. Here, L_q, σ_q, and A_q are respectively the length, electrical conductivity, and cross-sectional area of ITP segment q. Neglecting diffusive currents, Ohm's law gives:

$$\Delta V_q = R_q I_q = \frac{L_q}{A_q \sigma_q} I_q. \tag{6.3}$$

For every time step, L_q and A_q are known. σ_q takes one of three values:

$$\sigma_q = \begin{cases} \sigma_{LE} \text{ if the segment is an LE segment,} \\ \sigma_{ATE} \text{ if the segment is an TE segment,} \\ \frac{1}{2}(\sigma_{LE} + \sigma_{ATE}) \text{ if the segment is between two peaks.} \end{cases} \tag{6.4}$$

Equation 6.3 applies to every ITP segment, and therefore provides Q mathematically independent equations. These estimates of σ_q, of course, assume the ITP peak width is short compared to the channel section it occupies. The estimate of $\frac{1}{2}(\sigma_{LE} + \sigma_{ATE})$ is a rough approximation we use to account for the situation where multiple ITP peaks converge into smaller number of channels and thereby converge into a smaller number of ITP peaks (e.g., two ITP peaks merging into one). Before the ITP peaks converge, there can exist some region(s) in the channel(s) which contain a mixture of LE and TE ions. This situation is often localized to a small area of the network and of short duration, and we will discuss it further in Section 6.2.4.

Next, we assume that either voltage or current is controlled at each reservoir. This implies that for any boundary (reservoir) node $\gamma \in \{1, \ldots, \Gamma\}$:

$$\sum_{q \in Q_\gamma} I_q = I_\gamma^{ref} \text{ or } V_\gamma = V_\gamma^{ref}, \tag{6.5}$$

where either I_γ^{ref} or V_γ^{ref} is known for each boundary node γ. Equation 6.5 constitutes Γ independent conditions.

Finally, we note that each ITP peak p is formulated as a node which moves with a velocity determined

by local current density, and which accumulates analyte molecules (in this work, DNA) with a local accumulation rate α. This holds at all states of the network, regardless of whether the peak progresses in a microfluidic channel, splits, or merges. Therefore, we can write $2P$ equations of state for the ITP peaks that are solved iteratively to determine x_p and N_p. We provide these equations in Section F.1.

The equations detailed in this section form a set of $K+Q+\Gamma+2P$ mathematically independent equations. We assume the initial state of the ITP network is known and iterate to solve for future states.

6.2.1.3 Self-stability of parallel peak progression

We analyzed and performed experiments on a variety of fairly complex networks composed of successive generations of bifurcations and pair-wise junctions of channels. We observed that there is an inherent stability to ITP peaks traveling in similar, parallel channels, and we describe the nature of this stability here.

Consider the case wherein two peaks p_1 and p_2 travel in two parallel channels that share a common inlet and outlet (e.g., peaks p_1 and p_2 in Figure 6.1B). We denote η and λ as the channel cross-sectional area and length ratios, respectively. We also define the following conductivity ratio $\sigma' = \frac{\sigma_{ATE}-\sigma_{LE}}{\sigma_{LE}}$. The latter is necessarily less than zero since we consider only the very common ITP case that $\sigma_{ATE} < \sigma_{LE}$. We denote $\xi_i = \frac{x_i}{L_i}$ the position of peak p_i normalized by the channel length. The velocity of each ITP peak u_i in channel i can be expressed in terms of the local electric field in the LE $E_{LE,\,i}$ and the leading electrolyte effective mobility μ_{LE} as $u_i = \mu_{LE}E_{LE,i}$. This yields the following result:

$$\frac{\Delta u}{u_{th}} = (1+\eta)\left[\frac{\frac{\chi}{\lambda}-1}{\frac{\eta\chi}{\lambda}+1}\right], \tag{6.6}$$

where Δu is the difference in ITP peak velocity. I is the total current passing through both microfluidic channels, $\chi = \frac{\xi_1\sigma'+1}{\xi_2\sigma'+1}$, and u_{th} is the ITP velocity:

$$u_{th} = \frac{\mu_{LE}}{\sigma_{LE}}\frac{I}{(A_1+A_2)}. \tag{6.7}$$

We present the full derivation of this result in Section F.2.

An important result that stems from Equation 6.6 is the special case where channel lengths and cross-sectional areas are equal, so that $\eta = \lambda = 1$. In this case, the sign of the velocity difference is opposite to that of the position difference. That is, $\frac{\Delta u}{\Delta x} < 0$. This means that, in this configuration, if one of the peaks lags behind, it will thereafter travel faster than the leading peak until it catches up.

This stable situation can be explained as follows. The two channels behave like two variable-resistance resistors in parallel. Since $\sigma_{ATE} < \sigma_{LE}$, each channel's resistance depends on the position of its ITP peak. The channel with a lagging peak has a larger length occupied by LE and therefore lower resistance. This channel demands more current than the other, parallel channel. This increases the ITP velocity of the lagging peak relative to that of the leading peak.

6.2.2 Iterative solver for ITP networks

We developed in MATLAB an iterative solver to simulate the dynamic evolution of ITP networks, given an arbitrary network geometry and initial conditions. Each channel in the network is represented as a separate MATLAB object whose properties include geometric parameters (e.g., length, cross-sectional area, inlet and outlet nodes), physicochemical properties (electrolyte conductivities and species effective mobilities), and ITP peak information (e.g., number and position of the peaks). Electrolyte physicochemical properties were estimated using the online tool BEAN-ITP [136]. Within the network, channels are connected if an outlet node of one channel coincides with an inlet node of the other channel. General simulation variables also include the value of the current flowing through the entire ITP network and initial ITP peak(s) position(s). The source code for the solver is provided in github.com/alexandre-avaro/itp-networks.

The solver uses the explicit Euler time-advancement method with a constant time step. At each time step, given the state of the network (i.e., the position of the ITP peaks), the solver computes the electrical resistance of each ITP segment (as defined in Section 6.2.1) and determines the voltage at every node and the current through each channel. Positions of ITP peaks are then updated using values of the local current and ITP velocity. If an ITP peak reaches an outlet node, the ITP peak divides into and among all connected channels. The fraction of analyte distributed into the inlet of each channel is determined by the fraction of the current carried by each channel (following the experimental study and analysis of Persat and Santiago [190]). If an ITP peak propagates into a channel that already contains another peak, it generates a new ITP segment (between the two ITP peaks) with conductivity $\frac{1}{2}(\sigma_{LE} + \sigma_{ATE})$, as described in equation 6.4. If a peak overtakes another (within the same channel), the two peaks merge, resulting in a unique ITP interface that separates an ATE zone and an LE zone. Peaks are no longer tracked after they reach an LE reservoir node, and the simulation ends when all peaks have reached LE reservoir nodes.

The results of these simulations will be shown, discussed, and compared with experiments when we present Figures 6.2 and 6.3 (see "Model" panels).

6.2.3 Experimental imaging of ITP networks

6.2.3.1 Multifurcation of an ITP peak

We performed an experimental study of ITP multifurcation system dynamics in custom-fabricated chips with a variety of geometries. We also used these data to experimentally validate the network model. We show experimental results for an example fluidic network in Figure 6.2. In this microfluidic chip, we show the progression of ITP peaks in a multifurcation tree that consists of five successive binary, symmetric bifurcations, which eventually results in $2^5 = 32$ parallel ITP peaks. We show the full structure of the ITP network used in this validation and our experimental setup in Figure F.2. To track the position (and creation and destruction) of ITP peaks, we added a Cy5-labeled 21-mer ssDNA analyte in the TE. This dye migrates into the ATE and accumulates at ATE/LE interfaces (19). Short DNA molecules typically have an electrophoretic mobility in free solution of about -3×10^{-8} m^2/(V·s) [58, 192].

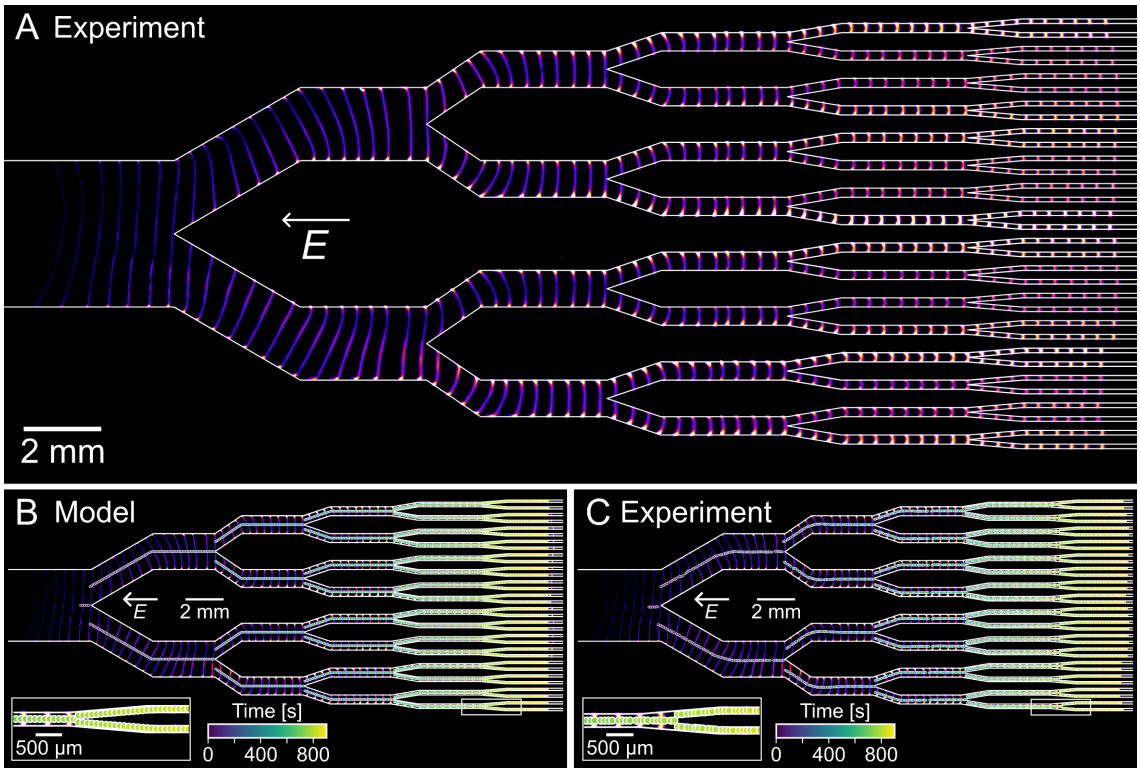

Figure 6.2: A Composite of experimental fluorescence images showing the progression of ITP peaks in a 1-to-32 multifurcation tree network. Shown are summed fluorescence images of the peaks taken every ~15 s. The composite image results from the stitching of 65 fluorescence images corresponding to three camera positions. B Corresponding predictions using the network model. Shown are predicted positions of the ITP peaks along the streamwise position of the microfluidic channel. The inset shows a zoomed-in detail in the fifth-generation bifurcation. C Measurements of ITP peak trajectories. Shown are ITP peak centers identified from image data taken every 3 s. Positions of the centroids account for movement of the sample stage (relative to camera) using a position sensor in the microscope stage. The inset shows the same region in the fifth-generation bifurcation as in B.

The image shown in Figure 6.2A is a composite of 65 fluorescence microscopy images of the ITP peaks in the same channel network and same experiment at varying times. Individual fluorescence images were taken every ~10 s and summed to yield the composite image. Because the field of view of the camera is smaller than the entire area of interest, the sample stage was moved during image acquisition to track ITP peaks. We therefore developed a method to register and stitch together images taken at different places and times (see Section 6.4 for further details). We highlight channel edges using white solid curves.

In Figure 6.2A, ITP peaks migrate in the direction opposite that of the electric field (i.e., they migrate left to right). The network was designed such that we conserve the total channel cross-sectional area after

each bifurcation. Hence, parallel channels within each generation of successive peaks have the same total channel area. Further, we applied constant current through the microfluidic chip. Hence, as per equations 6.1 and 6.3, this implies that the current density in all channel sections should be equal to each other and constant. This also implies uniform ITP peak velocities for all channel sections. This design feature and model aspects are validated by the observed dynamics. For example, the equal spacing between consecutive peaks for all ITP peaks in Figure 6.2A shows that peaks travel throughout the network at approximately uniform velocities. We show in Figure F.5 measurements of peak velocities throughout the chip. Further evidence of the uniformity of current density is the approximately equal ranges of intensity and width of each ITP peak. The latter quantities are inversely proportional to the local electric field.

Note that each channel bifurcation is designed with top/down symmetry with a "splitting wedge" positioned at the center of the spanwise direction. This symmetric bifurcation was incorporated to account for a well-known and common phenomenon in ITP experiments: analytes in ITP peaks tend to accumulate locally near the edges of the channel [147]. This local accumulation is visible for most of the ITP peaks, particularly in the larger channels of Figure 6.2A. We also performed experiments in multifurcation networks that do not satisfy this symmetric bifurcation design rule, and present example results in Section F.4. Such geometries exhibit severe channel-to-channel variations in peak intensities and integrated intensities, as well as asymmetric peak shapes.

Finally, we observe that parallel peaks initially progress at the same velocity with approximately equal positions in parallel channels. However, this synchronicity is progressively lost through increasingly greater channel bifurcations. Nevertheless, we estimate the variation in peak velocities to be smaller than about 10% (Figure F.5). We attribute this to variations in the cross-sectional area of the microfluidic chip generated by the chip fabrication process [193]. Such geometrical variation is expected, particularly among the small channels of the network. We show and further discuss this phenomenon in Section F.6.

Next, we compare our experimental observations with simulations using the network model described in Section 6.2.2. Figure 6.2B shows the predicted trajectory of the ITP peaks using our computational solver. Shown are positions and associated times of the simulated ITP peaks along the streamwise direction, where predicted time is indicated with a color scale. The network model yields ITP peak locations as a function of time along the streamwise dimension within each simulated channel section. These position (and time) values are plotted here on top of the composite image (Figure 6.2A) for ease of comparison with the experimental data. In Figure 6.2C, we again show the composite image but now superpose measured positions of the centroid of ITP peaks from the experimental image data (see Section 6.4 for the detailed protocol of the ITP peak center calculations). Figures 6.2B and 6.2C include as an inset a zoomed-in detail of the dynamics of fifth bifurcation. In Section F.8 (Figure F.12), we also present a comparison between experimental measurements of peak positions and peak velocities and the corresponding model predictions.

The comparison of Figure 6.2B and 6.2C shows that the dynamics of ITP progression in this network is well characterized by our simple model. There is excellent agreement in the number of ITP peaks created; the path that these peaks take as they migrate through and multiply at bifurcations; and the velocity of ITP

peaks in each channel section. Comparisons of Figures 6.2B and 6.2C show only approximate agreement on the temporal position of ITP peaks. However, the model-to-experiment differences in ITP positions are attributable to the ~10% variations of ITP velocities, particularly within the smallest channels in the network which we attribute to slight geometrical variations (see discussion above).

6.2.3.2 Successive merges of ITP peaks

The data presented in the previous section was obtained in approximately the left half of a microfluidic network chip. On the right side, this network also features a series of two-to-one channel junctions where ITP peaks merge. We next explore the dynamics of ITP peaks in the latter portion of the network which comprises five successive merges starting from 32 parallel channels. As before, the network merging dynamics of the ITP peaks are tracked using a fluorescently-labeled ssDNA as an example analyte.

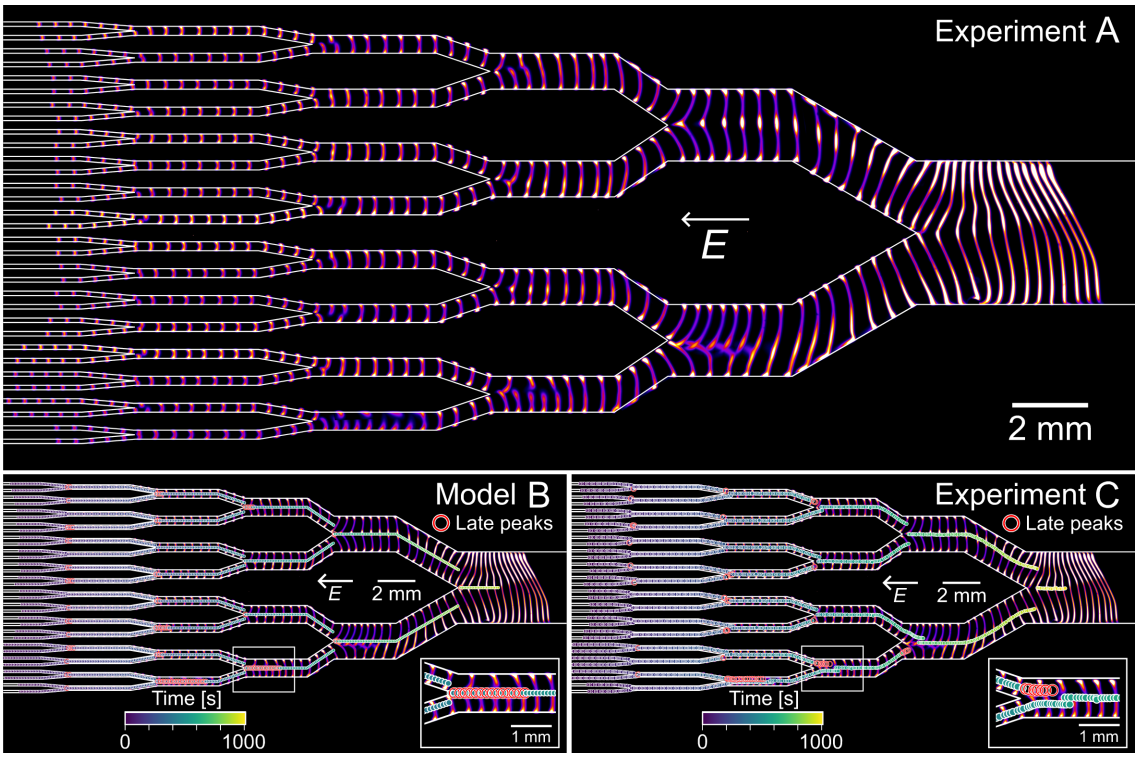

Figure 6.3: A Composite of experimental fluorescence images showing the progression of ITP peaks in a 32-to-1 multifurcation tree network. Shown are summed fluorescence images of the peaks taken every ~15 s. The composite image results from the stitching of 67 fluorescence images corresponding to four camera positions. B Corresponding predictions using the network model. Shown are predicted positions of the ITP peaks along the streamwise position of the microfluidic channel. The inset shows a zoomed-in detail of a merging within the third-generation. C Measurements of ITP peak trajectories. Shown are ITP peak centers identified from fluorescence images taken every 3 s. Positions of the centroids account for movement of the sample stage (relative to the camera) using a position sensor in the microscope stage. The inset shows the same region in the third-generation bifurcation as in B.

Figure 6.3A shows a composite of 67 fluorescence images similar to Figure 6.2A, but for this new section of the network. Once again, images were stitched together using the sample stage position data. We again highlight channel edges in Figure 6.3A using white solid curves.

The ITP peaks of Figure 6.3A travel left to right (the direction opposite that of the electric field) and we again applied a constant current through the channel network. The channels were designed so that the total cross-sectional area after each merge is conserved. Similar to Figure 6.2A, this implies that the current density is uniform (and constant) in all channel sections. Once again, this results in the observed equal spacing between consecutive peaks, and approximately equal width and range of intensity of the peaks.

At each merge, two peaks which arrive at the same time at a channel junction combine into a single,

larger ITP peak. The initial 32 peaks sequentially merge into 16, 8, 4, 2, and eventually one peak. The content of all the 32 ITP peaks is therefore eventually mixed and co-focused in a single ITP region whose volume is roughly 50 nl.

Next, we compare the experimental observations with our model results. Figure 6.3B shows model predictions using the observed (non-uniform) initial peak position of the experimental data as the initial condition. Similar to Figure 6.2B, shown are predicted positions (circles) of the space-time trajectories of the ITP peaks using our iterative solver overlaid on the composite image from Figure 6.3A. In Figure 6.3B, predictions for channel sections containing a single ITP peak are shown with closed symbols. In sections briefly containing two ITP peaks, we indicate the lead (early) and trailing (late) ITP peaks in closed and open symbols, respectively. For comparison, Figure 6.3C shows corresponding measured positions of the ITP peaks centroids from the experimental image data (using the same color scheme).

Figure 6.3A also highlights various non-uniformities and non-ideal behaviors not captured by the model. One is the non-uniformity of ITP peak intensities, even for channels within the same generation (i.e., channel sections of the same size). We attribute this primarily to the effect of the two- and three-dimensional shapes and non-uniform distributions of the ITP peaks along the spanwise direction (i.e., within the imaged plane but perpendicular to the local electric field). For example, solutes within a single ITP peak often exhibit increased concentrations at one or both walls (relative to the concentration near the spanwise middle). This wall accumulation is a well-known phenomenon of ITP peaks [147]. If the accumulation is biased toward the bottom wall, then the ITP peaks of channels benefiting from this bottom half will be brighter. See for example the non-uniform distribution of DNA in the ITP peaks of the eight parallel channels (4^{th} generation). In particular, note the non-uniformity of the ITP peak in the fourth (from the top) channel of the following generation. It is bright near the bottom wall, and this results in non-uniform intensities for subsequent daughter channels.

A second non-ideal behavior observed in experiments is the slight differences in the axial positions across the channels. After traversing the bifurcation portion of the network, 32 ITP peaks enter this part of the network. These 32 ITP peaks have varying initial positions along their respective channels. In some cases, this results in a significant time delay between the arrival of one of the two peaks at the two-channel junctions. In other words, an "early" peak arrives at the junction before a second "late" peak. After the late peak reaches the junction, the two peaks travel one ahead of the other in the same microfluidic segment. Recall from our model discussion, that such ITP peak pairs are each modeled as moving nodes in the circuit. Interestingly, across all junctions and experiments, we observe that the late peak travels faster than the early peak until the former catches up with the latter and the peaks merge. We will show the dynamics of this "catch-up" merge further in the next section.

Overall, the simple network model developed above yields a reasonable estimate of ITP peak number, position, and progression through the network. We observe a good agreement between our model predictions and the experimental observations in both the number of peaks progressing in the ITP network and the trajectory that these peaks follow. Moreover, we observe that our simple model captures the "catch-up"

events that we observe experimentally.

6.2.4 Dynamics of merging ITP peaks

We now discuss the dynamics of the merging of ITP peaks at an intersection of two microfluidic channels. Figure 6.4A shows six example composite images corresponding to merges of ITP peaks at different generations, using the network geometry of Figure 6.3A. Panels (a), (c), and (e) show asynchronous merging (i.e., staggered arrival of the two merging peaks), while panels (b), (d), and (f) show synchronous merging (i.e., simultaneous arrival). In all cases, the merge of the two incoming peaks results in a single peak. In the synchronous case, the two peaks reach the microfluidic junction together and merge immediately. The newly formed single peak then progresses at a constant velocity in the larger channel. Conversely, in the asynchronous case, the late peak (top peak in (a), bottom peak in (c) and (e)) rapidly catches up with the leading peak until the two peaks merge.

We show in panels (i) to (vi) of Figure 6.4B images corresponding to six instances of a more extremely asynchronous merge. In (i), we observe the two peaks traveling in parallel, and the bottom ITP peak is an early peak. The top peak initially lags by about seven channel widths. In (ii), the bottom (early) peak reaches the junction and enters the larger channel, while the top peak continues to migrate within the top channel. Both peaks maintain an approximately constant velocity and progress in their respective channels (iii) until the top peak reaches the junction (iv). Hereafter, the two peaks occupy the same (larger) channel, one peak traveling ahead of the other. The late peak travels faster than the early peak, decreasing the distance between them (v). This "catch-up" event ends when the late peak merges with the early peak, resulting in a single ITP peak (vi). We show in Figure F.8 measured peak velocities for both peaks throughout these merging dynamics.

Figure 6.4C shows the simulated peak evolution corresponding to Figure 6.4B. Shown are ITP segment evolution and peak positions predicted by our model (see Section 6.2.2). Panels (i) to (vi) match the corresponding panels in Figure 6.4B, and we show with a dashed black box in Figure 6.4C the field of view of the corresponding panel in Figure 6.4B. We show in grey and black the regions of the channel respectively occupied by ATE and LE according to our solution. As discussed earlier, for simplicity, the region between the peaks is modeled with a conductivity of $\frac{1}{2}(\sigma_{LE} + \sigma_{ATE})$ (see equation 6.4). This simple assumption is sufficient to capture the qualitative features of the merging event (late peak catching and merging with the early peak). The latter merge is consistent with the experimental observations shown in Figure 6.4B.

We note that the simple one-dimensional model that we developed here generally captures the catch-up phenomenon that we observe experimentally. However, we emphasize that any ITP merge (synchronous or not) involves highly three-dimensional electrohydrodynamic effects which are not included in our model. A more complete description of this system would likely require solving a system of stiff, nonlinear, and coupled partial differential equations [58]. Such solutions are complex and computationally expensive and we know of no such published models. Despite these complexities, the good agreement between our experimental observations and the network model (in Figures 6.2, 6.3, and 6.4) suggests that our simple network

model is useful and provides a good trade-off among model complexity, computing power, accuracy, and model utility.

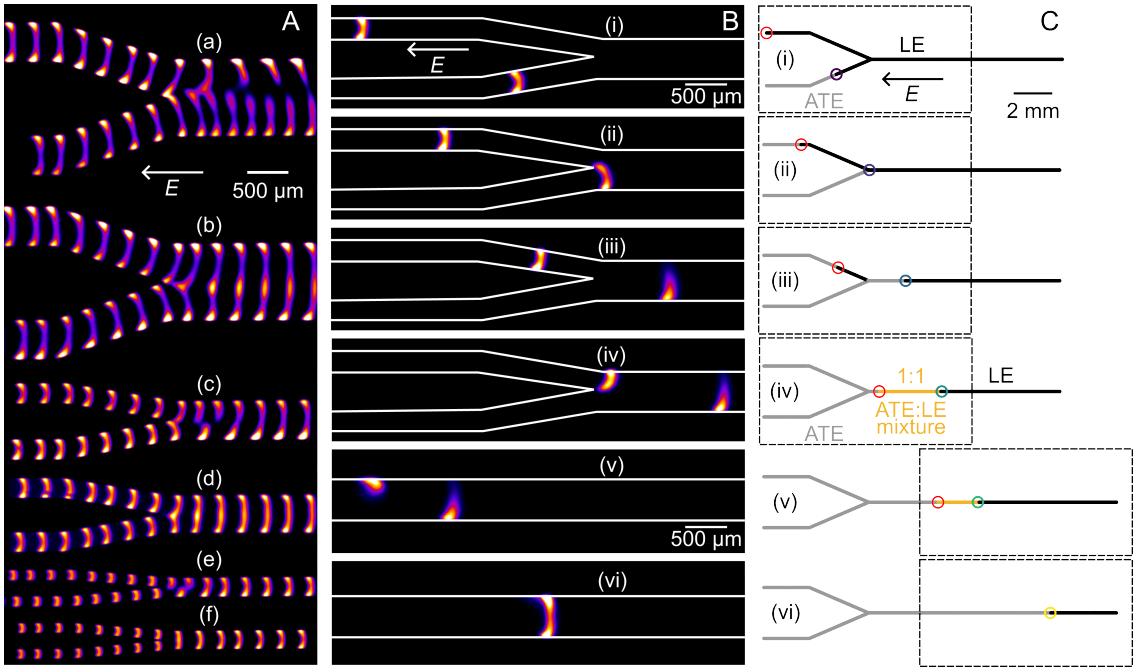

Figure 6.4: ITP peak merge dynamics. A Composite of experimental fluorescence images showing the progression and merging of ITP peaks in three varying channels, for asynchronous ((a), (c), (e)) or synchronous ((b), (d), (f)) merges of ITP peaks. Shown are summed fluorescence images of the peaks taken every ~10 s. B Experimental fluorescence images of a single peak merge. Shown are six step-by-step images of the merge of two peaks which arrived at staggered times at the microchannel junction. C Corresponding simulation results. Panels (i) to (vi) correspond to the matching panels in panel B. Shown are peak positions (open circles) and buffer composition of the ITP segments (grey: ATE, black: LE, orange: ATE/LE mixture). The dashed black box indicates the field of view of the corresponding images in panel B.

6.2.5 Parallelized CRISPR reactions using ITP multifurcation

In this section, we present an example demonstration of multifurcation of ITP to automate aliquoting, control, and quantification of parallel enzyme reactions. CRISPR-based methods enable detection of nucleic acids with high specificity [6, 102, 1]. They rely on two sequential reactions called *cis*- and *trans*-cleavage. In *cis*-cleavage, a ribonucleoprotein (RNP), which is constituted from a CRISPR-associated (CRISPR-Cas) enzyme and a guide RNA (gRNA), specifically cleaves a target nucleic acid (e.g., DNA for Cas12). Subsequently, in the *trans*-cleavage step, the RNP is activated and cleaves single-stranded nucleic acids indiscriminately [31, 30]. Typically, fluorophore-quencher reporter molecules whose quantum yield increases upon cleavage

are introduced to monitor *trans*-cleavage activity [12]. Ramachandran et al. [17] demonstrated an ITP-based CRISPR assay in a single, straight channel to carry out one CRISPR reaction at a time. In most assay applications of CRISPR, *trans*-cleavage is the rate limiting step and is therefore an important limit on sensitivity [2, 98].

We here use an ITP multifurcation tree to quantify reaction rates in four parallel processes. Figure 6.5A shows a schematic of the chip and initial setup. We use a 1-to-2-to-4 multifurcation tree to create four aliquots of fluorophore-quencher reporters from a single input TE buffer reservoir. The configuration uses a reservoir in each of four parallel channels to pre-load four concentrations of activated RNPs mixed with LE buffer. Once ITP is initiated, as shown in Figure 6.5B, reporter molecules focus in peak-mode ITP and are aliquoted in the four channels. ITP then co-focuses enzyme with the reporters to mix and initiate *trans*-cleavage reactions. As peaks progress through the network, reporters continue to accumulate in the peaks and RNPs cleave additional reporters, as shown in Figure 6.5C. Note that RNPs, uncleaved reporters, and cleaved reporters are simultaneously concentrated within the ITP peaks. Focusing of cleaved reporters facilitates detection.

Figures 6.5D-G show experimental spatiotemporal plots corresponding to peaks migrating in the four channels, and an associated four initial activated RNP concentrations (including one control with zero RNP concentration). In these spatiotemporal plots, one row of pixels corresponds to the spanwise-integrated fluorescence signal at a given time step. Each column corresponds to the time evolution of this integrated intensity with a data rate of 1 frame per second. The streaks represent the trajectories of the ITP peak, from left to right. The constant slope of the streaks over time and channels indicates that all peaks travel at the same, constant velocity (50 μm/s). The integrated intensity of the peaks provides a quantification of the number of cleaved and uncleaved reporters focused within each ITP peak. The intensity of the peaks increases with the simultaneous processes of reagent accumulation and *trans*-cleavage enzymatic activity. Figure 6.5H shows example composite images of the ITP peaks taken every 15 s for both the 10 nM target and the NTC channels. Consistent with Figures 6.5D and 6.5G, the fluorescence intensity is higher in the presence of activated RNPs. The signal of the no-template control (NTC) channel is significant as (accumulating) uncleaved reporters have finite fluorescence signal and reporters exhibit a finite rate of degradation. The latter effects are crucial in the determination of limits of detection and clearly demonstrated by this experiment.

Figure 6.5I shows the evolution of the integrated fluorescence in a box of 60 by 175 pixels moving with the ITP peaks for the four activated RNP concentrations (including NTC). The rates of increase in signal grow with the concentration of activated RNP concentration, demonstrating *trans*-cleavage enzymatic reaction activity.

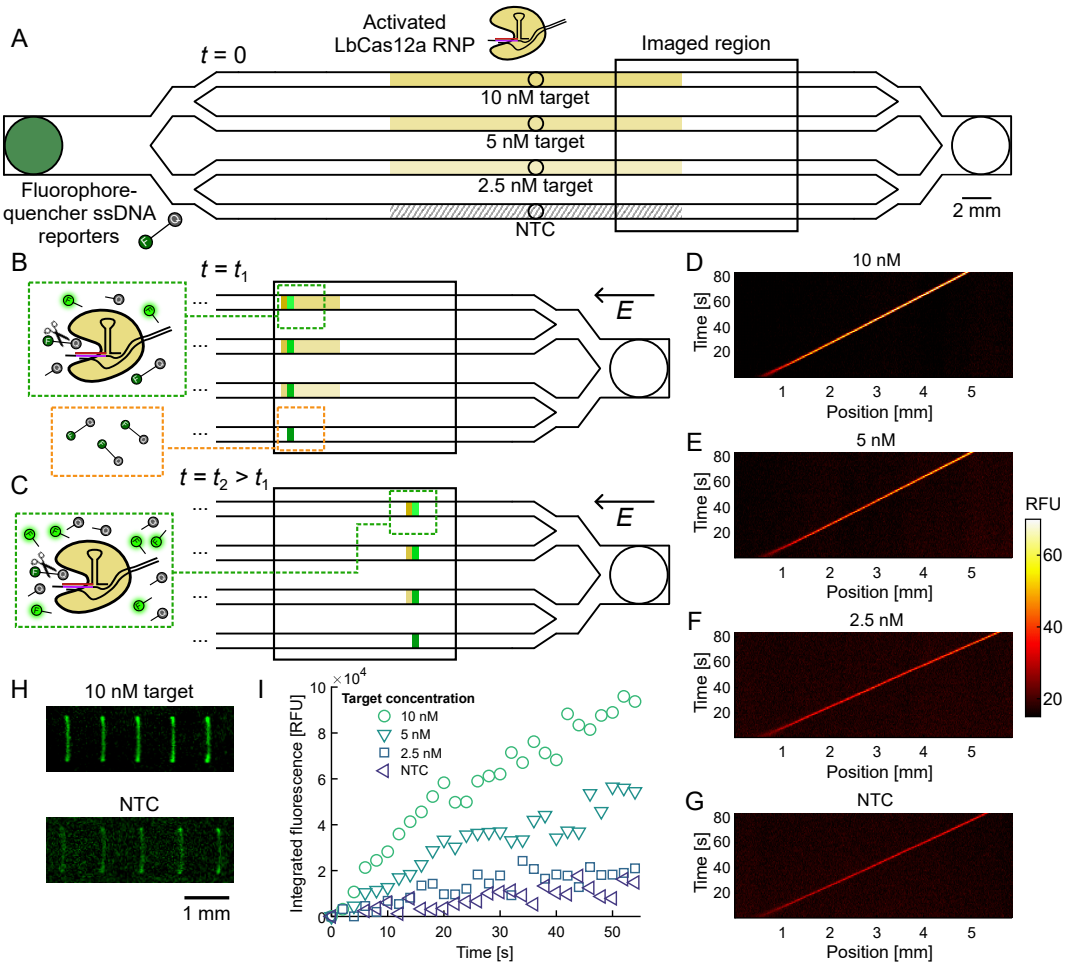

Figure 6.5: Parallelized CRISPR reactions using ITP multifurcation. A Chip design and initial loading. Fluorophore-quencher probes are dispensed into a single TE reservoir. Activated RNPs of varying initial concentrations are dispensed into reservoirs in four parallel channels. B-C Working principle: The ITP network aliquots reporters, mixes aliquots with activated RNPs, and initiates *trans*-cleavage. Reporters and RNPs co-focus at the LE-to-TE interface. RNPs cleave reporters, resulting in increased fluorescence signal. D-G Spatiotemporal intensity plots for each of the four different channels. H Composite of experimental fluorescence images showing the progression of the peak in the 10 nM and NTC channels. Shown are summed fluorescence images of the peaks taken every ~15 s. Images were binned 4 by 4 pixels. I Integrated fluorescence in a box of 60 by 175 pixels moving with the ITP peaks versus time, for each of the four channels.

6.3 Discussion

We introduced a new class of microfluidic networks that leverage ITP to selectively preconcentrate, aliquot, mix, and initiate reactions on-chip. We presented a theoretical framework, a numerical solver, and example demonstration experiments to characterize such networks. The example networks demonstrated 32 aliquots from one sample, and the merging of 32 ITP regions into one. We show in Section F.4 several other example network configurations consisting of asymmetric multifurcation and merge events.

The framework that we developed in Section 6.2.2 uses known one-dimensional, transient descriptions of ITP, which we generalized to a multidimensional graph to describe the time-evolution of ITP peaks progressing in branched networks. We developed numerical simulations of the progression of ITP peaks based on this framework. Our simple model and simulations show good agreement with our experimental observations. This engineering model is sufficient to the design, control, and prediction of network behavior, and represents a good trade-off between utility and fidelity of the computation. For example, a more comprehensive, quantitative description of ITP dynamics would require complex, computationally expensive three-dimensional, unsteady electrohydrodynamic simulations coupled with weak-electrolyte chemical equilibria [58].

The current model, fabrication techniques, and methods are applicable to fairly arbitrary ITP network geometries in one, two, or three dimensions. We here use SU-8 wafers and 3D-printed molds for fabrication, but ITP network devices can be manufactured using a variety of microfabrication methods. The equipment needed is typical of electrophoresis experiments including a power source and inert Faradaic electrodes. The system requires no moving parts to separate, preconcentrate, aliquot, mix, and initiate reactions and is easily compatible with a photonic readout. ITP-based devices, and therefore ITP networks, are self-stable and robust to small pressure perturbations [58]. The main design constraints imposed by ITP networks lie in the repeatable fabrication of microchannels of order 100 μm (or less) and an appropriate choice of buffers for a given chosen application [145]. There is a variety of ITP simulation tools available to select and optimize buffer chemistries and tailor them to a specific application [136, 145, 71, 73, 72].

ITP networks may offer unique functionalities to microfluidics including potential for sample extraction (e.g., from raw biological sample), purification, pre-concentration, aliquoting, serial dilutions, acceleration of biochemical reactions (including enzymatic reactions), mixing, incubation, and readout on a single chip. They also open the possibility to run parallel assays simultaneously and on the same chip. The process is compatible with a wide range of materials, length-scales, and configurations in fairly easy to fabricate systems with no moving parts [58].

6.4 Materials and methods

6.4.1 DNA and buffers

For all ITP visualization experiments, we used a 21-mer synthetic DNA oligonucleotide as focused analyte. The 5' terminus of the analyte was labeled with Cy5 to track the peak position at all times: 5'-/5Cy5/ATG CGA GTC ATA GCG CTA TTA-3'. For ITP-CRISPR experiments, we report the oligonucleotides used in this work in Section F.9. LbCas12a (a Cas12 ortholog from *Lachnospiraceae bacterium ND2006*) and NEBuffer r2.1 were purchased from New England Biolabs (MA, USA). NEBuffer r2.1 is composed of 50 mM NaCl, 10 mM Tris-HCl, 10 mM MgCl2, and 100 µg/ml recombinant albumin (pH 7.9 at 25°C). Reporter molecules were purchased from Eurofins Genomics (France) and resuspended at 100 µM. All other oligonucleotides were purchased from Integrated DNA Technologies (IDT). A 100 µM stock solution of the analyte in nuclease-free water (NFW) was aliquoted and stored at -20°C. For ITP visualization experiments, we mixed 200 nM analyte in the TE, composed of 100 mM HEPES, 500 mM Tris, and 0.1% polyvinylpyrrolidone (PVP). The LE consisted of 125 mM HCl, 500 mM Tris, and 0.1% PVP. PVP was included to suppress electroosmotic flow (EOF). For ITP-CRISPR experiments, the TE was composed of 100 mM HEPES, 200 mM Tris, and 0.5% PVP. The LE was composed of 100 mM HCl, 200 mM Tris, 0.5% PVP, and 10 mM $MgCl_2$. The agarose-LE solution (AgLE) consisted of 2% low-melting temperature agarose by weight in LE. Tris, HEPES, HCl, low-melting agarose, and PVP were obtained from Sigma-Aldrich.

6.4.2 PDMS chip fabrication

Prior to chip fabrication, LE and TE composition, channel geometry, and electric current values were tuned using CAFES [145]. We followed a fairly standard protocol for the microfabrication of a master mold on a silicon wafer for all symmetric bifurcation designs. We show in Figure F.2 the mask geometries, resulting microfluidic channels, and experimental setup. Briefly, wafers were dried at 200°C for 5 min. SU-8 photoresist was spin-coated on the wafer up to 100 µm, and soft baked at 65°C and 90°C, according to manufacturer's instructions. UV exposure was performed using the MA/BA6 mask aligner. Wafers were further baked at 65°C and 90°C again, and rinsed successively with propylene glycol methyl ether acetate (PGMEA) and isopropanol (IPA). Quality control of the wafer was performed using a mechanical profilometer. The wafer was finally hard baked at 200°C for 5 min. We provide in Figure F.11 optical profilometry measurements of the wafer (Keyence VK3030).

Asymmetric bifurcation molds were 3D printed using an Elegoo Mars 3 3D printer, and Elegoo photopolymer resin (Elegoo, Shenzhen, China). Once printed, the mold was cleaned in two successive IPA baths, and further cured under a UV lamp for 10 min. The mold was then baked at 70°C for 48 h. This step prevents residues of the photopolymer resin to inhibit the crosslinking of PDMS.

In both cases, PDMS chips were then fabricated using standard soft lithography methods. Sylgard 184 PDMS (Dow Corning, Midland, MI) was cast on the molds in a 10:1 ratio of base to crosslinker. PDMS was cured at 70°C for 4 h. We then peeled the cured PDMS from the wafer and punched 4 mm diameter holes

for the cathode and anode reservoirs. Finally, PDMS was plasma-bonded with a glass slide to create the microfluidic channels.

6.4.3 DNA focusing and ITP process control and imaging

For ITP visualization experiments, microfluidic channels were initially entirely filled with LE solution. Reservoirs were then emptied using a vacuum line. The anode reservoir was then filled with heated liquid AgLE solution. After gelation of the AgLE solution, the cathode reservoir was emptied, rinsed with TE, and subsequently filled with TE and analyte solution. The agarose was employed to minimize disturbances due to pressure-driven flow in the channel (e.g., due to unequal heights of reagents in reservoirs) [194]. Platinum electrodes were inserted in the reservoirs. ITP was then performed by supplying a constant current of 200 μA using a Keithley 2410 high-voltage sourcemeter. Voltage and current were monitored and controlled in real-time using a custom MATLAB code.

The ITP peak was monitored and imaged using an epifluorescence microscope (Nikon Eclipse Ti2-E) equipped with a 1× magnification objective (Plan UW, NA: 0.04) and a CMOS camera (Hamamatsu Orca-Flash 4.0). The microscope was equipped with a motorized stage (TI2-S-JS, Nikon) controlled with a joystick. The joystick was used to follow ITP peaks throughout the network during imaging. This stage includes a sensor which can provide real-time data of the current position of the stage. We used the software NIR-Elements AR to extract the stage positions versus time and synchronize this with camera image data. Images were acquired once per second with an exposure time of 200 ms.

6.4.4 Peak visualization and tracking

The field of view of each image obtained was 13.3 mm by 13.3 mm. This area is much smaller than the area of each network studied. For example, the networks shown in Figures 6.2 and 6.3 occupy an area of 29.3 mm by 11.4 mm. Hence, to capture the complex network dynamics, we created composite images by using images taken at multiple locations and at multiple times during a single experiment to visualize ITP dynamics throughout the entire network. To stitch together images taken at different locations, we used the aforementioned image and stage position data. We also summed images across time intervals of 10 s to show multiple positions for each ITP peak as it traveled through the network. The resulting composites across space and time are shown in Figures 6.2, 6.3, and 6.4A. For example, for Figure 6.2, we registered and stitched together over 65 images taken in a single ITP network experiment. These images cover 673 locations of ITP peaks and 3 positions of the motorized stage to show the development of the ITP peaks. Since all time intervals are uniform, the spacing between ITP peak images is indicative of local velocity in the network. The composite images also capture the creation of new ITP peaks at bifurcations in the network. Similarly, in Figure 6.3, the composite image captures many successive convergences of ITP peaks through the network.

6.4.5 Parallel CRISPR reactions

For ITP-CRISPR experiments, we first prepared a solution of 1 μM ribonucleoprotein (RNP) by incubating 1 μM synthetic gRNA and Cas12a at 37°C for 30 min. A solution of 200 nM dsDNA target was obtained by hybridization of ssDNA target strand and the corresponding reverse-complementary strand. RNPs were further activated with varying concentrations of dsDNA target (100, 50, and 25 nM) at 37°C for 30 min. Activated RNPs were then diluted 10-fold in LE buffer. In the control solution, activated RNPs were replaced by NFW. Reporter molecules were diluted to 300 nM in TE.

Microfluidic channels were first entirely filled with LE solution. The anode reservoirs was then emptied using a pipette tip attached to a vacuum line. The anode reservoir was then filled with heated liquid AgLE solution. After gelation of the AgLE solution (which suppresses pressure-driven flow in the system), the cathode reservoir was emptied, rinsed with TE, and subsequently filled with TE and reporter solution. 6 μl of a distinct RNP-in-LE solution was then dispensed into each of the four channel reservoirs (i.e., reservoirs at the center of the third generation channels). The final concentrations of activated RNPs on chip prior to ITP were respectively 10 nM, 5 nM, 2.5 nM, and 0 nM. The chip was placed on a transparent thermal plate (Tokai Hit) set to 40°C.

Finally, platinum electrodes were inserted in the reservoirs and ITP was then performed by supplying a constant current of 200 μA using a Keithley 2410 high-voltage sourcemeter. Current was increased to 400 μA in the imaging region to facilitate detection. The ITP peaks were monitored and imaged using an epifluorescence microscope (Nikon Eclipse Ti2-E) equipped with a 1× magnification objective (Plan UW, NA: 0.04) and a CMOS camera (Hamamatsu Orca-Flash 4.0). Images were acquired once per second with an exposure time of 300 ms.

ITP peak images shown in Figure 6.5H were obtained after spatial median subtraction, 4×4-pixel binning, and image summation every 15 frames. Intensity measurements in Figure 6.5I were obtained after spatial median subtraction, and by integrating the fluorescence in a square of 60 by 175 pixels moving with the ITP peaks. Initial fluorescence values were subtracted for each fluorescence profile.

Chapter 7

Conclusions and recommendations

In this chapter, we summarize the main conclusions and contributions of this work. We then present recommendations for future research directions based on the work presented in this dissertation.

We further analyzed the images to extract position and velocity data. To this end, we developed a custom MATLAB code to identify and track the position of peaks. From the raw fluorescence intensity data, we first applied adaptive, local thresholding to create binary masks and only conserved regions of high signal. We then proceeded to sequentially erode and dilate these masks using mathematical morphology functions prebuilt in MATLAB. We then computed the centroid coordinates of the binary masks to estimate ITP peaks positions. Peak positions and velocities obtained from the MATLAB code were corrected and registered using the real-time stage position data.

7.1 Summary of contributions

7.1.1 Uncertainty quantification of Michaelis–Menten kinetic rates and its application to the analysis of CRISPR-based diagnostics

1. We identified and modeled sources of experimental error and bias in the measurement of enzymatic kinetic rates. These include pipetting errors, inner-filter effect, signal originating from uncleaved reporters, number of data points in the Michaelis-Menten curve, and non-uniform sensor response.

2. We derived a closed-form solution for the fluorescent signal for a typical CRISPR assay. We used a known closed-form solution for the substrate concentration in the quasi-steady state and the reactant-stationary regime and we included the signal originating from cleaved reporters, uncleaved reporters, and inner-filter effect in this solution.

3. We showed the influence of several biases on the determination of the kinetic rates using both Monte Carlo-type simulations and experimental measurement of fluorescence for two Cas12 orthologs.

4. We analyzed the influence of individual error sources as well as various combinations of them. We showed that the determination of the catalytic efficiency (k_{cat}/K_M) is more robust to experimental errors than the one of the individual rates k_{cat} or K_M.

7.1.2 Degradation of reporter molecules imposes a fundamental limit of detection on CRISPR diagnostics

1. We demonstrated that the background signal that nearly completely governs the limit of detection of most CRISPR-based assays likely originates from the dynamic (progressive) degradation of reporter molecules.

2. We introduced a modified kinetic model for the *trans*-cleavage step of CRISPR-Cas assays that captures this (dynamic) degradation. We derived a closed-form solution for a fundamental limit of detection of CRISPR-based assays in terms of the enzyme and reporter kinetic rates.

3. We introduced a model for the late readout of the fluorescence signal, which is particularly significant in the high-target concentration regime. Neglecting this effect results in an underestimation of the initial reaction velocity.

4. We measured the kinetic rate of degradation of the reporter molecules, and experimentally validated both our kinetic model and our predicted limit of detection model.

7.1.3 High-throughput screening of gRNA for CRISPR-based diagnostics

1. We developed and implemented a molecular biology pipeline to screen 364 gRNA sequences for *trans*-cleavage activity in CRISPR-Cas12a assays. The pipeline includes in vitro transcription (IVT), automated dispensing, and magnetic bead-based RNA purification.

2. Using this pipeline, we identified gRNA sequences resulting in faster *trans*-cleavage compared to a reference gRNA that was used in several CRISPR-based diagnostic assays.

3. We developed a microfluidic-based pipeline to screen on the order of 10^5 gRNA sequences per experiment. This new pipeline uses hydrogel beads coated with PCR amplicons to serve as a template for IVT, and as an activator and a target for the CRISPR assay. The final activity readout leverages next-generation sequencing and unique molecular identifiers to count the number of cleaved reporter molecules per gRNA sequence.

4. As preliminary results, we showed that this pipeline could enable us to distinguish high *trans*-activity from low *trans*-activity gRNA sequences for two example gRNA sequences.

7.1.4 Simulation tools for isotachophoresis

1. We developed and implemented a web-based, steady-state, highly parallel buffer design tool for ITP experiments using AWS cloud computing. BEAN is available at microfluidics.stanford.edu/bean, and its source code can be found at github.com/adarschwarzbach/BEAN-ITP.

2. We integrated ionic strength effects into BEAN's mobility and pK_a calculations using the Onsager-Fuoss and the Debye-Hückel corrections.

3. We developed and implemented an open-source, web-based simulator for nonlinear and complex electrophoresis problems. CAFES is available for free at microfluidics.stanford.edu/cafes, and its source code can be found at github.com/alvinsunyixiao/itp-websim.

4. We validated CAFES on both peak- and plateau-mode ITP experiments. The predictions from CAFES showed very good agreement with the experimental observations.

5. Both BEAN and CAFES are open access, do not require compilation nor installation, and provide easy-to-use tools for non-expert users of ITP.

7.1.5 Microfluidic networks using isotachophoresis

1. We introduced a new class of microfluidic networks that leverage ITP to selectively preconcentrate, aliquot, mix, and initiate chemical reactions on-chip without moving parts.

2. We developed a theoretical framework where ITP peak and microchannel junctions are represented as the nodes of a 2D transient graph. This enabled modeling of arbitrary ITP networks using Kirchhoff-like relationships. Based on this model, we developed and implemented a numerical, open-source solver to characterize these networks.

3. We experimentally demonstrated various ITP network topologies. We demonstrated both symmetric aliquoting of up to 32 ITP zones starting from 1 ITP peak, and merging of 32 peaks into 1 zone. We showed good agreement between our model results and our experimental observations. We also performed ITP in asymmetric networks, i.e., splitting and merging of ITP zones traveling in channels with different lengths and/or cross-sectional areas.

7.2 Recommendations for future work

7.2.1 Degradation of reporter molecules imposes a fundamental limit of detection on CRISPR diagnostics

1. It would be beneficial to determine the mechanism of the degradation of the reporters. In this work, we identified photodegradation of the FRET quencher as the most likely candidate origin of the background signal. Further analysis of the degraded reporter should include liquid chromatography and/or mass spectrometry measurements.

2. It would also be interesting to investigate the dependence of the reporter degradation rate on reporter length, sequence, fluorophore, and quencher types. These properties also influence the enzymatic *trans*-cleavage, so an exhaustive screening to find the reporter composition that yields the best signal-to-noise ratio is not trivial.

3. Proper fluorescence calibration methods should be adopted by all labs performing fluorescence measurements. Many labs are still unaware of phenomena such as non-uniform sensor response and inner-filter effect, which induce biases in many measurements. To address this, it would be beneficial to develop an open-access tool for the easy calibration of fluorescence data taken in thermal cyclers or plate readers. Such a tool would serve as both an educational tool on calibration methods and a practical means to calibrate fluorescence data for accurate results.

7.2.2 High-throughput screening of gRNA for CRISPR-based diagnostics

1. Several steps of the microfluidic pipeline require further development and optimization. This includes PCR on the hydrogel beads in droplets, and IVT-CRISPR reaction in droplets.

2. A sequencing analysis pipeline will also need to be developed to analyze the results of this experiment.

3. It would be interesting to use the results of this screening as input for a machine learning algorithm, so that an arbitrary number of gRNA sequences could be designed on the basis of both *trans*-cleavage activity and specificity.

7.2.3 Simulation tools for isotachophoresis

1. It would be beneficial to spread isotachophoresis tools outside of the electrokinetics community. Isotachophoresis has a very high potential for many routine operations performed in biochemistry labs (e.g., sample purification and preconcentration), and it is often unknown in such labs. The design and implementation of ITP experiments is still quite complex and represents a significant hurdle to the adoption of ITP into a broader public.

2. It would be beneficial for a more comprehensive description of ITP in general to develop and implement 2D and 3D simulations of ITP. These would be especially useful to predict and understand the behavior of ITP networks such as the ones we have presented in this thesis. The transport phenomena at play in such networks are highly 2D and 3D, and corresponding multidimensional simulations tools would inform the design of optimized geometries for ITP networks.

7.2.4 Microfluidic networks using isotachophoresis

1. It would be beneficial to investigate further network topologies. The network geometries we have shown in this work are relatively simple, and more complex features could be integrated in ITP networks. For example, axially varying channel cross-section could be integrated in ITP networks to manipulate analytes more precisely and enhance the spatial resolution between ITP zones.

2. It would be interesting to investigate the behavior of 3D ITP networks. Microfluidic chips for such networks could be directly 3D-printed, or made from the superposition of several 2D layers. 3D topologies would enable even more elaborate ITP network geometries and shapes and ease integration of ITP networks with existing devices (e.g., plate readers, well plates, or tubes).

3. It would also be interesting to study ITP networks that comprise three or more electrodes. This would enable even more degrees of freedom in the design of ITP networks, and allow for finer molecular control of ionic species on chip. For instance, such a system would enable to simultaneously preconcentrate and mix the contents originating from different reservoirs. This would allow to precisely monitor chemical reactions on-chip as soon as the reagents are mixed.

4. ITP networks could also be integrated with different biochemical reactions. Potential applications include aliquoting varying amounts of reporters to construct Michaelis-Menten curves, or aliquoting sample DNA in channels containing different sets of primers for LAMP.

5. Ultimately, it would be particularly interesting to combine several applications of ITP on a single chip. For instance, this could include sample purification and separation, aliquoting, and mixing to multiplex biochemical reactions (e.g., for diagnostic assays).

Bibliography

[1] A. S. Avaro and J. G. Santiago, "A critical review of microfluidic systems for CRISPR assays," *Lab on a Chip*, vol. 23, pp. 938–963, 2023.

[2] D. A. Huyke, A. Ramachandran, V. I. Bashkirov, E. K. Kotseroglou, T. Kotseroglou, and J. G. Santiago, "Enzyme kinetics and detector sensitivity determine limits of detection of amplification-free CRISPR-Cas12 and CRISPR-Cas13 diagnostics," *Analytical Chemistry*, vol. 94, pp. 9826–9834, 2022.

[3] T. Hirokawa, M. Nishino, N. Aoki, Y. Kiso, Y. Sawamoto, T. Yagi, and J. I. Akiyama, "Table of isotachophoretic indices: I. Simulated qualitative and quantitative indices of 287 anionic substances in the range pH 3–10," *Journal of Chromatography A*, vol. 271, pp. D1–D106, 1983.

[4] R. D. Chambers and J. G. Santiago, "Imaging and quantification of isotachophoresis zones using non-focusing fluorescent tracers," *Analytical Chemistry*, vol. 81, no. 8, pp. 3022–3028, 2009.

[5] S. B. Moon, D. Y. Kim, J. H. Ko, and Y. S. Kim, "Recent advances in the CRISPR genome editing tool set," *Experimental and Molecular Medicine*, vol. 51, p. 130, 2019.

[6] M. M. Kaminski, O. O. Abudayyeh, J. S. Gootenberg, F. Zhang, and J. J. Collins, "CRISPR-based diagnostics," *Nature Biomedical Engineering*, vol. 5, pp. 643–656, 2021.

[7] S. Kim, S. Ji, and H. R. Koh, "CRISPR as a diagnostic tool," *Biomolecules*, vol. 11, p. 1162, 2021.

[8] J. G. Santiago, "Inconsistent treatments of CRISPR kinetics impair assessment of its diagnostic potential," *QRB Discovery*, vol. 3, pp. e9, 1–6, 2022.

[9] K. Pardee, A. A. Green, M. K. Takahashi, D. Braff, G. Lambert, J. W. Lee, T. Ferrante, D. Ma, N. Donghia, M. Fan, N. M. Daringer, I. Bosch, D. M. Dudley, D. H. O'Connor, L. Gehrke, and J. J. Collins, "Rapid, low-cost detection of zika virus using programmable biomolecular components," *Cell*, vol. 165, pp. 1255–1266, 2016.

[10] Y. Zhang, L. Qian, W. Wei, Y. Wang, B. Wang, P. Lin, W. Liu, L. Xu, X. Li, D. Liu, S. Cheng, J. Li, Y. Ye, H. Li, X. Zhang, Y. Dong, X. Zhao, C. Liu, H. M. Zhang, Q. Ouyang, and C. Lou, "Paired design

of dCas9 as a systematic platform for the detection of featured nucleic acid sequences in pathogenic strains," *ACS Synthetic Biology*, vol. 6, pp. 211–216, 2017.

[11] J. S. Gootenberg, O. O. Abudayyeh, J. W. Lee, P. Essletzbichler, A. J. Dy, J. Joung, V. Verdine, N. Donghia, N. M. Daringer, C. A. Freije, C. Myhrvold, R. P. Bhattacharyya, J. Livny, A. Regev, E. V. Koonin, D. T. Hung, P. C. Sabeti, J. J. Collins, and F. Zhang, "Nucleic acid detection with CRISPR-Cas13a/C2c2," *Science*, vol. 356, pp. 438–442, 2017.

[12] J. S. Chen, E. Ma, L. B. Harrington, M. D. Costa, X. Tian, J. M. Palefsky, and J. A. Doudna, "CRISPR-Cas12a target binding unleashes indiscriminate single-stranded DNase activity," *Science*, vol. 360, pp. 436–439, 2018.

[13] I. M. Slaymaker, P. Mesa, M. J. Kellner, S. Kannan, E. Brignole, J. Koob, P. R. Feliciano, S. Stella, O. O. Abudayyeh, J. S. Gootenberg, J. Strecker, G. Montoya, and F. Zhang, "High-resolution structure of Cas13b and biochemical characterization of RNA targeting and cleavage," *Cell Reports*, vol. 26, pp. 3741–3751, 2019.

[14] X. Wang, M. Zhong, Y. Liu, P. Ma, L. Dang, Q. Meng, W. Wan, X. Ma, J. Liu, G. Yang, Z. Yang, X. Huang, and M. Liu, "Rapid and sensitive detection of COVID-19 using CRISPR/Cas12a-based detection with naked eye readout, CRISPR/Cas12a-ner," *Science Bulletin*, vol. 65, pp. 1436–1439, 2020.

[15] L. Guo, X. Sun, X. Wang, C. Liang, H. Jiang, Q. Gao, M. Dai, B. Qu, S. Fang, Y. Mao, Y. Chen, G. Feng, Q. Gu, R. R. Wang, Q. Zhou, and W. Li, "SARS-CoV-2 detection with CRISPR diagnostics," *Cell Discovery*, vol. 6, p. 34, 2020.

[16] Z. Huang, D. Tian, Y. Liu, Z. Lin, C. J. Lyon, W. Lai, D. Fusco, A. Drouin, X. Yin, T. Hu, and B. Ning, "Ultra-sensitive and high-throughput CRISPR-powered COVID-19 diagnosis," *Biosensors and Bioelectronics*, vol. 164, p. 112316, 2020.

[17] A. Ramachandran, D. A. Huyke, E. Sharma, M. K. Sahoo, C. Huang, N. Banaei, B. A. Pinsky, and J. G. Santiago, "Electric field-driven microfluidics for rapid CRISPR-based diagnostics and its application to detection of SARS-CoV-2," *Proceedings of the National Academy of Sciences of the United States of America*, vol. 117, pp. 29518–29525, 2020.

[18] J. Joung, A. Ladha, M. Saito, M. Segel, R. Bruneau, M.-L. W. Huang, N.-G. Kim, X. Yu, J. Li, B. D. Walker, A. L. Greninger, K. R. Jerome, J. S. Gootenberg, O. O. Abudayyeh, and F. Zhang, "Point-of-care testing for COVID-19 using SHERLOCK diagnostics.," *medRxiv*, 2020.

[19] P. Fozouni, S. Son, M. D. de León Derby, G. J. Knott, C. N. Gray, M. V. D'Ambrosio, C. Zhao, N. A. Switz, G. R. Kumar, S. I. Stephens, D. Boehm, C.-L. Tsou, J. Shu, A. Bhuiya, M. Armstrong, A. R. Harris, P.-Y. Chen, J. M. Osterloh, A. Meyer-Franke, B. Joehnk, K. Walcott, A. Sil, C. Langelier, K. S. Pollard, E. D. Crawford, A. S. Puschnik, M. Phelps, A. Kistler, J. L. DeRisi, J. A. Doudna, D. A. Fletcher, and M. Ott,

"Amplification-free detection of SARS-CoV-2 with CRISPR-Cas13a and mobile phone microscopy," *Cell*, vol. 184, pp. 323–333, 2021.

[20] B. Casati, J. P. Verdi, A. Hempelmann, M. Kittel, A. G. Klaebisch, B. Meister, S. Welker, S. Asthana, S. D. Giorgio, P. Boskovic, K. H. Man, M. Schopp, P. A. Ginno, B. Radlwimmer, C. E. Stebbins, T. Miethke, F. N. Papavasiliou, and R. Pecori, "Rapid, adaptable and sensitive Cas13-based COVID-19 diagnostics using ADESSO," *Nature Communications*, vol. 13, p. 3308, 2022.

[21] L. Grobler, E. Suleman, and D. B. T. G. Raj, *Patents and technology transfer in CRISPR technology*, vol. 180. Elsevier Inc., 1st ed., 2021.

[22] J. A. Doudna, J. S. Chen, L. B. Harrington, and E. Ma, "US10253365B1 - type V CRISPR/Cas effector proteins for cleaving ssDNAs and detecting target DNAs," 2018.

[23] J. A. Doudna, M. R. O'Connell, A. East-Seletsky, S. C. Knight, and J. H. D. Cate, "US10494664B2 - methods and compositions for detecting a target RNA," 2017.

[24] J. M. Berg, J. L. Tymoczko, G. J. J. Gatto, and L. Stryer, *Biochemistry*. W.H. Freeman and Company, 2015.

[25] O. G. Chavez-Pineda, R. Rodriguez-Moncayo, D. F. Cedillo-Alcantar, P. E. Guevara-Pantoja, J. U. Amador-Hernandez, and J. L. Garcia-Cordero, "Microfluidic systems for the analysis of blood-derived molecular biomarkers," *Electrophoresis*, vol. 43, pp. 1667–1700, 2022.

[26] C. A. Heid, J. Stevens, K. J. Livak, and P. M. Williams, "Real time quantitative PCR," *Genome research*, vol. 6, no. 10, pp. 986–994, 1996.

[27] M. M. Parida, S. Sannarangaiah, P. K. Dash, P. V. Rao, and K. Morita, "Loop mediated isothermal amplification (LAMP): A new generation of innovative gene amplification technique; perspectives in clinical diagnosis of infectious diseases," *Reviews in Medical Virology*, vol. 18, pp. 407–421, 2008.

[28] R. K. Daher, G. Stewart, M. Boissinot, and M. G. Bergeron, "Recombinase polymerase amplification for diagnostic applications," *Clinical Chemistry*, vol. 62, pp. 947–958, 2016.

[29] A. Ramachandran and J. G. Santiago, "CRISPR enzyme kinetics for molecular diagnostics," *Analytical Chemistry*, vol. 93, pp. 7456–7464, 2021.

[30] S. Y. Li, Q. X. Cheng, J. K. Liu, X. Q. Nie, G. P. Zhao, and J. Wang, "CRISPR-Cas12a has both cis- and trans-cleavage activities on single-stranded DNA," *Cell Research*, vol. 28, pp. 491–493, 2018.

[31] D. C. Swarts and M. Jinek, "Mechanistic insights into the cis- and trans-acting DNase activities of Cas12a," *Molecular Cell*, vol. 73, pp. 589–600, 2019.

[32] Y. Jeon, Y. H. Choi, Y. Jang, J. Yu, J. Goo, G. Lee, Y. K. Jeong, S. H. Lee, I.-S. Kim, J.-S. Kim, C. Jeong, S. Lee, and S. Bae, "Direct observation of DNA target searching and cleavage by CRISPR-Cas12a," *Nature Communications*, vol. 9, p. 2777, 2018.

[33] D. Singh, J. Mallon, A. Poddar, Y. Wang, R. Tippana, O. Yang, S. Bailey, and T. Ha, "Real-time observation of DNA target interrogation and product release by the RNA-guided endonuclease CRISPR Cpf1 (Cas12a)," *Proceedings of the National Academy of Sciences of the United States of America*, vol. 115, pp. 5444–5449, 2018.

[34] I. Strohkendl, F. A. Saifuddin, J. R. Rybarski, I. J. Finkelstein, and R. Russell, "Kinetic basis for DNA target specificity of CRISPR-Cas12a," *Molecular Cell*, vol. 71, pp. 816–824, 2018.

[35] L. Michaelis and M. L. Menten, "Die Kinetik der Invertinwirkung/The kinetics of invertase action," *Biochemistry*, vol. 49, p. 333–369, 1913.

[36] A. Ramachandran, *Electric field driven microfluidics for acceleration of CRISPR enzyme kinetics and its application in molecular diagnostics.* PhD thesis, Stanford University (USA), 2021.

[37] H. Shinoda, T. Iida, A. Makino, M. Yoshimura, J. Ishikawa, J. Ando, K. Murai, K. Sugiyama, Y. Muramoto, M. Nakano, K. Kiga, L. Cui, O. Nureki, H. Takeuchi, T. Noda, H. Nishimasu, and R. Watanabe, "Automated amplification-free digital RNA detection platform for rapid and sensitive SARS-CoV-2 diagnosis," *Communications Biology*, vol. 5, p. 473, 2022.

[38] K. G. Barnes, A. E. Lachenauer, A. Nitido, S. Siddiqui, R. Gross, B. Beitzel, K. J. Siddle, C. A. Freije, B. Dighero-Kemp, S. B. Mehta, A. Carter, J. Uwanibe, F. Ajogbasile, T. Olumade, I. Odia, J. D. Sandi, M. Momoh, H. C. Metsky, C. K. Boehm, A. E. Lin, M. Kemball, D. J. Park, L. Branco, M. Boisen, B. Sullivan, M. F. Amare, A. B. Tiamiyu, Z. F. Parker, M. Iroezindu, D. S. Grant, K. Modjarrad, C. Myhrvold, R. F. Garry, G. Palacios, L. E. Hensley, S. F. Schaffner, C. T. Happi, A. Colubri, and P. C. Sabeti, "Deployable CRISPR-Cas13a diagnostic tools to detect and report Ebola and Lassa virus cases in real-time," *Nature Communications*, vol. 11, p. 4131, 2020.

[39] M. Azhar, R. Phutela, M. Kumar, A. H. Ansari, R. Rauthan, S. Gulati, N. Sharma, D. Sinha, S. Sharma, S. Singh, S. Acharya, S. Sarkar, D. Paul, P. Kathpalia, M. Aich, P. Sehgal, G. Ranjan, R. C. Bhoyar, K. Singhal, H. Lad, P. K. Patra, G. Makharia, G. R. Chandak, B. Pesala, D. Chakraborty, and S. Maiti, "Rapid and accurate nucleobase detection using fnCas9 and its application in COVID-19 diagnosis," *Biosensors and Bioelectronics*, vol. 183, p. 113207, 2021.

[40] Y. Dai, R. A. Somoza, L. Wang, J. F. Welter, Y. Li, A. I. Caplan, and C. C. Liu, "Exploring the trans-cleavage activity of CRISPR-Cas12a (Cpf1) for the development of a universal electrochemical biosensor," *Angewandte Chemie - International Edition*, vol. 58, pp. 17399–17405, 2019.

[41] Y. Zhang, M. Chen, C. Liu, J. Chen, X. Luo, Y. Xue, Q. Liang, L. Zhou, Y. Tao, M. Li, D. Wang, J. Zhou, and J. Wang, "Sensitive and rapid on-site detection of SARS-CoV-2 using a gold nanoparticle-based high-throughput platform coupled with CRISPR/Cas12-assisted RT-LAMP," *Sensors and Actuators, B: Chemical*, vol. 345, p. 130411, 2021.

[42] D. Najjar, J. Rainbow, S. S. Timilsina, P. Jolly, H. D. Puig, M. Yafia, N. Durr, H. Sallum, G. Alter, J. Z. Li, X. G. Yu, D. R. Walt, J. A. Paradiso, P. Estrela, and J. J. Collins, "A lab-on-a-chip for the concurrent electrochemical detection of SARS-CoV-2 RNA and anti-SARS-CoV-2 antibodies in saliva and plasma," *Nature Biomedical Engineering*, vol. 6, pp. 968–978, 2022.

[43] R. Hajian, S. Balderston, T. Tran, T. DeBoer, J. Etienne, M. Sandhu, N. A. Wauford, J. Y. Chung, J. Nokes, M. Athaiya, J. Paredes, R. Peytavi, B. Goldsmith, N. Murthy, I. M. Conboy, and K. Aran, "Detection of unamplified target genes via CRISPR–Cas9 immobilized on a graphene field-effect transistor," *Nature Biomedical Engineering*, vol. 3, pp. 427–437, 2019.

[44] R. Zeng, W. Wang, M. Chen, Q. Wan, C. Wang, D. Knopp, and D. Tang, "CRISPR-Cas12a-driven MXene-PEDOT:PSS piezoresistive wireless biosensor," *Nano Energy*, vol. 82, p. 105711, 2021.

[45] R. Bruch, M. Johnston, A. Kling, T. Mattmüller, J. Baaske, S. Partel, S. Madlener, W. Weber, G. A. Urban, and C. Dincer, "CRISPR-powered electrochemical microfluidic multiplexed biosensor for target amplification-free miRNA diagnostics," *Biosensors and Bioelectronics*, vol. 177, p. 112887, 2021.

[46] B. Yang and X. Fang, "Programmable CRISPR-Cas9 microneedle patch for long-term capture and real-time monitoring of universal cell-free DNA," *Nature Communications*, vol. 13, p. 3999, 2022.

[47] S. Schnell, "Validity of the Michaelis-Menten equation - steady-state or reactant stationary assumption: That is the question," *FEBS Journal*, vol. 281, pp. 464–472, 2014.

[48] G. E. Briggs and J. B. Haldane, "Note on the kinetics of enzyme action," *Biochemical Journal*, vol. 19, pp. 338–339, 1925.

[49] A. S. Avaro and J. G. Santiago, "Uncertainty Quantification of Michaelis-Menten Kinetic Rates and Its Application to the Analysis of CRISPR-Based Diagnostics," *Angewandte Chemie - International Edition*, vol. 61, p. e202209527, 2022.

[50] R. A. Lee, H. D. Puig, P. Q. Nguyen, N. M. Angenent-Mari, N. M. Donghia, J. P. McGee, J. D. Dvorin, C. M. Klapperich, N. R. Pollock, and J. J. Collins, "Ultrasensitive CRISPR-based diagnostic for field-applicable detection of plasmodium species in symptomatic and asymptomatic malaria," *Proceedings of the National Academy of Sciences of the United States of America*, vol. 117, pp. 25722–25731, 2020.

[51] A. Ramachandran and J. G. Santiago, "Enzyme kinetics of CRISPR molecular diagnostics," *bioRxiv*, 2021.

[52] T. Tian, B. Shu, Y. Jiang, M. Ye, L. Liu, Z. Guo, Z. Han, Z. Wang, and X. Zhou, "An ultralocalized Cas13a assay enables universal and nucleic acid amplification-free single-molecule RNA diagnostics," *ACS Nano*, vol. 15, pp. 1167–1178, 2021.

[53] S. Son, A. Lyden, J. Shu, S. I. Stephens, P. Fozouni, J. Gavin, D. C. J. Smock, T. Y. Liu, D. Boehm, C. Simoneau, G. Renuka, J. A. Doudna, M. Ott, and D. A. Fletcher, "Sensitive and multiplexed RNA detection with Cas13 droplets and kinetic barcoding," *medRxiv*, 2021.

[54] R. T. Fuchs, J. L. Curcuru, M. Mabuchi, A. Noireterre, P. R. Weigele, Z. Sun, and G. B. Robb, "Characterization of Cme and Yme thermostable Cas12a orthologs," *Communications Biology*, vol. 5, p. 325, 2022.

[55] J. P. Broughton, X. Deng, G. Yu, C. L. Fasching, V. Servellita, J. Singh, X. Miao, J. A. Streithorst, A. Granados, A. Sotomayor-Gonzalez, K. Zorn, A. Gopez, E. Hsu, W. Gu, S. Miller, C.-Y. Y. Pan, H. Guevara, D. A. Wadford, J. S. Chen, and C. Y. Chiu, "CRISPR–Cas12-based detection of SARS-CoV-2," *Nature Biotechnology*, vol. 38, pp. 870–874, 2020.

[56] W. X. Yan, P. Hunnewell, L. E. Alfonse, J. M. Carte, E. Keston-Smith, S. Sothiselvam, A. J. Garrity, S. Chong, K. S. Makarova, E. V. Koonin, D. R. Cheng, and D. A. Scott, "Functionally diverse type V CRISPR-Cas systems," *Science*, vol. 363, pp. 88–91, 2019.

[57] C. M. Ackerman, C. Myhrvold, S. G. Thakku, C. A. Freije, H. C. Metsky, D. K. Yang, S. H. Ye, C. K. Boehm, T. S. F. Kosoko-Thoroddsen, J. Kehe, T. G. Nguyen, A. Carter, A. Kulesa, J. R. Barnes, V. G. Dugan, D. T. Hung, P. C. Blainey, and P. C. Sabeti, "Massively multiplexed nucleic acid detection with Cas13," *Nature*, vol. 582, pp. 277–282, 2020.

[58] A. Ramachandran and J. G. Santiago, "Isotachophoresis: Theory and microfluidic applications," *Chemical Reviews*, vol. 122, pp. 12904–12976, 2022.

[59] J. L. Beckers and F. M. Everaerts, "Isotachophoresis: The qualitative separation of cation mixtures," *Journal of Chromatography A*, vol. 68, pp. 207–230, 1972.

[60] S. G. Hjalmarsson and F. M. Everaerts, "Capillary isotachophoresis," *C R C Critical Reviews in Analytical Chemistry*, vol. 11, pp. 261–352, 1981.

[61] A. Rogacs, L. A. Marshall, and J. G. Santiago, "Purification of nucleic acids using isotachophoresis," *Journal of Chromatography A*, vol. 1335, pp. 105–120, 2014.

[62] A. Kopwillem, W. G. Merriman, R. M. Cuddeback, A. J. Smolka, and M. Bier, "Serum protein fractionation by isotachophoresis using amino acid spacers," *Journal of Chromatography A*, vol. 118, pp. 35–46, 1976.

[63] B. Jung, R. Bharadwaj, and J. G. Santiago, "On-chip millionfold sample stacking using transient isotachophoresis," *Analytical Chemistry*, vol. 78, no. 7, pp. 2319–2327, 2006. PMID: 16579615.

[64] C. Eid and J. G. Santiago, "Isotachophoresis applied to biomolecular reactions," *Lab on a Chip*, vol. 18, pp. 11–26, 2017.

[65] M. Bercovici, C. M. Han, J. C. Liao, and J. G. Santiago, "Rapid hybridization of nucleic acids using isotachophoresis," *Proceedings of the National Academy of Sciences of the United States of America*, vol. 109, pp. 11127–11132, 2012.

[66] F. Paratore, T. Z. Kalman, T. Rosenfeld, G. V. Kaigala, and M. Bercovici, "Isotachophoresis-based surface immunoassay," *Analytical Chemistry*, vol. 89, pp. 7373–7381, 2017.

[67] D. A. Saville and O. A. Palusinski, "Theory of electrophoretic separations. Part I: Formulation of a mathematical model," *AIChE Journal*, vol. 32, pp. 207–214, 1986.

[68] A. Persat, L. A. Marshall, and J. G. Santiago, "Purification of nucleic acids from whole blood using isotachophoresis," *Analytical Chemistry*, vol. 81, no. 22, pp. 9507–9511, 2009. PMID: 19831356.

[69] A. Jangra, S. Shriyam, J. G. Santiago, and S. S. Bahga, "A neural network model for rapid prediction of analyte focusing in isotachophoresis," *Electrophoresis*, vol. 45, pp. 599–608, 2024.

[70] C. Schwer, F. Lottspeich, B. Gaš, and E. Kenndler, "Computer simulation and experimental evaluation of on-column sample preconcentration in capillary zone electrophoresis by discontinuous buffer systems," *Analytical Chemistry*, vol. 65, pp. 2108–2115, 1993.

[71] B. Gaš and P. Bravenec, "Simul 6: A fast dynamic simulator of electromigration," *Electrophoresis*, vol. 42, pp. 1291–1299, 2021.

[72] M. Bercovici, S. K. Lele, and J. G. Santiago, "Open source simulation tool for electrophoretic stacking, focusing, and separation," *Journal of Chromatography A*, vol. 1216, pp. 1008–1018, 2009.

[73] O. Dagan and M. Bercovici, "Simulation tool coupling nonlinear electrophoresis and reaction kinetics for design and optimization of biosensors," *Analytical Chemistry*, vol. 86, pp. 7835–7842, 2014.

[74] S. S. Bahga, M. Bercovici, and J. G. Santiago, "Ionic strength effects on electrophoretic focusing and separations," *Electrophoresis*, vol. 31, pp. 910–919, 2010.

[75] W. Stroberg and S. Schnell, "On the estimation errors of Km and V from time-course experiments using the Michaelis–Menten equation," *Biophysical Chemistry*, vol. 219, pp. 17–27, 2016.

[76] W. D. Ristenpart, J. Wan, and H. A. Stone, "Enzymatic reactions in microfluidic devices: Michaelis-Menten kinetics," *Analytical Chemistry*, vol. 80, pp. 3270–3276, 2008.

[77] C. T. Goudar, J. R. Sonnad, and R. G. Duggleby, "Parameter estimation using a direct solution of the integrated Michaelis-Menten equation," *Biochimica et Biophysica Acta*, vol. 1429, pp. 377–383, 1999.

[78] H. Dette and S. Biedermann, "Robust and efficient designs for the Michaelis-Menten model," *Journal of the American Statistical Association*, vol. 98, pp. 679–686, 2003.

[79] G. L. Atkins and I. A. Nimmo, "Current trends in the estimation of Michaelis-Menten parameters," *Analytical Biochemistry*, vol. 104, pp. 1–9, 1980.

[80] Željko Jeričević and Željko Kušter, "Non-linear optimization of parameters in Michaelis-Menten kinetics," *Croatica Chemica Acta*, vol. 78, pp. 519–523, 2005.

[81] J. N. Matthews and G. C. Allcock, "Optimal designs for Michaelis-Menten kinetic studies," *Statistics in Medicine*, vol. 23, pp. 477–491, 2004.

[82] P. Goovaerts, J. Semrau, and S. Lontoh, "Monte Carlo analysis of uncertainty attached to microbial pollutant degradation rates," *Environmental Science and Technology*, vol. 35, pp. 3924–3930, 2001.

[83] M. O. Palmier and S. R. V. Doren, "Rapid determination of enzyme kinetics from fluorescence: Overcoming the inner filter effect," *Analytical Biochemistry*, vol. 371, pp. 43–51, 2007.

[84] R. J. Ritchie and T. Prvan, "A simulation study on designing experiments to measure the Km of Michaelis-Menten kinetics curves," *Journal of Theoretical Biology*, vol. 178, pp. 239–254, 1996.

[85] C. Blanluet, D. A. Huyke, A. Ramachandran, A. S. Avaro, and J. G. Santiago, "Detection and discrimination of single nucleotide polymorphisms by quantification of CRISPR-Cas catalytic efficiency," *Analytical Chemistry*, vol. 94, pp. 15117–15123, 2022.

[86] C. L. Fasching, V. Servellita, B. McKay, V. Nagesh, J. P. Broughton, A. Sotomayor-Gonzalez, B. Wang, N. Brazer, K. Reyes, J. Streithorst, R. N. Deraney, E. Stanfield, C. G. Hendriks, B. Fung, S. Miller, J. Ching, J. S. Chen, and C. Y. Chiu, "Covid-19 variant detection with a high-fidelity CRISPR-Cas12 enzyme," *Journal of clinical microbiology*, vol. 60, no. 7, p. e0026122, 2022.

[87] M. J. Kellner, J. G. Koob, J. S. Gootenberg, O. O. Abudayyeh, and F. Zhang, "SHERLOCK: nucleic acid detection with CRISPR nucleases," *Nature Protocols*, vol. 14, pp. 2986–3012, 2019.

[88] W. Cleland, "The statistical analysis of enzyme kinetic data," *Advances in Enzymology and Related Areas of Molecular Biology*, p. 14, 1967.

[89] S. Schnell and C. Mendoza, "Closed form solution for time-dependent enzyme kinetics," *Journal of Theoretical Biology*, vol. 187, pp. 207–212, 1997.

[90] S. Chen, Y.-L. Yu, and J.-H. Wang, "Inner filter effect-based fluorescent sensing systems: A review," *Analytica Chimica Acta*, vol. 999, pp. 13–26, 2018.

[91] D. F. Swinehart, "The Beer-Lambert law," *Journal of Chemical Education*, vol. 39, pp. 333–335, 1962.

[92] A. J. Hedges, "Estimating the precision of serial dilutions and viable bacterial counts," *International Journal of Food Microbiology*, vol. 76, pp. 207–214, 2002.

[93] "Lab report 5: Setting tolerance limits for pipettes."

[94] "Python."

[95] "Scipy."

[96] J. Li, S. Yang, C. Zuo, L. Dai, Y. Guo, and G. Xie, "Applying CRISPR-Cas12a as a signal amplifier to construct biosensors for non-DNA targets in ultralow concentrations," *ACS Sensors*, vol. 5, pp. 970–977, 2020.

[97] M. Model, "Intensity calibration and flat-field correction for fluorescence microscopes," *Current Protocols in Cytometry*, vol. 68, pp. 10.14.1 – 10.14.10, 2014.

[98] A. S. Avaro, A. D. Griffiths, and J. G. Santiago, "Degradation of reporter molecules imposes a fundamental limit of detection on CRISPR diagnostics," *Analytical Chemistry*, 2025. In press.

[99] O. O. Abudayyeh and J. S. Gootenberg, "CRISPR diagnostics," *Science*, vol. 372, pp. 914–915, 2021.

[100] S. Y. Li, Q. X. Cheng, X. Y. Li, Z. L. Zhang, S. Gao, R. B. Cao, G. P. Zhao, J. Wang, and J. M. Wang, "CRISPR-Cas12a-assisted nucleic acid detection," *Cell Discovery*, vol. 4, pp. 1–4, 2018.

[101] S. Y. Wang, Y. C. Du, D. X. Wang, J. Y. Ma, A. N. Tang, and D. M. Kong, "Signal amplification and output of CRISPR/Cas-based biosensing systems: A review," *Analytica Chimica Acta*, vol. 1185, p. 338882, 2021.

[102] Z. Weng, Z. You, J. Yang, N. Mohammad, M. Lin, Q. Wei, X. Gao, and Y. Zhang, "CRISPR-Cas biochemistry and CRISPR-based molecular diagnostics," *Angewandte Chemie - International Edition*, vol. 62, p. e202214987, 2023.

[103] J. Zhang, H. Lv, L. Li, M. Chen, D. Gu, J. Wang, and Y. Xu, "Recent improvements in CRISPR-based amplification-free pathogen detection," *Frontiers in Microbiology*, vol. 12, p. 751408, 2021.

[104] S. Qian, Y. Chen, X. Xu, C. Peng, X. Wang, H. Wu, Y. Liu, X. Zhong, J. Xu, and J. Wu, "Advances in amplification-free detection of nucleic acid: CRISPR/Cas system as a powerful tool," *Analytical Biochemistry*, vol. 643, p. 114593, 2022.

[105] H. Li, Y. Xie, F. Chen, H. Bai, L. Xiu, X. Zhou, X. Guo, Q. Hu, and K. Yin, "Amplification-free CRISPR/Cas detection technology: challenges, strategies, and perspectives," *Chemical Society Reviews*, vol. 52, pp. 361–382, 2023.

[106] M. Azimzadeh, M. Mousazadeh, A. Jahangiri-Manesh, P. Khashayar, and P. Khashayar, "CRISPR-powered microfluidics in diagnostics: A review of main applications," *Chemosensors*, vol. 10, p. 3, 2022.

[107] L. Chen, M. Hu, and X. Zhou, "Trends in developing one-pot CRISPR diagnostics strategies," *Trends in Biotechnology*, vol. 43, pp. 98–110, 2024.

[108] H. Lv, J. Wang, J. Zhang, Y. Chen, L. Yin, D. Jin, D. Gu, H. Zhao, Y. Xu, and J. Wang, "Definition of CRISPR Cas12a trans-cleavage units to facilitate CRISPR diagnostics," *Frontiers in Microbiology*, vol. 12, p. 766464, 2021.

[109] H. Yue, B. Shu, T. Tian, E. Xiong, M. Huang, D. Zhu, J. Sun, Q. Liu, S. Wang, Y. Li, and X. Zhou, "Droplet Cas12a assay enables DNA quantification from unamplified samples at the single-molecule level," *Nano Letters*, vol. 21, pp. 4643–4653, 2021.

[110] J. C. Cofsky, D. Karandur, C. J. Huang, I. P. Witte, J. Kuriyan, and J. A. Doudna, "CRISPR-Cas12a exploits R-loop asymmetry to form double-strand breaks," *eLife*, vol. 9, p. e55143, 2020.

[111] J. S. Gootenberg, O. O. Abudayyeh, M. J. Kellner, J. Joung, J. J. Collins, and F. Zhang, "Multiplexed and portable nucleic acid detection platform with Cas13, Cas12a, and csm6," *Science*, vol. 360, pp. 439–444, 2018.

[112] W. Feng, H. Zhang, and X. C. Le, "Signal amplification by the trans-cleavage activity of CRISPR-Cas systems: Kinetics and performance," *Analytical Chemistry*, vol. 95, pp. 206–217, 2023.

[113] Y. Shan, X. Zhou, R. Huang, and D. Xing, "High-fidelity and rapid quantification of miRNA combining crRNA programmability and CRISPR/Cas13a trans-cleavage activity," *Analytical Chemistry*, vol. 91, pp. 5278–5285, 2019.

[114] E. A. Nalefski, S. Sinan, J. L. Cantera, A. G. Kim, R. M. Kooistra, R. E. Rivera, J. P. Janshen, S. Bhadra, J. D. Bishop, A. D. Ellington, I. J. Finklestein, and D. Madan, "Room temperature CRISPR diagnostics for low-resource settings," *Scientific Reports*, vol. 15, pp. 1–13, 2025.

[115] J. S. Chen, E. Ma, L. B. Harrington, M. D. Costa, X. Tian, J. M. Palefsky, and J. A. Doudna, "Erratum for the report "CRISPR-Cas12a target binding unleashes indiscriminate single-stranded DNase activity"," *Science*, vol. 371, 2021.

[116] I. M. Slaymaker, P. Mesa, M. J. Kellner, S. Kannan, E. Brignole, J. Koob, P. R. Feliciano, S. Stella, O. O. Abudayyeh, J. S. Gootenberg, J. Strecker, G. Montoya, and F. Zhang, "Correction to high-resolution structure of Cas13b and biochemical characterization of RNA targeting and cleavage," *CellReports*, vol. 34, p. 108865, 2021.

[117] W. Feng, H. Peng, H. Zhang, M. Weinfeld, and X. C. Le, "A sensitive technique unravels the kinetics of activation and trans-cleavage of CRISPR-Cas systems," *Angewandte Chemie - International Edition*, vol. 63, 2024.

[118] X. Wu, J. Li, and F. Nekka, "Closed form solutions and dominant elimination pathways of simultaneous first-order and Michaelis–Menten kinetics," *Journal of Pharmacokinetics and Pharmacodynamics*, vol. 42, pp. 151–161, 2015.

[119] J. M. Lesinski, N. K. Khosla, C. Paganini, B. Verberckmoes, H. Vermandere, A. J. deMello, and D. A. Richards, "FRETting about CRISPR-Cas assays: Dual-channel reporting lowers detection limits and times-to-result," *ACS Sensors*, vol. 9, pp. 3616–3624, 2024.

[120] "I am having a problem with background drift with my BHQ™ probe. what might the cause be? | LGC biosearch technologies."

[121] V. A. Ryabinin, E. V. Kostina, and A. N. Sinyakov, "Unexpected transformation of black hole quenchers in electrophoretic purification of the fluorescein-containing TaqMan probes," *Nucleosides, Nucleotides and Nucleic Acids*, vol. 36, pp. 418–427, 2017.

[122] B. Kamenická, "Chemical degradation of azo dyes using different reducing agents: A review," *Journal of Water Process Engineering*, vol. 61, p. 105350, 2024.

[123] J. Oakes and P. Gratton, "Kinetic investigations of azo dye oxidation in aqueous media," *Journal of the Chemical Society, Perkin Transactions*, vol. 2, pp. 1857–1864, 1998.

[124] K. Tanaka, K. Padermpole, and T. Hisanaga, "Photocatalytic degradation of commercial azo dyes," *Water Research*, vol. 34, pp. 327–333, 2000.

[125] I. Smirnov and G. E. Pozmogova, "MALDI Analysis of modified oligonucleotides containing dark quenchers," *Journal of Biomolecular Techniques*, vol. 24, p. S54, 2013.

[126] L. B. Harrington, D. Burstein, J. S. Chen, D. Paez-Espino, E. Ma, I. P. Witte, J. C. Cofsky, N. C. Kyrpides, J. F. Banfield, and J. A. Doudna, "Programmed DNA destruction by miniature CRISPR-Cas14 enzymes," *Science*, vol. 362, pp. 839–842, 2018.

[127] Y. Chen, S. Qian, X. Yu, and J. Wu, "Microfluidics: the propellant of CRISPR-based nucleic acid detection," *Trends in Biotechnology*, pp. 557–574, 2022.

[128] P. Li, H. Xiong, B. Yang, X. Jiang, J. Kong, and X. Fang, "Recent progress in CRISPR-based microfluidic assays and applications," *Trends in Analytical Chemistry*, vol. 157, p. 116812, 2022.

[129] J. Jiao, Y. Liu, M. Yang, J. Zheng, C. Liu, W. Ye, S. Song, T. Bai, C. Song, M. Wang, J. Shi, R. Wan, K. Zhang, P. Hao, J. Feng, and X. Zheng, "The engineered CRISPR-Mb2Cas12a variant enables sensitive and fast nucleic acid-based pathogens diagnostics in the field," *Plant Biotechnology Journal*, vol. 21, pp. 1465–1478, 7 2023.

[130] X. Tong, K. Zhang, Y. Han, T. Li, M. Duan, R. Ji, X. Wang, X. Zhou, Y. Zhang, and H. Yin, "Fast and sensitive CRISPR detection by minimized interference of target amplification," *Nature Chemical Biology*, vol. 20, pp. 885–893, 7 2024.

[131] L. T. Nguyen, B. M. Smith, and P. K. Jain, "Enhancement of trans-cleavage activity of Cas12a with engineered crRNA enables amplified nucleic acid detection," *Nature Communications*, vol. 11, pp. 1–13, 2020.

[132] Q. Zeng, M. Zhou, Z. Hu, W. Deng, Z. Li, L. Wu, and D. Liang, "Rapid and sensitive Cas12a-based one-step nucleic acid detection with ssDNA-modified crRNA," *Analytica Chimica Acta*, vol. 1276, p. 341622, 10 2023.

[133] R. Zilionis, J. Nainys, A. Veres, V. Savova, D. Zemmour, A. M. Klein, and L. Mazutis, "Single-cell barcoding and sequencing using droplet microfluidics," *Nature Protocols*, vol. 12, pp. 44–73, 2016.

[134] F. Diehl, M. Li, Y. He, K. W. Kinzler, B. Vogelstein, and D. Dressman, "BEAMing: Single-molecule PCR on microparticles in water-in-oil emulsions," *Nature Methods*, vol. 3, pp. 551–559, 2006.

[135] T. Liu, S. Patel, and A. M. Pyle, "Making RNA: Using T7 RNA polymerase to produce high yields of RNA from DNA templates," *Methods in Enzymology*, vol. 691, pp. 185–207, 2023.

[136] A. S. Avaro, A. Schwarzbach, A. Jangra, S. S. Bahga, and J. G. Santiago, "Highly parallel simulation tool for the design of isotachophoresis experiments," *Analytica Chimica Acta*, vol. 1337, p. 343553, 2025.

[137] P. Smejkal, D. Bottenus, M. C. Breadmore, R. M. Guijt, C. F. Ivory, F. Foret, and M. Macka, "Microfluidic isotachophoresis: A review," *Electrophoresis*, vol. 34, pp. 1493–1509, 2013.

[138] R. Khnouf and C. Han, "Isotachophoresis-enhanced immunoassays: Challenges and opportunities," *IEEE Nanotechnology Magazine*, vol. 14, pp. 6–17, 2020.

[139] G. Kaigala, M. Bercovici, M. Behnam, D. Elliott, J. G. Santiago, and C. J. Backhouse, "Miniaturized system for isotachophoresis assays," *Lab on a Chip*, vol. 10, pp. 2242–2250, 2010.

[140] P. Gebauer, Z. Malá, and P. Boček, "Recent progress in capillary ITP," *Electrophoresis*, vol. 28, pp. 26–32, 2007.

[141] W. Thormann and R. A. Mosher, "Dynamic computer simulations of electrophoresis: 2010–2020," *Electrophoresis*, vol. 43, pp. 10–36, 2022.

[142] P. Gebauer and P. Boček, "Zone order in isotachophoresis the concept of the zone existence diagram and its use in cationic systems," *Journal of Chromatography A*, vol. 261, pp. 49–65, 1983.

[143] W. Thormann, C. X. Zhang, J. Caslavska, P. Gebauer, and R. A. Mosher, "Modeling of the impact of ionic strength on the electroosmotic flow in capillary electrophoresis with uniform and discontinuous buffer systems," *Analytical Chemistry*, vol. 70, pp. 549–562, 1998.

[144] S. S. Bahga and P. Gupta, "Electrophoresis simulations using Chebyshev pseudo-spectral method on a moving mesh," *Electrophoresis*, vol. 43, pp. 688–695, 2022.

[145] A. S. Avaro, Y. Sun, K. Jiang, S. S. Bahga, and J. G. Santiago, "Web-based open-source tool for isotachophoresis," *Analytical Chemistry*, vol. 93, pp. 15768–15774, 2021.

[146] T. Hirokawa and Y. Kiso, "Isotachophoretic determination of mobility and pKa, by means of computer simulation," *Journal of Chromatography A*, vol. 252, pp. 33–48, 1982.

[147] G. Garcia-Schwarz, M. Bercovici, L. A. Marshall, and J. G. Santiago, "Sample dispersion in isotachophoresis," *Journal of Fluid Mechanics*, vol. 679, pp. 455–475, 2011.

[148] A. Persat, M. E. Suss, and J. G. Santiago, "Basic principles of electrolyte chemistry for microfluidic electrokinetics. Part II: Coupling between ion mobility, electrolysis, and acid-base equilibria," *Lab on a Chip*, vol. 9, pp. 2454–2469, 2009.

[149] L. Onsager and R. M. Fuoss, "Irreversible processes in electrolytes. diffusion, conductance, and viscous flow in arbitrary mixtures of strong electrolytes," *The Journal of Physical Chemistry*, vol. 36, pp. 2689–2778, 1932.

[150] A. Persat, R. D. Chambers, and J. G. Santiago, "Basic principles of electrolyte chemistry for microfluidic electrokinetics. Part I: Acid-base equilibria and pH buffers," *Lab on a Chip*, vol. 9, pp. 2437–2453, 2009.

[151] T. Hirokawa, M. Nishino, and Y. Kiso, "Isotachophoretic determination of mobility and pKa by means of computer simulation: II. Evaluation of m0 and pKa of 65 anions," *Journal of Chromatography A*, vol. 252, pp. 49–65, 1982.

[152] T. Hirokawa, S. Kabayashi, and Y. Kiso, "Isotachophoretic determination of mobility and pKa by means of computer simulation: III. Evaluation of mobility and pKa of fifteen nucleotides and seven phosphorus oxoacids and their isotachophoretic separation," *Journal of Chromatography A*, vol. 318, pp. 195–210, 1985.

[153] T. Hirokawa, T. Gojo, and Y. Kiso, "Isotachophoretic determination of mobility and pKa by means of computer simulation: IV. Evaluation of m0 and pKa, of twenty-six amino acids and assessment of the separability," *Journal of Chromatography A*, vol. 369, pp. 59–81, 1986.

[154] T. Hirokawa, T. Gojo, and Y. Kiso, "Isotachophoretic determination of mobility and pKa by means of computer simulation: V. Evaluation of m0 and pKa of twenty-eight dipeptides and assessment of separability," *Journal of Chromatography A*, vol. 390, pp. 201–223, 1987.

[155] S. H. Yalkowsky, Y. He, and P. Jain, *Handbook of Aqueous Solubility Data.* CRC Press, 2nd edition ed., 2010.

[156] L. Křivánková, F. Foret, P. Gebauer, and P. Boček, "Selection of electrolyte systems in isotachophoresis," *Journal of Chromatography A*, vol. 390, pp. 3–16, 1987.

[157] F. Loison and M. Boutigny, "PyPAPI," 2017.

[158] D. Voet and J. G. Voet, *Biochemistry.* Wiley & Sons, 4th ed., 2011.

[159] T. K. Khurana and J. G. Santiago, "Sample zone dynamics in peak mode isotachophoresis," *Analytical Chemistry*, vol. 80, no. 16, pp. 6300–6307, 2008.

[160] G. Garcia-Schwarz, A. Rogacs, S. S. Bahga, and J. G. Santiago, "On-chip isotachophoresis for separation of ions and purification of nucleic acids," *Journal of Visualized Experiments*, vol. 61, p. e3890, 2012.

[161] F. Everaerts, J. Beckers, and T. Verheggen, *Isotachophoresis: theory, instrumentation and applications.* Journal of chromatography library, Netherlands: Elsevier, 1976.

[162] S. S. Bahga and J. G. Santiago, "Coupling isotachophoresis and capillary electrophoresis: a review and comparison of methods," *Analyst*, vol. 138, pp. 735–754, 2013.

[163] C. Eid and J. G. Santiago, "Isotachophoresis applied to biomolecular reactions," *Lab on a Chip*, vol. 18, pp. 11–26, 2018.

[164] A. Jameson, "Analysis and design of numerical schemes for gas dynamics, 1: Artificial diffusion, upwind biasing, limiters and their effect on accuracy and multigrid convergence," *International Journal of Computational Fluid Dynamics*, vol. 4, no. 3-4, pp. 171–218, 1995.

[165] S. S. Bahga, M. Bercovici, and J. G. Santiago, "Robust and high-resolution simulations of nonlinear electrokinetic processes in variable cross-section channels," *Electrophoresis*, vol. 33, no. 19-20, pp. 3036–3051, 2012.

[166] R. J. LeVeque, *Finite Volume Methods for Hyperbolic Problems.* Cambridge Texts in Applied Mathematics, Cambridge University Press, 2002.

[167] "Plotly."

[168] M. Bercovici, S. K. Lele, and J. G. Santiago, "Compact adaptive-grid scheme for high numerical resolution simulations of isotachophoresis," *Journal of Chromatography A*, vol. 1217, no. 4, pp. 588–599, 2010.

[169] P. Boček, M. Deml, and J. Janák, "Effect of a concentration cascade of the leading electrolyte on the seperation capacity in isotachophoresis," *Journal of Chromatography A*, vol. 156, no. 2, pp. 323–326, 1978.

[170] D. Milanova, R. D. Chambers, S. S. Bahga, and J. G. Santiago, "Electrophoretic mobility measurements of fluorescent dyes using on-chip capillary electrophoresis," *Electrophoresis*, vol. 32, pp. 3286–3294, 2011.

[171] S. S. Bahga and J. G. Santiago, "Concentration cascade of leading electrolyte using bidirectional isotachophoresis," *Electrophoresis*, vol. 33, no. 6, pp. 1048–1059, 2012.

[172] K. W. Oh, K. Lee, B. Ahn, and E. P. Furlani, "Design of pressure-driven microfluidic networks using electric circuit analogy," *Lab on a Chip*, vol. 12, pp. 515–545, 2012.

[173] F. Paratore, V. Bacheva, M. Bercovici, and G. V. Kaigala, "Reconfigurable microfluidics," *Nature Reviews Chemistry*, vol. 6, pp. 70–80, 2021.

[174] J. Urteaga, "US2751933A - multiple servo selector," 1956.

[175] T. L. Etter, "US3057551A - fluid pressure digital computer," 1962.

[176] D. T. Chiu, E. Pezzoli, H. Wu, A. D. Stroock, and G. M. Whitesides, "Using three-dimensional microfluidic networks for solving computationally hard problems," *Proceedings of the National Academy of Sciences of the United States of America*, vol. 98, pp. 2961–2966, 2001.

[177] J. Linder, "US3786542A - method of forming circuit structures by photo etching-electroforming process," 1974.

[178] F. X. Kay, "US3391703A - fluid connector units," 1968.

[179] J. S. Dugan, "US5843385A - plate-type chemical reactor," 1998.

[180] K. H. Harbster and J. A. Perrotto, "US5595712A - chemical mixing and reaction apparatus," 1997.

[181] E. Delamarche, A. Bernard, H. Schmid, A. Bietsch, B. Michel, and H. Biebuyck, "Microfluidic networks for chemical patterning of substrates: Design and application to bioassays," *Journal of the American Chemical Society*, vol. 120, pp. 500–508, 1998.

[182] M. E. Webster, "US4848722A - valve with flexible sheet member," 1989.

[183] M. A. Unger, H. P. Chou, T. Thorsen, A. Scherer, and S. R. Quake, "Monolithic microfabricated valves and pumps by multilayer soft lithography," *Science*, vol. 288, pp. 113–116, 2000.

[184] S. K. Dertinger, D. T. Chiu, N. L. Jeon, and G. M. Whitesides, "Generation of gradients having complex shapes using microfluidic networks," *Analytical Chemistry*, vol. 73, pp. 1240–1246, 2001.

[185] K. Lee, C. Kim, G. Jung, T. S. Kim, J. Y. Kang, and K. W. Oh, "Microfluidic network-based combinatorial dilution device for high throughput screening and optimization," *Microfluidics and Nanofluidics*, vol. 8, pp. 677–685, 2010.

[186] J. Nilsson, M. Evander, B. Hammarström, and T. Laurell, "Review of cell and particle trapping in microfluidic systems," *Analytica Chimica Acta*, vol. 649, pp. 141–157, 2009.

[187] N. Lu, H. M. Tay, C. Petchakup, L. He, L. Gong, K. K. Maw, S. Y. Leong, W. W. Lok, H. B. Ong, R. Guo, K. H. H. Li, and H. W. Hou, "Label-free microfluidic cell sorting and detection for rapid blood analysis," *Lab on a Chip*, vol. 23, pp. 1226–1257, 2023.

[188] L. Nan, H. Zhang, D. A. Weitz, and H. C. Shum, "Development and future of droplet microfluidics," *Lab on a Chip*, vol. 24, pp. 1135–1153, 2024.

[189] T. Moragues, D. Arguijo, T. Beneyton, C. Modavi, K. Simutis, A. R. Abate, J. C. Baret, A. J. deMello, D. Densmore, and A. D. Griffiths, "Droplet-based microfluidics," *Nature Reviews Methods Primers*, vol. 3, pp. 1–22, 2023.

[190] A. Persat and J. G. Santiago, "Electrokinetic control of sample splitting at a channel bifurcation using isotachophoresis," *New Journal of Physics*, vol. 11, p. 075026, 2009.

[191] G. Goet, T. Baier, and S. Hardt, "Micro contactor based on isotachophoretic sample transport," *Lab on a Chip*, vol. 9, pp. 3586–3593, 2009.

[192] N. C. Stellwagen and E. Stellwagen, "Effect of the matrix on DNA electrophoretic mobility," *Journal of Chromatography A*, vol. 1216, pp. 1917–1929, 2009.

[193] S. Natarajan, D. A. Chang-Yen, and B. K. Gale, "Large-area, high-aspect-ratio SU-8 molds for the fabrication of PDMS microfluidic devices," *Journal of Micromechanics and Microengineering*, vol. 18, p. 11, 2008.

[194] A. Terzis, A. Ramachandran, J. Kang, and J. G. Santiago, "Simultaneous optical and infrared thermal imaging of isotachophoresis," *Analytica Chimica Acta*, vol. 1131, pp. 9–17, 2020.

[195] J. S. Bendat and A. G. Piersol, *Random Data: Analysis and Measurement Procedures: Fourth Edition*. Wiley Blackwell, 2012.

[196] E. A. Nalefski, N. Patel, P. J. Leung, Z. Islam, R. M. Kooistra, I. Parikh, E. Marion, G. J. Knott, J. A. Doudna, A. L. M. L. Ny, and D. Madan, "Kinetic analysis of Cas12a and Cas13a RNA-guided nucleases for development of improved CRISPR-based diagnostics," *iScience*, vol. 24, 2021.

[197] H. Shinoda, Y. Taguchi, R. Nakagawa, A. Makino, S. Okazaki, M. Nakano, Y. Muramoto, C. Takahashi, I. Takahashi, J. Ando, T. Noda, O. Nureki, H. Nishimasu, and R. Watanabe, "Amplification-free RNA detection with CRISPR–Cas13," *Communications Biology*, vol. 4, p. 476, 2021.

[198] M. Rossetti, R. Merlo, N. Bagheri, D. Moscone, A. Valenti, A. Saha, P. R. Arantes, R. Ippodrino, F. Ricci, I. Treglia, E. Delibato, J. V. D. Oost, G. Palermo, G. Perugino, and A. Porchetta, "Enhancement of CRISPR/Cas12a trans-cleavage activity using hairpin DNA reporters," *Nucleic Acids Research*, vol. 50, pp. 8377–8391, 2022.

[199] C. Blanluet, C. J. Kuo, A. Bhattacharya, and J. G. Santiago, "Design and evaluation of a robust CRISPR kinetic assay for hot-spot genotyping," *Analytical Chemistry*, vol. 96, pp. 7444–7451, 2024.

[200] T. Nolan, R. E. Hands, and S. A. Bustin, "Quantification of mRNA using real-time RT-PCR," *Nature Protocols*, vol. 1, pp. 1559–1582, 2006.

[201] "Distinguishing real signal from background noise - ask TaqMan 41 - behind the bench."

[202] S. Tyagi and F. R. Kramer, "Molecular beacons: Probes that fluoresce upon hybridization," *Nature Biotechnology*, vol. 14, pp. 303–308, 1996.

[203] S. A. Marras, F. R. Kramer, and S. Tyagi, "Efficiencies of fluorescence resonance energy transfer and contact-mediated quenching in oligonucleotide probes," *Nucleic Acids Research*, vol. 30, p. e122, 2002.

[204] K. Rütschlin, "Personal communication," *Eurofins Genomics*, 2025.

[205] R. Bharadwaj and J. G. Santiago, "Dynamics of field-amplified sample stacking," *Journal of Fluid Mechanics*, vol. 543, p. 57–92, 2005.

[206] S. S. Bahga, R. D. Chambers, and J. G. Santiago, "Coupled isotachophoretic preconcentration and electrophoretic separation using bidirectional isotachophoresis," *Analytical Chemistry*, vol. 83, pp. 6154–6162, 2011.

[207] D. C. Duffy, J. C. McDonald, O. J. A. Schueller, and G. M. Whitesides, "Rapid prototyping of microfluidic systems in poly(dimethylsiloxane)," *Analytical Chemistry*, vol. 70, pp. 4974–4984, 1998. PMID: 21644679.

Appendix A

Supplementary Information for Uncertainty quantification of Michaelis–Menten kinetic rates and its application to the analysis of CRISPR-based diagnostics

A.1 Michaelis-Menten kinetic rate system and derivation of the Schnell-Mendoza solution

In this section, we summarize the Michaelis-Menten system of rate equations, along with its initial conditions and conservation equations. Then, we present a derivation of the Schnell-Mendoza solution which we leverage in chapter 2. That is, we here show details of the derivation of Equation 2.3 in chapter 2. We also derive Equation 2.5 from chapter 2.

The Michaelis-Menten system of rate equation is given by: [35]

$$\frac{d[E]}{dt} = -k_f[E][S] + k_r[C] + k_{cat}[C], \tag{A.1}$$

$$\frac{d[S]}{dt} = -k_f[E][S] + k_r[C], \tag{A.2}$$

$$\frac{d[C]}{dt} = k_f[E][S] - k_r[C] - k_{cat}[C], \tag{A.3}$$

$$\frac{d[P]}{dt} = k_{cat}[C], \tag{A.4}$$

$$[E]_0 = [E] + [C], \tag{A.5}$$

$$[S]_0 = [S] + [P] + [C], \tag{A.6}$$

$$[P]_0 = [C]_0 = 0. \tag{A.7}$$

Under the reactant-stationary assumption and the quasi-steady state assumption, Equation A.2 can be reformulated as: [89]

$$\frac{d[S]}{dt} = -\frac{d[P]}{dt} = -\frac{k_{cat}[E]_0[S]}{K_M + [S]}. \tag{A.8}$$

Here, $K_M = \frac{k_{cat}+k_r}{k_f}$ is the Michaelis-Menten constant. The latter equation can be written as:

$$\left(1 + \frac{K_M}{[S]}\right) d[S] = -k_{cat}[E]_0 dt. \tag{A.9}$$

Then, integrating between $t = 0$ and t yields:

$$\frac{[S]}{K_M} - \frac{[S]_0}{K_M} + \ln\frac{[S]}{[S]_0} = -\frac{k_{cat}[E]_0 t}{K_M}, \tag{A.10}$$

whence:

$$\frac{[S]}{K_M}\exp\frac{[S]}{K_M} = \frac{[S]_0}{K_M}\exp\left(\frac{[S]_0}{K_M} - \frac{k_{cat}[E]_0 t}{K_M}\right). \tag{A.11}$$

We now introduce the Lambert-W function defined as:

$$xe^x = y \Leftrightarrow x = W(y). \tag{A.12}$$

Combining with the result above:

$$[S](t) = K_M W\left(\frac{[S]_0}{K_M} e^{\frac{[S]_0}{K_M} - \frac{k_{cat}[E]_0}{K_M} t}\right) \equiv K_M \mathcal{A}\left(t; [S]_0, [E]_0, k_{cat}, K_M\right). \tag{A.13}$$

Here, we have defined:

$$\mathcal{A}\left(t; [S]_0, [E]_0, k_{cat}, K_M\right) \equiv W\left(\frac{[S]_0}{K_M} e^{\frac{[S]_0}{K_M} - \frac{k_{cat}[E]_0}{K_M} t}\right).$$

Note that Equation A.13 is Equation 2.3 in chapter 2.

Recall that the so-called quasi-steady assumption is that the concentration of intermediate complex varies slowly relative to that of the substrate or product. Under this assumption, we assume $\frac{d[C]}{dt} \approx 0$,

therefore from Equation A.3 we derive the following:

$$[C](t) \approx \frac{k_f}{k_r + k_{cat}}[E](t)[S](t) = \frac{[E](t)[S](t)}{K_M}. \tag{A.14}$$

Figure A.1 shows the intermediate complex concentration profile solutions given by Equation A.14 (Equation 2.5) and by a complete solution of the Michaelis-Menten system (Equations A.1 to A.7) obtained using the stiff solver `ode23s` (MATLAB R2022a, MathWorks). We note that the approximate profile yielded by the solution we have derived for the main text agrees very well with the complete solution. We used the following values to solve the full Michaelis-Menten system: $[S]_0 = 2$ µM, $[E]_0 = 1$ nM, $k_{cat} = 0.75$ s^{-1}, $K_M = (k_{cat} + k_r)/k_f = 0.5$ µM, $k_f = 10^{10}$ M^{-1}s^{-1}. Note that the value of k_f was arbitrarily chosen. However, this choice does not influence the solution. Indeed, we varied k_f over many orders of magnitude (from 10^4 M^{-1}s^{-1} to 10^{10} M^{-1}s^{-1}) and noted that the numerical solution for $[C](t)$ was independent of k_f for a given k_{cat} and K_M. For $k_f < 10^4$ M^{-1}s^{-1} the solution to the system of ODEs yielded negative-valued functions and was therefore no longer representative of the physical system.

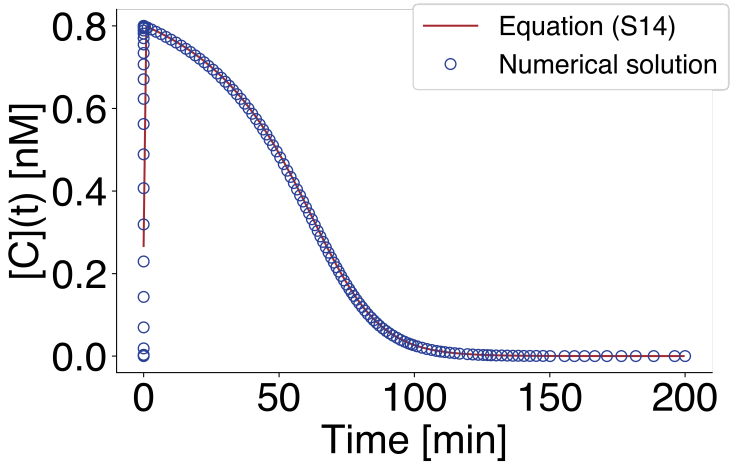

Figure A.1: Approximate concentration profile resulting from our estimate solution for the intermediate complex C (see Equation 2.5 in chapter 2). Shown are the temporal profiles obtained from the solution derived in this section (solid line) and a numerical solution of the full Michaelis-Menten system (symbols). The conditions for this case are given in the text but we obtain good agreement for the relevant ranges of this solution.

A.2 Influence of the dynamic range of the reporters

The vast majority of the published measurements of CRISPR enzyme kinetics do not report calibration curves, i.e. conversions from the fluorescence signal to the corresponding value of cleaved reporter concentration. Of those which do, only a small portion report separate calibrations for cleaved and uncleaved

reporters, and actually account for the signal due to uncleaved reporters. Neglecting the latter background signal induces an error in the measurement of the cleaved reporter concentration.

The measured intensity (due to both uncleaved and cleaved reporters) is given by Equation A.15 (Equation 2.7 in chapter 2) [17]:

$$I(t) = F_{Ucl}[S](t) + F_{Cl}[P](t). \tag{A.15}$$

We next analyze the error incurred in ignoring the signal of uncleaved reporters as is fairly common in the CRISPR-based diagnostic literature [19, 13, 11, 6]. To this end, we define $[\widetilde{P}]$ as the overprediction of the concentration $[P]$. That is, $[\widetilde{P}]$ is the estimated concentration of uncleaved reporters if one ignores the fact that uncleaved reporters have a significant signal (i.e., assuming that the calibration of intensity as a function of cleaved reporter concentration is strictly proportional to F_{Cl}). We then divide Equation A.15 by F_{Cl} and this yields:

$$[\widetilde{P}] = \alpha[S](t) + [P](t). \tag{A.16}$$

Here, we can define $\alpha = \frac{F_{Ucl}}{F_{Cl}} < 1$ as the inverse dynamic range of the reporters (i.e., the inverse of their cleaved-to-uncleaved ratio). Re-organizing Equation A.16 then yields:

$$\left[\widetilde{P}\right] - [P] = \alpha\left([S]_0 - [P]\right). \tag{A.17}$$

The latter equation is Equation 2.8 of chapter 2.

Further, we analyze the effect of neglecting uncleaved reporter signal on the measurement of reaction velocities by differentiating Equation A.17 with respect to time:

$$\widetilde{v} = (1 - \alpha)\, v. \tag{A.18}$$

Here, $\widetilde{v}$ is the underestimation of the (actual) reaction velocity v. This error in v results in an error in the estimation of the kinetic parameters k_{cat} and K_M.

To demonstrate this effect, we simulated apparent progress curves for varying values of the dynamic range α and computed the corresponding reaction velocities. This process is similar to the one presented in chapter 2 (section "Estimates of uncertainty distributions of k_{cat} and K_M based on Monte Carlo simulations"). Figure A.2 shows apparent reaction velocities for eight substrate concentrations (symbols) and Michaelis-Menten fits (solid lines), for six values of the dynamic range α. The case $\alpha = 0$ corresponds to an idealized limit where the fluorescence signal due to uncleaved reporter is identically zero. As predicted above, the apparent cleavage velocity decreases with increasing α. Figure A.2 shows the corresponding values of k_{cat} and K_M stemming from the Michaelis-Menten fit. k_{cat} linearly decreases with increasing α but the estimation of K_M is visibly independent from the value of α. We attribute this to the fact that the apparent Michaelis-Menten curves (shown in Figure A.2) are homotheties of ratio $\lambda = 1 - \alpha$ of the true curve ($\alpha = 0$). The saturating velocity $v_{max} = k_{cat}\,[E]_0$ depends on the absolute values of the reaction velocities,

which explains the variations in the apparent k_{cat}. In addition, the shape of the Michaelis-Menten curves is conserved by homotheties, and thus the computed value of K_M is not affected by $\lambda \neq 1$.

In conclusion, unlike the inner filter that affects both k_{cat} and K_M (and leaves η relatively unaffected), neglecting the background signal from reporters significantly impairs the accuracy of the determination of k_{cat} and η but does not alter the one of K_M.

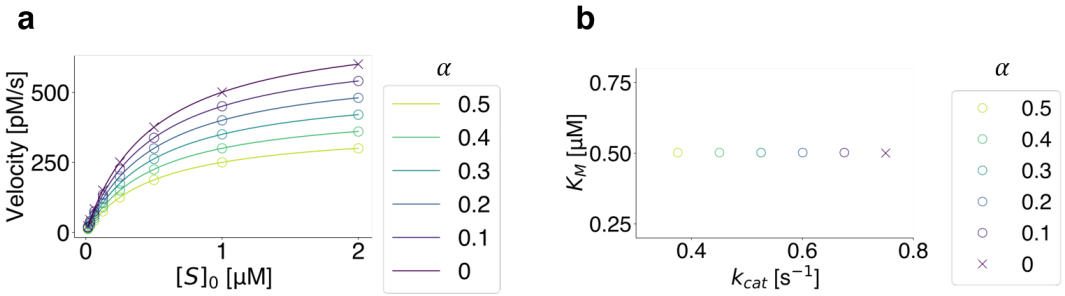

Figure A.2: Influence of the dynamic range $\alpha = \frac{F_{UcI}}{F_{CI}}$ on the estimation of k_{cat} and K_M. a Michaelis-Menten curves for six values of α. Shown are apparent velocities (circles) and Michaelis-Menten fits (solid lines). The case $\alpha = 0$ (crosses) corresponds to the ideal case where the signal due to uncleaved reporter is exactly zero and yields the theoretical values $k^*_{cat} = 0.75$ s^{-1} and $K^*_M = 0.5$ µM. b Corresponding values of the kinetic parameters k_{cat} and K_M.

A.3 Benchmark of the pipetting model

This section presents a benchmarking of the pipetting model we developed in chapter 2. For this benchmark, we compare the theoretical distribution derived in chapter 2 (section "Model for the uncertainty associated with pipetting and serial dilutions", see Equation 2.14 in chapter 2) to a distribution of the concentration obtained using a Monte Carlo simulation. Figure A.3 shows the distribution of 10,000 realizations of the pipetting protocol (Monte Carlo simulation, histogram) and the predicted distribution (solid line, Equation 2.14 in chapter 2) for seven dilutions of a stock solution (concentration $s_0 = 2$ µM, dilution factor $f = 2$ for each dilution). There is very good agreement between the results from the Monte Carlo simulation and the predicted distributions. The absolute variance in $[S]_{0,n}$ decreases with increasing dilutions but the coefficient of variation $CV_n = \frac{\sigma([S]_{0,n})}{\mathbb{E}([S]_{0,n})}$ (ratio of the standard deviation and mean of the n^{th} dilution concentration) increases with increasing dilutions.

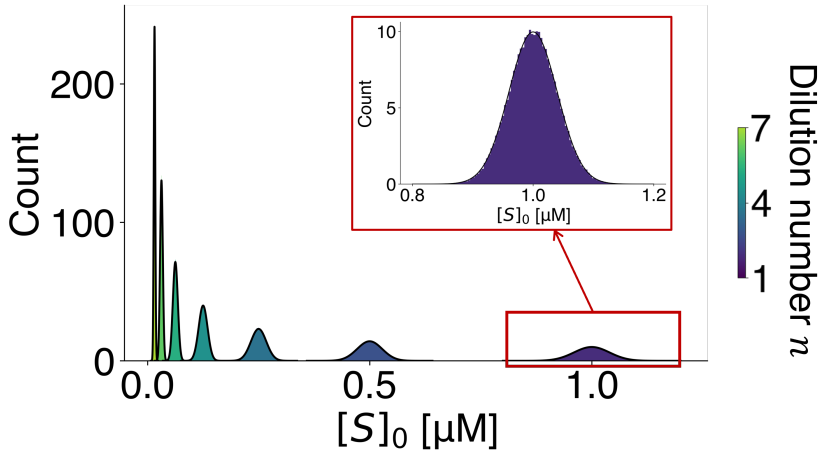

Figure A.3: Benchmark of the pipetting model against Monte Carlo simulations. Shown are distributions of 10,000 realizations for the concentration of dilutions based on the pipetting protocol (histogram) and the predicted distribution (solid line). The inset shows a close-up of the first dilution.

A.4 Influence of the number of replicates

In this section, we analyze the influence of performing replicates on the uncertainty on k_{cat} and K_M. Most experimental studies of enzyme kinetics perform replicates to reduce uncertainty on the reported kinetic parameters. Here, similarly to what is done in chapter 2 (section "Estimates of uncertainty distributions of k_{cat} and K_M based on Monte Carlo simulations" in chapter 2), we generate sets of eight progress curves (corresponding to eight dilutions $[S]_{0,n}$) using the closed-form solution of the fluorescence signal (Equation 2.10). Each progress curve is a realization of the pipetting error model for $[S]_0$ and $[E]_0$ developed in chapter 2 (section "Model for the uncertainty associated with pipetting and serial dilutions"). To mimic replicates, each progress curve is simulated n_r times (for $n_r = 1, 3, 6, 10$). The Michaelis-Menten fit is then performed as a single curve fitted to all $8n_r$ points. This entire process was then repeated 10,000 times in the Monte Carlo simulation. Hence, we simulated a total of $80,000n_r$ progress curves.

Figures A.4a, c, e, and g show distributions of initial reaction velocities (averaged along replicates) versus initial substrate concentration $[S]_{0,n}$ for varying number of replicates n_r. The uncertainties on both velocities and initial substrate concentrations decrease with increasing n_r. Figures A.4b, d, f, and h show the corresponding k_{cat} and K_M distributions resulting from the Michaelis-Menten fit. As expected, the uncertainty on the final estimation of both k_{cat} and K_M decreases with increasing n_r. Moreover, the distribution of K_M in the no replicate case ($n_r = 1$) is slightly skewed toward higher values. This skew is important as it shows that unbiased random errors in $[S]_{0,n}$ (and $[E]_0$) can cause a bias error in K_M. This skewness quickly diminishes with increasing repetitions n_r in accordance with Central Limit Theorem [195].

Next, we analyze the effects of all of the uncertainties concerted in the current study on the uncertainty

of k_{cat} and K_M. To this end, Figure A.5 shows distributions of k_{cat} and K_M for the combined effect of the following sources of uncertainty: pipetting uncertainty, omission of IFE, (improper) omission of uncleaved reporter signal in calibration, and omission of the flat-field correction (Equation 2.16 in chapter 2). We show these uncertainties for the case where triplicates (i.e., three progress curves per initial substrate concentration in the Michaelis-Menten curve, $n_r = 3$) are performed (A.5a) and for the case where they are not (i.e., one progress curve per initial substrate concentration, $n_r = 1$) (A.5b). Similarly to Figure A.4, the uncertainty on k_{cat} and K_M clearly decreases if triplicates of the progress curves are performed.

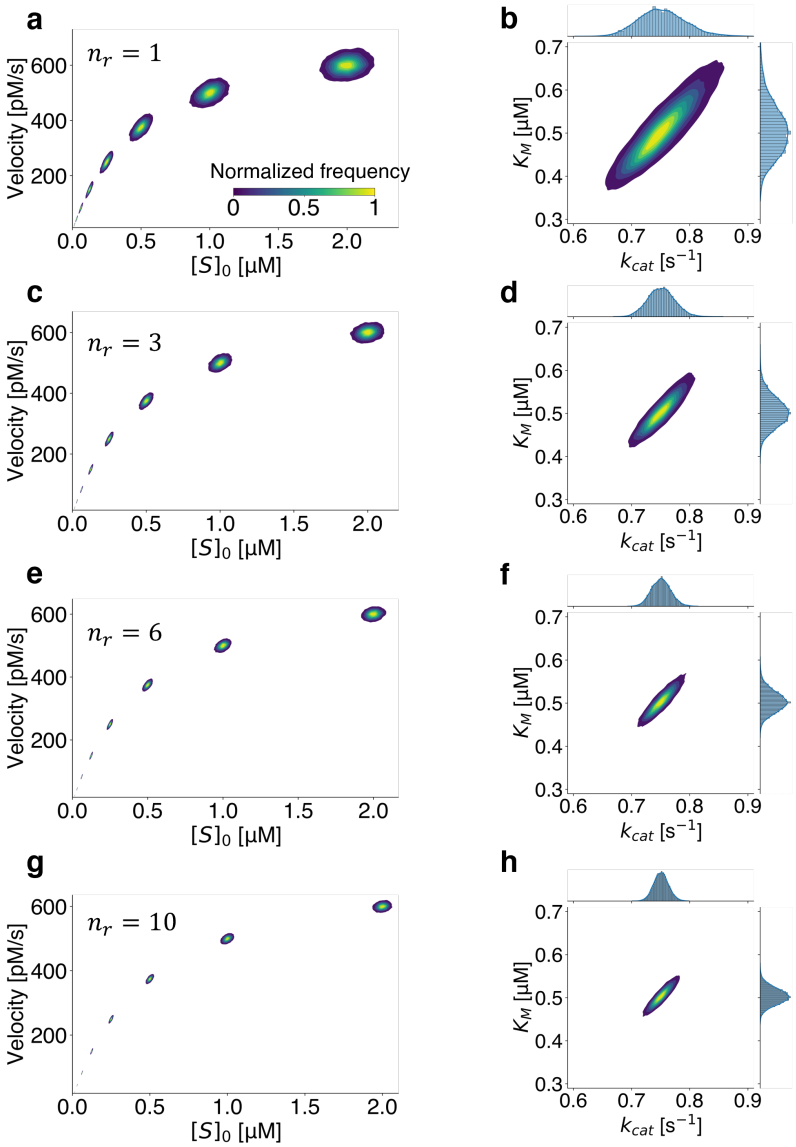

Figure A.4: Influence of the number of replicates on the uncertainty of k_{cat} and K_M for pipetting errors only. Shown are plots similar to Figures 2.1c and 2.1d for varying number of replicates n_r. a, c, e, and g show the distributions of the mean (along replicates) reaction velocities vs initial substrate concentration accounting for the pipetting error distribution given by Equation 2.14. a, c, e, and g respectively correspond to $n_r = 1, 3, 6$ and 10. b, d, f, and h show the respective distributions of k_{cat} and K_M. Exact values of the kinetic parameters (used to generate the simulated progress curves) are $k^*_{cat} = 0.75$ s^{-1} and $K^*_M = 0.5$ μM.

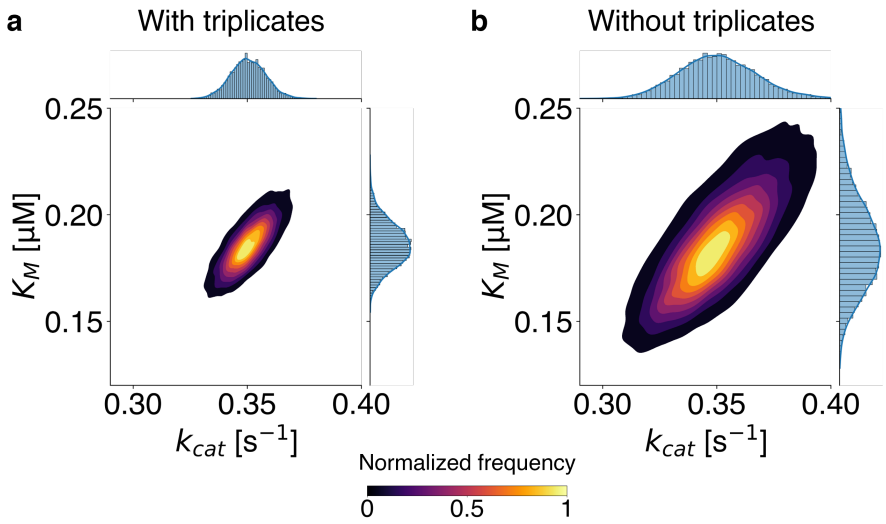

Figure A.5: Influence of the number of replicates on the uncertainty of k_{cat} and K_M for superposed sources of uncertainty. Shown are plots similar to 2.1d considering triplicates (a) or not (b). These simulations take into consideration several sources of uncertainty and bias: omission of the uncleaved reporter signal ($\alpha = 0.1$), omission of the inner filter effect ($c_0 = 7$ μM), and an estimate of typical pipetting error in both $[S]_0$ and $[E]_0$ (10,000 realizations of our pipetting error model). This corresponds to the case (a)+(b)+(c)+(d) in Figures 2.2 and 2.5, with the addition of the flat-field effect. Exact values of the kinetic parameters (used to generate the simulated progress curves) are $k^*_{cat} = 0.75$ s^{-1} and $K^*_M = 0.5$ μM.

A.5 Experimental signal from the thermal cycler

In this section, we present the raw experimental data collected by Huyke et al. [2] The latter study used these data (and significant additional data) to demonstrate that the kinetic rate parameters of CRISPR-Cas enzyme systems largely govern the achievable limits of detection with these systems. Huyke et al. [2] analyzed Michaelis-Menten type data for LbCas12a, AsCas12a, AapCas12b, LbuCas13a and LwaCas13a. For the current study, these data serve as a case example to show how the correction of optical effects and the number of points (i.e., values of $[S]_0$ resulting from serial dilutions) in the Michaelis-Menten curve affect uncertainties in k_{cat}, K_M and η (see Figures 2.3 and 2.4).

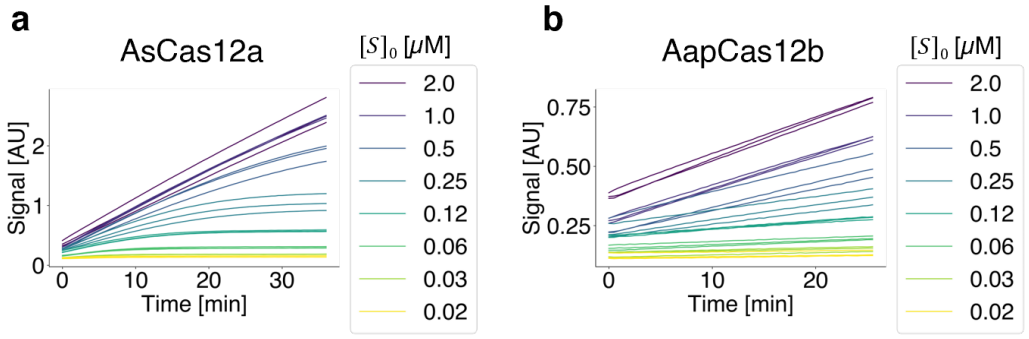

Figure A.6: Measured fluorescent signal versus time for two CRISPR-Cas systems: AsCas12a (a) and AapCas12b (b). Shown is the signal from a MiniOpticon thermal cycler (Bio-Rad Laboratories Inc., CA, USA) for eight substrate concentrations. Triplicates are plotted with the same color.

A.6 Fitting routine

We here summarize the curve fitting protocol we used to analyze extraction of kinetic rate parameters from progress curves and the Michaelis-Menten curve. All fits were performed using SciPy [95], an open-source package in Python [94] for mathematics, science, and engineering. All fits were performed using the function `curve_fit` in the `optimize` module. This function uses the Levenberg-Marquardt algorithm to solve the following non-linear least squares problem:

Find $\hat{\beta} = (\hat{k}_{cat}, \hat{K}_M)$ such that:

$$\hat{\beta} \in \text{argmin}_\beta \sum_{i=1}^{N} \left[v_{0,i} - f\left([S]_{0,i}, \beta\right) \right], \tag{A.19}$$

with:

$$f\left([S]_{0,i}, \beta\right) = f\left([S]_{0,i}, k_{cat}, K_M\right) = -\frac{k_{cat}\,[E]_0\,[S]_{0,i}}{K_M + [S]_{0,i}}. \tag{A.20}$$

Here, the initial activated enzyme concentration $[E]_0$ is known, $[S]_{0,i}$ is the initial substrate concentration, and the $v_{0,i}$ are the measured initial reaction velocities (from progress curves). N is the number of points in the Michaelis-Menten curve. The only unknown is therefore β.

We verified the performance of our protocol using several sample datasets which we pre-generated with known values of k_{cat} and K_M. Our code systematically yielded the exact input values of k_{cat} and K_M, even for low number of points in the Michaelis-Menten curve (see Figure 2.2 in chapter 2).

We compared the fitting routine described above to similar algorithms implemented in MATLAB and GraphPad Prism, two proprietary software packages that are often reported for Michaelis-Menten fits [19, 2, 196]. We performed tests where we used each routine to extract kinetic rate parameters from simulated progress curve data (using known kinetic rates). We performed these tests with and without typical

uncertainties in the form of random noise. We found that, on the same set of tests points and with known values of k_{cat} and K_M, our Python algorithm and GraphPad Prism resulted in, by far, the highest accuracy. As one example, one fit performed in MATLAB resulted in more than 90% relative error on k_{cat} and 70% relative error on K_M, without any noise added to the data. Our Python algorithm and GraphPad Prism fits both resulted in relative errors smaller than 1% on the same dataset.

A.7 *Cis*-cleavage in CRISPR-based diagnostics

We here briefly discuss the *cis*-cleavage step in CRISPR-based diagnostics. *Cis*-cleavage consists of the recognition of the target nucleic acid and then cleavage of the target nucleic acid as well as activation of the CRISPR-Cas enzyme. This activation initiates the indiscriminate activity of the enzyme (called *trans*-cleavage).

As described by Strohkendl et al. [34], the kinetics of the *cis*-cleavage step can be treated as a second-order reaction wherein the inactivated enzyme and the target are reactants and the activated enzyme (and cleaved target) are the products. The single turnaround *cis*-cleavage reaction can then be summarized with the following equation:

$$I + T \rightarrow E + N \tag{A.21}$$

Here, I is the inactivated Cas enzyme, T the target nucleic acid, E the activated enzyme and N the cleaved target nucleic acid.

For the typical case of concentrations of Cas12a much higher than that of target, the reaction is in the pseudo first-order regime (i.e., under the assumption $[I](t) \approx [I]_0$). Hence, the timescale of completion of this target recognition step scales inversely with the product of the kinetic on-rate of the recognition reaction (Equation A.21) and the Cas12a concentration (the abundant species). This has been confirmed experimentally for the case of AsCas12a by, for example, using single-molecule fluorescence imaging and single-molecule fluorescence energy transfer (FRET) [32]. Hence, even for trace target concentration, the *cis*-cleavage reaction occurs rapidly with typical reaction completion times of order 100 s [34, 110, 31, 33, 36]. The *trans*-cleavage is therefore the rate-limiting step in CRISPR-based assays. For these reasons, we here concentrate on the *trans*-cleavage kinetics and apply the Michaelis-Menten model to model the kinetics of the transduction mechanism in Figure 2.1 in chapter 2.

Appendix B

Supplementary Information for Degradation of reporter molecules imposes a fundamental limit of detection on CRISPR diagnostics

B.1 Signal calibration: basics and improvements

We here summarize successive improvements that have been reported in the calibration of fluorescence signals in CRISPR-based assays. As mentioned in chapter 3, errors in this process have led to gross errors in the estimation of the kinetic rates and limit of detection of CRISPR assays. Despite published corrections to these errors, most studies still do not report calibration data [8]. Studies which report at least some calibration data typically report a proportional relationship between fluorescence intensity and cleaved reporter concentration as follows [197, 37, 196]:

$$I(t) = F[P](t), \tag{B.1}$$

where F is a constant estimated using a calibration curve that depends on the reporter (including both fluorophore and quencher), the detection device, and the calibration process. Recall that $I(t)$ denotes the fluorescence intensity measured by the detector (in arbitrary units, such as RFU) and $[P]\,(t)$ is the time-dependent concentration of cleaved reporters (in molar units, such as nM). As we discuss later in below and in chapter 3, this simple relationship is overly simple and erroneous. As indicated by Figure 3.1b, a more complete calibration should account for other sources of signal. Ramachandran and Santiago [29]

first suggested the following correction to account for uncleaved reporters:

$$I(t) = F_{Cl}[P](t) + F_{Ucl}[S](t). \tag{B.2}$$

Here, $[S](t)$ is the uncleaved reporter concentration, and F_{Cl} and F_{Ucl} refer to calibration constants relative to the cleaved and uncleaved reporters, respectively. The second term on the right-hand-side (RHS) of this relation is depicted schematically by the row labeled "background reporter signal" in Figure 3.1b. This term can exceed the magnitude of the first term, particularly for low target concentrations and/or near the beginning of the *trans*-cleavage reaction. Despite the importance of the second term, this calibration method has been adopted by a minority of published studies [198, 108].

Equation B.2 is more complete than equation B.1 but can be improved upon significantly. In particular, depending on the vertical heights of liquids in reaction vessels, the quencher molecules in these systems can (whether a reporter is cleaved or not) strongly absorb fluorescence signals emitted by cleaved reporters. This potentially very strong absorbance effect is the so-called "inner-filter" effect associated with Beer-Lambert type photon absorption [90]. Huyke et al. [2] introduced the following calibration to account for this phenomenon:

$$I\left(t\right) = 10^{-\frac{[S]_0}{c_0}} \left(F'_{Cl}\left[P\right]\left(t\right) + F'_{Ucl}\left[S\right]\left(t\right)\right). \tag{B.3}$$

Here, F'_{Cl}, F'_{Ucl}, and c_0 are calibration constants, $[S]_0 = [S]\left(t = 0\right)$ is the total concentration of reporters in the reaction. A second important factor is that arrays of detectors (as in typical thermal cyclers) can be highly non-uniform in their response—even after careful servicing and maintenance of the system. We provide in Section B.8 below example responses from two machines. An effective mitigation strategy is to implement a "flat-field" correction for the detector array (a term we borrow from the image analysis field). Blanluet et al. [85] first suggested the following calibration relationship to account for the two latter effects:

$$I\left(t\right) = 10^{-\frac{[S]_0}{c_0}} \left(F'_{Cl}\left[P\right]\left(t\right) + F'_{Ucl}\left[S\right]\left(t\right)\right)\left(I_{FF} - I_{BG}\right) + I_{BG}. \tag{B.4}$$

I_{FF} and I_{BG} are respectively the flatfield and background signal arrays (associated with the array of reaction-tube-specific detectors). In their approach, I_{FF} and I_{BG} were averages in time [85, 199]. We note that, in our experience, detectors in typical thermal cyclers do not respond uniformly even after careful servicing of the system by its manufacturer. Neglecting the inner-filter effect and the flat-field correction can lead to large errors in the proper quantification of the reaction [49]. To our knowledge, the calibration introduced by Blanluet et al. [85] is the most complete calibration method for CRISPR-based assays published to date.

In this work, we introduce an improvement on the calibration described by Blanluet et al. [85] and summarized by equation B.4. Namely, to account for reporter degradation, we incorporate a time-dependence to the aforementioned flatfield and background signal arrays. Hence, we consider the fact that the fluorescence signal measured during the background and flatfield measurements is not constant (in time). Accordingly,

we introduce the following new calibration relationship:

$$I^{corr}(t) = \frac{I(t) - I_{BG}(t)}{I_{FF}(t) - I_{BG}(t)} = 10^{-\frac{[S]_0}{c_0}} \left(F'_{Cl}[P](t) + F'_{Ucl}[S](t)\right). \tag{B.5}$$

As before, the quantities denoted by I are two-dimensional arrays of detector signals. I_{FF} and I_{BG} are respectively the flatfield and background signal arrays (associated with the array of reaction-vessel-specific detectors).

B.2 Closed-form solution for the Michaelis-Menten system in the low target limit

In this section, we derive an approximate relation for the (flatfield-corrected) fluorescent signal in the limit of trace concentrations of target ($[E]_0 \to 0$) and without reporter degradation ($k_{rep} = 0$). That is, we present here a detailed derivation of equation 3.3. As mentioned in chapter 3, we denote this fluorescence intensity by $I^{corr}_{naïve}(t)$. Using the analytical solution reported by Avaro and Santiago [49, 89]:

$$I^{corr}_{naïve}(t; [E]_0) = 10^{-\frac{[S]_0}{c_0}} \left(F'_{Ucl} K_M \mathcal{A}(t) + F'_{Cl}\left([S]_0 - K_M \mathcal{A}(t) - [E]_0 \frac{\mathcal{A}(t)}{1 + \mathcal{A}(t)}\right)\right), \tag{3.1}$$

where:

$$\mathcal{A}(t) = W\left(\frac{[S]_0}{K_M} \exp\left(\frac{[S]_0}{K_M} - \frac{k_{cat}}{K_M}[E]_0 t\right)\right). \tag{3.2}$$

In the limit where $[E]_0 \to 0$:

$$\mathcal{A}(t) \approx W\left(\frac{[S]_0}{K_M} \exp\left(\frac{[S]_0}{K_M}\right)\left(1 - \frac{k_{cat}}{K_M}[E]_0 t\right)\right), \tag{B.6}$$

Alternately,

$$\mathcal{A}(t) \approx \frac{[S]_0}{K_M} - \left(\frac{[S]_0}{K_M} \exp\left(\frac{[S]_0}{K_M}\right)\frac{k_{cat}}{K_M}[E]_0 t\right) W'\left(\frac{[S]_0}{K_M} \exp\left(\frac{[S]_0}{K_M}\right)\right). \tag{B.7}$$

We recall the following identities for the Lambert-W function:

$$W(xe^x) = x, \tag{B.8}$$

$$W'(x) = \frac{1}{x + \exp(W(x))}, \tag{B.9}$$

so that:

$$W'\left(\frac{[S]_0}{K_M} \exp\left(\frac{[S]_0}{K_M}\right)\right) = \frac{1}{\left(1 + \frac{[S]_0}{K_M}\right) \exp\left(\frac{[S]_0}{K_M}\right)}. \tag{B.10}$$

Whence,

$$\frac{K_M}{[S]_0}\mathcal{A}(t) \approx 1 - \frac{\frac{k_{cat}}{K_M}[E]_0 t}{1 + \frac{[S]_0}{K_M}}, \tag{B.11}$$

Next, keeping only first order terms in $[E]_0$:

$$\frac{[E]_0}{[S]_0}\frac{\mathcal{A}(t)}{1+\mathcal{A}(t)} \approx \frac{\frac{[E]_0}{K_M} - \frac{\frac{k_{cat}}{K_M^2}[E]_0^2 t}{1+\frac{[S]_0}{K_M}}}{1 + \frac{[S]_0}{K_M} - \frac{\frac{[S]_0}{K_M}\frac{k_{cat}}{K_M}[E]_0 t}{1+\frac{[S]_0}{K_M}}} \approx \frac{\frac{[E]_0}{K_M}}{1 + \frac{[S]_0}{K_M} - \frac{\frac{[S]_0}{K_M}\frac{k_{cat}}{K_M}[E]_0 t}{1+\frac{[S]_0}{K_M}}}. \tag{B.12}$$

Re-ordering equation 3.1:

$$I^{corr}_{naïve}(t) = 10^{-\frac{[S]_0}{c_0}}[S]_0\left(F'_{Cl} + \left(F'_{Ucl} - F'_{Cl}\right)\frac{K_M}{[S]_0}\mathcal{A}(t) - F'_{Cl}\frac{[E]_0}{[S]_0}\frac{\mathcal{A}(t)}{1+\mathcal{A}(t)}\right). \tag{B.13}$$

This yields:

$$I^{corr}_{naïve}(t) = 10^{-\frac{[S]_0}{c_0}}[S]_0\left(F'_{Cl} - \left(F'_{Cl} - F'_{Ucl}\right)\left(1 - \frac{\frac{k_{cat}}{K_M}[E]_0 t}{1+\frac{[S]_0}{K_M}}\right) - F'_{Cl}\frac{\frac{[E]_0}{K_M}}{1 + \frac{[S]_0}{K_M} - \frac{\frac{[S]_0}{K_M}\frac{k_{cat}}{K_M}[E]_0 t}{1+\frac{[S]_0}{K_M}}}\right), \tag{B.14}$$

which, to first order, simplifies to:

$$I^{corr}_{naïve}(t) = 10^{-\frac{[S]_0}{c_0}}[S]_0\left(F'_{Cl}\left(1 - \frac{\frac{[E]_0}{K_M}}{1+\frac{[S]_0}{K_M}}\right) - \left(F'_{Cl} - F'_{Ucl}\right)\left(1 - \frac{\frac{k_{cat}}{K_M}[E]_0 t}{1+\frac{[S]_0}{K_M}}\right)\right). \tag{3.3}$$

Figure B.1 shows a comparison of the expected fluorescence signal versus time as predicted by the full Michaelis-Menten model (simulation, symbols) and the corresponding analytical approximation given by equation 3.3. The inset shows the relative error as a function of the ratio $[E]_0/[E]_{0,LoD}$ after 60 min. $[E]_{0,LoD}$ is provided by equation 3.22. We used the following values for this simulation: $k_f = 10^{10}$ $M^{-1}s^{-1}$, $k_{cat} = 2.0$ s^{-1}, and $K_M = 3.6$ μM. All simulations were performed using ode23s, a built-in solver for stiff ODE system in MATLAB 2024a. The approximation given by equation 3.3 yields a satisfactory approximation of the closed-form solution, especially in the low target concentration regime which is of most interest here. We use equation 3.3 to derive an expression for the limit of detection.

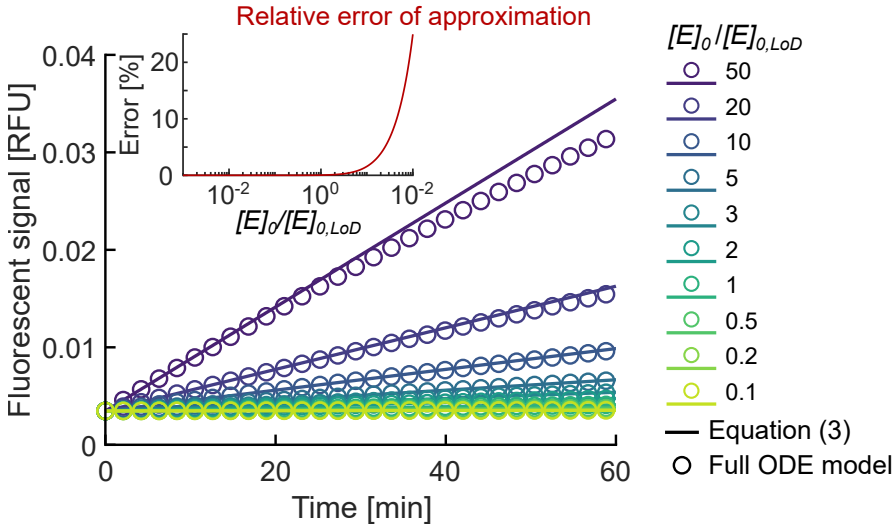

Figure B.1: Comparison of the analytical solution derived in the low target limit and the full Michaelis-Menten solution. a Fluorescent signal predicted by the full Michaelis-Menten system (symbols), and the Taylor expansion in equation 3.3. The inset shows the corresponding relative error, in %, between the two solutions after 60 min. Note how the error converges rapidly to zero in the low target limit. Values of k_{cat} and K_M are the same than used in Figure 3.2. Calibration constants are reported in Section B.8.

B.3 Analytical solutions and simulations results for the reaction velocity

Figure B.2 shows reaction velocity predictions for varying target concentration. Reaction velocities are normalized by the background degradation velocity $k_{rep}\,[S]_0$, and target concentrations are normalized by the characteristic concentration $[E]_{0,LoD}$ as defined in equation 3.22. Shown are predictions using numerical simulations of the ODE system corresponding to the Michaelis-Menten system (green circles), or to our augmented ODE system which accounts for reporter degradation (orange squares, equations 3.8 to 3.15). For comparison, we also provide the reaction velocity prediction given by equations 3.5 (green line, no reporter degradation) and 3.16 (orange line, reporter degradation set by $k_{rep} = 1.4 \times 10^{-6}$ s^{-1}). Figure B.2 shows a very good agreement between the analytical expressions and the simulations results over a large range of target concentrations.

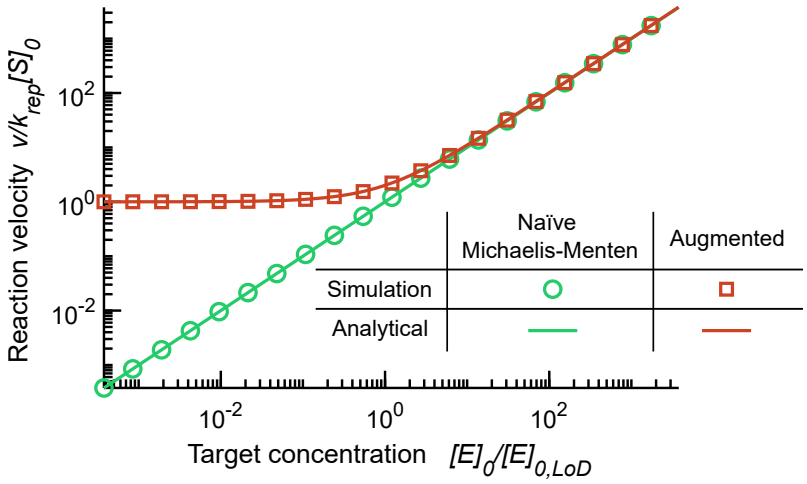

Figure B.2: Reaction velocity estimations based on numerical simulations and analytical solutions. Shown are normalized reaction velocities computed using either a numerical ODE solver (symbols) or using analytical expressions for the reaction velocity (solid lines), accounting (orange) or not (green) for the reporter degradation. Analytical solutions are reported as equations 3.5 and 3.16.

B.4 Estimation of the endpoint fraction of cleaved reporters

Figure B.3 shows contours of the predicted cleaved reporter fraction (a measure of the signal-to-background ratio) after 1h of reaction for varying initial reporter concentration and varying target concentration. Figure B.3a (left) shows the estimation from the naïve model (analogous to Figure 5 of Ramachandran and Santiago [29]), and Figure B.3b (right) shows the prediction from our augmented model (equations 3.8 to 3.15). We used the following values for this simulation: $k_f = 10^{10}$ $M^{-1}s^{-1}$, k_{cat}=2.0 s^{-1}, $K_M = 3.6$ µM, and $k_{rep} = 1.4 \times 10^{-6}$ s^{-1}. We observe that the degree of completion of the reaction varies greatly between the two models. Without accounting for the reporter degradation (B.3a), the amount of cleaved reporter remains a strong function of the target concentration as the latter decreases. Conversely, if reporter degradation is accounted for (B.3b), then the amount of cleaved reporter becomes roughly independent of target concentration for concentrations lower than about 1 pM. This implies that any target detection (and therefore, quantification) becomes particularly challenging, and the signal-to-background ratio becomes extremely low.

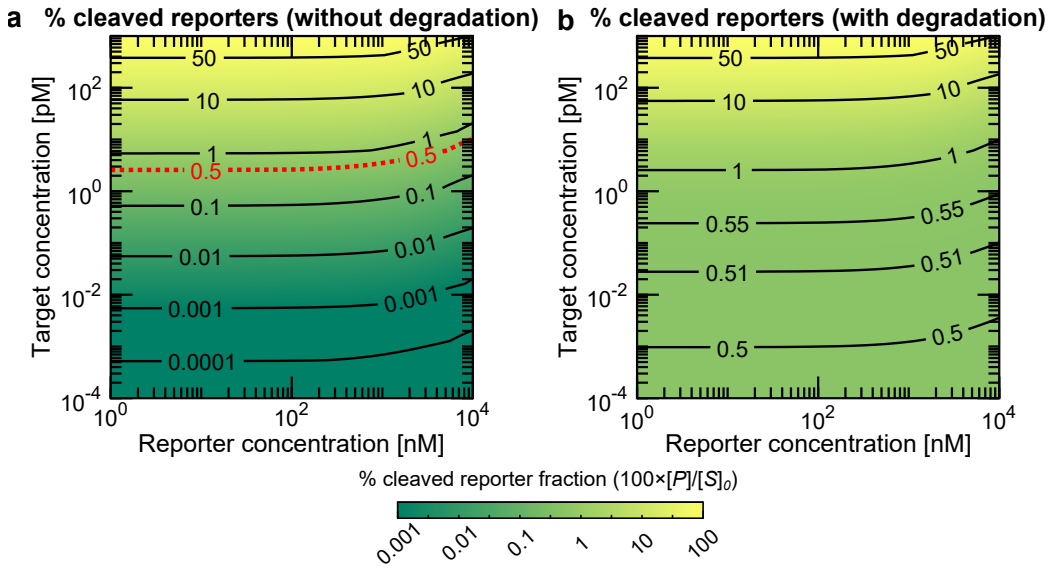

Figure B.3: Fraction of cleaved reporters (in % of total amount of reporters in solution) after 1h of reaction, using k_{cat}, K_M from Figure 3.4. a is shown without degradation (i.e., $k_{rep} = 0$), b with degradation ($k_{rep} = 1.4 \times 10^{-6}$ s^{-1}). As target concentration decreases, the augmented model with degradation asymptotes to a nonzero value.

B.5 Effect of late readout with varying delay times

In this section, we detail the influence of the so-called "late readout effect" on the estimated reaction velocity. As described in chapter 3, handling and mixing reagents, reaching incubation temperature, and initiating data acquisition require a finite time. This implies that a significant time delay may elapse between the start of the reaction (i.e., when reagents are mixed) and the instant at which the reaction velocity is measured. We denote this time τ_{pre}. This time can include pipetting of reagents into a reaction tube or plate; sealing of the tube or plate; loading of the tubes or plate into a thermal cycler; closing the thermal cycler; initiating a run (e.g., pressing buttons on the system); and the thermal cycler's time heating and reaching the set incubation temperature. The latter time ends when data acquisition begins.

Figure B.4 shows the predicted reaction velocity for varying initial target concentration for four values of this time delay τ_{pre} (1, 2, 5, and 7 min). Reaction velocities are normalized by the background degradation velocity $k_{rep}\,[S]_0$, and target concentrations are normalized by the characteristic concentration $[E]_{0,LoD}$ as defined in equation 3.22. Reaction velocities were computed using a numerical solution to the full ODE system (equations 3.8 to 3.15). As a reference, we also show the reaction velocity predicted by the "naïve" Michaelis-Menten model (dashed green) and our augmented kinetic model which accounts for reporter degradation, without any late readout ($\tau_{pre} = 0$, dashed orange). We used the following values for this simulation: $k_f = 10^{10}$ M^{-1}s^{-1}, $k_{cat} = 2.0$ s^{-1}, $K_M = 3.6$ µM, and $k_{rep} = 1.4 \times 10^{-6}$ s^{-1}. Figure B.4 shows

significant discrepancies between the kinetics models that do not account for the late readout effect (dashed lines) and the ones that do (solid lines) for high target concentrations only. Models that account for the late readout underestimate the initial reaction velocity because this velocity decays with time (with characteristic time $\tau_{MM} = \frac{K_M}{k_{cat}[E]_0}$) [29]. Significant discrepancies between the two models arise when τ_{MM} is smaller than (or on the order of) τ_{pre}. For low target concentrations, $\tau_{MM} \gg \tau_{pre}$, and the late readout effect becomes negligible. As a reference, we defined in chapter 3 a characteristic concentration $[E]_{0,late}$, defined such that $\tau_{MM} = \tau_{pre}$. Analysis of signals of target concentrations above $[E]_{0,late}$ should consider the late readout effect.

The late readout effect that we describe here has been observed in experimental data both from the current work and previous studies [2]. That is, reactions velocities measured for high target concentrations are lower than the ones predicted by the Michaelis-Menten model. However, we note that this effect only becomes significant at very high target concentrations and has limited influence on the reaction kinetics for trace amounts of target which are often the cases of interest for diagnostics purposes.

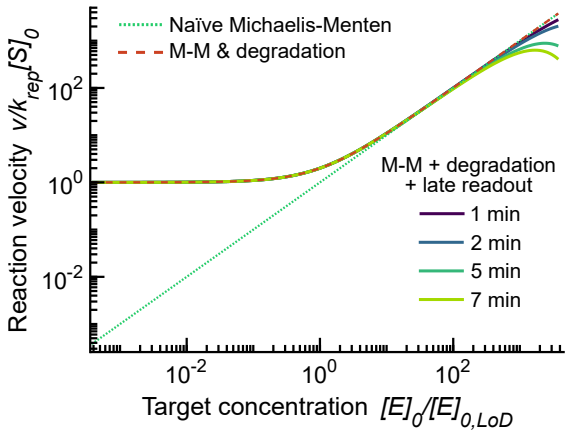

Figure B.4: Effect of late readout for varying delay time between the start of the reaction and the velocity readout. Shown are simulation results for the ODE system presented as equations 3.8 to 3.15 (solid lines), wherein the reaction velocity is evaluated after 1, 2, 5, or 7 min. As comparison, we provide the reaction velocity predicted by the Michaelis-Menten model (dotted green) and our augmented kinetics model that accounts for reporter degradation (equation 3.16, dashed orange).

B.6 Influence of k_{rep} and k_{cat} on the measured reaction velocity

Figure B.5 shows the predicted initial reaction velocity versus initial target concentration, for variations of k_{rep} and k_{cat}. Shown are numerical simulation results of the full ODE system (equations 3.8 to 3.15) for two values of k_{cat} and k_{rep}. We used the following values for this simulation: $k_f = 10^{10}$ M^{-1}s^{-1}, $k_{cat,1} = 2.0$ s^{-1}, $k_{cat,2} = 0.2$ s^{-1}, $K_M = 3.6$ µM, $k_{rep,1} = 1.4 \times 10^{-6}$ s^{-1}, and $k_{rep,2} = 1.4 \times 10^{-7}$ s^{-1}. Velocities are measured

after a time delay of $\tau_{pre} = 5$ min to incorporate the late readout effect.

We distinguish two regimes. At low target concentrations, the curves corresponding to simulations that used identical values of k_{rep} (i.e., same color) coincide. This corresponds to the regime wherein the reporter degradation dominates over the enzymatic *trans*-cleavage. The noise floor in this regime ($k_{rep}\ [S]_0$) is independent of target concentration. At higher target concentrations, the curves corresponding to simulations that used identical values of k_{cat} (i.e., same line style, dashed or solid) coincide. In this regime, the reaction velocity is mostly set by the *trans*-cleavage reaction and the reporter degradation (hence, the influence of k_{rep}) is negligible.

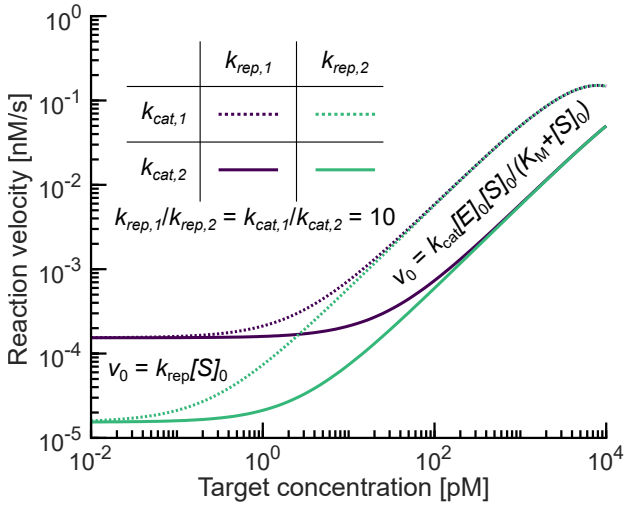

Figure B.5: Reaction velocities versus target concentration for varying values of k_{cat} and k_{rep}. Reaction velocity curves computed using the same value of k_{rep} are shown with the same color (purple for $k_{rep,1}$, blue for $k_{rep,2}$), whereas curves that use the same value of k_{cat} are shown with same line style (dashed for $k_{cat,1}$, solid for $k_{cat,2}$).

B.7 List of oligos used in this work

Table B.1: List of oligonucleotides used in this work. This table presents all oligonucleotides used in this work, including guide RNAs (gRNA), DNA targets, and reporters. All sequences are reported in 5' to 3' direction.

Name	**Sequence**
Reporters	[FAM] TTA TTA TT [BHQ1]
gRNA	UAA UUU CUA CUA AGU GUA GAU GUG GUA UUC UUG CUA GUU AC
TS	ATC GAA GCG CAG TAA GGA TGG CTA GTG TAA CTA GCA AGA ATA CCA CGA AAG CAA GAA AAA
NTS	TTT TTC TTG CTT TCG TGG TAT TCT TGC TAG TTA CAC TAG CCA TCC TTA CTG CGC TTC GAT

Analogy with qPCR TaqMan probes

We note that the degradation mechanism described in this work has some analogies to that observed in real-time qPCR experiments which use TaqMan probes [200, 201]. TaqMan probes are in part similar to CRISPR reporters in that they are synthetic oligonucleotides labeled with a fluorophore and a quencher. However, TaqMan probes are typically longer (18-22 bases, versus 5-8 bases for CRISPR reporters) and specific to a portion of the target sequence. Interestingly, in qPCR assays, the background degradation of TaqMan probes also results in an initially linear increase in fluorescence signal [200]. However, in the case of qPCR, this background signal is very typically easily distinguished from the exponential rise in signal associated with amplification, even for trace target concentrations. Hence, it is unlikely that TaqMan background signal rises would be confused with the amplification signal. In contrast to this, the discernment of signal versus background is extremely difficult in CRISPR assays, particularly for the case of trace concentrations. Consider that, with CRISPR, both the *trans*-cleavage and degradation signals rise linearly and *trans*-cleavage signal can be weaker than the degradation signal. The latter is particularly true when the sample concentration $[E]_0$ is significantly lower than the limit of detection $[E]_{0,LoD}$ (see equation 3.22).

B.8 Calibration protocol

We here provide the necessary calibration data that was used for all calibration steps described in chapter 3.

B.8.1 Flatfield correction

We found that the thermal cyclers used for this work (CFX384 Touch Real-Time PCR Detection System, Bio-Rad Laboratories) showed significant well-to-well differences in signals for equal concentrations of

fluorophores. This observation was observed and reported with other machines before [85, 49]. To account for this effect, all fluorescence intensities were corrected prior to calibration using the following flatfield correction:

$$I^{corr}(t) = \frac{I(t) - I_{BG}(t)}{I_{FF}(t) - I_{BG}(t)}. \tag{B.15}$$

We now detail the measurement procedure for I_{FF} and I_{BG}. For the flatfield image $I_{FF}(t)$, all wells of a 384-well plate (Hard-Shell 384-Well PCR Plates, thin wall, skirted) were filled with 20 µl of a solution of 10 µM fluorescein (Sigma-Aldrich) in nuclease-free water (NFW). To obtain the background image $I_{BG}(t)$, wells were filled with 20 µl NFW. Figure B.6 shows the time-averaged flatfield image measured over 35 min at 37°C for two different thermal cyclers. Figure B.7 shows the time-averaged background image measured over 35 min at 37°C for the same machines.

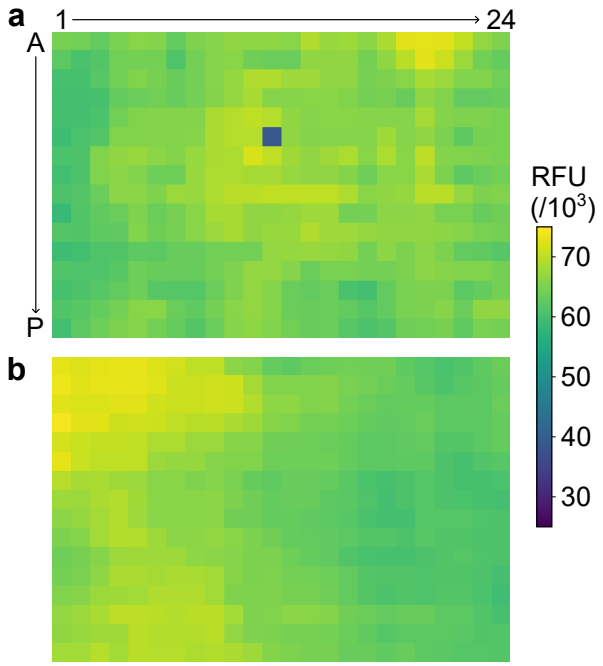

Figure B.6: Flat-field time-averaged image. Shown are raw signal values from the thermal cycler averaged over 35 min. Measurement were taken at 37°C.

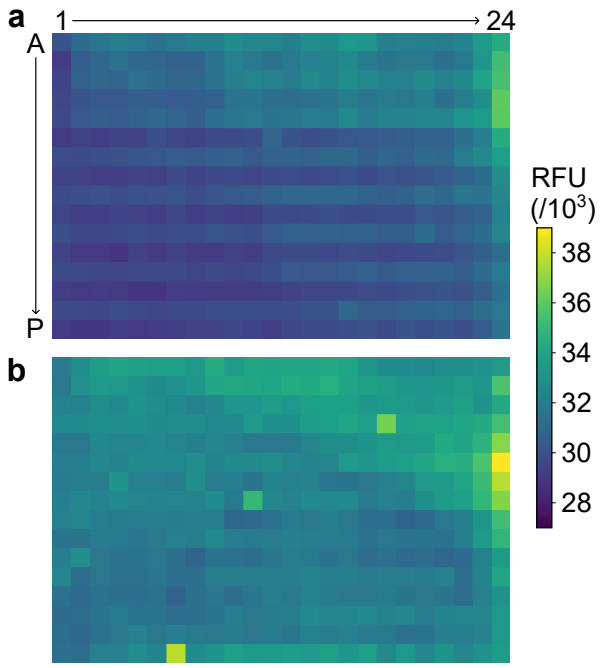

Figure B.7: Background time-averaged image. Shown are raw signal values from the thermal cycler averaged over 35 min. Measurements were taken at 37°C.

Further, we observed that the flatfield and background signals slightly increased with time. Figure B.8 shows time evolution of the flatfield data (B.8a) and the background data (B.8c). Even though this increase in signal is small compared to the absolute value of the signal, it introduces a bias in the measurement of the rate of increase of fluorescence, and, in turn, in the estimation of the reaction velocities. This bias is particularly important at trace target concentrations. Figures B.8b and B.8d show the distribution of fluorescence drifts among the wells, respectively for the flatfield and background data. In both cases, the distribution of fluorescence drifts is centered around a nonzero mean value. To account for these effects in our measurements of reaction velocities, we include a correction for this drift by accounting for the time-dependence of the flatfield and background images in equation 3.4. Note that, for typical enzyme kinetics measurements, the crucial background signal change with time is during the first ~1 min of reaction. In this short time, the background signals slightly decrease in time before leaving off.

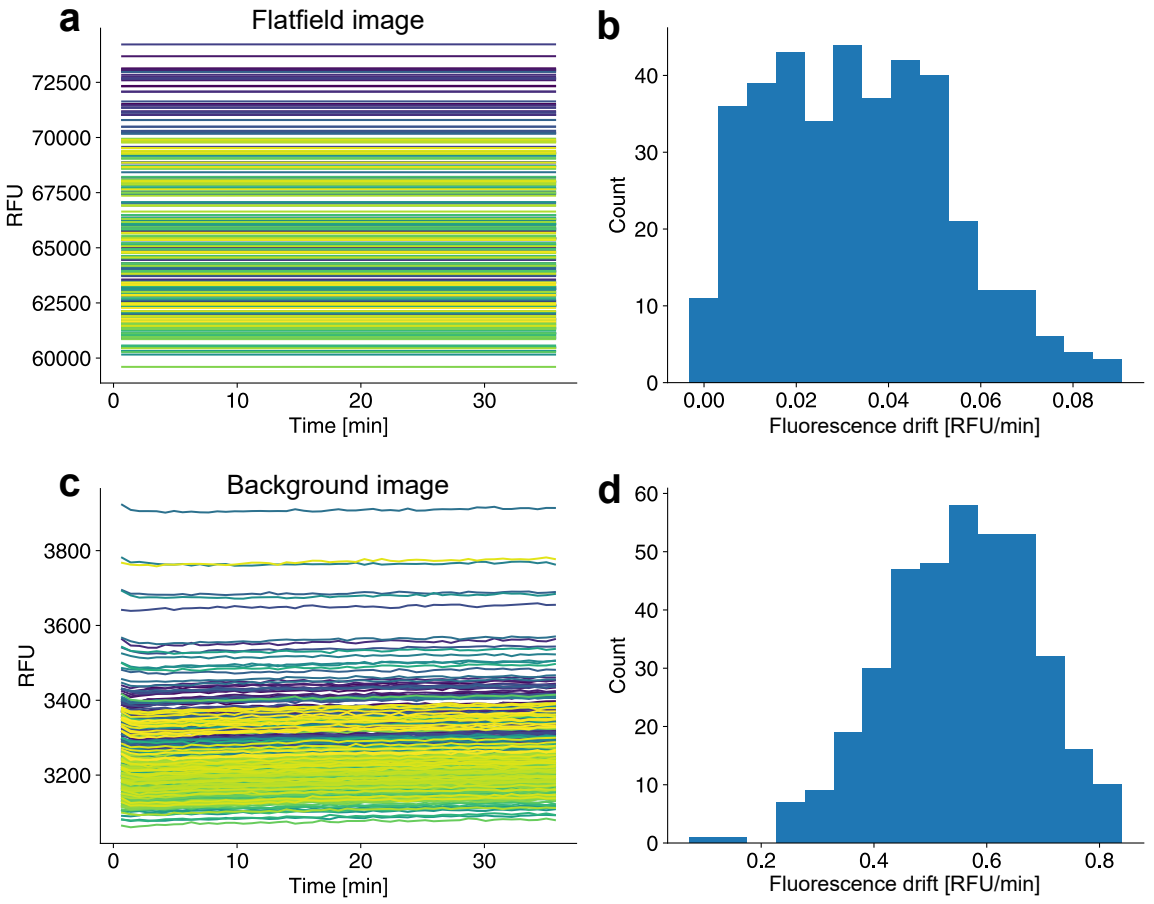

Figure B.8: Fluorescence measurements for flatfield and background images. a Raw fluorescence readouts for the flatfield image over time. b Distribution of the fluorescence increase rates (fluorescence drift) in a. c Raw fluorescence readouts for the background image over time. d Distribution of the fluorescence increase rates (fluorescence drift) in c.

B.8.2 Reporter calibration

Reporter molecules are composed of a short sequence of DNA functionalized with a fluorophore on one end, and a quencher molecule on the other end. The fluorophore and quencher modifications are attached to the nucleic acid via covalent bonds. The close proximity of the fluorophore and quencher causes the fluorescence emission of the fluorophore to be quenched via Förster resonance energy transfer (FRET) [202]. The result of this FRET is that energy received by the quencher is dissipated as heat (through non-radiative relaxation of the quencher molecule) rather than being emitted as light by the fluorophore. It is important to note that the presence of the quencher in the intact reporter does not perfectly prevent emission of light by the fluorophore [203]. That is, fluorescence is only partly quenched. Cleaving of the reporter molecule

(e.g., by the CRISPR-Cas enzyme) causes a physical separation between the fluorophore and the quencher, which strongly increases the quantum efficiency of the radiative fluorescence process [202, 12].

Solutions of varying concentrations were prepared using serial dilutions of cleaved and uncleaved reporters. Two nonlinear fits were performed on the calibration data, for cleaved and uncleaved reporters. Consistently with previous reports [85, 49], we modeled the inner-filter effect due to reporters using an exponential law. The fit function for calibration has the form:

$$I^{corr}(t) = 10^{-\frac{c_i}{c_0}} F_i' c_i, \tag{B.16}$$

where the subscript i denotes the uncleaved (Ucl) or cleaved (Cl) data, and I^{corr} is the flatfield-corrected fluorescence intensity. c_0 quantifies the absorbance due to reporter. Figure B.9 shows the resulting calibration curve. In this study, we estimated the ratio of cleaved-to-uncleaved fluorescence intensity to be around 40 (see Figure B.9).

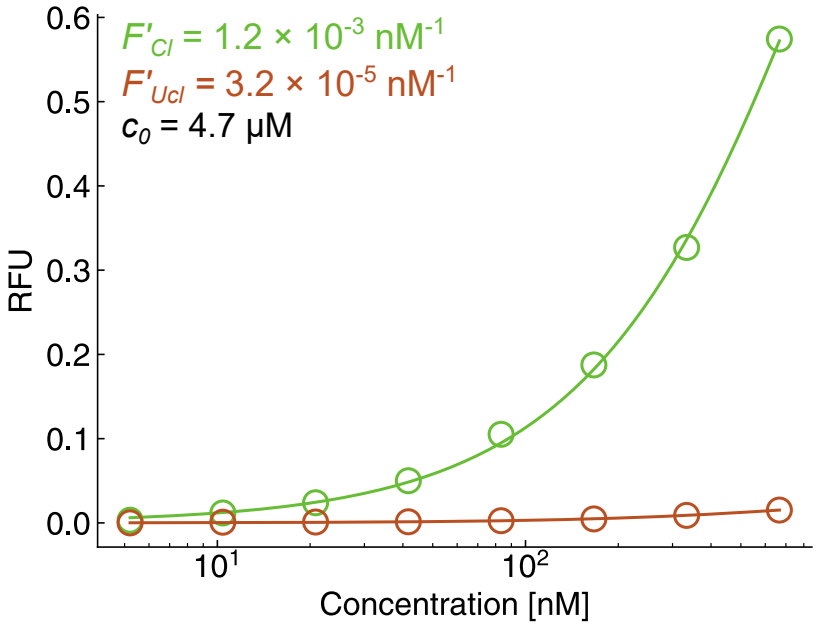

Figure B.9: Calibration curve for cleaved and uncleaved reporters. Shown are flatfield-corrected measurements of fluorescence (symbols) for varying concentrations of cleaved (green) and uncleaved (orange) reporters, and the corresponding fits (solid line) using equation B.16.

We note that calibration curves of any type are rare in published studies of CRISPR diagnostic assays and of CRISPR kinetics. It is therefore not surprising that publication of signal curves for reporters in absence of RNPs and/or target are even more rare. The only previous work of which we are aware is the data of Lv et al. [108] who reported signals for control experiment for DNA-based reporters with fluorophore-quencher pairs in absence of Cas enzyme. The data of Lv et al. exhibits a similar increase in cleaved reporters as the

one we report in Figure 3.3e. However, Lv et al. present no discussion of this phenomenon and apparently did not incorporate this observation into their calibration.

B.9 Influence of temperature on reporter degradation

Here, we discuss the influence of temperature on the reporter degradation rates. To do so, we used the temperature gradient function of our thermal cycler. Incubation temperatures were the following: 53.5°C, 51.7°C, 48.2°C, 43.5°C, 38°C, 34.1°C, 31.3°C, and 30°C. Reporters were diluted to 500 nM in NEBuffer r2.1. Three replicates were taken for each temperature. We then proceeded to fluorescence measurements. Fluorescence values were converted to concentrations using the calibration process described in chapter 3 and the calibration curves reported in Section B.8. Initial reaction velocities were computed using a linear fit to the first ~15 min of the reaction progress curves.

Figure B.10 shows the measured reaction velocity for varying incubation temperatures. We here used an initial concentration of reporters $[S]_0 = 500$ nM. We observe that the degradation rate of the reporters tends to increase with temperature. This suggests that the background degradation of reporters may be prevented by running the CRISPR reaction at a lower temperature than the optimal 37°C. Recent investigations [114] have shown that even though LbCas12a activity is severely undermined at room temperature, other Cas12a orthologs may be able to operate at such temperature.

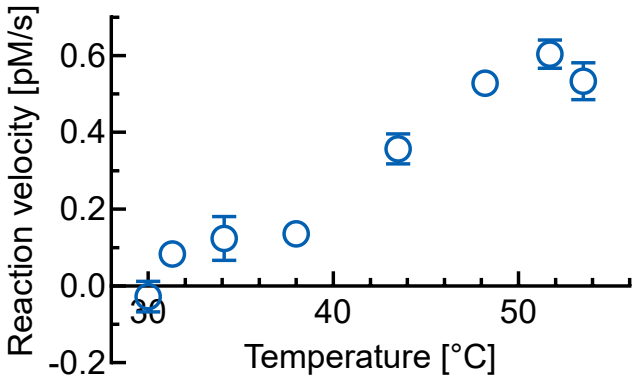

Figure B.10: Influence of incubation temperature on the reporter degradation. Shown are measured degradation velocity (i.e., in absence of Cas enzyme, dsDNA target, and gRNA) at varying incubation temperatures.

B.10 Influence of readout frequency on reporter degradation

Here, we discuss the influence of the readout frequency on the reporter degradation rates. To do so, we followed the exact protocol described in chapter 3, but we varied the sampling rate at which the fluorescence measurements were obtained. Three replicates were taken for each concentration. Fluorescence values were converted to concentrations using the calibration process described in chapter 3 and the calibration curves

reported in Section B.8. Initial reaction velocities were computed using a linear fit to the first ~20 min of the reaction progress curves.

Figure B.11 shows the measured reaction velocity for two fluorescence signal sampling rates. Shown are data taken every 30 s (squares) and every 5 min (triangles) for initial reporter concentrations between 14 and 900 nM. This sampling rate is controlled in our instrument by selecting different incubation times between readouts. The signal for both sets of experiments are different for the lowest concentrations. We attribute this to differences in handling, pipetting errors, and batch-to-batch differences in the preparation of samples. Importantly, the reaction velocity (associated with degradation) of the data obtained every 30 s grows significantly faster than that taken every 5 min. Linear regression fits of these data yield $k_{rep} = 1.4 \times 10^{-6}$ s^{-1} for readouts every 30 s, and $k_{rep} = 6.6 \times 10^{-7}$ s^{-1} for readouts every 5 min. This suggests that the sampling frequency of the assay affects the fluorescence measurement result and that, at equal times, reporters are less likely to be degraded with less fluorescence readouts. We attribute this difference mostly to the effect of photobleaching of the quencher during the times when the instrument is illuminating the sample in order to obtain data. More frequent sampling yields more net illumination and this is consistent with additional photobleaching. We note this interpretation of the data is consistent with previous reports that BHQ-1 modifications may be photodegraded [204, 125].

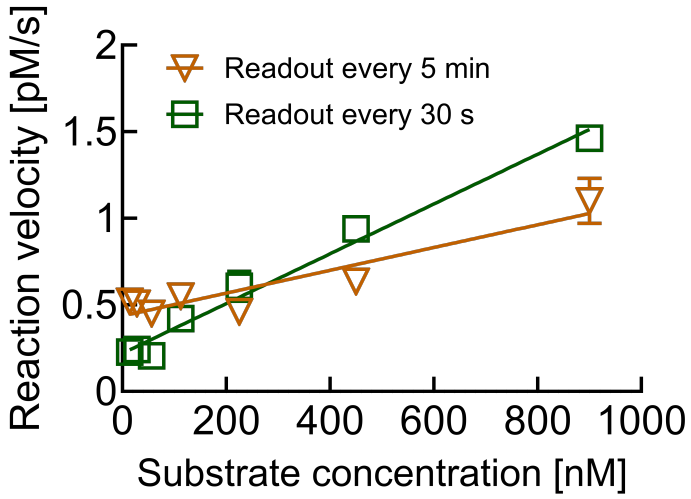

Figure B.11: Influence of the fluorescence readout frequency on reporter degradation. Shown are measured degradation velocities (i.e., in absence of Cas enzyme, dsDNA target, and gRNA) at varying initial substrate concentration, for readouts every 5 min (triangles) or every 30 s (squares).

B.11 Comparison between current augmented model and 11 sets of published CRISPR-Cas12 data and four sets of published CRISPR-Cas13 data

In this section, we present a comparison between our model and the experimental data of Huyke et al. [2] Huyke reported measurements of CRISPR-Cas12 and Cas13 kinetics, and this included careful measurements of the limit of detection using a variety of Cas12 and Cas13 orthologs and guide RNAs. Huyke et al. [2] presented these data as their figures S8, S9, S10, S11, S14, and S15. These data are plotted in Figure B.12. Figure B.12a shows measured reaction velocities versus initial target concentration for 11 different Cas12 RNP. These measurements correspond to 11 different gRNA sequences (shown with different colors), distributed among three different Cas12 orthologs: LbCas12a (crosses), AsCas12a (triangles), and AapCas12b (squares). Similarly, Figure B.12b shows measured reaction velocities versus initial target concentration for 4 different Cas13 RNP, distributed among two Cas13 orthologs: LwaCas13a and LbuCas13a. Importantly (and crucial to the current discussion), Huyke et al. [2] used a single ssDNA reporter molecule for all Cas12 experiments, and the same ssRNA reporter molecule for all Cas13 experiments. The ssDNA reporter molecule was nominally identical to the one used in the current study (although synthesized by a different provider). We describe this reporter and our source for it in Section B.7. The experimental data of Figure B.12 are reaction velocities (and therefore, kinetic rates) and these vary widely (by more than 2 orders of magnitude) among RNP type for target concentrations larger than about 10 pM. This target concentration is significantly above the limit of detection. In fact, the dependence of kinetic rates on enzyme ortholog and gRNA sequence is one of the major findings reported by Huyke et al. [2]

We now turn our attention to the low target concentration regime. Here, the situation is very different. In this regime, all reaction velocities values approximately collapse to a single plateau value irrespective of Cas ortholog and of gRNA sequence. We attribute this strong collapse at low target concentration directly to the effect of reporter degradation. Again, recall that the measurements performed by Huyke et al. [2] used the same reporter molecule at a concentration of 200 nM for Cas12 experiments, and 1 μM for Cas13 experiments. In the low target concentration regime, the reaction velocity is governed by the degradation of reporters ($k_{rep}\,[S]_0$) and becomes independent of the enzyme kinetic rates (i.e., k_{cat} and K_M) and so it is independent of the properties of the RNP and target. We refer the reader to the discussion of Figure B.5 in Section B.6 for an example comparison of reaction velocities using similar k_{rep} but different k_{cat}. We can estimate the degradation rate of reporters k'_{rep} for the set of experiments presented in Figure B.12a using the asymptote value of the reaction velocity. This estimate yields $k'_{rep} = 5 \times 10^{-6}$ s^{-1}. This value is on the same order of magnitude as the value k_{rep} measured in this work. We attribute the difference of our estimate of k_{rep} to differences in protocols, reagents, and the data acquisition apparatus of Huyke et al. [2] (which was different than that of the current work). Similarly, we estimate $k''_{rep} = 6 \times 10^{-7}$ s^{-1} for RNA reporters using the data presented in Figure B.12b. Note that the buffer conditions for Cas13 experiments are very different than those of Cas12 experiments (for both the work of Huyke et al. and for the current study).

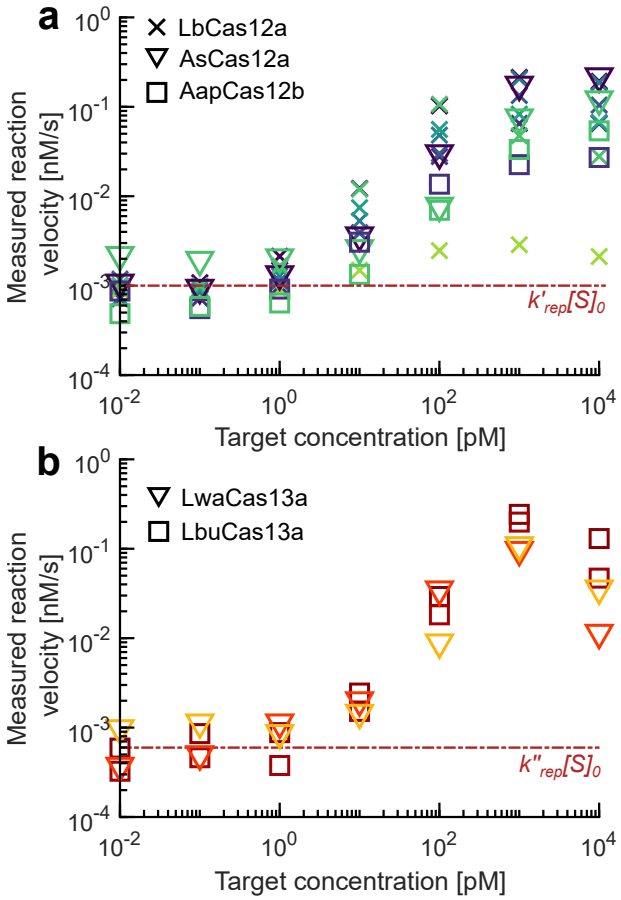

Figure B.12: Initial reaction velocities of progress curves for varying RNP and varying dsDNA target concentrations. a Limit of detection measurements for varying Cas12a orthologs. Shown are reaction velocities measured for $[S]_0$ = 200 nM ssDNA reporter initial concentration, for eleven different RNP. Different Cas12 orthologs are shown with different symbols (LbCas12a: crosses, AsCas12a: triangles, AapCas12b: squares), and measurements corresponding to the same RNP (i.e., same Cas12 ortholog and target sequence) are shown using the same symbol color. We also show with a red dashed line the asymptotic reaction velocity value as target concentration goes to zero. b Limit of detection measurements for varying Cas13a orthologs. Shown are reaction velocities measured for $[S]_0$ = 1 μM. Different Cas13 orthologs are shown with different symbols (LwaCas13a: triangles, LbuCas13a: squares), and measurement corresponding to the same RNP (i.e., same Cas13 ortholog and target sequence) are shown using the same symbol color. Once again, we show with a red dashed line the asymptotic reaction velocity value as target concentration goes to zero.

B.12 Raw fluorescence signals

We provide here the raw fluorescence signals (progress curves) which were used to generate the data shown in Figure 3.3. Figure B.13 shows raw fluorescence signals (i.e., expressed in RFU) vs. time for varying initial reporter concentration ($[S]_0$) in the presence or absence of the different components of the CRISPR reaction. Figures B.13a-e match the different cases shown in Figures 3.3a-e. Figure B.13a shows measured fluorescence signals in the presence of all the components of the reaction, including 1 nM target DNA. Figures B.13b, B.13c, and B.13d show measured fluorescence signals in the absence of either dsDNA target, gRNA, or LbCas12a enzyme. Figure B.13e shows measured signal of reporters incubated in buffer at 37°C in the absence of Cas enzyme, DNA target, and gRNA (i.e., only in reaction buffer). All the signals shown in Figure B.13 were corrected for non-uniform detector response and converted to concentrations using the calibration process detailed in Section B.8.

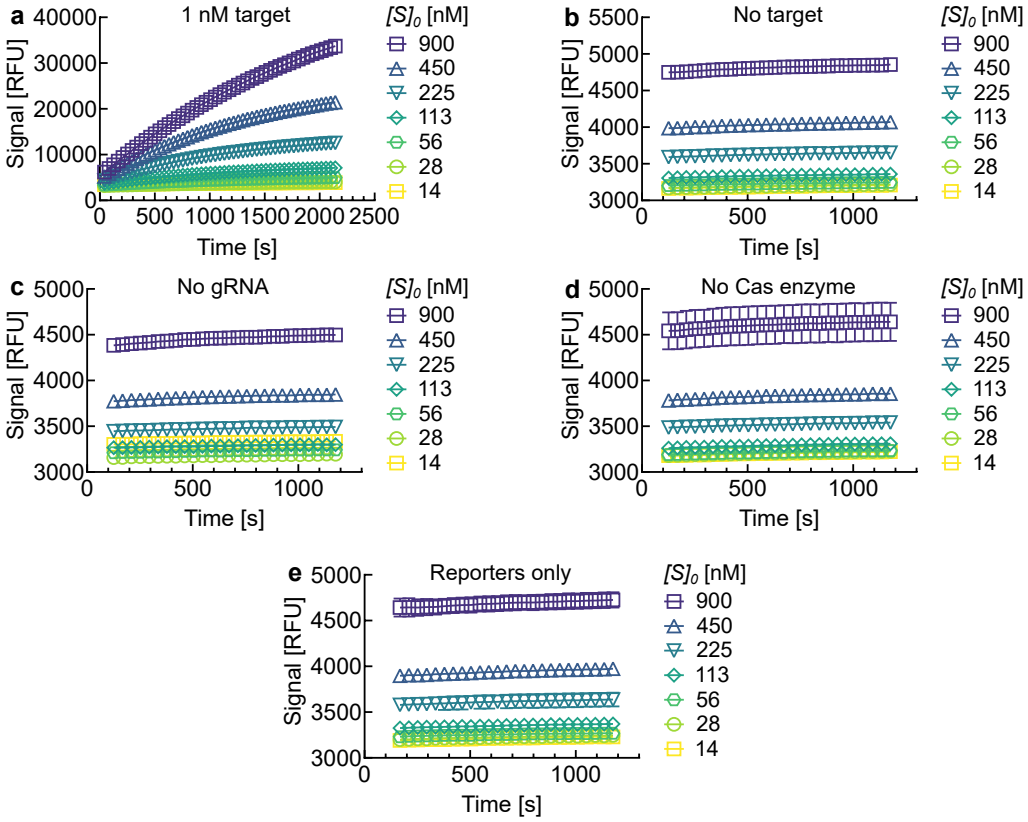

Figure B.13: Raw fluorescence signals corresponding to the data shown in Figure 3.3. a Measurements of fluorescence signal with a target concentration of 1 nM (i.e., maximum value of $[E]_0 = 1$ nM) and eight representative values of the initial reporter concentration $[S]_0$. b Measurements of fluorescence signal for the same chemistries as in a, but in the absence of target DNA. c Measurements of fluorescence signal for the same chemistries as in a, but in the absence of gRNA. d Measurements of fluorescence signal for the same chemistries as in a, but in absence of Cas enzyme. e Measurements of fluorescence signal for the same eight reporter concentrations as in a in buffer only.

Appendix C

Supplementary Information for Preliminary screening of gRNA for CRISPR-based diagnostics

C.1 List of oligos used in this work

Table C.1: List of the oligos used in chapter 4. Sequences are reported 5' to 3'.

Name	**Sequence**
T7 promoter	TAA TAC GAC TCA CTA TAG
LbCas12a crRNA	UAA UUU CUA CUA AGU GUA GAU
5' TS flanking	GAA CAC CAT GG
3' TS flanking	ATG CCC GCT ATC C
Bead primer	TTT TTG GCG CGC CTG CAG GTT TTT GCG TCC GGC GTA GAG GAT CG
Acrydited bead primer	[5Acryd] TTT TTG GCG CGC CTG CAG GTT TTT GCG TCC GGC GTA GAG GAT CG
"E" template	GCG TCC GGC GTA GAG GAT CGT AAT ACG ACT CAC TAT AGT AAT TTC TAC TAA GTG TAG ATG TGG TAT TCT TGC TAG TTA CCG AAG AGC CCT GTA GCG ACG
"7" template	GCG TCC GGC GTA GAG GAT CGT AAT ACG ACT CAC TAT AGT AAT TTC TAC TAA GTG TAG ATC GTC GCC GTC CAG CTC GAC CCG AAG AGC CCT GTA GCG ACG
Reverse primer	TTA TTA TTG GCC CGC GAA GAG CCA TTA TTA TTA TTG AAG AGC CGC TAT CAT AGG TCC ACA TCG CNN NNN NNN NNN NNN NCG TCG CTA CAG GGC TCT TCG
Binding site A	GCG TCC GGC GTA GAG GAT CG
Binding site C	CCG CTA TCA TAG GTC CAC ATC GC
Binding site D	TTA TTA TTG GCC CGC GAA GAG CC
Reporters	[FAM] TTA TTA TT [BHQ1]

Table C.2: List of screened gRNAs and measured activities.

Well	Variable sequence	Sequence length	Standardized velocity
A1	CCUCCCUGGGAGUCAGCCCCUUA	23	0.017065
A2	GCCAGCUGGGUGAGUCCAGGCAC	23	0.011728
A3	UUGAUAAUACAUGAUUGGUGUCA	23	0.311581
A4	UCAAAAUACACACACAUAUGAGU	23	0.143627
A5	UGAUCUCACUCAUAUGUGUGUGU	23	0.492084
A6	UGACCAAAAAACUUCGCUUGUCU	23	0.002503
A7	UGUAUUAAUACAAAAAGAUCAAC	23	0.328919
A8	UGAUACCAAAAGUUGGAAAAAGC	23	0.107972
A9	GCUCCCAAGGAUGUUAAUGC	20	0.375815
A10	CAAGGAUGUUAAUGCAGGCG	20	0.181386
A11	GCAGUGAGUUUGCAGACAGU	20	0.871736
A12	CAGGCUGGCGUCCGAGUCCA	20	0.029185
A13	CAUGGACUCGGACGCCAGCC	20	0.517992
A14	CGGGCGGCUGGACACCAGGC	20	0.097112
A15	ACGACGGGCGGCUGGACACC	20	0.472271
A16	AGAGGCGCUGGACACAGCCGC	21	0.034132
A17	CGCUGCUGCUGCCGGGUGCGC	21	0.293525
A18	GCCCGGAGUAAGGGCAGCAGC	21	0.038545
A19	CAGGAUGGGGUGGUGCACCGC	21	0.042738
A20	CCCGUCGGCCUGCGGCGGCCU	21	0.022900
A21	GCAGUCACUCGGGGUGGACGA	21	0.469252
A22	UGCUGCCGGGUGCGCGGUGGC	21	0.050042
A23	CAGCCCGGAUCCGGGCAGAGA	21	0.013778
A24	AGCGGGGGCUUCCAGCACUGG	21	0.259044
B1	CGCAGCUCGGCGCUCAGCUCC	21	0.006052
B2	GCUCGGCGCUCAGCUCCGGCG	21	0.105506
B3	CGGCGUGCGCUGCUGCUGCCG	21	0.038201
B4	UGCCGCUGCUGCCCUUACUCC	21	0.075055
B5	GCAGGGGCGCGGAGUGCGCCA	21	0.000296
B6	CUUCAUCUCCUCCAGCGAGUUGG	23	0.092385
B7	GGAUCCGGGCAGAGAGGCGCUGG	23	0.001928
B8	GCCGCUGCUGCCCUUACUCCG	21	0.123420

Continued on next page

Table C.2: List of screened gRNAs and measured activities.

Well	Variable sequence	Sequence length	Standardized velocity
B9	GCUGGAGGAGAUGAAGCGACUGG	23	0.161103
B10	CUGCCGCGGCCGCCCCGCUGG	21	0.008452
B11	CAGGAAGCCCUCAAGCAAACAUC	23	0.447260
B12	ACCUGAUGAGAAAUACCCACA	21	0.144137
B13	UGAAGCUAAUGAGUUGACUG	20	0.092255
B14	ACUGCUAGCUAGCUACUAA	19	0.063627
B15	CCAUGUCCCUUCACCCAUAC	20	0.249872
B16	UGAAGGUUAAGUUGAUUGCCA	21	0.202106
B17	AGCUGAACAGGUUGCAGUUCC	21	0.011991
B18	GCACCUGGUCCCGGCCAGCCU	21	0.372694
B19	ACCUGAGCUGGUCCAGUAGACAU	23	0.230954
B20	GUGUAGACAGCACGGCCCAGGCA	23	0.229034
B21	GUUAGCCUGACCCGUGCCCGGGA	23	0.070762
B22	GUUGACAUAUGGGAAAUCAUCCA	23	0.048707
B23	UGAGGAACUUGUUAGGAACUGGA	23	0.001269
B24	CUUGUUAGGAACUGGAGCAAAGA	23	0.134983
C1	GUGGUAUUCUUGCUAGUUAC	20	0.408382
C2	AAUUACUUGGGUGUGACCCU	20	0.058332
C3	CUCAGGGCGGACUGGGUGCU	20	0.493331
C4	UGUAUGGCAUGAGUAACGAA	20	0.231671
C5	CCCCCAGCGCUUCAGCGUUC	20	0.055447
C6	CCGCGGGUGGUCCCGGACAG	20	0.001053
C7	CGUCGCCGUCCAGCUCGACC	20	0.041050
C8	GUGGUAUUCUUGCUAGUAAC	20	0.543989
C9	GUGGUACCUUGCUAGUAAC	19	0.589207
C10	GUGCUAGAGUAGCUUGACAC	20	0.084274
C11	CUGGUAAUCUUGCUAGAAAG	20	0.671943
C12	GUCCUAUUCUUGGUAGUAAC	20	0.070602
C13	GUGGUAAUCAUGCUAGUAAC	20	0.716314
C14	GUCCUAUUCUAAGUGGUUAG	20	0.039243
C15	CUGGUAGUGUUGCUAGAGAC	20	0.264280
C16	GUUCCGCGCGUGCUAGUUAC	20	0.056654

Continued on next page

Table C.2: List of screened gRNAs and measured activities.

Well	Variable sequence	Sequence length	Standardized velocity
C17	UUCAAAUGAAGCGCCGCCGUCU	22	0.641171
C18	UCAAAUGAAGCGCCGCCGUCUC	22	0.300409
C19	UGAGACGGCGGCGCUUCAUUUG	22	0.206385
C20	UGAAGCGCCGCCGUCUCAUUGG	22	0.171455
C21	UCACGGGACCAAUCGGUGAGCA	22	0.761096
C22	UCCUCGUCACGGGACCAAUCGG	22	0.233918
C23	UCCGGCCGCCAAUCGCUAUCUG	22	0.225418
C24	UUGCAUCCGGCCGCCAAUCGCU	22	0.203937
D1	UUGAAUGAUUGCAUCCGGCCGC	22	0.198686
D2	UCCGCAGAUAGCGAUUGGCGGC	22	0.346084
D3	ACGCCAACCCUCUGUGAUGGAUG	23	0.202427
D4	AUCCAUCACAGAGGGUUGGCGUG	23	0.080428
D5	AUUGGUCCUUGAAUGGGUGAGCA	23	0.083450
D6	AAACUGCCCAGACGGUUGGACAG	23	0.018562
D7	AUCUUCCUAAUAUGUAGGCUCAC	23	0.300418
D8	ACACGCCAACCCUCUGUGAUGGA	23	0.058425
D9	AGGGUCCAAGAGUAUAACCAGCA	23	0.344043
D10	ACAGAGGGUUGGCGUGUGCUCAC	23	0.289021
D11	ACUCCCAGGCCAAGGGUCCAAGA	23	0.243781
D12	ACUGUAGGCCAGUCUCCCAUGGC	23	0.259798
D13	ACUACUUGACUCCCAGGCCAAGG	23	0.133467
D14	AUGGGAGACUGGCCUACAGUCCC	23	0.002465
D15	AAUGGGUGAGCACACGCCAACCC	23	0.100833
D16	AACCGUCUGGGCAGUUUGAAAGA	23	0.058513
D17	AGAAACUACUUGACUCCCAGGCC	23	0.214844
D18	AUACUCUUGGACCCUUGGCCUGG	23	0.041097
D19	AGUUUCUCCCAGGUGACUUUGCA	23	0.049077
D20	AGCUGCUGGUUAUACUCUUGGAC	23	0.021958
D21	AACACAAGCUGCUGGUUAUACUC	23	0.628885
D22	AGUAUAACCAGCAGCUUGUGUUU	23	0.310979
D23	ACCAGCAGCUUGUGUUUACCAUA	23	0.002101
D24	AAAUGUUCUAGUGAGCCUACAUA	23	0.201274

Continued on next page

Table C.2: List of screened gRNAs and measured activities.

Well	Variable sequence	Sequence length	Standardized velocity
E1	AAAGUCACCUGGGAGAAACUACU	23	0.113641
E2	AGUCACCUGGGAGAAACUACUUG	23	0.038219
E3	AUAUUCCCAAAAAAAAUCUUCAAA	23	0.044146
E4	AGCCUCAUUGUCCAAUAUUCCCA	23	0.030548
E5	GAGCUCAUCAGUGACAUUCUAUG	23	0.165405
E6	UCUAUGAUUCUCUCGUUAGAUAA	23	0.001033
E7	CAAUGUAUUGUAUUCUGCAGUCA	23	0.662442
E8	AGAUUCCAGUGUCUACGCUGU	21	0.277660
E9	UGAACCCAGUGAUACGGACCC	21	0.309239
E10	UCCUAUCGACUCACCAGAGCC	21	0.563705
E11	AGUUGCGGCCGAACCGUUCCC	21	0.000820
E12	GUUGCGUCGCUAUUUGGUGCU	21	0.089020
E13	GGGAACGGUUCGGCCGCAACU	21	0.388394
E14	UAGCGACGCAACUGCCGGUCA	21	0.711638
E15	CCGGCAGUUGCGUCGCUAUUU	21	0.791894
E16	CUUCAACCAGGAACGCCCGAA	21	0.147245
E17	GCUGACUUACCAGCCGGAGAG	21	0.492040
E18	GAUCACUGUCCGGAGUCCGAUGG	23	0.430236
E19	GCCUAUACUCACGGGGACUGAGG	23	0.241143
E20	CGCUCACGGGUUCCGGACCGC	21	0.025149
E21	ACCGGCCAGCGUCCGCAACAC	21	0.261894
E22	CGAGACGCGCUGCAGAUGGUC	21	0.561852
E23	AUCUGCAGCGCGUCUCGUUGC	21	0.326331
E24	CGGCGCUCGUAGGUGAAGGCC	21	0.043962
F1	CGGCGCAUGGACACGUCCUGC	21	0.144058
F2	UACCUUGGCAACGAGACGCGC	21	0.075255
F3	UAUACCUUGGCAACGAGACGC	21	0.050985
F4	AGUGACUUCUGCGAGCGGCGC	21	0.033679
F5	GCGCUCGUAGGUGAAGGCCUC	21	0.149005
F6	CAUGCGGCGCAUGGACACGUC	21	0.035973
F7	ACGCACUUCGACCUAUGAUCC	21	0.606071
F8	AGGCCUUCACCUACGAGCGCC	21	0.482855

Continued on next page

Table C.2: List of screened gRNAs and measured activities.

Well	Variable sequence	Sequence length	Standardized velocity
F9	CCUUCACCUACGAGCGCCGGC	21	0.086438
F10	GAAGCGCCGCUCGCAGAAGUC	21	0.215897
F11	ACGCCCACGUGGUCGCGGAAC	21	0.151455
F12	CCGUUGGCCUGGUCGACCAUC	21	0.007098
F13	AUCCAACGUGCAGUCCACACUGG	23	0.461759
F14	UCCCAGUGUGGACUGCACGUUGG	23	0.000000
F15	UGGACUGCACGUUGGAUCUGAGG	23	0.000340
F16	UCAGACACGCCAUCAGCAUUUGG	23	0.000000
F17	CAGACACGCCAUCAGCAUUUGGG	23	0.228703
F18	CAGGCAAUUAUAAUCACAGC	20	0.444119
F19	AAUUAUAAUCACAGCUAGUA	20	0.832145
F20	GUGGCAGGCAAUUAUAAUCA	20	0.274340
F21	GCAAUUAUAAUCACAGCUAG	20	0.568232
F22	UUAUAAUCACAGCUAGUAGG	20	0.079910
F23	CCUACUAGCUGUGAUUAUAA	20	0.083343
F24	GGCUGAGGCAGGAGAAUUGC	20	0.219921
G1	AAACAGCACACGUAAGAUCGGGU	23	0.259063
G2	AAACCAGCAGAGAUUCACCCCAC	23	0.514661
G3	AACGGGAAUGGAGGCUCGGUGCA	23	0.010878
G4	AAUUCCUCCCGCGGUUAGCCUGA	23	0.045507
G5	ACACACAGGCACUCUCCUGCACA	23	0.563044
G6	ACACACCAAACCACACCCCCA	21	0.000655
G7	ACACACCACUGUCGGGCACACAC	23	0.279734
G8	ACACACCGUCACCUGCCUGGGCC	23	0.148054
G9	ACACCGUCACCUGCCUGGGCCGU	23	0.257359
G10	ACACUAGAGCACCCUGCGCAAUC	23	0.385922
G11	ACAGGAGCUGGUGAGAUGUCAGA	23	0.268423
G12	ACCGUCACCUGCCUGGGCCGUGC	23	0.138608
G13	ACCUGCCUGGGCCGUGCUGUCUA	23	0.268166
G14	ACGCCUGCGUGGAUGUAAACGGG	23	0.073423
G15	ACGGGAAUGGAGGCUCGGUGCAG	23	0.230686
G16	ACGGGUCAGGCUAACCGCGGGAG	23	0.241431

Continued on next page

Table C.2: List of screened gRNAs and measured activities.

Well	Variable sequence	Sequence length	Standardized velocity
G17	ACGGUGUGUAGACAGCACGGCCC	23	0.236430
G18	ACUAGAGCACCCUGCGCAAUCAC	23	1.000000
G19	ACUCACCACUCACCACUCACUCA	23	0.231000
G20	ACUCAGACACACAGGCACUCUCC	23	0.370502
G21	ACUCUAGAUUAAAUUCCUCCCGC	23	0.593898
G22	ACUGAGUCCCGGGCACGGGUCAG	23	0.024139
G23	ACUGGAGAGGCCCGUCCACACCG	23	0.242332
G24	AGACACACAGGCACUCUCCUGCA	23	0.162979
H1	AGACAGCACGGCCCAGGCAGGUG	23	0.358604
H2	AGAGCACCCUGCGCAAUCACUAA	23	0.505663
H3	AGAGGAUGCUCACAGAGCAGGGG	23	0.193587
H4	AGAUUAAAUUCCUCCCGCGGUUA	23	0.021023
H5	AGCACACGUAAGAUCGGGUGUGC	23	0.094590
H6	AGCACCCUGCGCAAUCACUAACA	23	0.071377
H7	AGCACGGCCCAGGCAGGUGACGG	23	0.446252
H8	AGCAGGCCCUUCAUCUCCCUCAG	23	0.178302
H9	AGGCUCCUCCCCAUCCACAGAGG	23	0.301128
H10	AGGGAGAUGAAGGGCCUGCUGAG	23	0.177122
H11	AGGGGAAACGCCUGCGUGGAUAU	23	0.000000
H12	AGGGGUGUGGAGGGCUGUGGAGG	23	0.000000
H13	AGGUCCUCAUCUCCCUCAGCAGG	23	0.282610
H14	AGUGAUUGCGCAGGGUGCUCUAG	23	0.000000
H15	AGUGGUGAGUGAUGAGUGAGUGG	23	0.119742
H16	AGUGGUGAGUGGUGAGUGAGUGG	23	0.000293
H17	AUAUAAACGGGAAUGGAGGCUCG	23	0.034013
H18	AUAUCAUCAGUAACAUCCAUCAC	23	0.367448
H19	AUAUGGGAAAUCAUCCAUGUUGA	23	0.694847
H20	AUCAGUAACAUCCAUCACCCCAA	23	0.423266
H21	AUCAUCCAUGUUGACAUAUGGGA	23	0.151406
H22	AUCCACAGAGGAUGCUCACAGAG	23	0.104663
H23	AUCCAGUGGGGUCUGCAGCCUGG	23	0.004193
H24	AUCCAUGUUGACAUAUGGGAAAU	23	0.314051

Continued on next page

Table C.2: List of screened gRNAs and measured activities.

Well	Variable sequence	Sequence length	Standardized velocity
I1	AUCCUCUGUGGAUGGGGAGGAGC	23	0.515467
I2	AUCUCCCUCAGCAGGCCCUUCAU	23	0.326818
I3	AUCUGACAUCUCACCAGCUCCUG	23	0.212259
I4	AUGGAUGUUACUGAUGAUAUGAG	23	0.063761
I5	AUGGGAAAUCAUCCAUGUUGACA	23	0.492798
I6	CAAACCAGCAGAGAUUCACCCCA	23	0.000389
I7	CACACACCACUGUCGGGCACACA	23	0.070608
I8	CACACCGUCACCUGCCUGGGCCG	23	0.129056
I9	CACAGAGGAUGCUCACAGAGCAG	23	0.588692
I10	CACAGCCCUCCACACCCCUCCAC	23	0.029090
I11	CACGGGUCAGGCUAACCGCGGGA	23	0.131482
I12	CACUAGAGCACCCUGCGCAAUCA	23	0.439132
I13	CAGGCAGGUGACGGUGUGUAGAC	23	0.430417
I14	CAGGUCCUCAUCUCCCUCAGCAG	23	0.698955
I15	CAGUAACAUCCAUCACCCCAAAA	23	0.508652
I16	CAUAUCAUCAGUAACAUCCAUCA	23	0.483677
I17	CAUUCACUCUCUCUAUGGAUCCA	23	0.522843
I18	CCAGGCAGGUGACGGUGUGUAGA	23	0.250475
I19	GCAGCAAAGCAUUCAAGAGG	20	0.390693
I20	GAUAGUAAAUAAGUCUCAAG	20	0.469214
I21	UGUGAUGGGAGAGGCUGCCA	20	0.222808
I22	GAAGAAGACAGGAAAAUGUG	20	0.116461
I23	CCUAGGCUGUACACAGCACA	20	0.537475
I24	AUAAAGACAUACCUGAAACU	20	0.468636
J1	GCUGCUGAUAAAGACAUACC	20	0.241330
J2	GGAGGGCUCAGAAGAAGACA	20	0.538007
J3	GAAUGCACCCCACGGGUCC	19	0.364008
J4	CACGAAUAGUAUUAGACAA	19	0.199384
J5	UCUGGCACACGAAUAGUAUU	20	0.376266
J6	CCCCAAGGAUAAUCCUUAGA	20	0.633184
J7	AACUGUAACUUGGGGAAGCG	20	0.180766
J8	CUGUAACUUGGGGAAGCGUG	20	0.063722

Continued on next page

Table C.2: List of screened gRNAs and measured activities.

Well	Variable sequence	Sequence length	Standardized velocity
J9	CCUCCCCAAGGCGUGCUGAG	20	0.364978
J10	UAAACAUAUAUCCGUGUAUGUAA	23	0.254021
J11	UAGAGCACCCUGCGCAAUCACUA	23	0.187919
J12	UCAGCAGGUCCUCAUCUCCCUCA	23	0.000000
J13	UCAGUAACAUCCAUCACCCCAAA	23	0.555429
J14	UCAUCCAUGUUGACAUAUGGGAA	23	0.000025
J15	UCCACACCCCUCCACAGCCUCCA	23	0.263777
J16	UCCCCAUCCACAGAGGAUGCUCA	23	0.000000
J17	UGCGGUGUGGACGGGCCUCUCCA	23	0.003377
J18	CGCGGUUAGCCUGACCCGUGCCC	23	0.109954
J19	CGGGCACGGGUCAGGCUAACCGC	23	0.015425
J20	CGGUGUGUAGACAGCACGGCCCA	23	0.361694
J21	CGUCCGCCUGGAACCUCGGGAAG	23	0.010583
J22	CGUGCUGUCUACACACCGUCACC	23	0.141951
J23	CUAAACAUAUAUCCGUGUAUGUA	23	0.146629
J24	CUCACCAGCUCCUGUUCCAUUCC	23	0.136972
K1	CUCCACACCCCUCCACAGCCUCC	23	0.166643
K2	CUGUGAAGCACCUGCUCAAGGCA	23	0.415478
K3	CUUACCUGCACCGAGCCUCCCGC	23	0.164095
K4	GAAACGCCUGCGUGGAUAUAAAC	23	0.090630
K5	GAACAGGAGCUGGUGAGACAUCA	23	0.338709
K6	GAACAGGAGCUGGUGAGAUGUCA	23	0.001591
K7	GAAUGGAGGCUCGGUGCAGGUAA	23	0.666120
K8	GACAGCACGGCCCAGGCAGGUGA	23	0.237543
K9	GAGCUGGUGAGAUGUCAGAUGAA	23	0.530034
K10	GAUCCAUGCAUUCAUCCAUGUAC	23	0.144027
K11	GAUGGAACAGGAGCUGGUGAGAC	23	0.445311
K12	GAUGGAUGUUACUGAUGAUAUGA	23	0.219458
K13	GCACACACCACUGUCGGGCACAC	23	0.366292
K14	GCACCCUGCGCAAUCACUAACAC	23	0.431823
K15	GCAGGCCCUUCAUCUCCCUCAGC	23	0.354769
K16	GCAGGUGACGGUGUGUAGACAGC	23	0.334081

Continued on next page

Table C.2: List of screened gRNAs and measured activities.

Well	Variable sequence	Sequence length	Standardized velocity
K17	GCAUCCUCUGUGGAUGGGGAGGA	23	0.034294
K18	GCAUGGAUCCAUAGAGAGAGUGA	23	0.016532
K19	GCCCACGUGCCCACUGUGAUGCC	23	0.415039
K20	GCCGUGCUGUCUACACACCGUCA	23	0.193880
K21	GCCUGCGUGGAUAUAAACGGGAA	23	0.271979
K22	GCGUGGAUAUAAACGGGAAUGGA	23	0.256605
K23	GCUCUGUGAGCAUCCUCUGUGGA	23	0.207035
K24	GGAAUGGAGGCUCGGUGCAGGUA	23	0.555290
L1	GGACUGACACGGCGAUGCUGACA	23	0.099539
L2	GGAGCUGGUGAGACAUCAGAUGA	23	0.395126
L3	GGAGGCUCCUCCCCAUCCACAGA	23	0.042641
L4	GGAUGGAACAGGAGCUGGUGAGA	23	0.017795
L5	GGCACUCUCCUGCACACACACAC	23	0.113095
L6	GGCGGGAGGCUCGGUGCAGGUAA	23	0.164703
L7	GGGUCAGGCUAACCGCGGGAGGA	23	0.298640
L8	GGGUGUUGCGAAAUUGGCAGAAA	23	0.059397
L9	GGUCACCUACAGGCAGCUCAAAC	23	0.508580
L10	GGUGAGAUGUCAGAUGAAAUAGA	23	0.101329
L11	CACUGGCUUGGUCCAAAAAGGAU	23	0.229696
L12	GACCAAGCCAGUGUAAAAGCCAG	23	0.230896
L13	AUACAUAAAGUUGUGUGUAUUGA	23	0.598243
L14	CGGGAGUGGUGUCGGGGGUCGAU	23	0.358842
L15	CCUGAAAGCGUGCCUGACUGCAA	23	0.153341
L16	UCUAAUACUAUUCGUGUGCCAGA	23	0.485515
L17	UAUCCUUGGGGUGCUCCAACAGA	23	0.000382
L18	UGCUCCAACAGAGGCGGGUCUGA	23	0.002000
L19	UGUCCCUCAGCACGCCUUGGGGA	23	0.182774
L20	GCACCCCAAGGAUAAUCCUUAGA	23	0.029075
L21	GGGUCAGACCCGCCUCUGUUGGA	23	0.042132
L22	CCUCUGUUGGAGCACCCCAAGGA	23	0.196523
L23	AGGAUAAUCCUUAGAUGAGGAGA	23	0.138776
L24	GUGAGGGGAGGGAAGGGGAGGGA	23	0.151309

Continued on next page

Table C.2: List of screened gRNAs and measured activities.

Well	Variable sequence	Sequence length	Standardized velocity
M1	GGGAGGGGAGGUGAGGGGAGGGA	23	0.076633
M2	GUCAUAAAUAAAACAAAAUAUGA	23	0.357984
M4	UGAAAAGGUACCGCUGUGUGCAU	23	0.117700
M5	UUAGAAAACCAUAUUCUCCCAAA	23	0.111172
M6	CAUGGGGAAGGCCCAGGGUCAGA	23	0.001493
M7	UCUCCUGCUCAUGAAAAAACAGA	23	0.304385
M8	GACAAAUGCAUUAAUAUCUGUGA	23	0.139739
M9	GGAACCUCCUAGAGACUUGUUGA	23	0.369424
M10	ACAAGUUCCUCAUCUCCAUAUGA	23	0.031652
M11	GUGGUCUCAUAUGGAGAUGAGGA	23	0.462161
M12	GGUGAGUGAGUGGUGAGUGGUGA	23	0.029360
M13	GGUGAUGGAUGUUACUGAUGAUA	23	0.644349
M14	GUCAGCAUCGCCGUGUCAGUCCA	23	0.246699
M15	GUCCCGGGCACGGGUCAGGCU	21	0.282871
M16	GUGAAUGCGCUUCCGCCACUGAA	23	0.470665
M22	CGCGGCCCGAAACCCAGGAUC	21	0.066208
M23	AGGUCAUACGGUCGCUGACUA	21	0.643805
M24	AUACGGUCGCUGACUACUUGA	21	0.504097
N1	GCGGGGCUUGUAGAUACACUA	21	0.288762
N2	UCAGUACAGUGACCGUCGCCA	21	0.324960
N3	GACCGUCGCCAGCCAAACAUA	21	0.327611
N4	GUCAGGUCAUACGGUCGCUGA	21	0.354163
N5	CCUAACACGAAAGUUUGCGCA	21	0.044757
N6	GUUGCGCAAACUUUCGUGUUA	21	0.077952
N7	ACAGUGACCGUCGCCAGCCAA	21	0.135954
N8	AGUCAAUUUCGUAACGAUCCA	21	0.057584
N9	UACAGUGACCGUCGCCAGCCA	21	0.128025
N10	AUCUACAAGCCCCGCCAUGGA	21	0.066016
N11	UAUCGGUCUCCAGAGGUGCUA	21	0.083354
N12	CGAGGGGUCUCUUUGAACCUA	21	0.196378
N13	CGAUCUCCUGUUGGACACGGC	21	0.047349
N14	UCGCGCAGAAAGCCCGACUCC	21	0.040618

Continued on next page

Table C.2: List of screened gRNAs and measured activities.

Well	Variable sequence	Sequence length	Standardized velocity
N15	ACCUCGCGCAGAAAGCCCGAC	21	0.029251
N16	CGCCCCAACGGUCUCUUGGAC	21	0.039400
N17	UUGGCGCCGGUGCAUCAGGUC	21	0.025581
N18	UCCGCACCUCGCGCAGAAAGC	21	0.023273
N20	CUCGCCGUGGGUCACCAGCGC	21	0.134891
N21	GUCGUCGAUCUCCUGUUGGAC	21	0.087306
N22	UGGACCUGAUGCACCGGCGCC	21	0.224390
N23	CUCGCGCAGAAAGCCCGACUC	21	0.056536
N24	AGCCGUGAGCAACGUGAUCGC	21	0.165009
O1	UGGAGAUGAGGAACUUGUUAGGA	23	0.100369
O2	UACCCAGGGUAGGCCGGUGGAG	22	0.048706
O3	UAAGGGAAGGGUCACGCGCUCG	22	0.219641
O4	UGGUCGGAGAAGUCACCCCCUC	22	0.408391
O5	UCAGCACACCGAGCGCGUGACC	22	0.330710
O19	CUUGGGAACGCGGCCCGAAAC	21	0.389306
O20	CGUCGUACUCGAAGCGGCGCC	21	0.189982
O21	UCGUCGUACUCGAAGCGGCGC	21	0.026697
O22	CCUAUCACGUCGUCGAUCUCC	21	0.455702
O23	CCCUAUCACGUCGUCGAUCUC	21	0.660907
O24	UGCGGGCGCCGCUUCGAGUAC	21	0.157656
P1	CGCUGCUGUCCGGUCUACUUU	21	0.067996
P2	UGUCGUCGUGAAACAUCCGGU	21	0.140984
P3	CUAAAGCGGCCCAGACUCGAU	21	0.478281
P4	GCCUCGGAGGAUUCCGUGCUU	21	0.192456
P5	CGUCAUACCAAAGCCGUCAAU	21	0.280677
P6	CACGCCGGCAGACGCCAGUCU	21	0.174398
P7	UCGUGAAACAUCCGGUAGCUU	21	0.760663
P8	UGAGUUUCACUCCCGACGGAU	21	0.389490
P9	GUUUCACUCCCGACGGAUCUU	21	0.713496
P10	UGCCGGCGUGGACACCAAUGU	21	0.006834
P11	AAGCCGUCAAUGUUGUGCGUU	21	0.354347
P12	GUCGUGAAACAUCCGGUAGCU	21	0.275536

Continued on next page

Table C.2: List of screened gRNAs and measured activities.

Well	Variable sequence	Sequence length	Standardized velocity
P13	CGAGUCUGGGCCGCUUUAGCU	21	0.558461
P14	UUCAUCGAGUCUGGGCCGCUU	21	0.237561
P15	CCUGGCGAAGACCCUCGAUGU	21	0.337122
P16	GCUACGAAACACACCUGGCGU	21	0.517186
P17	UUCGCUGCUGUCCGGUCUACU	21	0.518545
P18	UGGGGACGAAGGUCCAGCGAU	21	0.333304
P19	UUCAGAGUGACCCUCCGGGAU	21	0.280079
P20	CGGAAAGUCUGGACCCUUGAU	21	0.379977
P21	UUCACGACGACAGCAUGAAGU	21	0.278903
P22	GGAGGAUCCACAGACUGGCGU	21	0.767855
P23	GUGAAACAUCCGGUAGCUUCU	21	0.389319
P24	UAAUGAGCCAUCACCCCUCUAC	22	0.396180

C.2 PCR thermocycling conditions

We used the following thermocycling conditions for PCR in chapter 4.

Table C.3: PCR thermocycling conditions for PCR reported in chapter 4.

Step	Bulk PCR	qPCR	PCR with hydrogel beads
Initial denaturation	98°C (5 min)	95°C (2 min)	98°C (5 min)
Number of cycles	40	40	40
Denaturation	98°C (20 s)	95°C (5 s)	98°C (20 s)
Extension	72°C (5 s)	60°C (30 s)	72°C (120 s)
Plate read	N/A	1 per cycle	N/A
Final extension	72°C (7 min 30 s)	60°C (30 s)	72°C (7 min)
Melting curve	N/A	60°C to 95°C at 0.1°C/s, readout every 5 s.	N/A

Appendix D

Supplementary Information for ITP buffer design using BEAN-ITP

D.1 Initial conditions and ITP zone profiles

Figure D.1 shows a schematic of concentration profiles of ITP zones. BEAN computes ion properties (e.g., concentrations, mobilities, and pH) of the plateau zones and not details of the interfaces between plateau zones. Figure D.1A shows an example initial condition in ITP (immediately before any electromigration has occurred). Shown are total concentration distributions for all four species in ITP systems. Note that "total concentration" refers to net concentration for a species family summed over all ionization states of that species (including any neutral state). The latter is also known as "analytical concentration" in the analytical chemistry community. BEAN considers a basic ITP process including a trailing ion (TI), analyte (A), counterion (CI), and leading ion (LI). In the example shown here, a finite amount of A is initially injected with the TI. The initial concentration of CI is in this example uniform throughout the domain. The plateau values correspond to the input concentrations specified by the user in the input panel.

Figure D.1B shows a schematic of example concentration profiles for the same species after ITP concentration plateaus have formed. In this example, anionic species (TI, A, and LI) migrate from left to right (electric field is oriented right to left). We here distinguish four zones, denoted by black, vertical dashed lines in Figure D.1B. First, the trailing electrolyte (TE) and the adjusted trailing electrolyte (ATE) both consist of a mixture of TI and CI. The sample (S) zone is a mixture of A and CI, and the LE zone is a mixture of LI and CI. Concentrations in the LE and TE are specified by the user, whereas concentrations in the ATE and S regions are results of the simulation performed by the tool. The properties of the plateaus computed by BEAN (including species concentrations and pH) can be interpreted as originating from a finite injection as shown in Figure D.1A. Such a finite injection leads to a "purified" adjusted TE zone (ATE) zone that contains TI, CI, and negligible concentration of A. Importantly, the lengths of the plateaus are not predicted by BEAN. Such

estimations require computations of the species fluxes in all zones and the unsteady accumulation rates which may occur at various interfaces. Ramachandran and Santiago [58] provide analytical expressions for such computations. More complex computations of the dynamics involve solutions to partial differential equation involving weak electrolytes, and we recommend for these solvers such as SPRESSO [72] or CAFES [145].

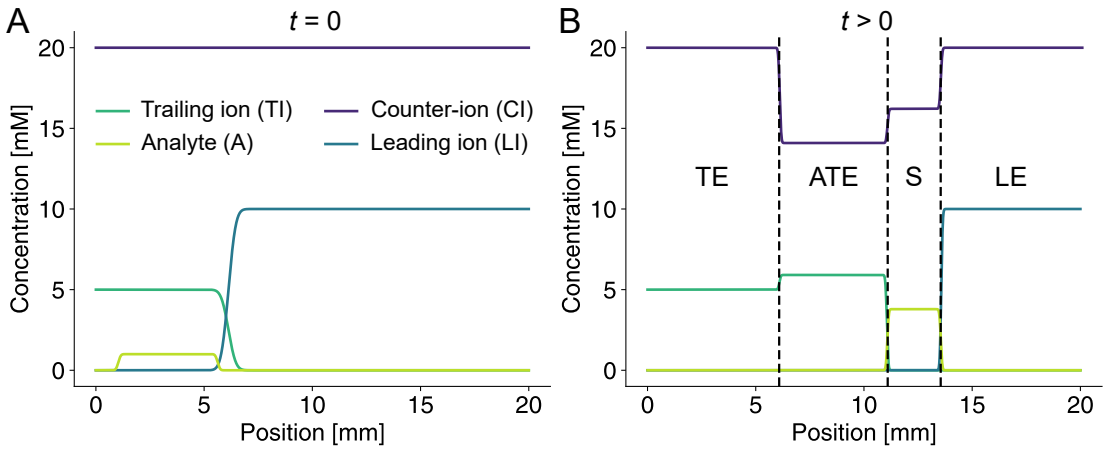

Figure D.1: Schematics of the initial and steady-state (in the frame of moving plateaus) distributions of species total concentrations in plateau-mode ITP. A Example initial conditions and finite-sample injection profiles for a simulation in BEAN. The ITP configuration consists of the four basic ionic species shown. B The resulting ITP plateau zones and the concentration distributions of these zones. The species concentration values and pH of all plateaus are one of the outputs of a BEAN simulation, as summarized in Table 5.2 in Section 5.1.4.1.

D.2 Onsager-Fuoss ionic strength correction

In this section, we provide some details of the calculation of the Onsager-Fuoss correction for electrophoretic mobility given an electrolyte system. Onsager and Fuoss [149] derived and later Bahga et al. [74] applied and discussed the following correction for the electrophoretic mobility:

$$\mu^{o}_{X,z} = \mu^{\infty}_{X,z} - \left(A_{X,z}\mu^{\infty}_{X,z} + B_z\right)\frac{\sqrt{2I}}{1 + aD\sqrt{I}}\,, \tag{D.1}$$

$$D = \sqrt{\frac{2e^2 N_A}{\varepsilon k_B T}}, \tag{D.2}$$

$$A_{X,z} = z\frac{e^3}{12\pi}\sqrt{\frac{N_A}{(\varepsilon k_B T)^3}}\sum_{n=0}^{+\infty} C_n R^n_{X,z}\,, \tag{D.3}$$

$$B_z = |z| \frac{e^2}{6\pi\eta} \sqrt{\frac{N_A}{\varepsilon k_B T}} \,. \tag{D.4}$$

Here, $\mu^{\infty}_{X,z}$ is the fully ionized electrophoretic mobility of a given valence state at infinite dilution, and $\mu^{o}_{X,z}$ is the corrected (for ionic strength effects) fully ionized electrophoretic mobility. e is the fundamental charge, N_A the Avogadro number, ε is the permittivity of the solution, k_B Boltzmann's constant, T the temperature of the solution, and η is the dynamic viscosity of the solution. a represents the mean distance of closest approach for the ions. Bahga et al. [74] report that a good approximation for a broad range of species is $aD \approx 1.5\sqrt{2}$ mol$^{-1/2}$ mol$^{-3/2}$, where D is determined solely by absolute temperature as shown in equation D.2.

Onsager and Fuoss [149] recommend that the first six terms of the infinite summation in equation D.3 yield a satisfactory approximation for the numerical implementation of the correction. We use the following values for C_n:

C_0	0.2929
C_1	−0.3536
C_2	0.0884
C_3	−0.0442
C_4	0.0276
C_5	−0.0193

The values of R_i^n $(0 \leq n \leq 5)$ are computed iteratively using:

$$R_i^0 = z_i - \frac{\sum_t z_t \alpha_t}{\sum_p \frac{z_p \alpha_p}{|\mu_p^0|}} \frac{|z_i|}{|\mu_i^0|}, \tag{D.5}$$

$$R_i^n = \sum_s (2H - I)_{is} R_s^{n-1}. \tag{D.6}$$

Here, I is the identity matrix. Each coefficient h_{ij} of the matrix H is computed as follows:

$$h_{ji} = \sum_s \alpha_s \omega_{sj} \delta_{ji} + \alpha_i \omega_{ij}, \tag{D.7}$$

$$\alpha_i = \frac{c_i z_i^2}{\sum_s c_s z_s^2}, \omega_{ij} = \frac{\omega_j}{\omega_i + \omega_j}, \; \omega_i = \frac{|\mu_i^0|}{|z_i|}. \tag{D.8}$$

Appendix E

Supplementary Information for ITP experimental design with CAFES

E.1 General user interface of CAFES

Figure E.1 shows an example of a set of input parameters specified by a user of CAFES for an anionic ITP process. At the top, the user specifies the Simulation time and number of Steps per plot update. The latter is the number of computational steps the code computes between each update of the plotting interface. Raising this value to greater than unity helps achieve longer duration simulations using a computer with limited memory. Next, the user specifies two Numerics Settings: Number of Grid Points and ODE tolerance. The scalar error is computed as the $\mathcal{L}^2$ norm of the spatial error vector, which is composed of the error values computed at each grid point. This ODE tolerance ensures the correct time-integration step to keep the scalar error bounded.

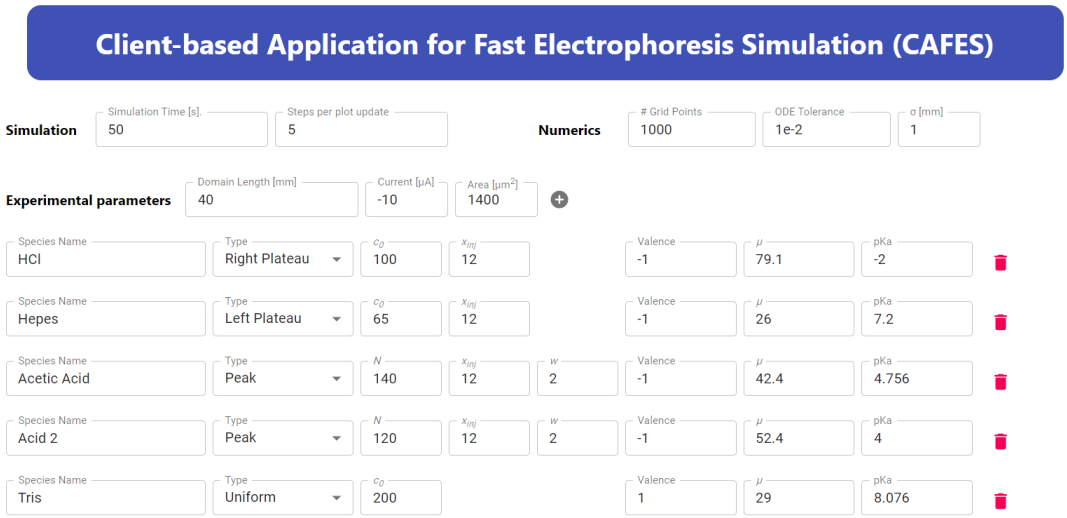

Figure E.1: Main input panel of CAFES's General User Interface (GUI). Shown is an image of upper section of the CAFES web page. The example input parameters shown here are for an anionic ITP simulation involving four chemical species with chloride as a leading electrolyte ion and HEPES as a trailing electrolyte ion. The buffering counter ion is Tris and Alexa Fluor 488 (AF488) is an example simulated analyte.

E.2 Plotly interface

Plotly.js is an open-source visualization JavaScript library. In CAFES, it provides an interactive interface which displays the pH, electric field and electrolyte concentration profiles in real-time while the simulation runs. Generic documentation for the Plotly.js library is available at plotly.com/javascript.

As shown in Figure E.2, the plots interface includes ten button icons in the top right. From left to right, these buttons allow 1) quick download of the plots in a PNG file (camera icon); 2) manual zoom (looking glass icon); 3) pan (cross arrow icon); 4) zoom in (plus sign icon); 5) zoom out (negative sign icon); 6) autoscale (arrowed cross icon); 7) reset of axes (home icon); 8) spike lines (dotted corner icon); 9) see only the closest data on hover (leftward single arrow); and 10) compare data on hover (leftward double arrow). Most of these functions are self-explanatory and are best understood by trial interactions with the tool. The spike line option (icon 8 in Figure E.2) activates vertical and horizontal dashed lines which cross on the current mouse icon location, and which can help to position the cursor more precisely. Note that the ninth icon activates a display of the x-location (in mm) and ordinate value (in mM or pH unit, depending on plot) of the curve point nearest to the mouse icon. The tenth icon activates the display of all ordinate values of the curve points with a y-location nearest to the mouse icon.

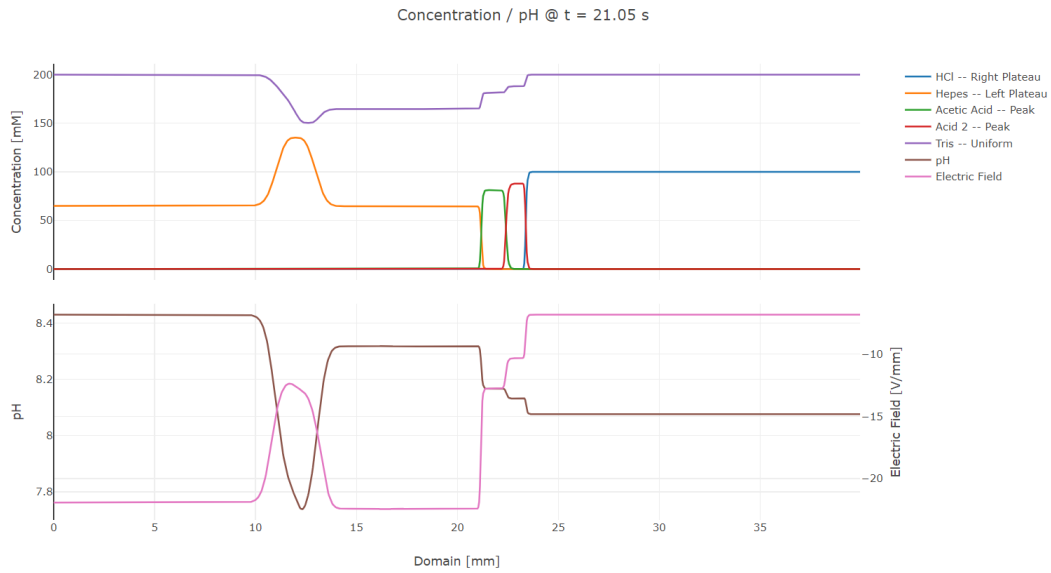

Figure E.2: Plotly interface for real time interactive solution. This feature is a real time and interactive display of the solution. The two plots respectively show the electrolyte concentration and pH profiles in the simulated domain. Interactive tools are located on the top right of the figure. The example plots shown here have activated the tenth icon (leftward single arrow), indicating a "compare data on hover" feature.

E.3 Post-processing of the exported result files

The Export Results feature outputs a ZIP file containing one JavaScript Object Notation (JSON) file and three binary files. The JSON file stores the user input information of the simulation run. The three binary files contain the concentration profiles, the list of time instants of the simulation, and the hydronium concentration. These files are not directly readable by the user. For this reason, we have provided a Python module to read and manipulate these files at the following GitHub address: github.com/alvinsunyixiao/itp-websim. The script `matlab_converter.py` automatically transforms the raw results from CAFES to a readable MATLAB table. We have also provided some tools for analysis and plotting, for example to generate spatio-temporal plots similar to those shown in Figure 5.5 in Section 5.2.

E.4 Chip geometry and initial injection profiles

Figure E.3 shows the geometry of the NS12AZ chip and the initial configuration of the buffers in the experiments of Figure 5.5 of Section 5.2. Reservoirs 1 to 4 were initially filled with 10 µL of leading electrolyte (LE) buffer. Reservoir 2 is then emptied, rinsed with deionized water (DI), and then filled with 10 µL of trailing electrolyte (TE) buffer. We then applied a slight vacuum at Reservoir 1 for about thirty seconds. A constant

current is then applied between Reservoirs 2 and 4.

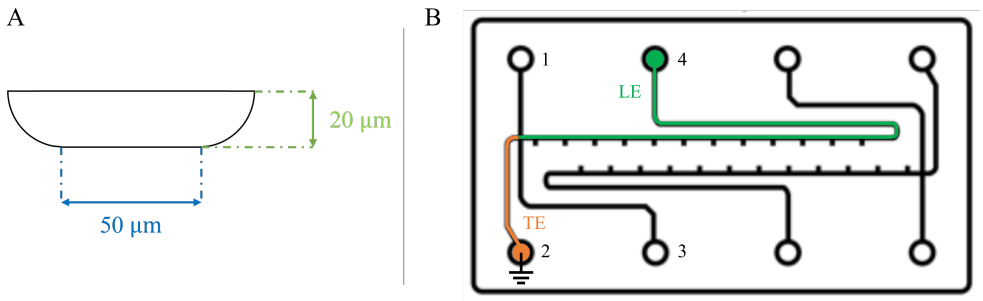

Figure E.3: Geometry of the NS12AZ chip (PerkinElmer) and initial injection configuration for the experiments of Figure 5.5 of Section 5.2. (A) Schematic of the cross-section of the microchannels. (B) Top view schematic of the chip. The color sections show the initial distribution of injected LE and TE buffers for the peak-mode ITP experiments.

E.5 MATLAB post-processing of experimental movies for spatio-temporal plots

Presented in this section are details of the processing of the CMOS experimental images which led to Figure 5.5 of Section 5.2.

E.5.1 Flat-field correction

We first performed a flat-field correction of the raw images to account for inhomogeneous illumination. We used the following correction for each image:

$$I_{\text{corr}}(x,y,t) = \frac{I_{\text{raw}}(x,y,t) - I_{\text{bg}}(x,y)}{I_{\text{flat-field}}(x,y) - I_{\text{bg}}(x,y)}. \tag{E.1}$$

Here, I_{raw}, I_{bg}, $I_{\text{flat-field}}$ and I_{corr} are respectively the raw signal from the CMOS camera, the background signal, the flat field signal, and the corrected image. The background image was obtained by filling the channel with LE buffer (no dye), activating the illumination source (along with any small lights in the room, including from computer monitor), and taking an image. The flat-field image was obtained by filling the channel with LE mixed with about 50 µM concentration of Alexa Fluor 488 dye and obtaining an image. Of course, all images were obtained with the same illumination source (activated), the same objective, the same epifluorescence color filters, and the same camera. The image algebra above was performed for each time t (i.e., each raw image) using MATLAB (version R2021a, MathWorks).

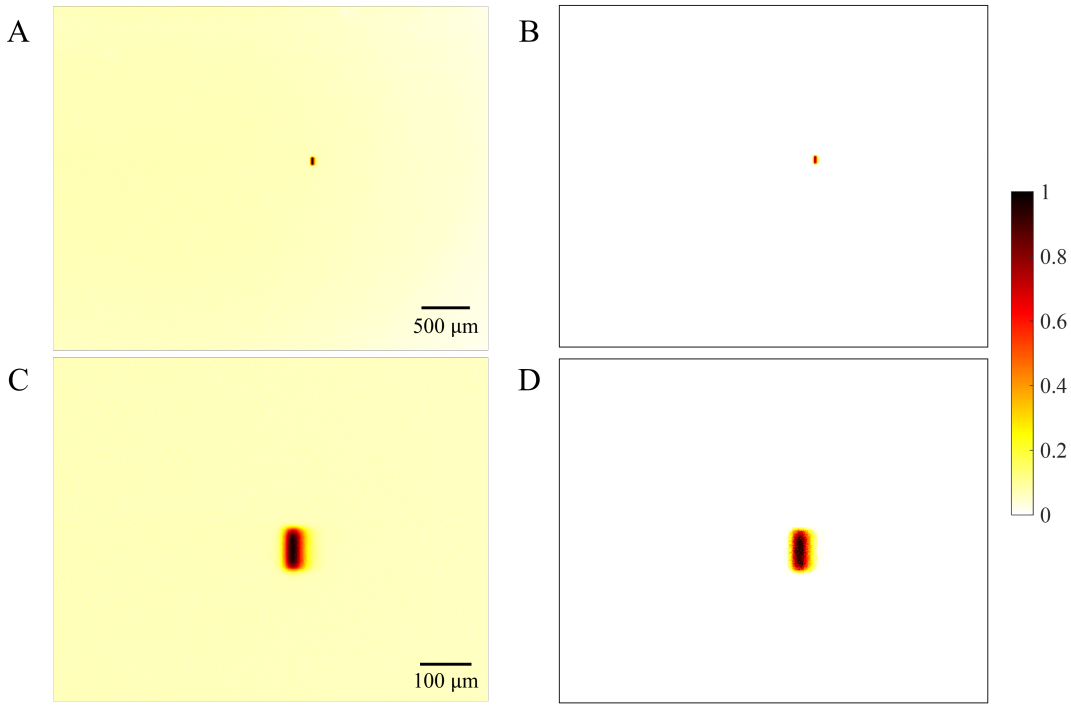

Figure E.4: Example flat-field correction of a CMOS camera experimental image. (A) Raw image from the CMOS camera. Pixel intensities shown here are visualized using the flipped "hot" colormap (i.e., false color images of the intensities of the 16-bit image data file). The background (yellow zone) is visibly inhomogeneous mostly due to (expected) non-uniform illumination. This non-uniformity affects image analysis, including quantitative integration of the ITP peak (red zone). (B) Shown here is the flat-field corrected image using a single image. Note the background intensity is now homogeneous. Images (C) and (D) are respectively zoomed in versions of the images of (A) and (B).

E.5.2 Spatial averaging

We here describe our post processing of images. We performed all image processing on the flatfield corrected images. To this end, we analyzed only image data within the rectangular area of the microchannel. The height of this image area (along the y-direction in Figure E.4) corresponded to the spanwise ~90 µm width of the channel. The width of this area (x-direction in Figure E.4) corresponded to the entire length of the microchannel within the field of view. For each time step (i.e., each image), we spatially averaged this rectangle over the spanwise y-direction of the image. This averaging operation is described as follows:

$$\bar{I}(x,t) = \frac{1}{L}\int_0^L I_{\text{corr}}(x,y,t)dy. \tag{E.2}$$

Here, L is the spanwise width of the channel (corresponding to 90 μm in object space). x is the axis of the channel (e.g., the direction of ITP zone motion). This averaging operation results in an axial distribution for each time. This spatiotemporal information was used to generate the spatio-temporal plots of Figure 5.5 of Section 5.2.

E.6 Cationic and bidirectional ITP using CAFES

CAFES solves the advection-diffusion equations for arbitrary mixtures of weak electrolytes, so its capabilities are not limited to simple anionic isotachophoresis. In fact, the tool can be used to solve problems of, for example, capillary zone electrophoresis, electromigration dispersion, and/or field-amplified sample stacking [205, 63]. To demonstrate the versatility of the tool, we provide here examples of cationic and bidirectional isotachophoresis.

Figure E.5A is a simulation of a cationic ITP process with sodium as an LE ion and BisTris as a TE ion (with HEPES as the counter ion). Here, imidazole and a generic, user-specified "Analyte" cation (pK_a of 7 and fully ionized mobility of 40×10^{-9} m^2/(V·s)) are focused into two plateaus. Figure E.5B is a simulation of a bidirectional ITP process. In this process, simultaneous anionic and cationic ITP zones are created at the left and right sides of the computational domain. The two ITP waves migrate toward each other, interact, and create new zones. Here, we use the various buffers to focus two anionic analytes within the anionic ITP zone. When the anionic and cationic ITP zones interact, the new conditions around the analytes initiate a capillary zone electrophoresis separation of the analytes. See Bahga et al. [206] for more discussion of such processes.

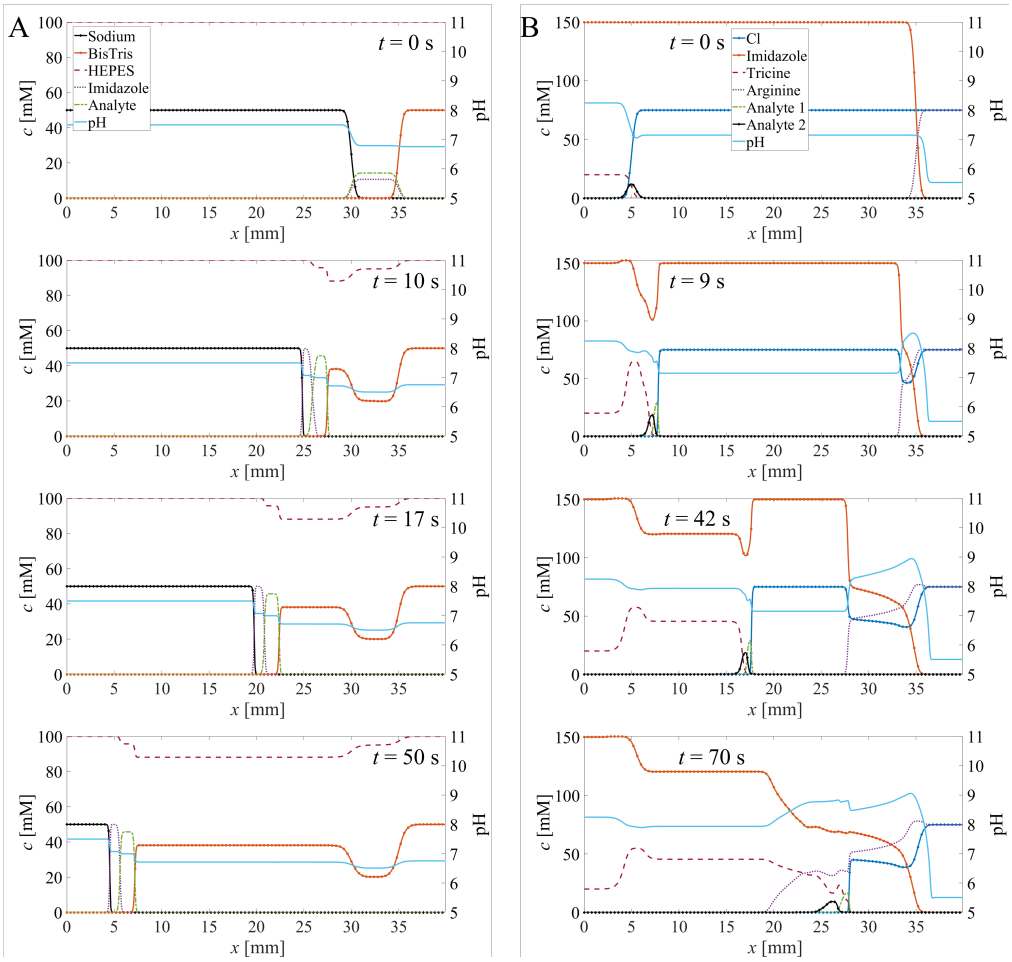

Figure E.5: Cationic ITP (A) and bidirectional ITP (B) simulations using CAFES. Plotted are the concentrations of the electrolytes (left ordinate) and pH (right ordinate, light blue curve). (A) The cationic ITP simulation was performed using an LE cation (sodium), a TE cation (BisTris), a uniform background anion (HEPES) and two analytes (Imidazole and a custom-specified analyte). (B) The bidirectional ITP simulation includes anionic ITP focusing (traveling right) of two anionic analytes (custom analytes labeled Analytes 1 and 2). Cationic ITP is initiated at the right and travels leftward. The interaction of the two ITP interfaces initiates electrophoretic separation of the analytes.

E.7 Grid independence study

We completed a grid independence study of the simulations yielded by CAFES. This study ensures that the numerical solution converges toward a unique solution as the mesh becomes finer. For this study we considered a simple anionic ITP system consisting of an LE buffer (50 mM HCl and 100 mM Tris, pH = 8.21)

and a TE buffer (50 mM HEPES and 100 mM Tris, pH = 8.07). We set the current to −1 µA, the computational domain length to 40 mm, and the channel cross-sectional area to 1400 µm^2, and the maximum simulation time to 240 s. We first verified that the predicted concentrations and pH of the adjusted TE zone matched the one predicted by BEAN (Browser-based Electrolyte Analyses for ITP, [136]).

We then examined the width of the steady state LE-TE interface. Analogous to the definition of a boundary layer in fluid mechanics, we defined the interface width w as the length of the subspace of the simulated domain where the concentration of the LE anion is between $\alpha c_{\max}$ and $(1-\alpha)c_{\max}$. Here, $c_{\max}$ represents the maximum concentration of LE anion and α is an arbitrary constant between 0 and 0.5. To continue the analogy with boundary layers, we selected $\alpha = 0.01$, but we show that our results are insensitive to this parameter.

We then simulated the same physical process but changing the number of grid points, N. All other input parameters were held constant. We performed simulations using $N = 101, 200, 500, 750, 1000, 1500, 2000$ and 3000 grid points. Let w_0 be the interface width computed for the largest number of grid points. This is the most precise value of the interface width computed, i.e. for $N = 3000$. We then defined a relative error as $u_{\text{rel}} = \frac{w - w_0}{w_0}$ and computed this value for each grid size.

The results are shown in Figure E.6 for three values of the (arbitrary) definition of the interface width, α.

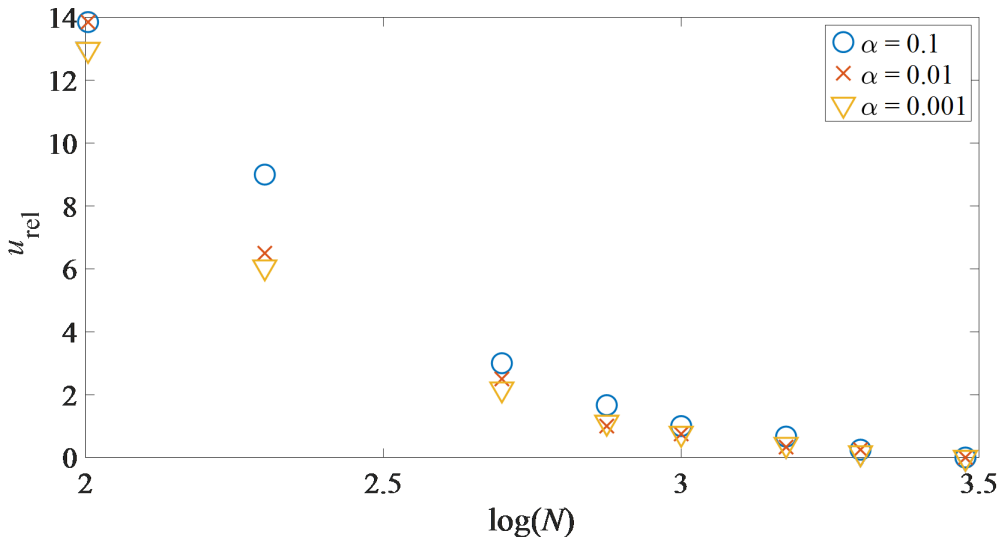

Figure E.6: Grid independence of CAFES simulations. Plotted is the relative error on the interface width of an anionic LE-TE interface for three values of the cutoff parameter α. The relative errors converge towards zero for mesh numbers above about 3000 ($\log(N) = 3.48$), regardless of the value of the parameter α.

In addition, we verified that the mean time step that is computed with the fifth order Runge-Kutta

Dormand-Prince method also scales with the mesh size. To this end, we performed simulations using N = 101, 200, 400, 800, 1600, and 3200 grid points and the same simulation settings (i.e., ITP chemistry and simulation parameters) as described above. Figure E.7 shows the mean time step in each simulation as a function of the number of grid points. We also show for reference an order −1 slope line. Figure E.7 shows that the mean time step scales inversely with the number of grid points. This verifies that the time stepping method developed in CAFES automatically adapts the time step for the mesh size chosen by the user.

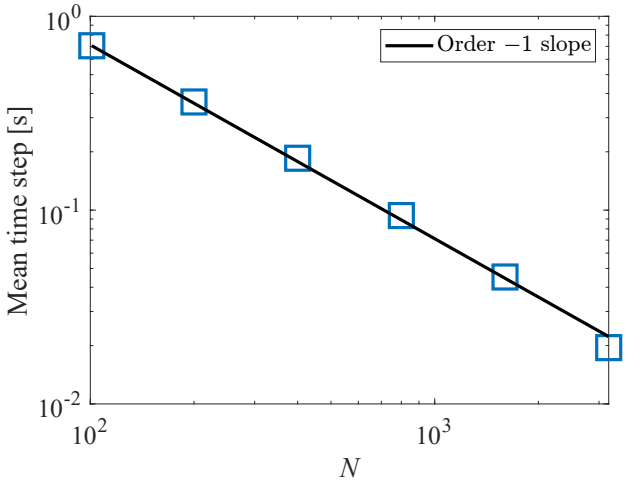

Figure E.7: Mean time step during the grid independence study. Shown are mean time steps for six simulations using the same parameters, except for the number of mesh grid points N varied from 101 to 3200. The mean time step, which results from the Runge-Kutta Dormand-Prince method, scales linearly with the mesh size (i.e., inversely proportional to the number of grid points).

E.8 Comparison of the time stepping scheme

We compared the Dormand-Prince scheme (DORPRI45-RK45) used in CAFES with a lower-order scheme. To do so, we implemented an alternative version of CAFES that uses the Bogacki-Shampine scheme (a third-order Runge-Kutta method). This is the method used by the `ode23` function in MATLAB.

Similar to what we presented in Section 5.2.2, we first implemented the Bogacki-Shampine scheme (RK23) in Python. The scheme was converted into a TensorFlow graph, which can then be called upon by the React-based JavaScript interface. A version of CAFES that uses RK23 for time stepping is available at web.stanford.edu/group/microfluidics/cafesrk23/.

We first completed a grid independence study similar to the one presented in Section E.7. We used the same simulation inputs as the ones listed in Section E.7. Figure E.8 shows the relative error as a function of the number of mesh grid points N and the cutoff parameter α (see Section E.7).

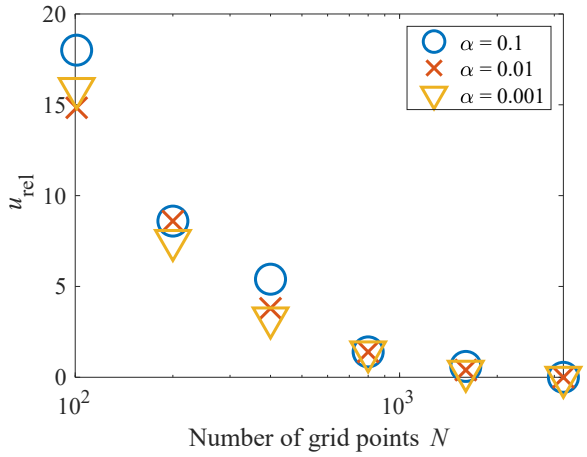

Figure E.8: Comparison of the RK23 and RK45 time stepping schemes. A Mean time step for six successively refined meshes. All simulation parameters are conserved, except for the number of mesh grid points N, which varies from 101 to 3200. In both cases, the mean time step scales linearly with the mesh size. RK45 typically yields slightly larger mean time steps than RK23. B Number of time steps for the same conditions.

Further, we compared the mean time step using both Runge-Kutta methods. Figure E.9A shows the mean time step as function of the number of grid points for both the fifth- and third-order Runge-Kutta methods. We show for reference an order -1 slope line. Figure E.9B shows the corresponding number of time steps as function of the number of grid points and time stepping scheme. We show for reference an order 1 slope line.

We note that the RK45 simulations result in slightly larger time step values across all meshes. This results in a lower number of time steps when RK45 is used, compared to RK23. There is significant computational overhead at each time step, due to the chemical equilibrium calculation and the plot update in the JavaScript interface. We estimate that the latter step dominates the computational time, as a single plot update takes approximately three times longer than the time integration step (as measured using the `performance.now()` function).

Overall, we find that the RK45 method results in slightly faster solutions, especially when the interface plot is updated often. For this reason, we chose RK45 over RK23 for time stepping.

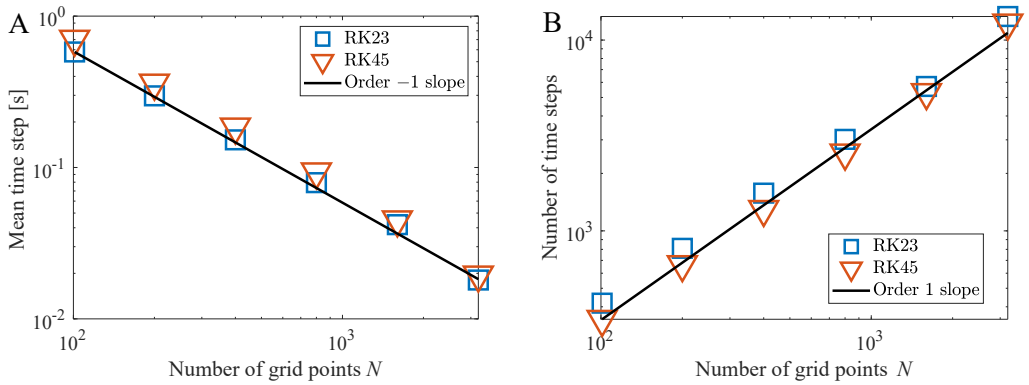

Figure E.9: Grid independence study for CAFES simulations using RK23 for time stepping. Shown is the relative error on the interface width of an anionic LE-TE interface for three values of the cutoff parameter α. The relative error converges towards zero as the number of grid points increases, regardless of the value of α.

Appendix F

Supplementary Information for Microfluidic networks using isotachophoresis

F.1 Model equations for peak evolution

F.1.1 Derivation of the network equation

We derive the network equation that relates the total number of vertices in the network (including Γ reservoirs and K three-way channel junctions), ITP peaks (P), and ITP segments (Q). We assume that all channel junctions are three-way junctions, and that each reservoir is linked to exactly one ITP segment. These assumptions are true for all the networks that we present in Figures 6.2 to 6.5, but they do not necessarily hold true for all ITP networks. For instance, the network presented in Figure F.4 does not satisfy the first assumption.

Each ITP segment is bound by two vertices, so there is a total of $2Q$ segment vertices in the ITP network. Vertices may be located at ITP peaks, reservoirs, or channel junctions. Each reservoir is linked to exactly one ITP segment. This represents a total of Γ vertices. ITP peaks define the interface between two ITP segments. Therefore, each ITP peak represents two ITP segment vertices. This represents a total of $2P$ vertices. Finally, channel junctions are at the intersections of three ITP segments; therefore, each channel junction represents three ITP vertices. This represents a total of $3K$ vertices. Equating the total number of ITP segment vertices, it comes: $2P + 3K + \Gamma = 2Q$.

F.1.2 Peak evolution equations

In this section, we detail the state equations that describe ITP peak evolution in arbitrary networks. The equations we describe here, plus equations 6.1 to 6.5, form the $K + \Gamma + Q + 2P$ mathematically independent equations necessary to iteratively solve for the state of ITP networks.

We first introduce $2P$ equations that describe the evolution of ITP interface positions and accumulated analyte quantity in the peak. We indicate as x_p the position of peak p, and use N_p for the quantity of analyte (e.g., in moles and initially stored in the TE reservoir) contained in peak p. The superscript i denotes the time step. We assume controlled-current, peak-mode ITP in semi-infinite injection [58]. During each time step, peaks can travel in the channel, split at a channel junction, or merge with another ITP interface. We detail the state equations in each of these cases below.

If an ITP interface p located at x_p travels through a segment q, and does not encounter a bi- or multifurcation, then:

$$x_p^{i+1} = x_p^i + \frac{\mu_{LE} j_q}{\sigma_q} \Delta t, \tag{F.1}$$

$$N_p^{i+1} = N_p^i + \alpha \Delta t. \tag{F.2}$$

Here, j_q and σ_q respectively denote the current density and the conductivity in the ITP segment q. α represents the analyte accumulation rate in the ITP peak and can be computed as a function of the TE and sample electrophoretic mobilities, ITP velocity, cross-sectional area, and sample concentration in the ATE [58]. Δt represents the time interval between instants i and $i + 1$. Note that these equations are still valid if multiple peaks progress in the same channel.

If a peak p reaches the end of the channel in which it is traveling and encounters a bi- or multifurcation, it splits in Π peaks p_m, such that $1 \leq m \leq \Pi$ (e.g., $\Pi = 2$ for a bifurcation). We note with the subscript m quantities (current I_m, current density j_m, and conductivities σ_m) that refer to the ITP segment of LE downstream of the peak p_m. The position of peak p_m and the quantity of analyte in peak p_m are determined by:

$$x_{p_m}^{i+1} = x_p^i + \frac{\mu_{LE} j_m}{\sigma_m} \Delta t, \tag{F.3}$$

$$N_{p_m}^{i+1} = N_p^i \frac{I_m}{\sum_{m'=1}^{\Pi} I_{m'}} + \alpha \Delta t. \tag{F.4}$$

We refer the reader to the work of Persat and Santiago [190] for a study on the relative amounts of sample in each of the two outlet ITP peaks are controlled by the current ratio of the outlet peaks.

Lastly, if two peaks p_1 and p_2 progress in the same microfluidic channel such that $x_{p_2} < x_{p_1}$, then we observe experimentally that the late peak p_2 migrates faster than the early peak p_1. When p_2 catches up with p_1, the two peaks merge into a new peak p_3. We model this phenomenon with the following state

equations:

$$x_{p_2}^i < x_{p_1}^i \text{ and } x_{p_2}^{i+1} > x_{p_1}^{i+1} \Rightarrow x_{p_3}^{i+1} = x_{p_1}^i + \frac{\mu_{LE} j_1}{\sigma_1} \Delta t, \tag{F.5}$$

$$x_{p_2}^i < x_{p_1}^i \text{ and } x_{p_2}^{i+1} > x_{p_1}^{i+1} \Rightarrow N_{p_3}^{i+1} = N_{p_1}^i + N_{p_2}^i + \alpha \Delta t. \tag{F.6}$$

Here, we denote with the subscript 1 the ITP segment ahead of the early peak p_1.

F.2 Derivation of peak self-stability

In this section, we derive equation 6.6. Here, we consider the configuration shown in Figure F.1, wherein two ITP peaks progress in parallel channels whose inlets and outlets are connected. We respectively denote R_i, A_i, L_i, σ_i, the electrical resistance, cross-sectional area, length, and conductivity of channel i ($i = 1$ or 2).

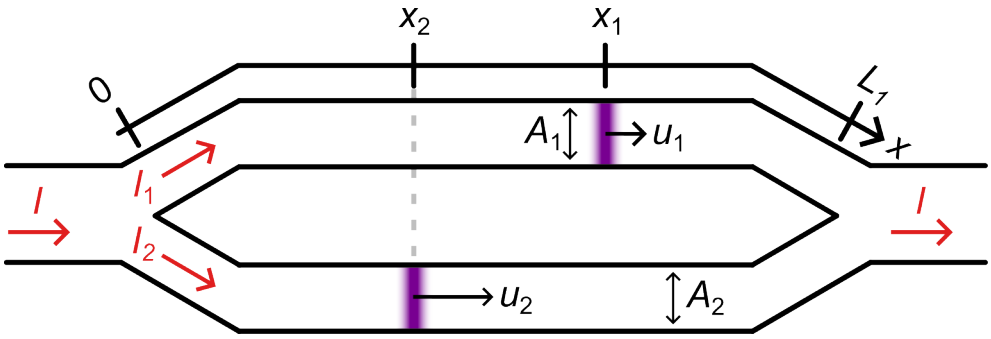

Figure F.1: Schematic of two ITP peaks progressing in parallel channels whose inlets and outlets are connected.

As shown in Figure F.1, we denote with x_i the position of the ITP peak in channel i, and we define $\xi_i = \frac{x_i}{L_i}$. Similarly, we indicate with I_i the electrical current running through channel i, and $I = I_1 + I_2$. We write $\lambda = \frac{L_1}{L_2}$ and $\eta = \frac{A_1}{A_2}$. This configuration represents a simple current divider circuit, which therefore satisfies:

$$I_1 = \frac{R_2}{R_1 + R_2} I = \frac{I}{1 + \frac{R_1}{R_2}}. \tag{F.7}$$

The net electrical resistance varies in time and can be written as:

$$R_i = \frac{L_i}{\sigma_i A_i} = \frac{L_i}{(\xi_i \sigma_{ATE} + (1 - \xi_i)\, \sigma_{LE})\, A_i} = \frac{L_i}{A_i \sigma_{LE}} \frac{1}{\xi_i\, \sigma' + 1}. \tag{F.8}$$

Here, $\sigma' = \frac{\sigma_{ATE} - \sigma_{LE}}{\sigma_{LE}} < 0$. Hence:

$$I_1 = \frac{I}{1 + \frac{\lambda}{\eta}\frac{\xi_2\sigma'+1}{\xi_1\sigma'+1}}, \tag{F.9}$$

$$I_2 = \frac{I}{1 + \frac{\eta}{\lambda}\frac{\xi_1\sigma'+1}{\xi_2\sigma'+1}}. \tag{F.10}$$

The ITP velocity $u_i = \frac{dx_i}{dt}$ can be expressed as [58]:

$$u_1 = \frac{\mu_{LE}}{\sigma_{LE}}\frac{I_1}{A_1} = \frac{\mu_{LE}}{\sigma_{LE}A_1}\frac{I}{1 + \frac{\lambda}{\eta\chi}}, \tag{F.11}$$

$$u_2 = \frac{\mu_{LE}}{\sigma_{LE}}\frac{I_2}{A_2} = \frac{\mu_{LE}}{\sigma_{LE}A_2}\frac{I}{1 + \frac{\eta\chi}{\lambda}}, \tag{F.12}$$

Where we have defined $\chi = \frac{\xi_1\sigma'+1}{\xi_2\sigma'+1}$. The velocity difference between the two peaks is then:

$$\Delta u = u_1 - u_2 = \frac{I\mu_{LE}}{A_1\sigma_{LE}}\left[\frac{\frac{\eta\chi}{\lambda} - \eta}{\frac{\eta\chi}{\lambda} + 1}\right], \tag{F.13}$$

$$\frac{\Delta u}{u_{th}} = (1+\eta)\left[\frac{\frac{\chi}{\lambda} - 1}{\frac{\eta\chi}{\lambda} + 1}\right]. \tag{F.14}$$

where $u_{th} = \frac{\mu_{LE}}{\sigma_{LE}}\frac{I}{(A_1+A_2)}$.

In the special case where the two channels have the same geometry, $\lambda = \eta = 1$. Then:

$$\frac{\Delta u}{u_{th}} = 2\left[\frac{\chi - 1}{\chi + 1}\right]. \tag{F.15}$$

If the two peaks are at the same position in their respective channels ($x_1 = x_2$), then $\xi_1 = \xi_2$ and $\chi = 1$, so $\Delta u = 0$. In other words, the two peaks are progressing at the same velocity.

Let us now examine the situation where one peak (e.g., peak 1) travels ahead than another (i.e., $x_1 > x_2$). Because the channel geometries are the same, $\xi_1 > \xi_2$, so $\xi_1\sigma' < \xi_2\sigma'$, and $\chi < 1$. Per equation F.15, this results in $\Delta u < 0$, so $u_1 < u_2$. In other words, if one of the peaks lags, it will thereafter travel faster than the leading peak until it catches up.

Importantly, the aforementioned self-correction is not necessarily true if the parallel channels have different cross-sections and/or different lengths. For this reason, differences among parallel channels due to fabrication limitations can result in one peak moving faster than a parallel "neighbor" peak. We therefore attribute some of the imperfect peak progressions in our experiments (e.g., see Figure 6.2 or Section F.6) to small errors associated with the fabrication process of the molds associated with our multifurcation channel designs. Varying channel length and cross-sectional areas could be explored using our iterative model.

F.3 Experimental setup

In this section, we describe the experimental setup used in this study. Figures F.2A and F.2B show the channel geometries used for the fabrication of the symmetric and asymmetric multifurcation. We show in Figures F.2C and F.2D brightfield microscope images of the fabricated microfluidic chip corresponding to the regions highlighted in Figures F.2A and F.2B with dashed boxes. Note that the fabrication processes for the mold of both chips differ significantly, as mentioned in the Section 6.4. Figure F.2E shows our setup, consisting of the microfluidic chip mounted on the stage of an epifluorescence microscope, and connected to the Keithley sourcemeter using electrodes shown here in red and black. Finally, we show in Figure F.2F a stitched brightfield image of our 1-to-32 multifurcation chip.

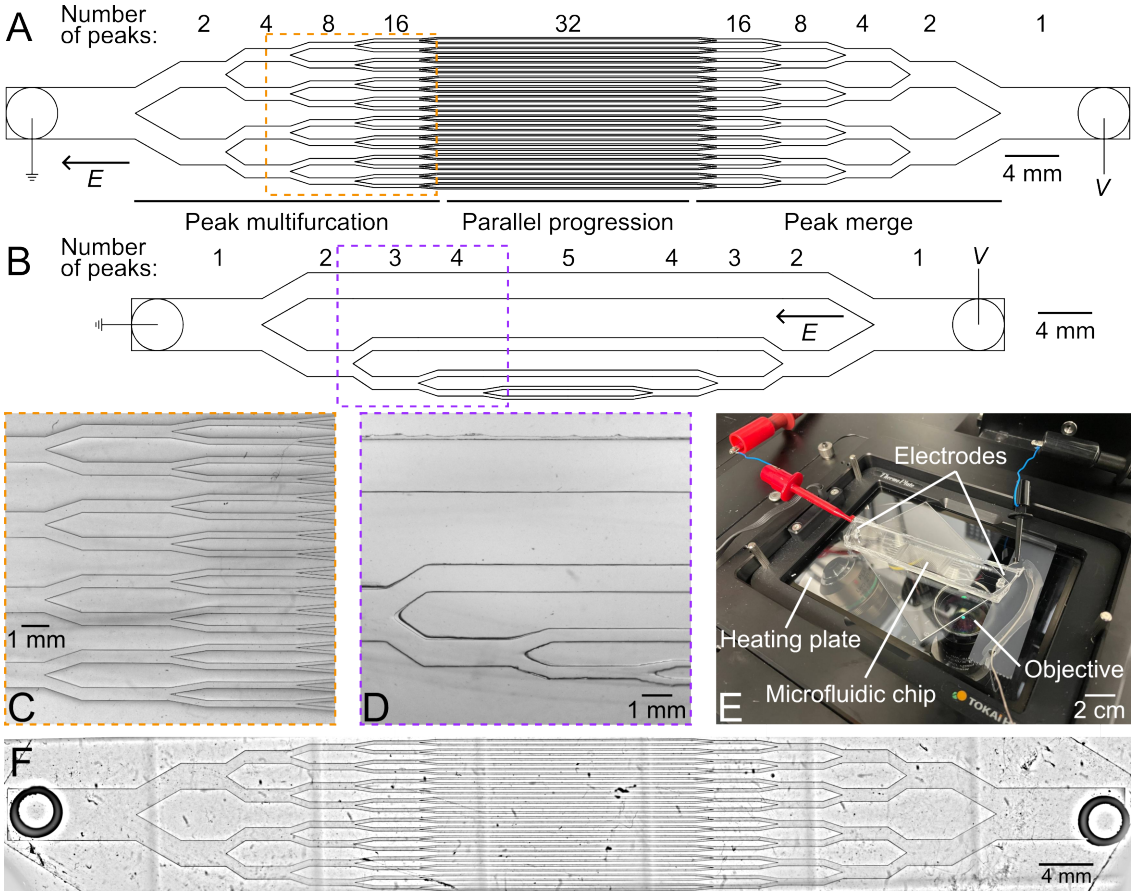

Figure F.2: A Chip geometry for the 1-to-32-to-1 multifurcation and merge. B Asymmetric peak chip geometry. C Brightfield image showing the fabricated microfluidic chip corresponding to the orange dashed box region shown in A. D Brightfield image showing the fabricated microfluidic chip corresponding to the purple dashed box region shown in B. E Experimental setup showing the microfluidic chip (center) sitting on the motorized microscope stage, and connected to the Keithley sourcemeter with the two electrodes (red and black). F Stitched brightfield image (i.e., multiple images registered and superposed) of the 1-to-32 chip.

F.4 Asymmetric bifurcations and merging of peaks

Here, we show composite fluorescence images (similar to Figures 6.2A and 6.3A) for three network geometries different than those of chapter 6. Shown are composite (experimental) fluorescence images for two example asymmetric multifurcation networks (Figure F.3) and merging of peaks within a varying cross-sectional channels (Figure F.4).

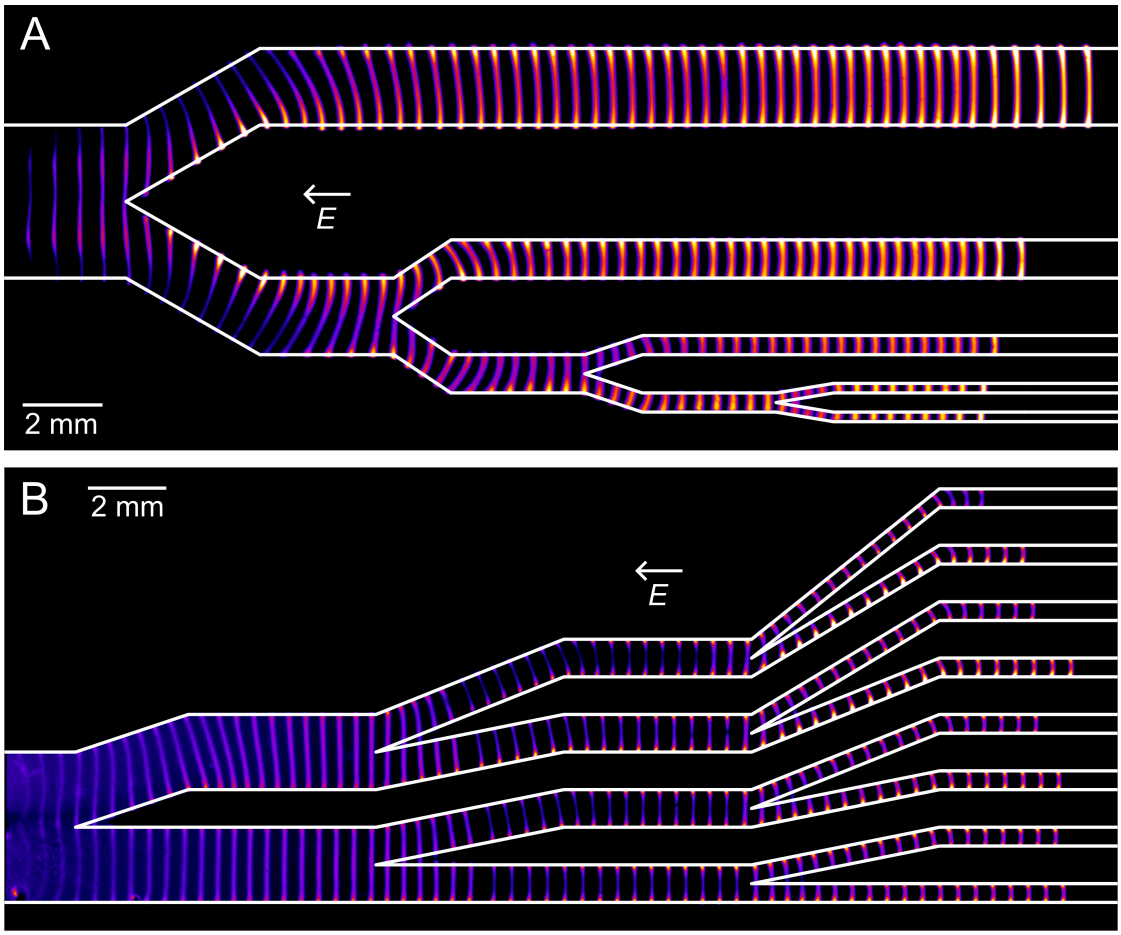

Figure F.3: Composite of experimental fluorescence images showing the progression of ITP peaks in multifurcation tree networks. A Multifurcation network with varying cross-sectional area. Shown are summed fluorescence images of the peaks taken every ~20 s. In this experiment, the analyte is fluorescein. B Multifurcation network with varying channel lengths. Shown are summed fluorescence images of the peaks taken every ~30 s. In this experiment, the analyte is a Cy5-labeled ssDNA molecule.

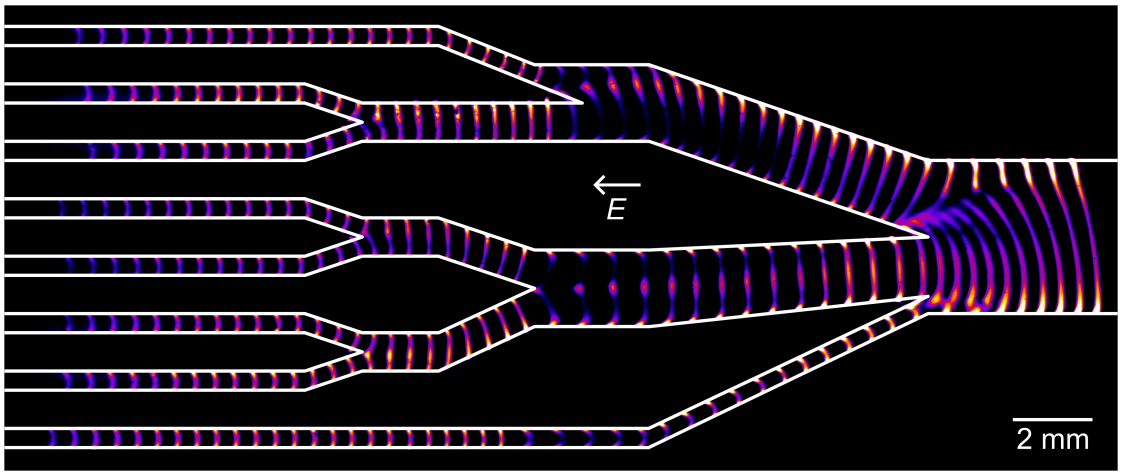

Figure F.4: Peak merging within an asymmetric network. Network has varying channel lengths and cross-sectional areas. Shown are summed fluorescence images of the peaks taken every ~30 s. In this experiment, the analyte is a Cy5-labeled ssDNA molecule.

F.5 ITP peak velocity measurements

We show ITP peak velocity measurements in various networks. Figure F.5 shows the measured peak velocities during the 1-to-32 peak multifurcation experiment. Each velocity measurement is shown with an open circle, and colors indicate peak number (from 1 to 32). We show with solid lines the moving median of the peak velocity across five measurements. In Figure F.5, peak velocities are estimated by computing the numerical gradient of the peak position. The peak position is determined by identifying the coordinates of the peak image centroid, as described in Section 6.4.4 "Peak visualization and tracking". The coordinates $x_{c,p}$ and $y_{c,p}$ of the centroid corresponding to peak p are computed using the following equations:

$$x_{c,p} = \frac{1}{S_p} \sum_{i=1}^{S_p} x_{i,p}, \tag{F.16}$$

$$y_{c,p} = \frac{1}{S_p} \sum_{i=1}^{S_p} y_{i,p}, \tag{F.17}$$

where S_p is the number of foreground pixels in the binary masks, and $x_{i,p}$ and $y_{i,p}$ are the coordinates of each foreground pixel (i.e., nonzero pixel) in the binary region corresponding to peak p.

The identification of peaks is not precise during the brief process where a peak meets a bifurcation and splits. This splitting temporarily results in highly two-dimensional image intensity profiles which are difficult to repeat across experiments and across parallel bifurcations in a single experiment. The tracking algorithm that we developed requires a frame or two to adapt to a newly deformed and split peak. Further,

the computation of the centroid in these highly deformed peak shapes is subject to some noise and irreproducibility. We further note that artifacts in peak tracking are also introduced during the times when the microscope stage is moved by the experimentalists to track the motion of the multiple peaks through the chip. This stage motion occurs over one or two frames and errors in registration of image vs. recorded time can cause scatter in velocity estimates, as shown in Figure F.5.

Figures F.6 to F.8 show ITP peak measurement during merge events. Shown in A are measurements of the velocities of the two merging ITP peaks (open circles), five-frame moving median values (solid lines), and corresponding peak positions (inset). We show in B fluorescence images corresponding to the different phases of the merges, similar to Figure 6.4B.

Figure F.6 shows the velocity measurement for a synchronous merge, i.e. a merge wherein the two peaks arrive at the channel junction at the same time. In this case, we observe that the two peaks travel at the same velocity prior to the merge, and that the merged peak travels at this same velocity. Figures F.7 and F.8 show similar data in the case of an asynchronous merge, for two different generations of merges. In both cases, we observe that an early peak (red) travels at a lower velocity once it reaches the channel junction. Conversely, the late peak (green) travels at a higher velocity once it reaches the junction. This velocity difference persists until the two peaks merge. We attribute this to the fact that the late peak travels in a region of lower conductivity than the LE (a mixture of LE and ATE ions), and therefore experiences a higher electric field than the early peak. After the merge, the resulting merged peak velocity is roughly the same as that of the peaks immediately prior to the merge event.

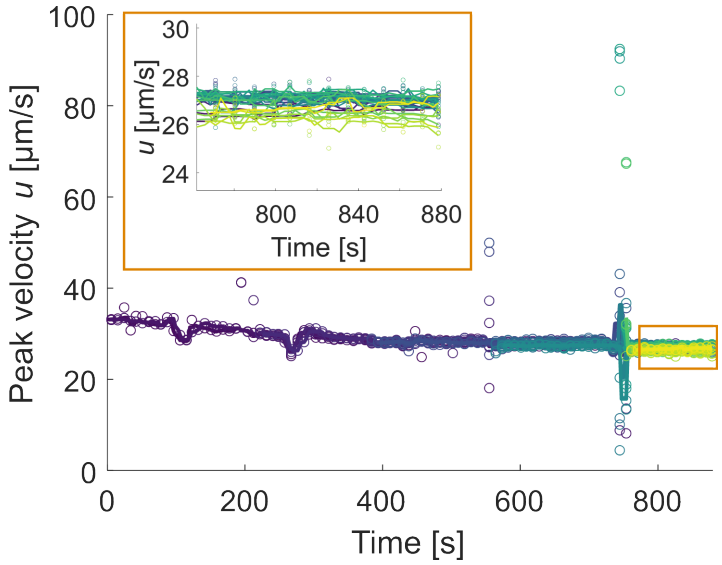

Figure F.5: Velocity measurements during the 1 to 32 peak multifurcation. Points are measurement of the derivative of the x position with respect to time. Solid lines show the value of the moving median every five measurements.

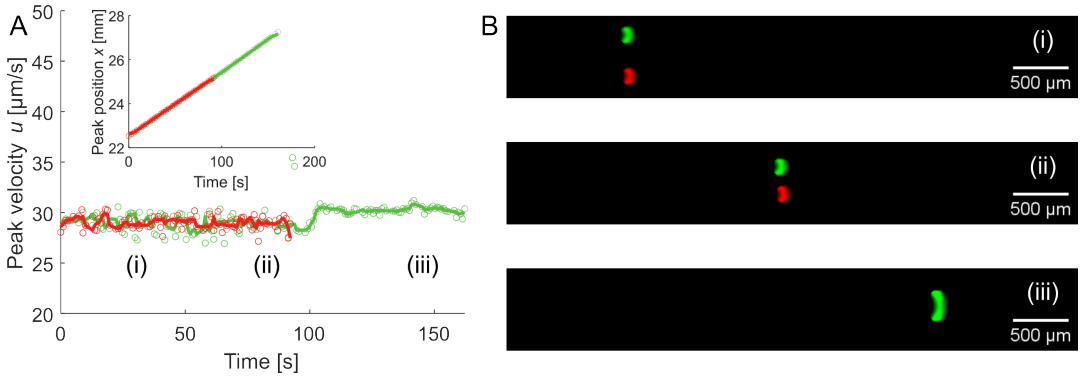

Figure F.6: A Peak velocity evolution during a peak merge event. Shown are measurements of the derivative of the x position with respect to time. Solid lines indicate the values of the moving median across five frames. We show in the inset the corresponding measured peak positions versus time. B Fluorescence images of the peaks at three different stages of the merges. Shown with false colors (green and red) are the two merging peaks.

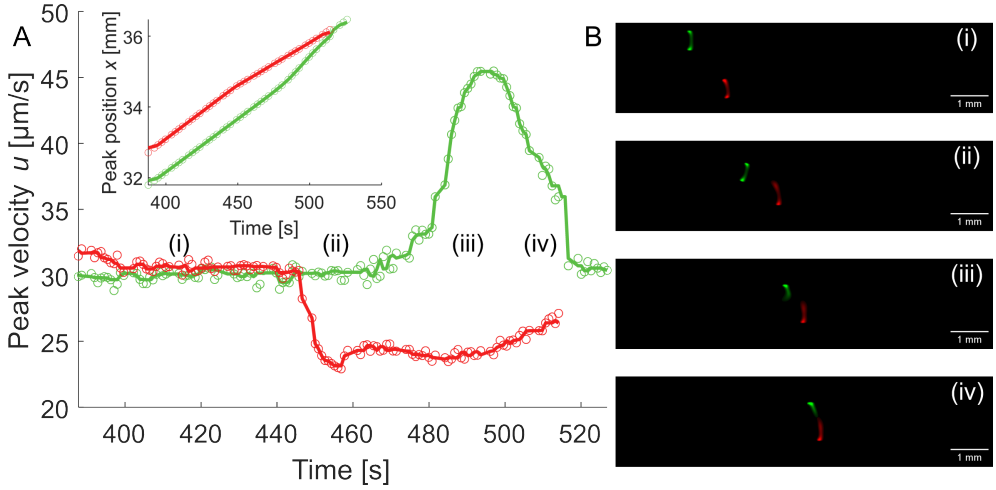

Figure F.7: A Peak velocity evolution during a peak merge event. Shown are measurements of the derivative of the x position with respect to time. Solid lines indicate the values of the moving median across five frames. We show in the inset the corresponding measured peak positions versus time. B Fluorescence images of the peaks at three different stages of the merges. Shown with false colors (green and red) are the two merging peaks.

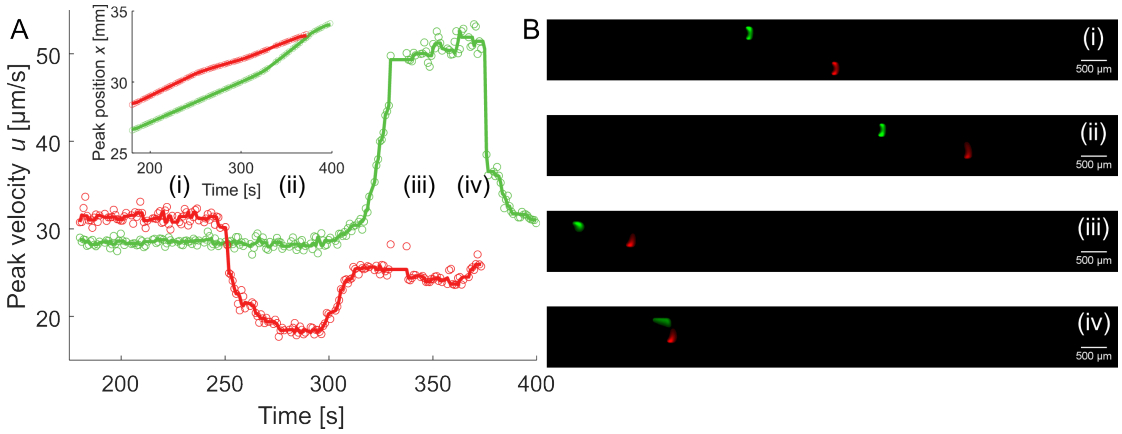

Figure F.8: A Peak velocity evolution during a peak merge event. Shown are measurements of the derivative of the x position with respect to time. Solid lines indicate the values of the moving median across five frames. We show in the inset the corresponding measured peak positions versus time. B Fluorescence images of the peaks at three different stages of the merges. Shown with false colors (green and red) are the two merging peaks.

F.6 Peak progression in parallel channels

Here, we focus on the movement of ITP peaks in parallel channels. Figure F.9A shows a composite fluorescence image of 32 peaks moving in parallel channels. Figure F.9B shows the corresponding positions of the peak centroids (here, color indicates frame number), and Figure F.9C shows the corresponding peak velocities (color indicates peak number). We observe that the peak velocity is roughly uniform across the different peaks, and there is a ~10% maximum difference (between the fastest and slowest peaks). We attribute these differences to small variations in the cross-sectional area of the microfluidic chip, mostly along the smallest channels of the network.

In Figure F.10, we compare each peak with the peak traveling in the channel that shares the same inlet and outlet as the channel it is traveling in (we call this peak the "neighbor peak"). This results in 16 pairs of ITP peaks. We show in Figure F.10A the absolute value of the peak position difference within each pair. We normalize this difference by subtracting the value of the difference at $t = 0$ to observe the time evolution of the position difference. We show in Figure F.10B the corresponding relative ITP peak velocity between two peaks of a pair. As described above (and predicted in Section F.2), we observe that neighbor ITP peaks travel at roughly the same velocity. However, small differences in peak velocity (within ±1 μm/s) over long times (100 s) result in measurable shifts between neighbor ITP peaks. We leverage such differences in peak positions to study asynchronous ITP peak merge downstream (Figure 6.3).

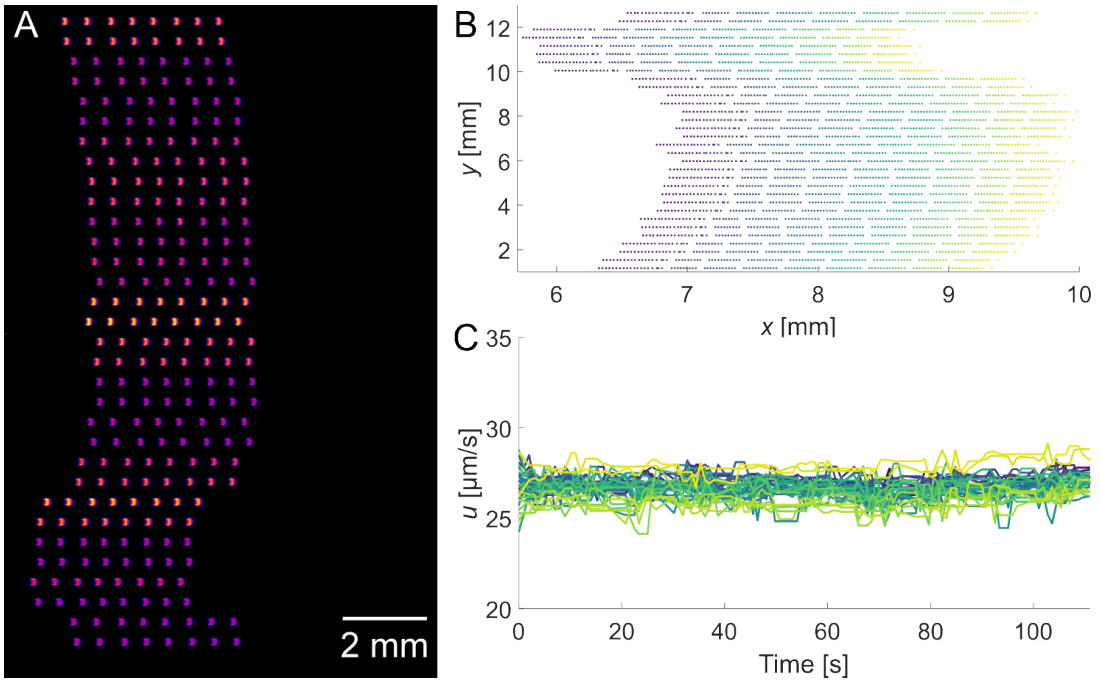

Figure F.9: A Composite experimental fluorescence images showing the progression of ITP peaks in 32 parallel microfluidic channels. B Measurements of ITP peak trajectories. Shown are ITP peak centers identified from image data using our custom image processing code. C Measured velocities of the 32 peaks. Shown is the moving median of the time-derivative of the peak positions across five frames.

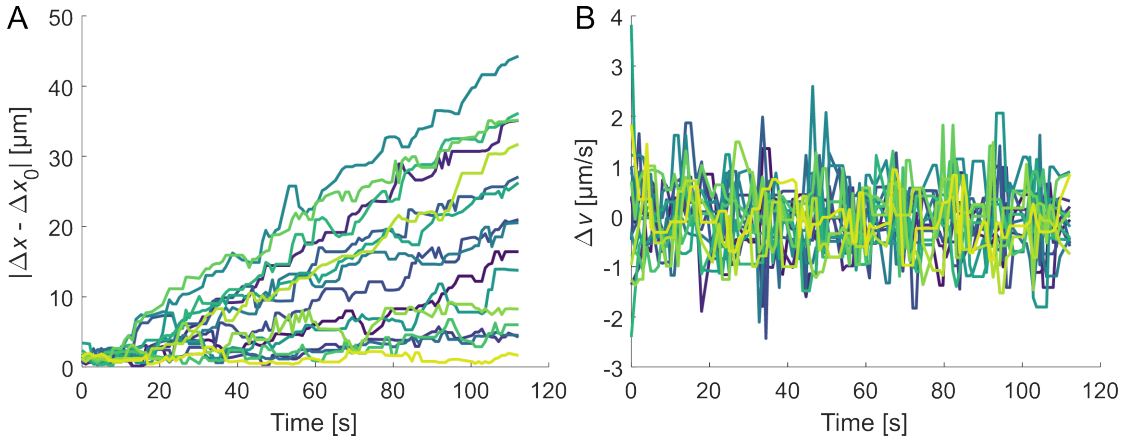

Figure F.10: Neighboring peak comparisons. All data here are moving median data across five frames. A Absolute distance difference between neighbor peaks vs time. The position difference is set to 0 at $t = 0$. B Relative velocity of ITP peaks within a pair of neighbor peaks.

F.7 Optical profilometry measurements

In this section, we present optical profilometry measurements for the SU-8 silicon wafer mold [207] that was used to fabricate the 1-to-32 multifurcation tree microfluidic channel. These measurements were performed using white light interferometry in a Keyence VK3030 optical profilometer. Figure F.11 shows example measurements in four different regions of the wafer. Figures F.11A-D show brightfield images of the measured zones. Figures F.11E-H show the corresponding height measurements. Finally, Figures F.11I-L show a sample height profile. The path along which height is plotted in Figures F.11I-L is shown with a blue line in Figures F.11A-D.

We note that the height of the features is close to the target height of 100 μm on average. However, there is some significant variation in the height of channels (relative to design) across parallel channels and across generations. We estimate that there is roughly 10% variation in the channel heights in the 5^{th} generation of microfluidic channels. Such variations can be expected in high aspect ratio channels like the one we use here [193].

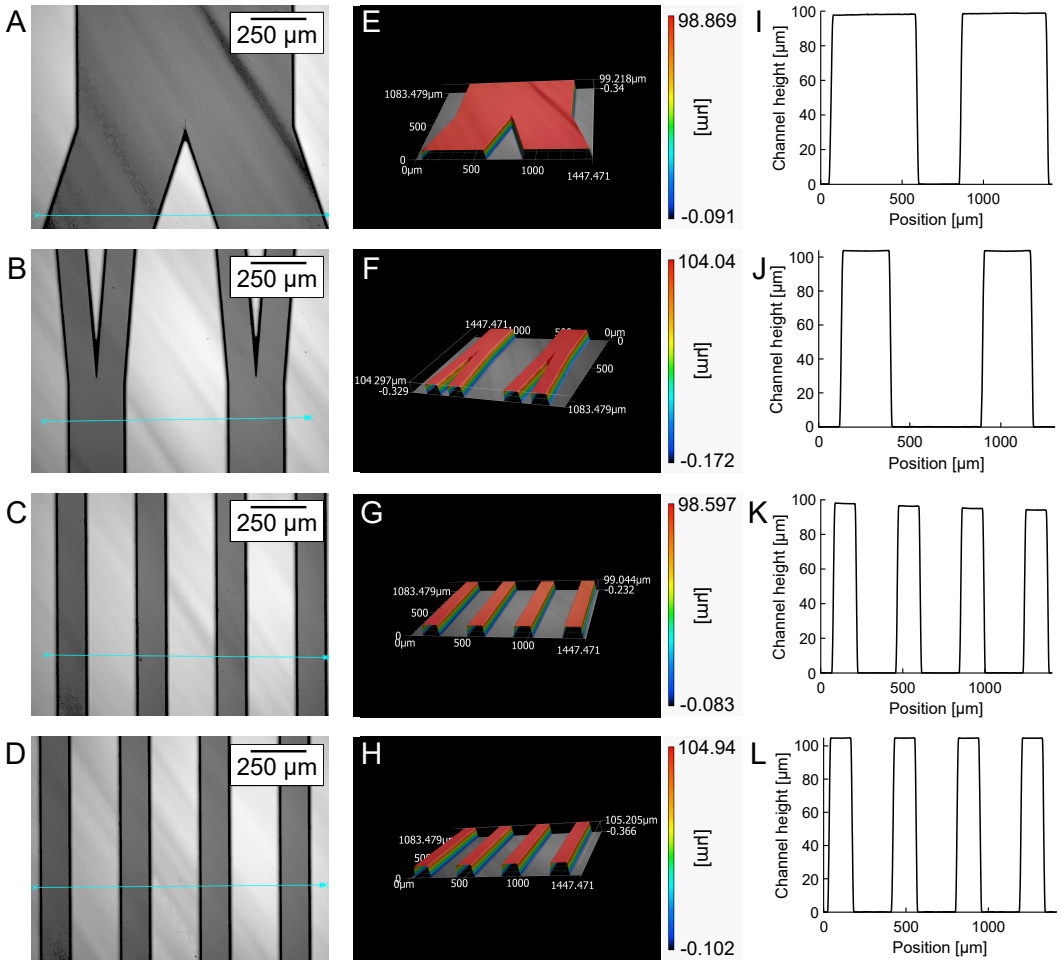

Figure F.11: Optical profilometry measurements. A-D Brightfield images of four regions of the wafer. E-H 3D measurements of the feature heights corresponding to regions shown in A-D. I-L Height profile along a path shown in blue in A-D.

F.8 Experiment-to-model comparison

In this section, we compare the solution from the solver described in Section 6.2.2 with the experimental data shown in Figure 6.2. Figure F.12 shows the positions of ITP peaks vs time in a 1-to-32 ITP multifurcation tree. Symbols show the experimentally measured position of peaks (every 15 frames). Here, peak position is determined using the estimate of the centroid of each ITP peak. Different peaks are shown with different symbols and colors. We show with a solid black line the trajectory predicted by the solver. We also show in the inset the peak velocities, computed as the temporal gradient of the data shown in the main figure. As discussed in Section 6.2.3.1, there is a strong agreement between the measured peak positions and the ones

predicted by the model.

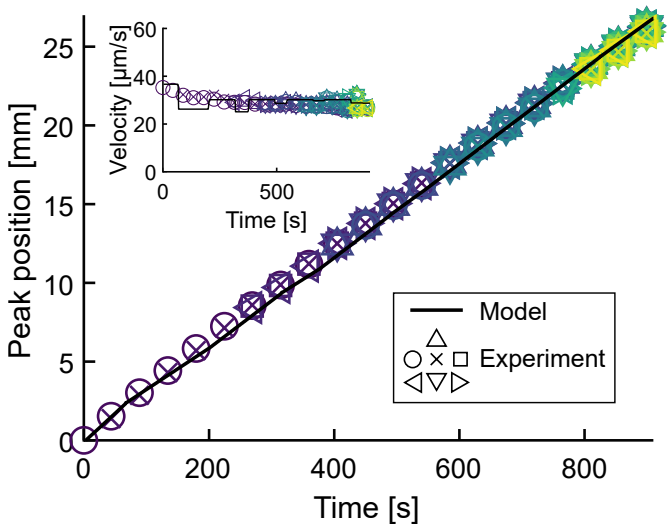

Figure F.12: ITP peak trajectories. Shown are measured peak positions vs time (symbols) and the corresponding peak trajectory predicted by the computational model described in Section 6.2.2 (black solid line).

F.9 List of oligos used in this work

Table F.1: List of oligonucleotides used in this work. This table presents all oligonucleotides used in this work, including guide RNAs (gRNA), DNA targets, and reporters. All sequences are reported in 5' to 3' direction.

Name	**Sequence**
Reporters	[FAM] TTA TTA TT [BHQ1]
gRNA	UAA UUU CUA CUA AGU GUA GAU GUG GUA UUC UUG CUA GUU AC
TS	ATC GAA GCG CAG TAA GGA TGG CTA GTG TAA CTA GCA AGA ATA CCA CGA AAG CAA GAA AAA
NTS	TTT TTC TTG CTT TCG TGG TAT TCT TGC TAG TTA CAC TAG CCA TCC TTA CTG CGC TTC GAT

Appendix G

Detailed experimental protocols

G.1 Calibration for CRISPR kinetics measurements

In this section, we detail the protocol used to calibrate CRISPR experiments that use fluorophore-quencher reporter molecules. The steps include:

1. Flat-field correction of the fluorescence readout,
2. Calibration of the reporter fluorescence signal and inner-filter effect.

The protocol we detail here applies to the CFX384 Touch Real-Time PCR Detection System (Bio-Rad Laboratories) using hard-shell, thin-wall, skirted 384-Well PCR Plates, but it is generally applicable to any reaction vessel (plate or tube).

In this machine, fluorescence readouts are performed one well at a time. An optics shuttle moves from well to well and directs the excitation light from a filtered LED into the center of each well. The emitted fluorescent light is collected using a lens system and detected by a filtered photodiode. The generated electrical current is amplified and passed through an analog-to-digital converter. The resulting unitless value is called "relative fluorescence units" (RFU, denoted $I(t)$ here) and is not standardized across detectors.

G.1.1 Flat-field correction of the fluorescence readout

The sensitivity of microwell-type arrays fluorescence detectors is not uniform. The flatfield correction for this effect is discussed in chapters 2 and 3. This correction is given by the following equation:

$$I_{corr}\left(t\right) = \frac{I\left(t\right) - I_{BG}\left(t\right)}{I_{FF}\left(t\right) - I_{BG}\left(t\right)}. \tag{G.1}$$

This correction must be applied for each well, such that I_{FF} and I_{BG} are matrices. Example flatfield and background images are provided in Figure 2.3d and B.6.

Modern plate reader calibrations processes include flatfield correction ("ROI/Uniformity calibration" and "Background calibration"), but this option is not available on all machines (e.g., the devices we used in this thesis). Ready-made 96- or 384-well plates for flatfield and background calibration can be purchased (e.g., Applied Biosystems 4432364 and 4432320). In the following sections, we detail the protocol to measure the flatfield and background images.

1. Dispense 20 µl of 1X NEBuffer r2.1 in each of the 384 wells of the well plate. If possible, use automated liquid handling or multi-channel pipette to reduce the pipetting error. Example signals for two machines are shown in Figure G.1.

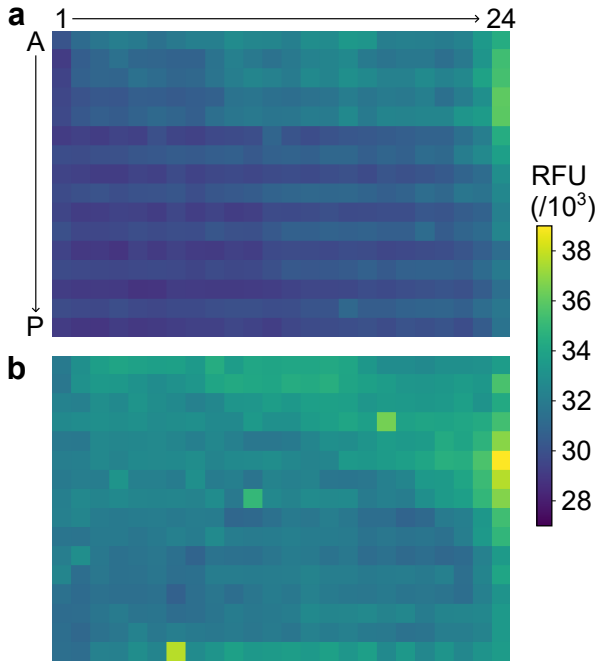

Figure G.1: Background time-averaged image. Shown are raw signal values from the thermal cycler averaged over 35 min. Measurements were taken at 37°C.

2. Dispense 20 µl of the fluorophore solution as used in the assay. Here, we used 10 µM FAM. Example signals for two machines are shown in Figure G.2.

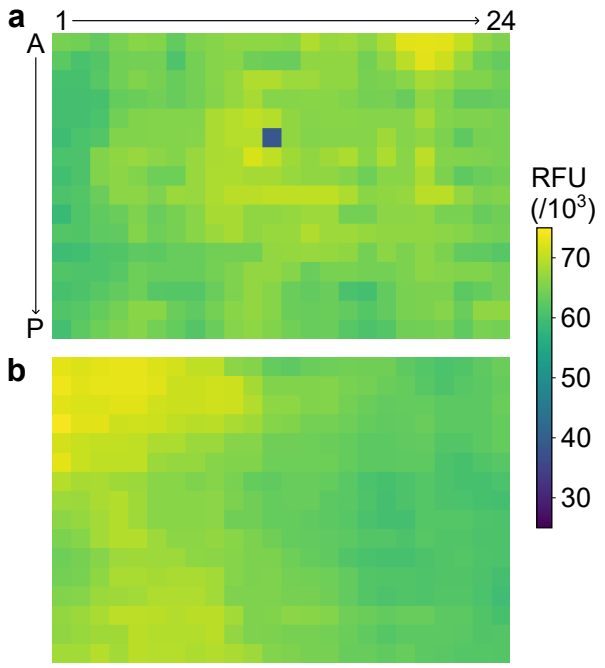

Figure G.2: Flat-field time-averaged image. Shown are raw signal values from the thermal cycler averaged over 35 min. Measurement were taken at 37°C.

3. For both plates, proceed to fluorescence acquisition using the same settings as the assay, including incubation temperature, readout frequency, and duration of assay.

All fluorescent signals measured using the same device can then be corrected using equation G.1. If no significant variations in time are observed in the readouts for $I_{FF}(t)$ and $I_{BG}(t)$ (compared to the measured signal I), then these signals may be averaged, and the following correction can be applied:

$$I_{corr}(t) = \frac{I(t) - \overline{I_{BG}}}{\overline{I_{FF}} - \overline{I_{BG}}}, \tag{G.2}$$

where overbars denote time averages.

G.1.2 Reporter calibration

1. Prepare a solution of 10 nM activated LbCas12a RNP (i.e., after *cis*-cleavage). Refer to Ramachandran [36] for a detailed step-by-step protocol. Alternatively, use the endonuclease DNase I (New England Biolabs M0303S) diluted to 0.4 U/µl.

2. Prepare a dilution series of fluorophore-quencher reporters at varying concentrations. To do so, prepare a solution of 200 µl of 2 µM reporters in NEBuffer r2.1. Mix 100 µl of the reporter solution with

100 µl NEBuffer r2.1. Repeat the dilution step to obtain a total of eight solutions of varying concentrations (100 µl each, 200 µl for the most dilute).

3. Dispense 15 µl of each solution in a well plate. Make triplicates (e.g., dispense into wells B2-B4, D2-D4, ..., P2-P4). Add 5 µl activated RNP (final concentration 2.5 nM), or 5 µl of the DNase I solution (2 U). These wells are used to calibrate the cleaved reporter signal.

4. Dispense 15 µl of each solution in a well plate. Make triplicates (e.g., dispense into wells B6-B8, D6-D8, ..., P6-P8). Add 5 µl NEBuffer r.2.1. These wells are used to calibrate the uncleaved reporter signal.

5. Proceed to take fluorescence measurements using the same settings as the assay, including incubation temperature, and readout frequency. Ensure that steady-state has been reached for the cleaved reporter signal (typically very fast if using DNase I, on the order of 1h if using Cas12a RNPs).

6. Apply the flatfield correction to the fluorescence signal using the data collected in step 1.3.

7. For the cleaved reporter signal: fit the following equation for c_0 and F'_{Cl}:

$$I_{corr}\left(c_{Cl}\right) = 10^{-\frac{c_{Cl}}{c_0}} F'_{Cl} c_{Cl}. \tag{G.3}$$

   Where c_{Cl} is the cleaved reporter concentration, and $I_{corr}(c_{Cl})$ is the flatfield-corrected fluorescence intensity averaged across triplicates at steady-state. We recommend the `curve_fit` function from the `scipy.optimize` module (Python) to perform the fit.

8. For the uncleaved reporter signal: fit the following equation for F'_{Ucl}:

$$I_{corr}\left(c_{Ucl}\right) = 10^{-\frac{c_{Ucl}}{c_0}} F'_{Ucl} c_{Ucl}. \tag{G.4}$$

   The resulting calibration curves will look like Figure G.3.

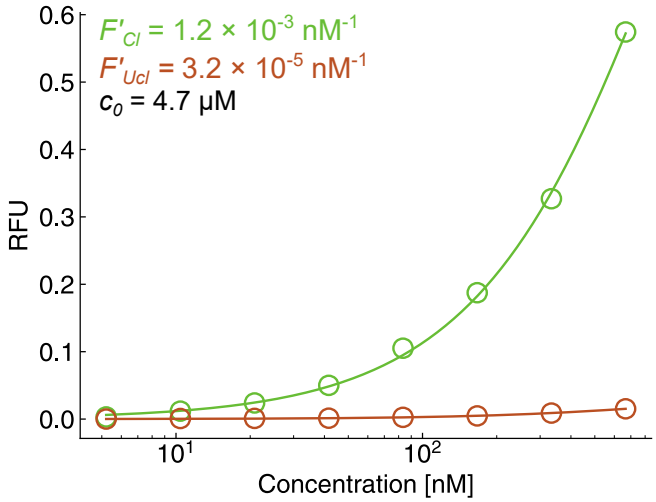

Figure G.3: Calibration curve for cleaved and uncleaved reporters. Shown are flatfield-corrected measurements of fluorescence (symbols) for varying concentrations of cleaved (green) and uncleaved (orange) reporters, and the corresponding fits (solid line) using equations G.3 and G.4.

9. Given the total amount of reporters in solution $[S]_0$, cleaved reporter concentrations $[P](t)$ may be computed using:

$$[P](t) = \frac{10^{\frac{[S]_0}{c_0}} I_{corr}(t) - F'_{Ucl}[S]_0}{F'_{Cl} - F'_{Ucl}}. \tag{G.5}$$

G.2 3D stereolithography with Elegoo Mars

This protocol details how to print a 3D piece with the Elegoo Mars printer. This printer uses the stereolithography technique. It consists of a screen, a tray filled with resin and a platform that can move in the vertical direction (which we will call the "z" direction). We detail here the common protocol to print any piece, along with general design guidelines. This protocol can be easily adapter to other 3D printers, such as the Elegoo Saturn.

How it works: The 3D piece is divided in layers of a given step size (typically 50 to 100 µm). The UV screen of the printer iteratively displays each layer for a given exposure time (on the order of a few seconds). The resin hardens (it "cures") under the UV light of the screen. This results in the formation of hard material on a moving platform. Between each step, the platform moves upwards, with a given step size (z-resolution). The piece is therefore assembled layer by layer on the platform, as it moves upwards and the screen displays the consecutive layers.

G.2.1 Create the 3D design of the piece

1. Use a CAD software to design your piece. This step obviously depends on the geometry of the piece. We recommend SolidWorks or Fusion360, but there is a long list of available software (Autodesk, etc.). For microfluidic chips, we found the following guidelines useful:

    - Make the bottom wall relatively thick (i.e., about 7 or 8 mm). This will prevent the bottom base for distorting (i.e., "potato chip" effect) with increasing temperatures.
    - For the same reason, do not hesitate to make thick vertical walls (about 3 mm).
    - Do not make very high walls. The purpose of the walls is to prevent the liquid PDMS from spilling out of the chip. The PDMS chips do not need to be very thick (only significantly thicker than the maximum height of your channel). Very high walls will also result in significant resin residues stuck in corners after the printing. This will likely result in uneven surfaces and deformed patterns.
    - All z-direction features should (ideally) be integer multiples of the step size.

2. Convert your design to STL.

3. Open Chitubox. Drag your STL file in Chitubox and choose the printing settings. Most preset settings are fine, but the following parameters should be changed in priority if running into printing issues:

    - Exposure time: This is the time during which each layer will be displayed on the screen. Higher exposure times result in harder pieces, but also more diffraction effects (i.e., larger features in the x-y plane). The total printing time also directly depends on this exposure time. For the translucent resin, we recommend 7 s exposure time.

- Bottom layers: The first layers of any design should have a higher exposure time compared to the others. This is to ensure that the piece will adhere to the moving platform and will not drop into the resin tray. We recommend about 10 bottom layers, exposed for 30 s each. This results in a slightly larger height of the bottom wall, and this should have no impact on the chip design.
- z-resolution (step size): This is the step size of the moving platform. Between each step, the platform will move of a distance equal to this parameter. A smaller z-resolution should result in higher vertical resolution, and the smallest z-resolution is ~50 µm for ELEGOO Mars 3 Pro. However, we recommend choosing a step size closer to the smallest feature of your piece. For example, if the smallest feature is 500 µm, we recommend using 100 µm step size and not 50 µm.

4. Make sure your chip is properly oriented. The printer will start with the bottom layers first so they should correspond to the bottom base layer of your chip. Also make sure all the chip geometry fits within the printing platform. You can print the chip at an angle (using the rotation tools in Chitubox). We do not recommend this as it results in strongly pixelated channels. If you do this, add supports to your piece so that it nevertheless adheres to the platform. Supports can be automatically generated and customized in Chitubox.

5. Slice your design and export the CBDDLP file on a USB stick. If you need to change the printing settings, do not open the CBDDLP in Chitubox directly (even though the software will let you do it). This may result in printing issues. You should start from the STL (start from step 3) to edit any printing parameter.

G.2.2 Print your design with the Elegoo Mars

1. Remove the hood of the printer. Make sure nothing is stuck to the platform (e.g., some portion of a previously printed piece) and that the platform is correctly placed above the screen. Use a wipe to clean it with isopropanol.

2. Clean the screen with isopropanol.

3. Place the resin tray on top of the screen. With a small spatula, make sure that the resin is homogeneous and that there is no residual cured piece in the tray. Check that there is sufficient resin for your design, but do not completely fill the tray. The tray should at most be half full. Make sure that the resin tray is properly placed and locked over the screen.

4. Place the hood of the printer back on the printer.

5. Turn on the printer. Connect your USB stick. On the printer touch screen, select your CBDDLP file. Start the printing. You should see the moving platform immersed in the tray. The printer will then display a printing time estimate. For each step, it will also show the layer projected by the UV screen.

G.2.3 Washing and curing

1. Install the isopropanol bath on the Elegoo Mercury. This is about 2.5 L of isopropanol. Make sure it is clean, otherwise replace it.

2. Once the printing is complete, the platform should move to the upmost position. Remove the hood and unscrew the platform. Be careful: at this point, the piece is still wet and covered with uncured resin, which is not desired. This situation means that the piece should not be exposed to sunlight, because this would result in the curing of this unwanted layer of uncured resin. Also, the printed features remain fragile at this point. Check that no piece has fallen into the resin tray.

3. Screw the platform on the Elegoo Mercury. The piece should be immersed in isopropanol. Make sure you are in "washing" mode. Wash for 3 min. During the wash, you should see the isopropanol flow in the container. Unscrew the platform. Make final isopropanol washes with a wash bottle if necessary. *Important note*: For complex designs, or if you suspect that there is an air bubble trapped in the piece during the isopropanol wash, perform step 4 (to un-stick piece from the platform) prior to step 3. Then, place the free (not stuck) piece in the Elegoo Mercury basket for the isopropanol wash (i.e., the piece is washed in the basket instead of being washed on the platform). Make sure all uncured resin is removed (with isopropanol) and move on to step 5 (UV curing).

4. Remove the piece from the platform. Use a metal spatula. Be very gentle to not damage the piece or the platform. Always use the straight part of the spatula and absolutely not the sharp corners of the spatula which would damage the piece. Start from the $x-y$ corners of the piece and insert the scraper between the platform and the piece to separate them. The piece may be difficult to remove, and you may have to gently tap the scraper with a hammer. Unstick one of the corners of your piece first. Do not try to unstick everything at once, otherwise it may deform the piece. Try to unstick all angles of the piece first and then unstick the remaining parts of the piece. You can dry the piece using an air gun if all the isopropanol has not already evaporated.

5. Once the piece is free, place it on the Elegoo Mercury in UV mode. Attach the hood of the Mercury in place and expose to UV curing for 15 min. If using transparent resin, you should see the piece light up with a bright green color.

6. Thoroughly clean the platform, the screen, scraper, spatula, and working space with isopropanol. Make sure you get rid of all uncured resin everywhere.

7. Bake the piece for 24 to 48h at 70°C. Thermal treatment is important as the resin releases chemicals that interfere with PDMS reticulation. After baking, the exterior sides of the molds may peel off a bit–this is not an issue as long as the design part is not affected.